



THESE DE L'UNIVERSITE DE LYON

Délivrée par



L'UNIVERSITE CLAUDE BERNARD LYON 1

préparée au sein de

**ECOLE DOCTORALE
ELECTRONIQUE, ELECTROTECHNIQUE, AUTOMATIQUE DE LYON**

DIPLOME DE DOCTORAT

(arrêté du 7 août 2006)

soutenue publiquement le 24/11/2014

par

M. HILAL Alaa

TITRE:

**Magnetic Components Modeling Including Thermal
Effects for DC-DC Converters Virtual Prototyping**

Directrice de thèse : Mme Marie-Ange RAULET

Co-directeur de thèse : M Christian MARTIN

JURY :

M José COBOS	(Rapporteur)
M Yvan LEFEVRE	(Rapporteur)
M Nadir IDIR	(Président)
M Bruno ALLARD	(Examineur)
Mme Marie-Ange RAULET	(Encadrante)
M Christian MARTIN	(Co-Encadrant)

Acknowledgements

This thesis would not have been possible without the help and support of several individuals who in one way or another contributed and extended their valuable assistance in the preparation and completion of this PhD.

I would like to thank my committee members, Professor José COBOS, Doctor Yvan LEFEVRE, Professor Nadir IDIR and Professor Bruno ALLARD not only for their time and extreme patience, but also for their brilliant comments and suggestions. Thank you.

I would like to express my deepest gratitude to my advisors, Marie-Ange RAULET, and Christian MARTIN for their excellent guidance, caring, patience, and providing me with an excellent atmosphere for my research.

It was a pleasure working at AMPERE Laboratory. Many thanks go to all lab members for their support and the great working environment, with special thanks to our site director Professor Noël BURAI. I would like also to thank our team members Fabien SIXDENIER and Laurent MOREL for their expert advice and encouragement throughout this thesis process, as well as Julien MORAND for his brilliance in the lab.

A special acknowledgement goes to my office mates and colleagues for supporting me over the years and for the good times we spent together. Elias, Arnaud, Oualid, Aurelien, Justine, Albert and Atef, I appreciated sharing my office with you.

I would like to show my greatest appreciation to my Friends who supported me in writing, and incited me to strive towards my goals.

Words cannot express how grateful I am to my Family. My mother, father, sisters and brother receive my deepest gratitude and love for their dedication and the many years of support during my undergraduate studies that provided the foundation for this work. I am particularly grateful to my mother for all of the sacrifices that you've made on my behalf. Your prayer for me was what sustained me this far.

UNIVERSITE CLAUDE BERNARD - LYON 1

Président de l'Université

M. François-Noël GILLY

Vice-président du Conseil d'Administration

M. le Professeur Hamda BEN HADID

Vice-président du Conseil des Etudes et de la Vie Universitaire

M. le Professeur Philippe LALLE

Vice-président du Conseil Scientifique

M. le Professeur Germain GILLET

Secrétaire Général

M. Alain HELLEU

COMPOSANTES SANTE

Faculté de Médecine Lyon Est – Claude Bernard

Directeur : M. le Professeur J. ETIENNE

Faculté de Médecine et de Maïeutique Lyon Sud – Charles Mérieux

Administrateur provisoire : M. le Professeur G. KIRKORIAN

UFR d'Odontologie

Directeur : M. le Professeur D. BOURGEOIS

Institut des Sciences Pharmaceutiques et Biologiques

Directeur : Mme la Professeure C. VINCIGUERRA.

Institut des Sciences et Techniques de la Réadaptation

Directeur : M. le Professeur Y. MATILLON

Département de formation et Centre de Recherche en Biologie Humaine

Directeur : M. le Professeur P. FARGE

COMPOSANTES ET DEPARTEMENTS DE SCIENCES ET TECHNOLOGIE

Faculté des Sciences et Technologies

Directeur : M. le Professeur F. De MARCHI

Département Biologie

Directeur : M. le Professeur F. FLEURY

Département Chimie Biochimie

Directeur : Mme le Professeur H. PARROT

Département GEP

Directeur : M. N. SIAUVE

Département Informatique

Directeur : M. le Professeur S. AKKOUCHE

Département Mathématiques

Directeur : M. le Professeur A. GOLDMAN

Département Mécanique

Directeur : M. le Professeur H. BEN HADID

Département Physique

Directeur : Mme S. FLECK

Département Sciences de la Terre

Directeur : Mme la Professeure I. DANIEL

UFR Sciences et Techniques des Activités Physiques et Sportives

Directeur : M. C. COLLIGNON

Observatoire de Lyon

Directeur : M. B. GUIDERDONI

Polytech Lyon

Directeur : M. P. FOURNIER

Ecole Supérieure de Chimie Physique Electronique

Directeur : M. G. PIGNAULT

Institut Universitaire de Technologie de Lyon 1

Directeur : M. C. VITON

Institut Universitaire de Formation des Maîtres

Directeur : M. R. BERNARD

Institut de Science Financière et d'Assurances

Directeur : Mme la Professeure V. MAUME-DESCHAMPS

TITRE

Modélisation de composants magnétiques avec prise en compte de la température pour prototypage virtuel de convertisseurs DC-DC

RESUME

La complexité croissante des dispositifs en électronique de puissance nécessite l'intervention de la conception assistée par ordinateur. Le développement de systèmes électriques/électroniques est effectué à l'aide du prototypage virtuel dans lequel les logiciels de simulation sont utilisés pour prédire le comportement des composants. De ce fait, le prototypage virtuel permet une économie de temps et d'argent pour la réalisation de prototypes. La demande croissante d'appareils à faible puissance et à haut rendement a obligé les concepteurs à analyser précisément les pertes de chaque composant constituant du système. Les composants magnétiques constituent une partie importante des appareils en électronique, par conséquent la modélisation précise des matériaux magnétiques est nécessaire afin de prédire leur comportement réaliste dans des conditions de fonctionnement variables selon l'application.

Notre travail s'inscrit dans ce contexte et propose un modèle dynamique non linéaire de composants magnétiques pour une utilisation dans des simulateurs de circuits électriques. Ce modèle de composant magnétique inclut le comportement d'hystérésis non linéaire du matériau et permet une modélisation précise des pertes fer et des pertes joule avec de plus la prise en considération des effets thermiques qui, généralement, ne sont pas pris en compte par les modèles existants. Le modèle est basé sur le principe de la séparation des contributions statiques et dynamiques des pertes fer et s'appuie sur la théorie de Bertotti. Le langage de programmation VHDL-AMS est utilisé en raison de sa fonctionnalité de modélisation multi-domaines, permettant un couplage avec un modèle thermique. Le modèle de composant magnétique est mis en œuvre dans le logiciel de simulation de circuit "Simplorer". Il est ensuite testé dans une application de convertisseur de puissance, le convertisseur abaisseur qui permet de fournir une excitation non-conventionnelle. Le modèle est validé pour différents noyaux d'inductances, différentes ondulations de courant et niveaux de charge, différentes températures et une large gamme de fréquence.

DISCIPLINE

Génie Électrique

MOTS-CLES

Simulation de circuit, composants magnétiques, modélisation magnétique dynamique, couplage magnétothermique, convertisseurs DC-DC, pertes de puissance, noyaux nanocristallins et poudre fer.

INTITULE ET ADRESSE DE L'U.F.R. OU DU LABORATOIRE :

Laboratoire AMPERE, UMR 5005, Bâtiment OMEGA, Université Lyon 1

43 Bd du 11 novembre 1918 69622 Villeurbanne

TITLE

**Magnetic Components Modeling Including Thermal Effects for DC-DC Converters
Virtual Prototyping**

ABSTRACT

The increasing complexity of power electronic devices requires the intervention of computer-aided design in electrical engineering. Development of electric/electronic systems nowadays is carried out by the help of virtual prototyping, in which simulation software are used to predict components behavior without investing time and money to build physical prototypes. The increasing demand of low power, high efficiency devices forced designers to precisely analyze losses in each component constituting the system. Magnetic components constitute a major part of electronics devices. Therefore accurate modeling of magnetic materials is mandatory in order to predict their realistic behavior under variable operating conditions.

Our work takes place in this context by proposing a non-linear dynamic model of magnetic components for use in circuit simulators. It includes the material nonlinear hysteretic and dynamic behaviors with accurate modeling of winding and core losses in addition to thermal effects that are not taken into account by existing models. The model is based on the principle of separation of static and dynamic contributions as well as Bertotti's theory. VHDL-AMS is used as a modeling language due to its multi-domain modeling feature, allowing coupling with a thermal model. The magnetic component model is implemented in circuit simulation software "Simplorer". It is then tested in a widely used power converter application, the buck converter, to ensure non-conventional excitation. The model is validated for different core inductors, different current ripples, different loads, different temperatures and a wide frequency range.

DISCIPLINE

Electrical Engineering

KEYWORDS

Circuit simulation, magnetic components, dynamic magnetic modeling, magneto-thermal coupling, DC-DC converters, power losses, nanocrystalline and powder cores.

LABORATORY NAME AND ADDRESS:

AMPERE Laboratory, UMR 5005, Bâtiment OMEGA, Université Lyon 1
43 Bd du 11 novembre 1918 69622 Villeurbanne

Table of Contents

Introduction	6
Chapter 1	8
1. Magnetic Materials in Power Electronics.....	8
1.1 Introduction	8
1.2 Magnetic materials in power electronics	8
1.2.1 Materials Classifications and applications	8
1.2.2 Soft magnetic materials	10
1.2.3 Materials used in power electronics	12
1.3 Temperature Effects	14
1.3.1 Curie temperature	14
1.3.2 Influence of temperature on magnetic properties	14
1.4 Magnetic materials characterization.....	16
1.4.1 Principle of characterization.....	16
1.4.2 Experimental test Bench.....	18
1.4.3 Variable Temperature and Frequency Measurements	19
1.4.4 Self-heating Measurements	21
1.5 Conclusion.....	22
1.6 References	23
Chapter 2	26
2. Magnetic and Thermal Modeling	26
2.1 Introduction	26
2.2 Magnetic modeling.....	26
2.2.1 Static magnetic hysteresis models	26
2.2.2 Dynamic magnetic hysteresis models.....	32
2.2.3 Models available in circuit simulation and their drawbacks	35
2.2.4 Parameters identification.....	36
2.3 Thermal modeling	37
2.3.1 Heat transfer	37
2.3.2 Thermal elements	38
2.3.3 Thermal model	38
2.3.4 Parameters identification.....	40
2.4 Magneto thermal coupling.....	42
2.5 Conclusion.....	42
2.6 References	43

Chapter 3	46
3. Virtual Prototyping and Developed Model	46
3.1 Introduction	46
3.2 Magnetic component modeling for circuit simulators	46
3.2.1 Modeling Theory and Techniques	47
3.2.2 Multi/Mixed domain modeling	50
3.2.3 VHDL-AMS modeling language	51
3.2.4 Circuit simulation software	53
3.3 Developed Model	54
3.3.1 Model Structure	55
3.3.2 Choice of Materials	61
3.3.3 Choice of static and dynamic laws	61
3.3.4 Temperature dependence and parameters extraction	64
3.4 Simulation and Model Validation	68
3.5 Conclusion	74
3.6 References	75
Chapter 4	77
4. Power Electronics Application	77
4.1 Introduction	77
4.2 Buck Converter	77
4.3 Realized Circuit and Measurements	81
4.3.1 Buck Converter Circuit	81
4.3.2 Choice of Inductors and Magnetic Materials Characterization	83
4.3.3 Core Losses Measurements and Calculation	86
4.3.4 Copper Losses Measurements and Calculation	94
4.4 Model Implementation and Simulation Results	98
4.5 Other Results and Applications	101
4.5.1 TRACOPWER commercial converter	101
4.5.2 Single phase transformer	105
4.6 Conclusion on Application	108
4.7 References	109
Conclusion	111

List of Figures

Figure 1-1: Magnetic materials classification[3].....	9
Figure 1-2: Magnetic materials applications 2007 [6].....	9
Figure 1-3: Magnetic hysteresis loop[12].....	10
Figure 1-4: domain walls movement [13].	11
Figure 1-5: Ferrite sample (left) and core shapes (right) [21]	12
Figure 1-6: Iron powder sample (left) and core shapes (right) [25]	13
Figure 1-7: Nanocrystalline sample (left) and core shapes (right) [31].....	13
Figure 1-8: Saturation magnetization as a function of temperature for Fe and Fe ₃ O ₄ [11].....	15
Figure 1-9 : Temperature dependence of initial permeability for ferrite Mn _{0.700-x} Zn _{0.233} Co _x Fe _{2.067} O ₄ (left)[40] and for nanocrystalline Fe-Cu-Nb-V-Si-B alloy annealed at 480–590°C (right)[37].....	15
Figure 1-10 : Temperature dependence of coercive field for manganese-substituted cobalt ferrite CoMn _x Fe _{2-x} O ₄ (left)[36] and for some nanocrystalline alloys (right)[34].	16
Figure 1-11: Principle of B-H characterization	17
Figure 1-12: Materials characterization bench	18
Figure 1-13: Dimensions and properties of N14E1 [41].	19
Figure 1-14: Measured flux density as function of applied field at f=10 Hz (left) and 10 kHz (right) for different temperatures (N14E1).....	19
Figure 1-15: Measured flux density as function of applied field at T= 25°C for different frequencies.	20
Figure 1-16: Magnetic components self-heating measurements test bench.	21
Figure 1-17: Self-heating measurements: core and winding temperatures as function of time.	22
Figure 2-1: Polynomial model.....	29
Figure 2-2: Nonideal Relay Hysteron.....	30
Figure 2-3: Models in circuit simulation summary	35
Figure 2-4: Nodal analysis	39
Figure 2-5: thermal model of an inductor (thermal equivalent circuit)	40
Figure 2-6: Steady state analysis	41
Figure 2-7: Magneto-thermal coupling	42
Figure 3-1: Resistor model example.....	47
Figure 3-2: a) Signal flow (gain block) and b) conserved energy models (Resistor model).	48
Figure 3-3: IC on heat sink equivalent thermal circuit.	49
Figure 3-4: E-core two-winding transformer equivalent magnetic circuit.	49
Figure 3-5: Winding model concept and connections.	50
Figure 3-6: VHDL-AMS entity and architecture.	52
Figure 3-7: Multi-Domain ANSYS Simplorer [16].	53
Figure 3-8: Magnetic Component Structure.	55
Figure 3-9: Winding Model Block.	56
Figure 3-10: Dynamic Model Block.....	57
Figure 3-11: Static Model Block.	58
Figure 3-12: Temperature source component.....	59
Figure 3-13 : Thermal model (equivalent circuit) of an inductor in Simplorer.....	60
Figure 3-14: thermometer component (left) and heat flow source component (right).....	60
Figure 3-15: Measured and simulated static BH curves by Jiles-Atherton model at f = 1 Hz	61

Figure 3-16: Measured and simulated static BH curves by Piecewise Polynomial model at $f = 1$ Hz .	62
Figure 3-17 : Measured and simulated dynamic BH curves by Bertotti's model at $f = 10$ kHz	63
Figure 3-18: Static parameters variations with temperature (approximated by dotted curves).....	64
Figure 3-19: principle of four-point resistivity measurement technique	65
Figure 3-20: Resistivity measurement of a nanocrystalline ribbon.....	66
Figure 3-21 : Electric resistivity variation with temperature.....	66
Figure 3-22: Dynamic parameter γ variation with temperature.....	67
Figure 3-23 : Dynamic parameter α variation with temperature	67
Figure 3-24 : Measurement (left) and simulation (right) circuits.	68
Figure 3-25 : Circuit simulation in Simplorer (schematic).....	68
Figure 3-26: Measured and simulated static ($f = 1$ Hz) BH curves at $T = 25$ °C (left) and $T = 155$ °C (right).....	69
Figure 3-27: Measured and simulated dynamic ($f = 10$ kHz) BH curves at $T = 25$ °C (left) and $T = 155$ °C (right)	69
Figure 3-28: Measured and simulated dynamic BH curves at 20 kHz (left) and 40 kHz (right)	69
Figure 3-29: Measured and simulated field at 0.5T applied flux density at $f=10$ kHz.	70
Figure 3-30: Measured and simulated magnetic fields for 0.5 T applied triangular flux density	71
Figure 3-31 : Circuit simulation in Simplorer including thermal model	71
Figure 3-32: Thermal image of nanocrystalline core	72
Figure 3-33: Core geometric parameters.....	73
Figure 3-34: Measured and simulated core (T_c) and winding (T_w) temperatures.	74
Figure 4-1: Buck converter circuit	78
Figure 4-2: Buck voltages and currents waveforms	78
Figure 4-3: Continuous and Discontinuous Conduction modes	80
Figure 4-4: Buck converter circuit including the magnetic component model	81
Figure 4-5: Circuit design of buck circuit	81
Figure 4-6: PCB layouts of buck and load circuits.....	82
Figure 4-7: Buck with optically isolated gate driver circuit.....	82
Figure 4-8: Chosen Nanocrystalline and Powder cores inductors (including secondary windings)	83
Figure 4-9: Static and dynamic characterization of the powder magnetic material (HKBH)	84
Figure 4-10: Static and dynamic characterization of the Nanocrystalline magnetic material (K44B200)	84
Figure 4-11: Parameter α variation with maximum flux density level for HKBH (left) and K44B200 (right).....	85
Figure 4-12: Measured sine and square losses and datasheet losses at $B = 100$ mT.	86
Figure 4-13: Measured core losses at different flux density levels in buck application.....	87
Figure 4-14: Measured core losses for variable load currents.....	88
Figure 4-15: Effect of variable DC bias	88
Figure 4-16: Minor loops in continuous and discontinuous conduction modes	89
Figure 4-17: Inductor voltage and current in continuous and discontinuous conduction modes	90
Figure 4-18: Core losses of both powder core HKBH and nanocrystalline core K44B200 materials under 50 mT applied “sinusoidal” flux density	91
Figure 4-19: Core losses of both powder core HKBH and nanocrystalline core K44B200 materials in the buck converter at constant flux density operating points ($f/V=10k$)	91
Figure 4-20: Setup for variable temperature measurements in buck converter.....	92

Figure 4-21: Core losses variation in the buck application for the nanocrystalline material as function of both frequency and temperature.....	93
Figure 4-22: Measured flux density of nanocrystalline material as function of applied static field at different temperatures.....	93
Figure 4-23: Measured AC resistance of W1 as function of frequency	96
Figure 4-24: Measured AC resistance of W2 as function of frequency	96
Figure 4-25: Measured AC resistance of W3 as function of frequency	97
Figure 4-26: Buck converter simulation circuit.....	98
Figure 4-27: Measured and simulated core losses in powder core HKBH.....	98
Figure 4-28: Measured and simulated inductor voltage at $f=50$ kHz	99
Figure 4-29: Measured and simulated inductor current at $f=50$ kHz	99
Figure 4-30: Simulated and measured core losses under variable load currents.	100
Figure 4-31: Measured and simulated core losses in nanocrystalline core K44B200	100
Figure 4-32: TRACOPOWER TSI-10N circuit and dimensions in mm	101
Figure 4-33: TSI converter adjusted circuit.....	102
Figure 4-34: Measured and simulated inductor voltage	103
Figure 4-35: Measured and simulated inductor current.....	103
Figure 4-36: measured and simulated B-H loops	104
Figure 4-37: Simulation circuit of a two-winding transformer	105
Figure 4-38: Primary current and secondary current referred to the primary side variation with load	106
Figure 4-39: Core (left) and copper (right) losses as function of load	107
Figure 4-40: Converter efficiency as function of load	107

Introduction

The increasing complexity of power electronic devices requires the intervention of computer-aided design in electrical engineering. Development of electric/electronic systems nowadays is carried out by the help of virtual prototyping, in which simulation software are used to predict components behavior without investing time and money to build physical prototypes. In the design and analysis of systems in general, specifically power converters, virtual prototyping assure time, failure rate and cost reduction. Indeed modeling and simulation allow the prior knowledge of the power converter behavior using circuit simulators to optimize complex circuit prototypes. Individual passive and active components models exist and are associated together to form a complete converter model.

Power consumption and efficiency have always been of great concern in the development of power electronics systems. The increasing demand of low power, high efficiency devices forced designers to precisely analyze losses in each component constituting the system. Magnetic components constitute a major part of electronics devices. Therefore accurate modeling of magnetic materials is mandatory in order to predict their realistic behavior under variable operating conditions. In fact nonlinear characteristics of magnetic materials and both dynamic and thermal effects have a non-negligible influence on device's performance and must be taken into account in circuit simulations. Furthermore, temperature induces major changes in component's behavior and is not considered in these pre-defined software magnetic models.

Our work takes place in this context by proposing a non-linear dynamic model of magnetic components for use in circuit simulators. It includes the material nonlinear hysteretic and dynamic behaviors with accurate modeling of winding and core losses in addition to thermal effects that are not taken into account by existing models. The model is based on the principle of separation of static and dynamic contributions as well as Bertotti's theory. VHDL-AMS is used as a modeling language due to its multi-domain modeling feature, allowing coupling with a thermal model. The thermal model is represented by a temperature source for static thermal conditions or by an equivalent thermal circuit for self-heating conditions. The magnetic component model is implemented in circuit simulation software "Simplorer" and validated by modeling a Nanocrystalline-core inductor. The effects of frequency, temperature and waveform are studied. It is then tested in a widely used power converter application, the buck converter, to ensure non-conventional excitation. The model is validated for different core inductors, different current ripples, different loads, a wide frequency range (10-100 kHz) and for temperatures up to 200 °C.

This thesis is a continuation to the work began several years ago at Ampere's Laboratory in magnetic materials dynamic modeling. Four chapters other than the introduction and the conclusion constitute this manuscript. The first chapter introduces magnetic materials and their classification and presents the materials currently used in power electronics applications. Then temperature effects on these materials and their characterization by variable frequency and temperature measurements are studied. The principle of characterizing magnetic materials

including the results of wide temperature range (25°C to 250°C) B-H measurements is explained.

Chapter 2 concerns both magnetic and thermal modeling and coupling between them. Static and dynamic modeling laws that are well known and widely used are presented focusing on the models that are used in circuit simulation. Thermal modeling approach and thermal model structure are explained using the concepts of thermal elements and thermal energy transfer. Parameters identification of both magnetic and thermal models is also presented.

The work on developing the magnetic component model is described in chapter 3. We expose modeling techniques, modeling languages and circuit simulation software. Then we explain the modular structure of the magnetic component model and its implementation in the circuit simulation software Simplorer using VHDL-AMS modeling language. The choice of both static and dynamic material laws depending on the choice of material is explained. Temperature effects are introduced to the component model which is validated for nanocrystalline material for different temperatures and frequencies.

In many power applications, magnetic materials are excited with non-sinusoidal waveforms. This induces different losses compared to those provided by manufacturers based on sinusoidal flux density. Based on that, the forth chapter is dedicated to the adaptability, reliability and precision of developed model for use in power electronics applications. The magnetic component behavior in a buck converter is investigated. A circuit design with variable voltage, frequency and load is realized. Core and winding losses measurements under variable conditions are performed. Measured results are compared to simulated ones for different core inductors, frequencies, flux densities, DC bias and temperatures. Advantages of the model with respect to analytical losses formulas, as well as its limitations are discussed.

Finally a general conclusion summarizes the thesis and clarifies our perspectives for future work.

Chapter 1

1. Magnetic Materials in Power Electronics

1.1 Introduction

Electrical power supplies and transformers, electric motors, mobile phones, computers and many other devices used in everyday life rely on magnetism and magnetic materials. The phenomenon of magnetism is known for thousands of years by which materials exhibit attractive or repulsive forces on other materials. Recent researches led to a better understanding of the phenomena's underlying principles. In fact the origin of magnetism lies in the spin and orbital motions of electrons creating an electron magnetic moment. These moments may point in random directions or are aligned together to define the magnetic properties of the material. So the magnetic behavior of a material depends on its structure, particularly its electron configuration. The response of a magnetic material to an applied magnetic field H (A/m) specify if the material is magnetic or not and its type of magnetism. [1] [2].

1.2 Magnetic materials in power electronics

1.2.1 Materials Classifications and applications

Based on their magnetization M (A/m), resulting from the response to applied magnetic field, magnetic materials are classified into five major groups summarized in Figure 1-1. Ferromagnetic and ferrimagnetic materials are usually considered magnetic. The remaining three are so weakly magnetic that they are usually thought of as "nonmagnetic" [3]. Thus only ferromagnetic and ferrimagnetic materials are used in power electronics. Furthermore magnetic materials are classified as soft or hard according to the ease of magnetization [4]. If a material is easily magnetized and demagnetized then it is referred to as a soft magnetic material (applied field below 100 A/m), whereas if it is difficult to demagnetize then it is referred to as a hard magnetic material (applied field above 1000 A/m).

Fields of applications of magnetic materials depend on their magnetic properties. Soft materials are mainly used in power conversion, power adaption, and signal transfer. Hard materials are used as permanent magnets. Magnetic recording applications mix both soft and hard magnetic materials to enhance data storage capacity [5].

Figure 1-2 shows the world market of magnetic materials applications. Soft magnetic products occupy about 45% of world market (being estimated at USD 12 billion) where hard magnets occupy about 20% of world market (being estimated at USD 4.5 to 5 billion). The remaining 35% are magnetic recording applications to attain a total of USD 30 billion as a global market of magnetic materials [6][7].

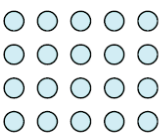
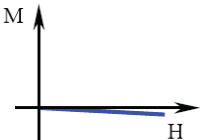
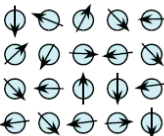
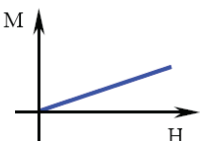
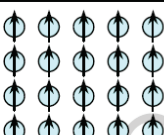
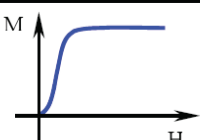

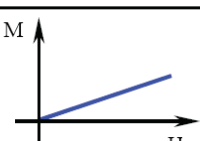
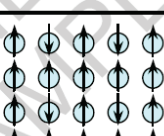
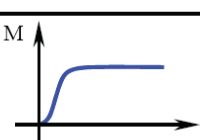
Type	Atomic / Magnetic Behaviour	
Dia-magnetism	 <p>Atoms have no magnetic moment</p>	
Para-magnetism	 <p>Atoms have randomly oriented magnetic moments</p>	
Ferro-magnetism	 <p>Atoms have parallel aligned magnetic moments</p>	
Antiferro-magnetism	 <p>Atoms have anti-parallel aligned magnetic moments</p>	
Ferri-magnetism	 <p>Atoms have mixed parallel and anti-parallel aligned magnetic moments</p>	

Figure 1-1: Magnetic materials classification[3]

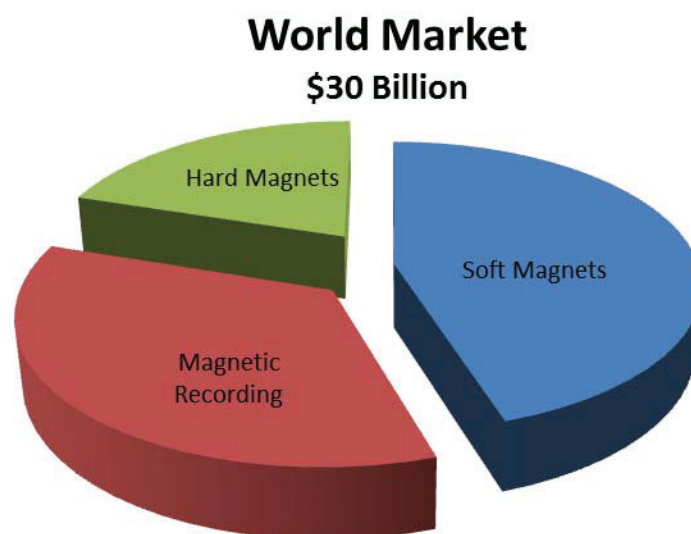


Figure 1-2: Magnetic materials applications 2007 [6]

1.2.2 Soft magnetic materials

Soft magnetic materials are extensively used in power electronics, motors, power supplies, power transformers, and inductors [8][9]. The operating frequency of these devices varies from DC up to 10 MHz [10]. In our domain of application, the study of magnetic properties and material's behavior under variable operating conditions is essential. The macroscopic properties of soft magnetic materials will be explained briefly hereafter.

When a soft magnetic material is magnetized in one direction, it will not relax back to zero magnetization when the imposed magnetizing field is removed. It must be driven back to zero by a field in the opposite direction. If an alternating magnetic field is applied to the material, its magnetization will trace out a loop called a hysteresis loop (Figure 1-3). The lack of retrace ability of the magnetization curve is the property called hysteresis and it is related to the existence of magnetic domains in the material. Once the magnetic domains are reoriented, it takes some energy to turn them back again. This property of ferromagnetic materials is called a magnetic "memory"[11].

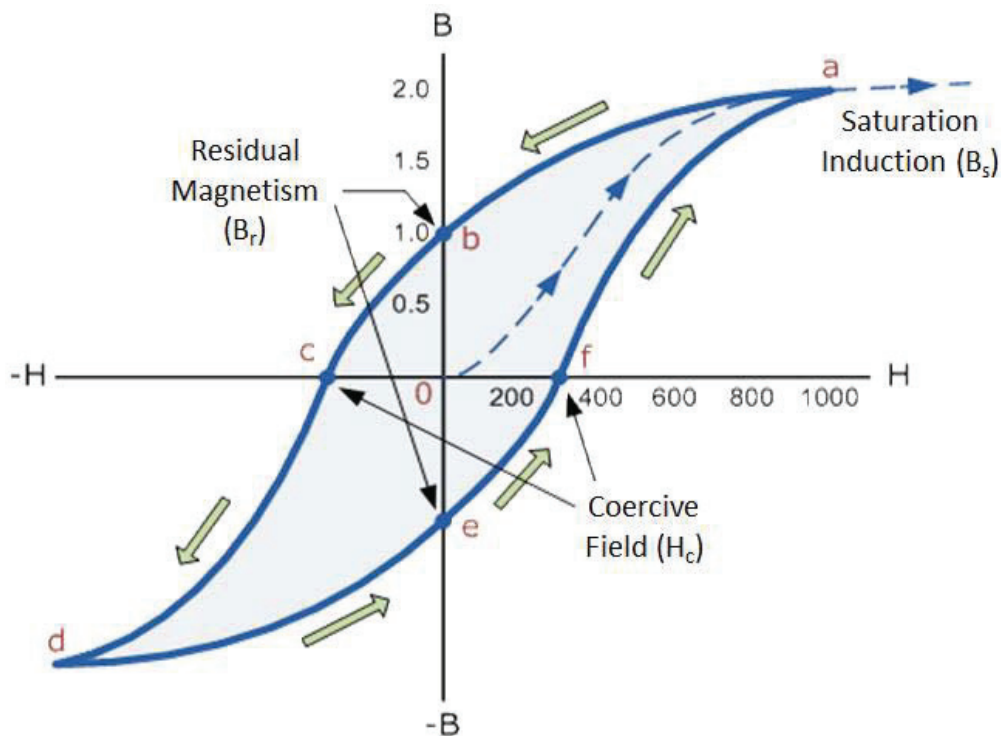


Figure 1-3: Magnetic hysteresis loop[12]

The hysteresis loop shown in Figure 1-3 is generated by measuring the magnetic flux of a ferromagnetic material while the magnetizing field is changed. From the hysteresis loop, a number of primary magnetic properties of a material can be determined like permeability, Saturation Induction, Residual Magnetism and Coercive Field. The Residual Magnetism is the magnetic flux density that remains in a material when the magnetizing force is zero. And the Coercive Field is the amount of reverse magnetic field which must be applied to a magnetic material to make the magnetic flux return to zero.

The size and shape of the hysteresis curve is of considerable importance. The area within a loop represents magnetic energy losses per unit volume of material per cycle. Soft magnetic materials have small hysteresis loops and thus lower energy losses. Also they have a high initial permeability and a low coercivity, consequently the material may reach its saturation magnetization with a relatively low applied field. The phenomenon of hysteresis corresponds to the rotation of magnetization and the movement of magnetic domains walls within the grains of the material. The domain wall movement illustrated in Figure 1-4 changes the size and number of magnetic domains according to the magnitude and/or direction of the external magnetic field [13].

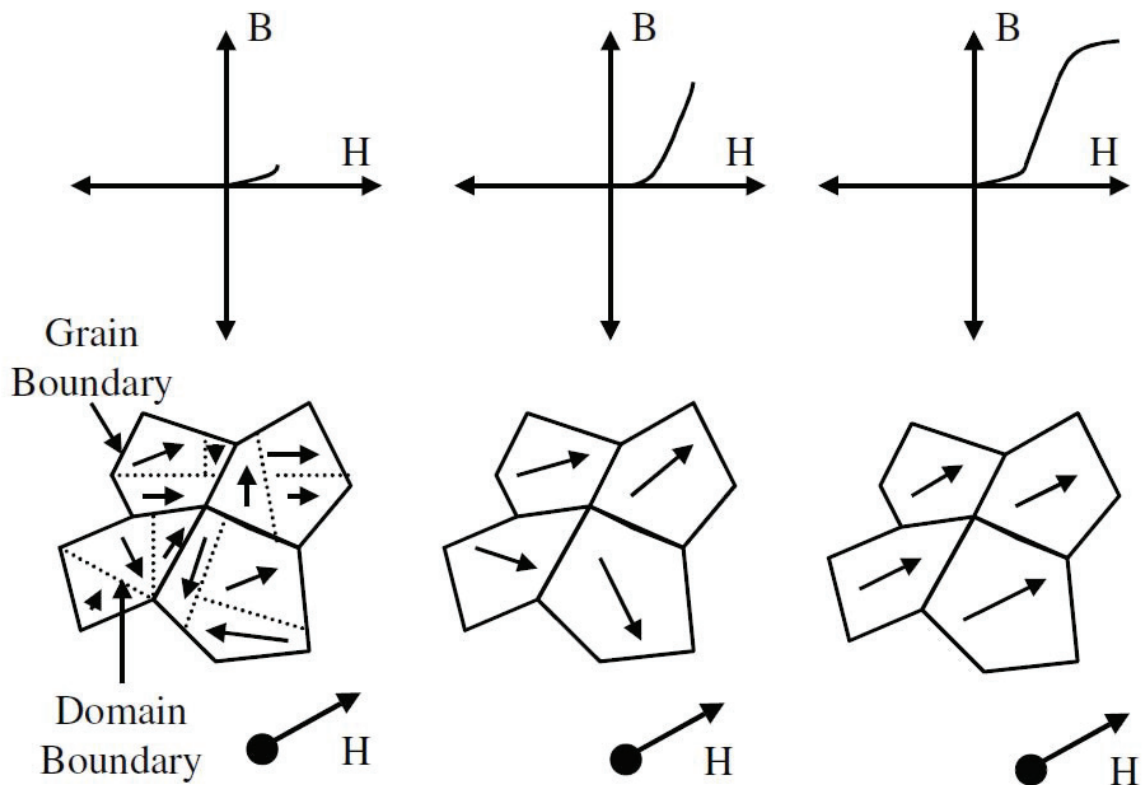


Figure 1-4: domain walls movement [13].

Another property consideration for soft magnetic materials is the electrical resistivity. As energy losses may result from eddy currents that are induced in the material, it is most desirable to minimize these energy losses by increasing the electrical resistivity. This is accomplished by forming solid solution alloys such as iron–silicon, iron–nickel and other alloys. Both electric resistivity and hysteresis characteristics of soft magnetic materials may be enhanced for some applications by an appropriate annealing or by applying mechanical stress. These treatments change impurities, average grain size, anisotropy and crystallization of magnetic materials. This consecutively changes magnetic and electric properties of the material, mainly saturation induction, coercivity and resistivity [14].

1.2.3 Materials used in power electronics

Based on their hysteresis characteristics, soft magnetic materials occupy different applications in the field of power electronics. Depending on their composition and structure soft magnetic materials used in power electronics are classified into 3 main categories having different properties (saturation, coercivity, permeability, and resistivity). These 3 main magnetic core materials are ferrite cores, iron powder cores and nanocrystalline cores [15].

1.2.3.1 Ferrite cores

Ferrites are chemically inert ceramic materials, having a magnetic cubic structure. They are physically hard, brittle, stable and high resistivity materials. Ferrites are Metallic Oxides with the general structure XFe_2O_4 where X is one of the transition metals: Fe, Ni, Zn, Mn, Cu, Ba, Co, and Mg. These metals are mixed, milled, shaped and finally pressed to ensure the required grain size and the final shape of magnetic core. Heating up to 1300°C is required to physically harden the material and ensure desired magnetic properties [16].

The common types of ferrites are Mn-Zn ferrites used for low frequencies applications up to several kHz and Ni-Zn ferrites used for higher frequencies applications up to few MHz [17][18]. They exist in different core shapes including toroid, E, I and U shapes shown in Figure 1-5 [19][20].



Figure 1-5: Ferrite sample (left) and core shapes (right) [21]

1.2.3.2 Powder cores

A powder core consists of small particles of pure iron and/or metal alloys, coated with a thin insulating layer and pressed with an addition of lubricant to a bulk material at high pressure. The insulating coating reduces eddy currents by increasing the resistivity of bulk material and decreases the permeability by acting as small air gaps inside the core material. During compaction, internal stresses are generated in the material. A heat treatment process is applied to relieve these stresses and increases the strength of the material. Finally powder cores are covered by a protective coating to improve the mechanical strength and provide insulation. Iron powder materials are most often magnetically, thermally and mechanically isotropic in their behavior [22] [23] [24].

Powder cores have a lower value of permeability but a higher saturation flux density, than ferrites. They are used for medium frequencies applications (hundreds of kHz) like chokes, transformers, EMI filters and RF applications. Notable characteristics of powder cores are

their low hysteresis and DC losses, stable inductance and slight sensibility to thermal aging. Iron powder cores are made in different shapes and sizes as in Figure 1-6 [23].



Figure 1-6: Iron powder sample (left) and core shapes (right) [25]

1.2.3.3 Nanocrystalline cores

Nanocrystalline materials are the result of high-tech production process from low cost raw materials like silicon and iron to produce a new generation of magnetic materials with interesting soft magnetic properties [26]. They combine the high flux of Fe-Si with improved high frequency performance of ferrites, namely low losses and wide permeability range. Due to these advantages, in addition to their low weight and volume, nanocrystalline materials are mainly used in EMI filters and other power electronics applications like switched mode power supplies, static converters, and electrical welding sources [27][28].

Magnetic nanocrystalline materials are formed by an assembly of regions of coherent crystalline structure (the grains), having an average grain diameter from 1 to 50 nm, exhibiting magnetic order and embedded in a magnetic or nonmagnetic matrix. Ribbons of nanocrystalline alloys are made by rapid solidification, deposition techniques and solid state reactions where the initial material may be in the amorphous state and subsequently crystallized. The alloy composition, crystal structure, microstructure and morphology determine the material's magnetic properties like the saturation flux density B_s (up to 1.5 T), permeability μ (wide range from 200 to 200 000) the coercive field H_C (down to 0.5 A/m) and the Curie temperature T_C (up to 600 °C). The produced ribbons are then used to form fragile toroidal cores (Figure 1-7) which are annealed under the presence of a magnetic field to form ultrafine crystals [29][30].



Figure 1-7: Nanocrystalline sample (left) and core shapes (right) [31]

In this thesis we study powder and nanocrystalline cores only due to their high performance in our domain of application (DC-DC converters) and frequency range (a few hundred of kHz). Besides, ferrites were extensively studied unlike nanocrystalline and powder materials. In fact powder and nanocrystalline materials have higher saturation flux density, lower hysteresis losses, and lower DC bias effect than ferrites but ferrites have lower cost and losses at very high frequencies due to their high resistivity. Concerning thermal behavior, ferrites have lower operating and Curie temperatures. Temperature effects on magnetic materials are presented in the following section.

1.3 Temperature Effects

For all solids, including magnetic materials, a temperature rise increases the thermal vibration of atoms. This vibration tends to randomize the directions of magnetic moments modifying magnetic behavior of materials.

1.3.1 Curie temperature

Ferrimagnetic and ferromagnetic materials show magnetic behavior below a critical temperature called the Curie temperature (T_c). Above this temperature magnetic moments are oriented randomly, resulting in a zero net magnetization [32][33]. In this region the mutual spin coupling forces are completely destroyed and materials become paramagnetic. This temperature depends on the substance thus varies from one material to another, its order of magnitude is for example about 768°C for iron, 1120°C for cobalt, and 335°C for nickel. The approach to ferromagnetism as a function of temperature is described by the Curie-Weiss Law which gives the magnetic susceptibility as a function of temperature shown in equation (1.1).

$$\chi = \mu - 1 = \frac{C}{T - T_c} \quad (1.1)$$

Equation (1.1) is valid only for temperatures above the Curie temperature ($T > T_c$) where χ and μ are the magnetic susceptibility and relative magnetic permeability of the material respectively. C is a constant characteristic for a given substance and T_c is the Curie temperature.

1.3.2 Influence of temperature on magnetic properties

Temperature influences the material's magnetic behavior by modifying its magnetic properties [13][34]. A nonlinear evolution of magnetic parameters (saturation magnetization, relative permeability, coercive field) as function of temperature exists [35][36][37][38][39][40]. Saturation magnetization for both ferri- and ferro- magnetic materials decrease with temperature. The saturation magnetization is a maximum at 0 K, temperature at which the thermal vibrations are minimum [11]. With increasing temperature, the saturation magnetization diminishes gradually and then drops to zero at T_c . As an example the saturation magnetization of Fe and Fe₃O₄ as function of temperature are represented in Figure 1-8.

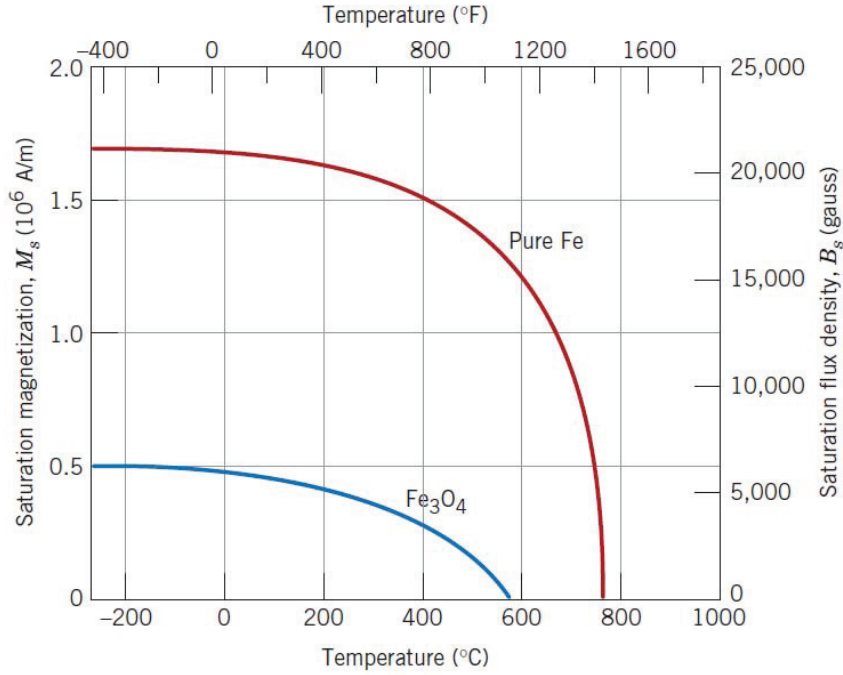


Figure 1-8: Saturation magnetization as a function of temperature for Fe and Fe₃O₄ [11]

The saturation magnetization as function of temperature can be approximated by equation (1.2) where M_s^a is the saturation magnetization at ambient temperature and τ is a constant.

$$M_s(T) = M_s^a \cdot \left(1 - \exp\left(-\frac{T - T_C}{\tau}\right) \right) \quad (1.2)$$

Unlike saturation magnetization, permeability may increase or decrease with temperature depending on the material. For example Figure 1-9 shows initial permeability variation as function of temperature for a ferrite and a nanocrystalline material. These materials have inverse variation of permeability as function of temperature. The permeability of the ferrite material increases and that of the nanocrystalline material decreases with temperature.

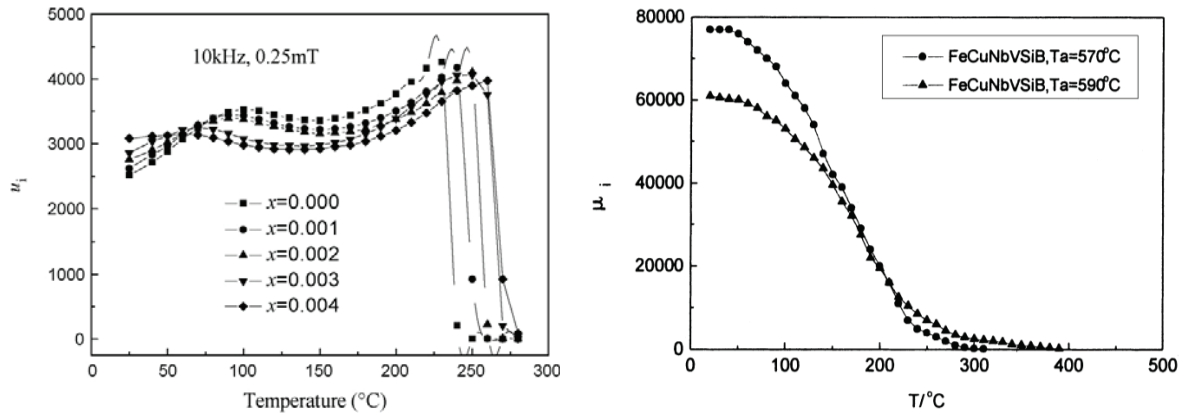


Figure 1-9 : Temperature dependence of initial permeability for ferrite $\text{Mn}_{0.700-x}\text{Zn}_{0.233}\text{Co}_x\text{Fe}_{2.067}\text{O}_4$ (left)[40] and for nanocrystalline Fe-Cu-Nb-V-Si-B alloy annealed at 480–590°C (right)[37].

Similarly, coercive field may vary differently from one material to another as shown in Figure 1-10. For the manganese-substituted cobalt ferrite H_c decreases with temperature whereas for most nanocrystalline alloys presented here H_c increases with temperature.

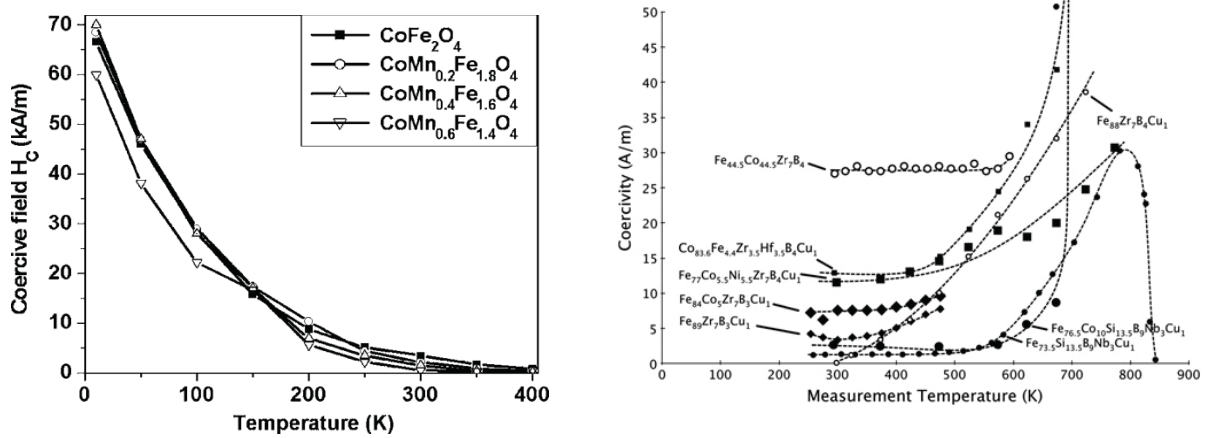


Figure 1-10 : Temperature dependence of coercive field for manganese-substituted cobalt ferrite $\text{CoMn}_x\text{Fe}_{2-x}\text{O}_4$ (left)[36] and for some nanocrystalline alloys (right)[34].

Since different magnetic materials do not possess same behavior for the same thermal conditions, performance of the system containing magnetic components depends greatly on operating temperature range. Thus thermal effects must be taken into account before introducing materials in the application. To predict temperature influence on materials and the trend of variation of magnetic parameters as function of temperature, magnetic material characterization is necessary. From this characterization, magnetic properties, losses and frequency dependence are also deduced. So the next section will explain the principle of characterization of magnetic materials.

1.4 Magnetic materials characterization

1.4.1 Principle of characterization

Magnetic materials are characterized using different methods. In this thesis, B-H characterization is mainly used. From a measured B - H loop most macroscopic magnetic properties such as permeability, saturation flux density, residual magnetism, and coercive field can be extracted. Magnetic losses are also available from the area of hysteresis loop. Then hysteresis loops are measured at different temperatures and frequencies to study their effects on magnetic behavior.

B - H characterization consists of tracing the magnetic flux density B as function of applied magnetic field H deduced from their corresponding electrical quantities. A toroid structure of magnetic material is considered to insure lowest flux leakage. The core under test must be provided with two windings. The first winding is fed with an alternating current. This current is directly proportional with the field strength H . The second winding is used for measuring the voltage and the flux density B is derive therefrom. The measurement could also be done with a single winding on the core, but the voltage drop over the internal resistance of the

winding caused by the current would introduce a measurement error. Another advantage by using a dual winding is that it simplifies the current measurement. Considering the core shown in Figure 1-11 having N_1 primary turns and N_2 secondary turns. The magnetic field on the surface of the material created by the primary current I_1 is calculated by (1.3). Then the flux density is deduced by integrating the measured voltage V_2 of the secondary winding using (1.4). Where l_m is the average length and S is the cross section of the toroid.

$$\oint H(t) dl = N_1 i_1(t)$$

$$\Rightarrow H(t) = \frac{N_1 \cdot i_1(t)}{l_m} \quad (1.3)$$

$$v_2(t) = -N_2 \cdot \frac{d\phi(t)}{dt}$$

$$\Rightarrow B(t) = -\frac{1}{S \cdot N_2} \int v_2(t) \cdot dt \quad (1.4)$$

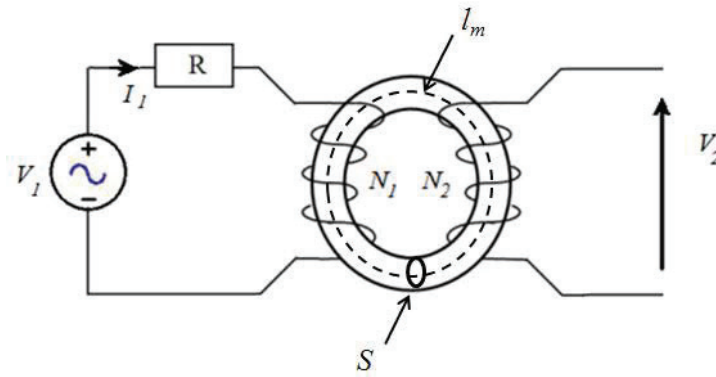


Figure 1-11: Principle of B-H characterization

From equations (1.3) and (1.4) the temporal magnetic field $H(t)$ and flux density $B(t)$ are available and used to trace the B - H loop over one period.

It is important that the core have a uniform cross-sectional area otherwise it is difficult to interpret the results because B won't be uniform in the material. Basically in order to minimize the effect of core geometry, a diameter ratio (outer diameter OD over inner diameter ID) of at least 1.25 must be considered.

1.4.2 Experimental test Bench

In order to characterize magnetic materials under variable operating conditions, an experimental test bench is assembled in our laboratory allowing variable waveform, induction level, frequency and temperature measurements. The test bench is shown in Figure 1-12 and consists of the following equipment:

- PC 3.0 GHz 4 GHz RAM
- Function generator Tektronix AFG320 with GPIB interface (IEEE-488.2)
- Linear power amplifier AE TECHRON 200V/10A
- National instruments PXI platform with multifunction 16-bit 32 analog inputs DAQ module and 14-bit 100 MS/s digitizer
- Spectrum MI.3112 Transient recorder 12-bit 8 channels with PCI interface
- Analogical integrators
- Rheostats
- Thermal chamber (furnace) SNOL 30/1100
- Thermal sensors (thermocouples type k)
- Current sensors (shunt resistors)

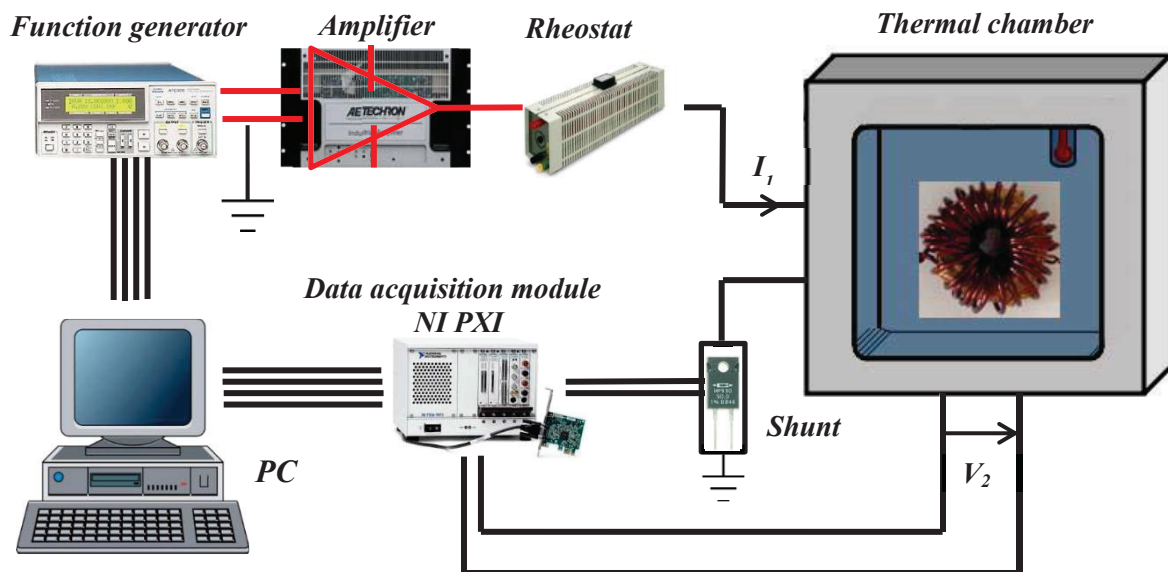


Figure 1-12: Materials characterization bench

This experimental test bench exists in two versions, a low frequency bench (bench 1) and a high frequency bench (bench 2). These two allow measurements under the following variable conditions:

- Temperature range: 25 °C to 1100°C
- Frequency range:
 - 0.1 Hz to 1 kHz (bench 1)
 - 500 Hz to 20 kHz (bench 2)
 - Up to 60 kHz (using a digital oscilloscope)
- Waveforms: sinusoidal, triangular, and predefined set of points (file.txt)
- Possibility to impose both field H and flux density B

1.4.3 Variable Temperature and Frequency Measurements

The above test bench is used to characterize different materials with different shapes (here we used only toroid). Among studied materials, nanocrystalline Nanophy® cores N14E1, provided by Mecagis, are chosen due to their interesting properties including high saturation flux density, low coercive field and high relative permeability as shown in Figure 1-13.

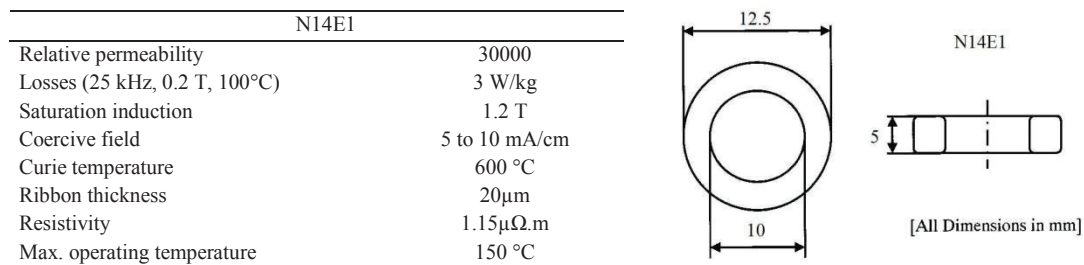


Figure 1-13: Dimensions and properties of N14E1 [41].

To characterize this material, variable temperature and frequency measurements are performed on a test transformer consisting of 4 primary turns and 10 secondary turns wound on a small N14E1 core having above dimensions (figure 13). A sinusoidal current is applied to the primary winding, to create a magnetic field H and the flux density B is obtained from the secondary voltage measured under temperatures between 25°C and 275°C. Measurement results are shown in Figure 1-14 and Figure 1-15. Figure 1-14 shows temperature influence on the material's magnetic behavior at static and dynamic conditions, 10 Hz and 10 kHz respectively. While Figure 1-15 shows frequencies effects (up to 40 kHz) at 25 °C.

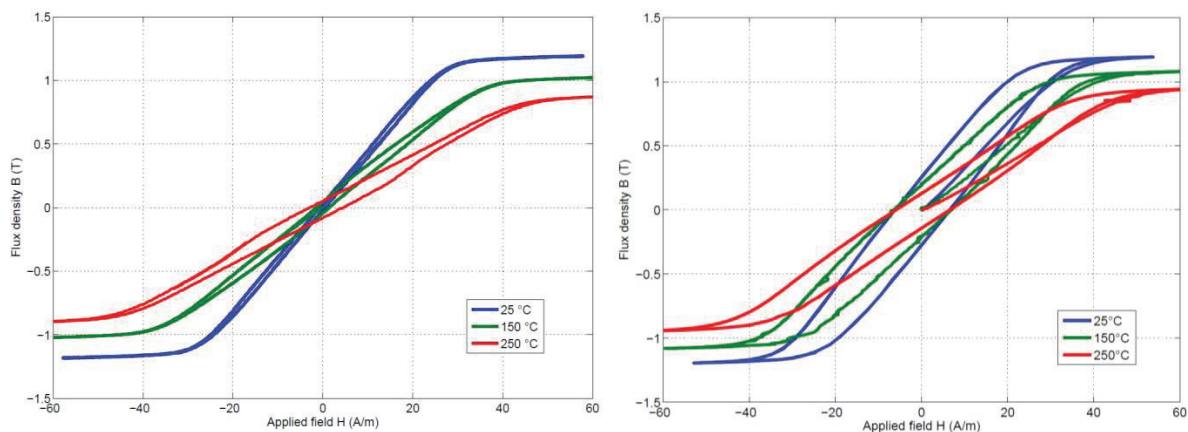


Figure 1-14: Measured flux density as function of applied field at $f=10$ Hz (left) and 10 kHz (right) for different temperatures (N14E1).

We notice that the static coercive field increases with the temperature, but remains relatively low. This phenomenon is usually observed in some nanocrystalline materials [34]. Temperature increase causes a decrease of both saturation flux density and permeability for both static and dynamic conditions. Effects of frequency are summarized by the B-H loop enlargement with the frequency increase, thus bigger area, signifying higher losses at higher frequencies. However temperature effects on low permeability nanocrystalline materials may be different, as their permeability increases with temperature (these cores are studied in the fourth chapter of this thesis).

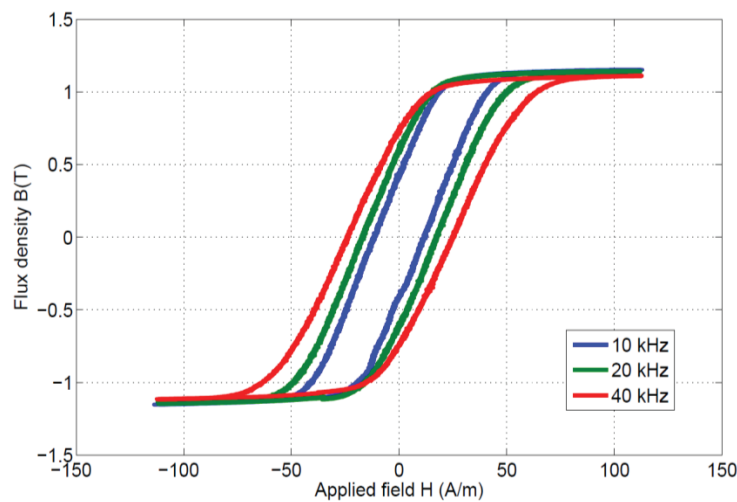


Figure 1-15: Measured flux density as function of applied field at $T= 25^\circ\text{C}$ for different frequencies.

These B-H loop measurements are then used to predict appropriate static and dynamic models to describe the material's behavior. Also parameters of these models and their variation as function of temperature are extracted from these measurements. This procedure is explained in details in the second chapter. In addition the aim of these measurements is to study the iron losses arising in the material due to relatively high frequency applied field as well as the influence of temperature on these losses.

The measurements performed in this section are for two or three periods of time only in order to avoid self-heating of the magnetic cores. Thus they aim to study magnetic behavior under a constant applied temperature.

Nevertheless self-heating is another aspect of magnetic materials that is due to long time operation. This aspect is also important in the characterization of magnetic materials since different materials attain different temperatures in different time durations.

Self-heating measurement principles and corresponding test bench are discussed in the next section.

1.4.4 Self-heating Measurements

In previous characterization, the magnetic component was under static thermal conditions. The component is placed in an oven/furnace and constant temperatures (between 25°C and 275°C) are imposed during short time measurements. Another important thermal aspect is the self-heating or dynamic thermal condition. When magnetic components operate constantly, iron and copper losses cause self-heating in both core and winding. Both temperatures increase exponentially with time. Dynamic self-heating measurements are necessary for the development of thermal models which is a part of our work. Thermal modeling and magneto-thermal coupling are explained in next chapter. This section is consecrated for self-heating measurements principle and test bench shown in Figure 1-16.

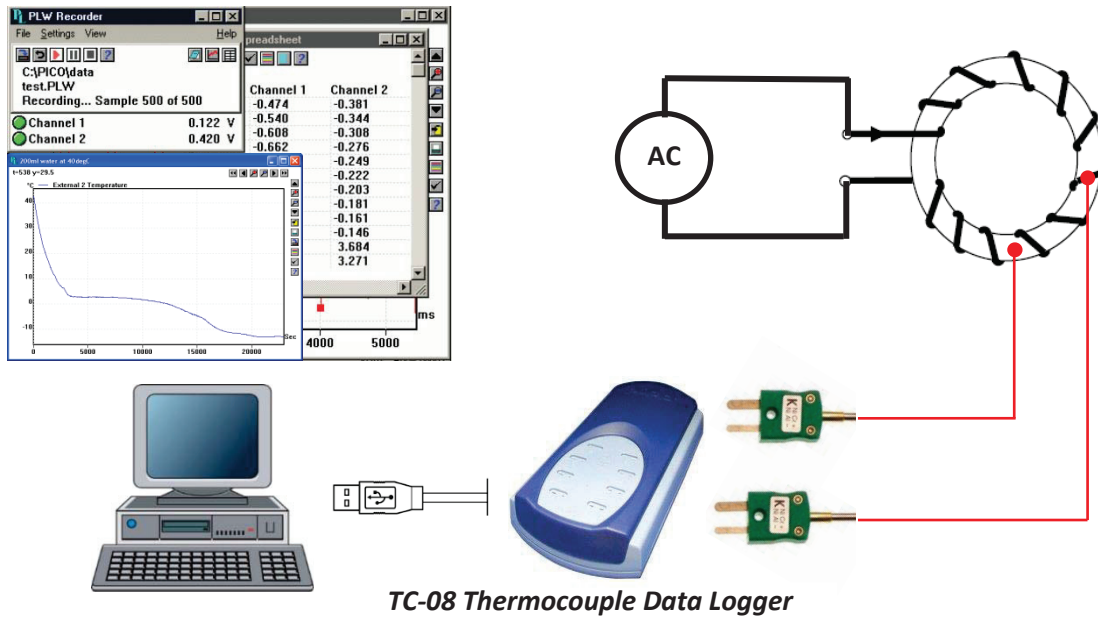


Figure 1-16: Magnetic components self-heating measurements test bench.

In self-heating measurements, an inductor of same material (N14E1) is fed with a sinusoidal current of 0.6 A at 20 and 40 kHz to insure self-heating. Then core and winding temperatures dynamic evolution is measured by the help of the test bench presented in figure 16. Two N-type thermocouples are placed in contact with the core and winding. A thermocouple data logger is used and connected to a PC to allow dynamic temperature reading and registration. Temperatures are registered for 500 seconds with a time step of 5 seconds. As a result core and winding temperatures (T_{core} and $T_{winding}$) as function of time are obtained and presented in Figure 1-17. Core Temperatures at 20 kHz and 40 kHz are shown in red while those of winding are shown in blue. We notice that T_{core} is higher than $T_{winding}$ in both cases and that core temperature passes 70 °C on steady state for 40 kHz.

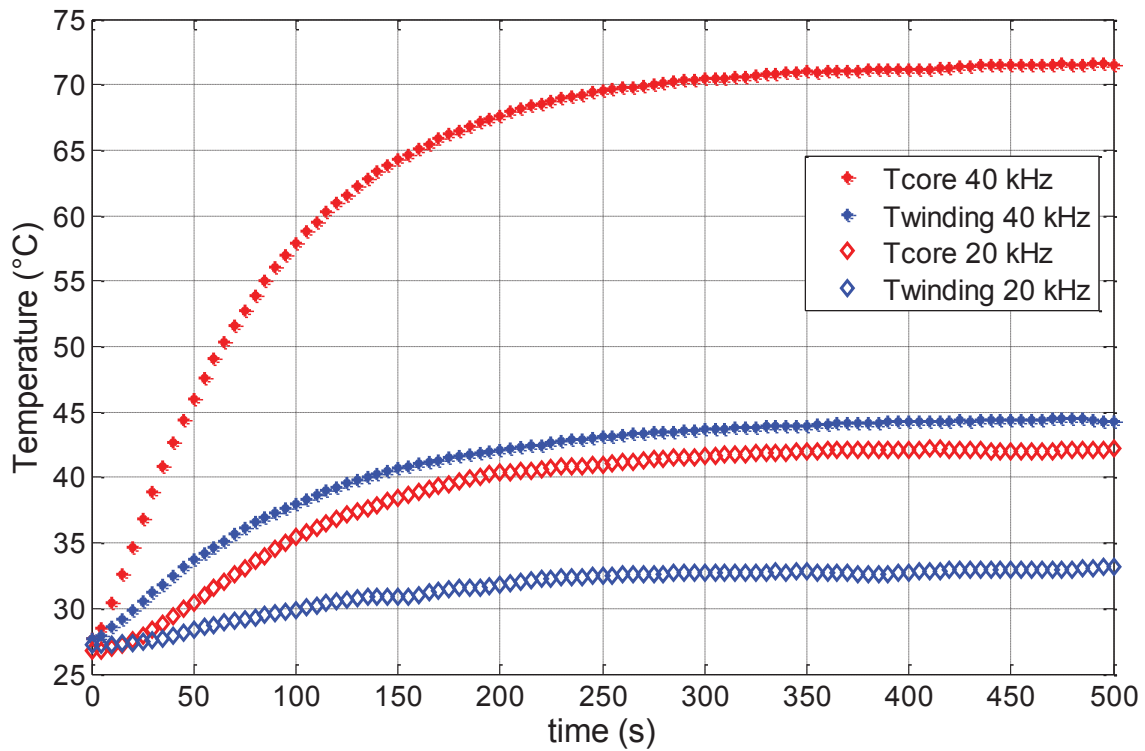


Figure 1-17: Self-heating measurements: core and winding temperatures as function of time.

Temperature rise of the magnetic core due to self-heating has a non-negligible effect on magnetic properties. Note that at higher frequency magnetic losses are more extensive and thus core temperature is higher. For better performance this thermal aspect must be taken into account before introducing materials in their application. This aspect is treated by integrating a thermal model along with the magnetic one. Both models and their coupling are detailed in next chapter.

1.5 Conclusion

In this chapter materials used in power electronics and their properties are presented. Temperature influence on these materials is discussed including examples of magnetic parameters variations with temperature. Magnetic materials characterization and available test benches are treated in this chapter as well.

Eventually each material has its specific hysteresis, dynamic and thermal behaviors. The macroscopic properties of soft magnetic materials are extracted from their measured hysteresis loops at different temperatures and frequencies. Materials characterizations allow the prediction of appropriate static and dynamic models that are able to represent these behaviors. In fact it is the indispensable stage before modeling. Therefore, after introducing magnetic materials used in power electronics, temperature effects and materials characterization in this chapter, magnetic and thermal modeling of magnetic components are explained in the following chapter.

1.6 References

- [1] B. M. Moskowitz, "Hitchhiker's Guide to Magnetism," in *Environmental Magnetism Workshop*, 1991, vol. 279, no. 1, p. 48.
- [2] B. D. Cullity and C. D. Graham, "Ferromagnetism," in *Introduction to Magnetic Materials*, 2008, pp. 115–149.
- [3] I. R. Harris and A. J. Williams, "MAGNETIC MATERIALS," in *School of Metallurgy and Materials, University of Birmingham*, vol. II, .
- [4] A. Hernando and J. M. González, "Soft and hard nanostructured magnetic materials," *Hyperfine Interact.*, vol. 130, no. 4, pp. 221–240, 2000.
- [5] T. J. Zhou, K. M. Cher, P. W. Lwin, and J. F. Hu, "Energy barrier measurement and optimization in exchange coupled FePt/TiO₂ nano-composite thin films," *J. Magn. Magn. Mater.*, vol. 331, pp. 187–192, 2013.
- [6] M. Coey, "Magnetism and Magnetic Materials," University of Dublin, 2007.
- [7] O. Gutfleisch, M. a Willard, E. Brück, C. H. Chen, S. G. Sankar, and J. P. Liu, "Magnetic materials and devices for the 21st century: stronger, lighter, and more energy efficient," *Adv. Mater.*, vol. 23, no. 7, pp. 821–42, Feb. 2011.
- [8] F. Fiorillo, "Soft Magnetic Materials," pp. 25–88, 2004.
- [9] P. Marin and a. Hernando, "Applications of amorphous and nanocrystalline magnetic materials," *J. Magn. Magn. Mater.*, vol. 215, pp. 729–734, 2000.
- [10] Ferroxcube, "Soft Ferrites," *Ferrite Mater. Surv.*, pp. 1–4, 2008.
- [11] D. W. Van Krevelen, "Magnetic Properties," pp. 343–365, 1997.
- [12] electronics-tutorials, "Magnetic Hysteresis." [Online]. Available: <http://www.electronics-tutorials.ws/>.
- [13] P. R. Wilson, "MODELING AND SIMULATION OF MAGNETIC COMPONENTS IN ELECTRIC CIRCUITS," 2001.
- [14] L.-Z. Li, Z. Yu, Z.-W. Lan, K. Sun, and R.-D. Guo, "Effects of annealing temperature on the structure and static magnetic properties of NiZnCo ferrite thin films," *J. Magn. Magn. Mater.*, vol. 368, pp. 8–11, Nov. 2014.
- [15] H. L. Chan, K. W. E. Cheng, T. K. Cheung, and C. K. Cheung, "Study on Magnetic Materials Used in Power Transformer and Inductor," *2006 2nd Int. Conf. Power Electron. Syst. Appl.*, pp. 165–169, 2006.
- [16] P. R. Wilson and J. N. Ross, "Definition and application of magnetic material metrics in modeling and optimization," *IEEE Trans. Magn.*, vol. 37, no. 5, pp. 3774–3780, 2001.
- [17] Epcos, "Ferrite Toroids," 2008.
- [18] Ferroxcube, "Soft Ferrites applications," 2008.

- [19] TDK, “Ferrite Cores for Coil DR/FT/THP /P/TH series,” no. February, 2009.
- [20] TDK, “Ferrite for Switching Power Supplies,” no. June, 2012.
- [21] Direct Industry, “Soft ferrite Core.” [Online]. Available: www.directindustry.com.
- [22] H. Skarrie, “Design of Powder Core Inductors,” Lund Institute of Technology, Lund University, SWEDEN, 2001.
- [23] MAGNETICS, “Magnetics Powder Cores.” [Online]. Available: www.mag-inc.com/products/powder-cores.
- [24] M. Yagi, I. Endo, I. Otsuka, H. Yamamoto, R. Okuno, H. Koshimoto, and A. Shintani, “Magnetic properties of Fe-based amorphous powder cores produced by a hot-pressing method,” *J. Magn. Magn. Mater.*, vol. 215–216, no. 0, pp. 284–287, 2000.
- [25] Crown Ferrite Enterprise Co., “Sendust Cores.” [Online]. Available: www.cfe.com.tw.
- [26] H. Gleiter, “NANOCRYSTALLINE MATERIALS,” *Progress in Materials Science*, vol. 33, pp. 223–315, 1990.
- [27] M. Ferch, “Nanocrystalline core materials for modern power electronic designs,” *GmbH, Magnetec*.
- [28] Vacuumschmelze, “Soft Magnetic Materials and Semi-finished Products,” 2002. [Online]. Available: www.vacuumschmelze.com.
- [29] O. Geoffroy, “Soft nanocrystalline alloys (Melt Spun),” *Inst. Néel, CNRS - Univ. Joseph Fourier*, 1987.
- [30] G. Herzer, “NANOCRYSTALLINE SOFT MAGNETIC ALLOYS,” *Handb. Magn. Mater. Vacuumschmelze, GmbH*, vol. 10, 1997.
- [31] Aperam Amilly Alloys, “Magnetic Cores.” [Online]. Available: www.aperam.com.
- [32] “Ferromagnetism—The Curie Temperature of Gadolinium,” in *Advanced Laboratory, University of Wisconsin*, 2003, pp. 1–9.
- [33] A. L. Wysocki, “Finite temperature effects in magnetic materials : Model and ab initio studies,” *Dep. Phys. Astron. Univ. Nebraska*, 2009.
- [34] M. a. Willard, M. Daniil, and K. E. Kniping, “Nanocrystalline soft magnetic materials at high temperatures: A perspective,” *Scr. Mater.*, vol. 67, no. 6, pp. 554–559, Sep. 2012.
- [35] T. Kulik, J. Ferenc, a. Kolano-Burian, X. B. Liang, and M. Kowalczyk, “Magnetically soft nanomaterials for high-temperature applications,” *J. Alloys Compd.*, vol. 434–435, pp. 623–627, May 2007.
- [36] Y. Melikhov, J. E. Snyder, D. C. Jiles, a. P. Ring, J. a. Paulsen, C. C. H. Lo, and K. W. Dennis, “Temperature dependence of magnetic anisotropy in Mn-substituted cobalt ferrite,” *J. Appl. Phys.*, vol. 99, no. 8, p. 08R102, 2006.

- [37] Z. Wang, K. He, J. Jin, J. He, L. Zhang, H. Zhang, and B. Shen, "Temperature dependence of permeability for Fe–Cu–M–Si–B alloys," *Mater. Sci. Eng. A*, vol. 304–306, pp. 1046–1049, May 2001.
- [38] D. Holzer, I. Pe, H. De Albe, R. Gro, and H. Sassik, "Low temperature properties of nanocrystalline Fe Cu Nb Si B ribbons," vol. 203, pp. 82–84, 1999.
- [39] R. Kolano, a. Kolano-Burian, J. Szynowski, L. Varga, F. Mazaleyrat, T. Kulik, N. Wojcik, L. Winczura, and L. Kubica, "Dependence of magnetic properties of the Fe–Co–Cu–Nb–Si–B nanocrystalline alloys on magnetic field frequency and temperature," *Mater. Sci. Eng. A*, vol. 375–377, pp. 1072–1077, Jul. 2004.
- [40] L. Li, Z. Lan, Z. Yu, K. Sun, and Z. Xu, "Effects of Co-substitution on wide temperature ranging characteristic of electromagnetic properties in MnZn ferrites," *J. Alloys Compd.*, vol. 476, no. 1–2, pp. 755–759, May 2009.
- [41] ArcelorMittal, "Data sheet Nanocrystalline cores Nanophy."

Chapter 2

2. Magnetic and Thermal Modeling

2.1 Introduction

Modeling is an imperative step in any engineering design project. It allows viewing systems being realized from multiple perspectives to ensure their desired performance. Modeling also allows a designer to discover errors earlier and reduce system defects. Much effort has been applied to model individual components in the system's design, like switching power devices.

With the need for efficient generation and conversion of power in electronic circuits, it is becoming very important to ensure that the magnetic components in the design operate within their specified thermal, magnetic and electrical safe operating regions and performance limits. For that purpose, standard modeling and linear models of magnetic components for circuit simulation are not enough. In many applications like switching power supplies and power converters, an accurate model of the magnetic material employed to build inductors and transformers is required. This magnetic material model would take into account saturation, nonlinear and hysteresis characteristics of materials. The model would also consider material's dynamic behavior (eddy currents, domain wall motion...) and temperature effects allowing exact core losses calculation.

Our purpose is to develop magnetic components models for the virtual prototyping of power converters. So in this chapter we introduce approaches for modeling magnetic components in general. We focus on magnetic materials modeling, by the investigation of existing magnetic material models. The models available in circuit simulators and their drawbacks are presented. Thermal modeling including heat transfer concepts and thermal networks are also studied to develop a dynamic thermal model in the aim of magneto-thermal coupling.

2.2 Magnetic modeling

In the aim of accurate modeling of magnetic components, a model of the magnetic material consisting the component's core is essential. This material's model describes their hysteresis behavior under static operating conditions (static model) in addition to their dynamic behavior due to eddy currents and wall motion effects (dynamic model). Based on the hypothesis of loss separation, different static and dynamic material models exist, we explain briefly below the best known in our domain.

2.2.1 Static magnetic hysteresis models

A wide choice of static magnetic models exists to describe the material's static behavior. Some of them are purely analytical like Rayleigh model [1], Fröhlich model [2], Chan-Vladimirescu model [3], and Hodgson model [4]. These models are simple to implement but have no physical aspect, are not reversible and have many limitations described later. Polynomial model is reversible but limited to materials with low coercivity [5]. Other models

are based on phenomenological and statistical considerations such as the Preisach-Néel [6] that needs a distribution function and a lot of experimental data. There exist other magnetic models that are based on physical principles, rather than strictly mathematical arguments or experimental curve fitting. The most known is the Jiles-Atherton [7] model introduced in 1983 presenting some equations for magnetization in ferromagnetic materials.

2.2.1.1 Rayleigh Model

Rayleigh model is one of the oldest magnetic models developed by Lord Rayleigh in the 19th century. It relates B and H on the initial magnetization curve by (2.1).

$$B = \mu_{in}H + \frac{1}{2}\eta H^2 \quad (2.1)$$

Where μ_{in} is the initial permeability and η is the Rayleigh parameter.

For an applied sinusoidal field having a maximum H_{max} , the general equation of the model would be as follows:

$$B = (\mu_{in} + \eta H_{max})H \pm \frac{1}{2}\eta(H^2 - H_{max}^2) \quad (2.2)$$

The positive sign in the equation corresponds to the increasing field and the negative sign corresponds to the decreasing field. Therefore “ \pm ” could be replaced by a sign function.

This model has low number of parameters and is easy to be implemented in simulators; however, it is limited for low applied fields only. Saturation is not considered by this model and hysteresis loops are always centered and elliptical [1].

2.2.1.2 Fröhlich Model

This model is also an analytical one that was originally developed to describe only the initial magnetization curve using (2.3). It has two parameters α and β depending on the characteristics of the material.

$$B = \frac{H}{\alpha + \beta|H|} \quad (2.3)$$

Then in 1991 this model was extended to model a major hysteresis loop [8] by the equation (2.4)

$$B = \begin{cases} \frac{(H - H_c)}{\alpha + \beta|H - H_c|} & \text{for } \dot{H} > 0 \\ \frac{H + H_c}{\alpha + \beta|H + H_c|} & \text{for } \dot{H} < 0 \end{cases} \quad (2.4)$$

Where

$$\alpha = H_c \left(\frac{1}{B_r} - \frac{1}{B_s} \right) \quad \text{and} \quad \beta = \frac{1}{B_s} \quad (2.5)$$

Fröhlich model is based on mathematical approximations as Rayleigh model, but in contrary it is limited to major loops. It represents saturation but can't model minor loops.

2.2.1.3 Chan-Vladimirescu Model

The model proposed by Chan and Vladimirescu in [3] describes hysteresis using polynomial techniques. Authors consider that a major hysteresis is composed of an upper and a lower branch related to decreasing and increasing applied fields H respectively. These branches are modeled using two expressions or “*branch equations*”:

$$B'_+(H) = B_s \frac{H + H_c}{|H + H_c| + H_c \left(\frac{B_s}{B_r} - 1 \right)} \quad \dot{H} < 0 \quad (\text{upper branch}) \quad (2.6)$$

$$B'_-(H) = B_s \frac{H - H_c}{|H - H_c| + H_c \left(\frac{B_s}{B_r} - 1 \right)} \quad \dot{H} > 0 \quad (\text{lower branch}) \quad (2.7)$$

The initial magnetization curve is calculated by averaging these two equations:

$$B'_{mag}(H) = \frac{B'_+(H) + B'_-(H)}{2} \quad (2.8)$$

Minor loops are not well considered in this model. They are modeled by translating the major loops branch by a value “ B_d ”. Generation of different types of minor loops is explained in [3]. The main advantage of this model is that it requires only 3 parameters H_c (Coercive field), B_r (Residual magnetism) and B_s (Saturation flux density) which are found on manufacturers' data sheets, or by standard measurements.

2.2.1.4 Hodgson Model

This model proposes a differential equation that links the time rate of change of H to the time rate change of B [4]. The final equation is presented in (2.9) where α is a constant, $s(\dot{B})$ is a sign function (2.10), and f (2.11) and g (2.12) are 2 functions called by Hodgson “*material functions*” [9]

$$\frac{dH}{dB} = \alpha * s(\dot{B}) * [f(B) - H] + g(B, \dot{B}) \quad (2.9)$$

Sign function:

$$s(\dot{B}) = \begin{cases} +1 & \text{if } \dot{B} > 0 \\ -1 & \text{if } \dot{B} < 0 \end{cases} \quad (2.10)$$

Material functions:

$$f = \begin{cases} D_1(B + B^*) - D_2B^* & \text{if } B < -B^* \\ D_2B^* & \text{if } |B| \leq B^* \\ D_1(B - B^*) + D_2B^* & \text{if } B > B^* \end{cases} \quad (2.11)$$

$$g = \begin{cases} (1 + D_3)D_2 & \text{if } |B| \leq B^* \\ D_1 & \text{if } |B| > B^* \end{cases} \quad (2.12)$$

Equations (2.11) and (2.12) are the simplest form of f and g functions respectively, where D_1 , D_2 , D_3 , D_4 and B^* are model parameters. More complex trigonometric functions are also proposed by Hodgdon for better accuracy [10]. Hodgdon model also addresses the issue of loop closure at saturation and supports minor loops.

2.2.1.5 Polynomial Model

This static model does not represent the hysteresis phenomenon in materials, it is a purely mathematical model adapted to materials of very low coercive field. In fact it is a piecewise polynomial function (based on spline function). The saturation is modeled by a polynomial of order 1 and slope μ_0 and the central zone of the hysteresis curve is modeled by a polynomial of order n , as shown in Figure 2-1.

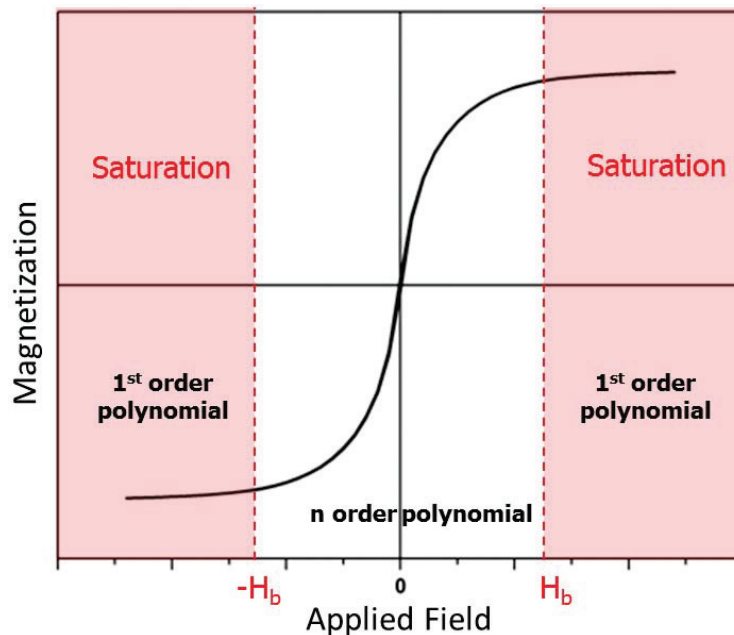


Figure 2-1: Polynomial model

H_b is the value of H needed to reach saturation. This model is defined by the following equations:

$$B = \begin{cases} \mu_0(H - H_b) + P(H_b) & \text{if } H \geq +H_b \\ P(H) & \text{if } |H| < H_b \\ \mu_0(H + H_b) - P(H_b) & \text{if } H \leq -H_b \end{cases} \quad (2.13)$$

Where P is a polynomial in \mathbb{R} such that:

$$P(X) = \sum_{i=0}^n p_i X^i \quad (2.14)$$

The precision and number of parameters of this model depend on the order of the central polynomial n . For example for $n=5$, 4 parameters (p_1 , p_3 , p_5 and H_b) are required considering the even parameters are null due to the odd parity of the curve. It would be convenient to choose an order according to the static behavior of each material since different materials may require different polynomial orders.

2.2.1.6 Preisach-Néel Model

The original Preisach-Néel model was proposed by the German physicist Friedrich Preisach-Néel in 1935 to describe hysteresis in ferromagnetic materials [6]. Later in the 1970s the model was extended by the Russian mathematician M. Krasnoselskii into a pure mathematical formulation to describe hysteresis in general [11][12].

This model supposes that the magnetic material consists of infinite set of magnetic dipoles, each of which behaves like a relay. These relays or generally called *hysteron* are the fundamental building blocks of the Preisach-Néel model. The most known among hysterons is the *Nonideal Relay Hysteron* shown in Figure 2-2. It is a dissymmetric rectangular cycle having two possible outputs ($M=+1$ or $M=-1$) and two transition fields α and β ($\alpha > \beta$). Thus the magnetization at an instant t is just the weighted superposition of these relays.

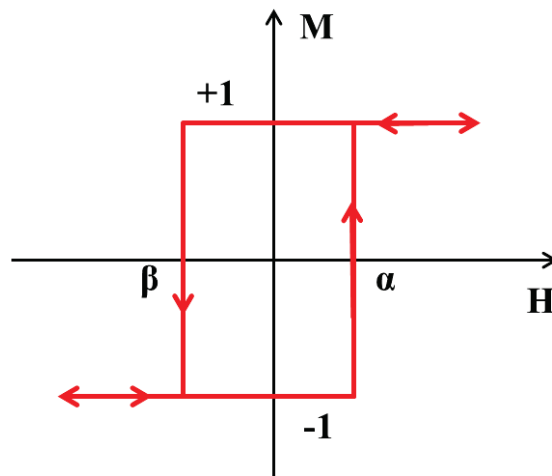


Figure 2-2: Nonideal Relay Hysteron

The Magnetization $M(t)$ resulting from an applied field $H(t)$ is calculated using equation (2.15), where $\rho(\alpha, \beta)$ is a distribution function called the “Preisach distribution function”. $\phi_{\alpha\beta}[H(t)]$ is a mathematical operator associated to a hysteron that equals (+1) in the case of increasing field and (-1) in the case of decreasing field.

$$M(t) = \iint \rho(\alpha, \beta) \cdot \phi_{\alpha\beta}[H(t)] d\alpha d\beta \quad (2.15)$$

The Preisach-Néel model is one of the best mathematical descriptions of magnetic hysteresis. It is very accurate and widely used in Finite Element Analysis applications [13][14]. Preisach-Néel model is able to represent both major and minor hysteresis loops. The main drawback in its application is that it requires the accurate determination of a large number of parameters of the distribution function by performing significant number of measurements. In addition, double integration is required to calculate the magnetization [15]. For these reasons the Preisach-Néel model has not been largely used in circuit simulation and, according to [16], there are no commercial circuit simulators that implement the Preisach-Néel model, except saber that is, as authors said, “inefficient” in circuit simulation.

2.2.1.7 Jiles-Atherton Model

The Jiles-Atherton model is widely used for modeling the nonlinear characteristics of magnetic hysteresis. It describes the B–H curve using five parameters. Numerous literatures deal with the identification of these parameters based on their physical meaning [17]–[20]

The magnetization M is composed of two terms in the Jiles-Atherton model of hysteresis, an irreversible (M_{irr}) and a reversible (M_{rev}) component (2.16). The irreversible component represents the irreversible domain wall motion. The reversible magnetization corresponds to the reversible domain wall bending.

$$M = M_{irr} + M_{rev} \quad (2.16)$$

The variations of the irreversible (2.17) and reversible (2.18) magnetization as function of H are defined by the following equations respectively

$$\frac{dM_{irr}}{dH_e} = \frac{(M_{an} - M_{irr})}{k\delta} \quad (2.17)$$

$$M_{rev} = c(M_{an} - M_{irr}) \quad (2.18)$$

Where M_{an} and H_e are the anhysteretic magnetization and effective field respectively, defined as follows:

$$M_{an} = M_s \left[\coth\left(\frac{H_e}{a}\right) - \frac{a}{H_e} \right] \quad (2.19)$$

$$H_e = H + \alpha M \quad (2.20)$$

A general equation of the model is given by (2.21):

$$\frac{dM}{dH} = \frac{(1-c) \frac{dM_{irr}}{dH_e} + c \frac{dM_{an}}{dH_e}}{1 - \alpha c \frac{dM_{an}}{dH_e} - \alpha(1-c) \frac{dM_{irr}}{dH_e}} \quad (2.21)$$

Hence the five parameters of Jiles-Atherton model to be determined are:

M_s : saturation magnetization

α : interaction between magnetic domains

a : domain density

c : reversible wall motion coefficient

k : loss coefficient

δ : sign coefficient

This model is able to represent major hysteresis loops with a good accuracy. The main strengths of this model besides its physical nature are its ease of implementation and its reasonable convergence in circuit simulators. However, a major limitation of Jiles-Atherton model is the fact that it is not able to reproduce properly minor loops [21]. The extraction of this model parameters is not simple either [22], [23].

2.2.2 Dynamic magnetic hysteresis models

When magnetic materials are subjected to dynamic magnetic fields, losses due to eddy currents and domain walls movements are induced. These losses increase with frequency and are not taken into account by static magnetic models. Hence dynamic models are needed to represent the materials dynamic magnetic behavior. Concerning dynamic models, there is not a vast choice, due to the fact that magnetic losses are still not completely understood, especially anomalous losses due to domain wall motion. We present here some of these models.

2.2.2.1 Preisach-Néel dynamic Model

Various works have been published on extending the original Preisach-Néel model to include dynamic effects [24][25][26]. In the extended model, the rate dependent hysteresis was discussed, by introducing the time variation of input field to either the $\phi(\alpha, \beta, t)$ operator, or to the distribution function $\rho(\alpha, \beta, t)$. This extension of the original Preisach-Néel model added new parameters to the static one. Including a time derivative in the distribution function made its numerical implementation even more complicated.

Including time dependence to $\phi(\alpha, \beta)$:

$$\frac{\partial \phi(\alpha, \beta, t)}{\partial t} = \begin{cases} k \cdot [H(t) - \alpha] & \text{when } H > \alpha \text{ and } \phi(\alpha, \beta, t) < 1 \\ k \cdot [H(t) - \beta] & \text{when } H < \beta \text{ and } \phi(\alpha, \beta, t) > -1 \\ 0 & \text{otherwise} \end{cases} \quad (2.22)$$

k is a constant.

Including time dependence to $\rho(\alpha, \beta)$:

$$M(t) = \iint \rho(\alpha, \beta, \chi \left(\frac{d(H)}{dt} \right) \cdot \phi_{\alpha\beta}[H(t)] d\alpha d\beta \quad (2.23)$$

2.2.2.2 Jiles-Atherton dynamic Model

D.C. Jiles also proposed a dynamic model of hysteresis [27] in 1993 that applies to *non-conducting* media. In this model effects of eddy currents are ignored and it is applied to high frequency ferrites only. In fact this model describes the domain wall motion only using a second order differential equation (2.24)

$$\frac{d^2}{dt^2} \Delta M(t, H) + 2\lambda \frac{d}{dt} \Delta M(t, H) + \omega_n^2 \Delta M(t, H) = 0 \quad (2.24)$$

With

$$\Delta M(t, H) = M(t) - M_\infty(H) \quad (2.25)$$

$M_\infty(H)$ is uniquely defined by the magnetic field history when all transients in the magnetization process have been completed. It is represented by the value of bulk magnetization on the static hysteresis loop, thus it's time independent. Therefore the time derivative of $M_\infty(H)$ is zero, and the equation (2.24) becomes as shown below:

$$\frac{d^2}{dt^2} M(t) + 2\lambda \frac{d}{dt} M(t) + \omega_n^2 M(t) = \omega_n^2 M_\infty(H) \quad (2.26)$$

Where ω_n is called the natural frequency representing the frequency at which the magnetic moments can oscillate in the absence of any external damping forces. λ is a decay constant that determines the response rate of the magnetization to an external field. These model parameters are difficult to determine. For instance, ω_n is function of domain wall thickness and average domain size. More details on this model are explained in [27].

2.2.2.3 Dynamic Static Feedback Model (DSF Model)

This model, developed by our laboratory, is based on loss separation into static and dynamic. It represents the different dynamic effects created in magnetic materials using the first order differential equation (2.27). $H(t)$ is the magnetic field related to the current by Ampere's law, $B(t)$ is the average flux density and $H_{stat}(B)$ is the material's static law [28][29].

$$H(t) = H_{stat}(B(t)) + \beta \cdot \frac{dB(t)}{dt} \quad (2.27)$$

The *DSF* model requires only one parameter β lumping eddy currents and wall motion effects, and a static magnetic model representing materials static characteristics. Advantages of *DSF* are assembled in its unique parameter, short calculation time, and reversibility. The model is quite accurate in the case of low excess losses. However, the frequency range of this model is not very wide. For a wider frequency range the Bertotti's model is used.

2.2.2.4 Bertotti's Model

The dynamic model is also based on the principle of separation of losses into static and dynamic contributions, as well as Bertotti's theory [30] adding that the dynamic losses are the sum of both classical and excess losses.

G. Bertotti states in his theory that the large-scale behavior of magnetic domains can be describe in terms of \tilde{n} Magnetic Objects (MO). Each of these dynamic, statistically-independent, magnetic objects corresponds to a group of neighboring interacting domain walls. The magnetization process in a given cross section of the material can be described in terms of \tilde{n} simultaneously active magnetic objects. This quantity \tilde{n} described by (2.28), is a function of the excess field H_{exc} and the set $\{P\}$ of parameters characterizing the microstructure and domain structure of the material.

$$\tilde{n}(H_{exc}, \{P\}) = \tilde{n}_0 + \frac{H_{exc}}{V_0} \quad (2.28)$$

where the microstructural information in this case is carried by \tilde{n}_0 , which represents the limiting number of simultaneously active MO's when $f \rightarrow 0$ and by the magnetic field V_0 characterizing the statistical distribution of the local coercive fields.

This theory gives a natural interpretation of the dependence of excess energy losses on both peak polarization and frequency. Based on it, the total magnetic field is the sum of static field due to hysteresis, and dynamic fields due to eddy currents and wall motion effects (2.29).

$$H_{total} = H_s + H_{eddy} + H_{excess} \quad (2.29)$$

$$H_{total}(t) = H_s(B(t)) + \gamma \cdot \frac{dB(t)}{dt} + \alpha \cdot \delta \cdot \left| \frac{dB(t)}{dt} \right|^{\frac{1}{2}} \quad (2.30)$$

Where γ , α , and δ are the eddy current, the wall motion, and the sign coefficients respectively, presented in (2.31). γ depends on the material's conductivity σ and ribbon thickness d for ribbon materials (or particle average size for powder core). It is derived from the general equation proposed in [31]. α is a function of the characteristic field V_0 , a dimensionless coefficient G ($G \approx 0.136$), and the magnetic cross section S as proposed by Bertotti.

$$\gamma = \frac{\sigma d^2}{12} \quad \alpha = \sqrt{\sigma G V_0 S} \quad \delta = \text{sign}\left(\frac{dB}{dt}\right) \quad (2.31)$$

2.2.3 Models available in circuit simulation and their drawbacks

The choice of an appropriate magnetic material model for use in circuit simulation comes down to a variety of factors including ease of implementation, accuracy, speed of simulation and good convergence. The Jiles–Atherton’s model has been widely used as it generally satisfies these requirements [32][33]. It is implemented using simple equations with meaningful parameters related to physical aspects. This is convenient when the temperature dependence of parameters is considered. The Preisach’s model serves mainly in finite element analysis, but has not been extensively used for circuit simulation [14]. The Hodgdon model would be especially useful in frequency dependent applications [34].

Magnetic materials models introduced into circuit simulation are listed below:

- Jiles–Atherton model in *SPICE*, *Simplorer* and *Saber*
- Chan–Vladirimescu model in *I-Spice*
- Preisach–Néel model in *Saber*.
- Hodgdon model in *Saber*.

These models are mainly static ones, but no dynamic models were implemented in circuit simulators. In fact some techniques were considered to include eddy currents to previously mentioned models. For example, in Simplorer, a resistor is virtually connected in parallel to the Jiles-Atherton model to have an electric circuit equivalent to DSF model. But, generally, dynamic effects and losses are not investigated in circuit simulators.

The models available in circuit simulation and their review for different modeling aspects are summarized in the table below (Figure 2-3).

	Jiles-Atherton	Preisach	Hodgdon	Chan-Valdirimrscu
Major Loop	Good	Good	Good	Good
Symmetric Minor Loop	Possible but poor	Possible	Possible	Possible Only elliptical
Asymmetric Minor Loop	X	Possible	Possible	Poor
Dynamic effects	X	X	Available	X
Temperature dependence	Available	X	X	Available
Parameters Number	Average	Very high	Very high	Low
Parameters Extraction	Difficult	Difficult	Very Difficult	Easy
Practical implementation	Easy	Difficult	Difficult	Average

Figure 2-3: Models in circuit simulation summary

In conclusion, the Jiles-Atherton model emerges as the most used in circuit simulation (available in 3 commercial simulators). Advantages of JA include practical implementation and temperature dependence [35][36][37] while disadvantages include minor loops modeling and parameters extraction. The Preisach-Néel model suffers from a poor implementation due to temperature dependence, parameters extraction, and difficulty to implement [15][16]. The Hodgdon model has a specific strength as frequency dependence and Chan-Valdirimrscu has a specific strength as parameters extraction.

2.2.4 Parameters identification

Each static or dynamic magnetic law has a set of parameters as described above. The set of parameters for some is easy to extract like for Chan-Valdirimrscu model. For others like Jiles-Atherton's model, the parameters are determined by comparing a $B-H$ measured cycle to a simulated one and by calculating the error function between these cycles. Then this objective error function is minimized using different methods or algorithms. We mention briefly here the two algorithms that are used in our work.

- *Nelder-Mead Simplex algorithm*

The Nelder-Mead technique was proposed by John Nelder & Roger Mead (1965) [38]. It is a technique for minimizing an objective function in a many-dimensional space. Nelder-Mead generates a new test position by extrapolating the behavior of the objective function measured at each test point arranged as a simplex. The algorithm then chooses to replace one of these test points with the new test point and so on.

- *Particle Swarm Optimization algorithm (PSO)*

PSO [39] is a computational method used in computer Science that optimizes a problem by trying to improve a candidate solution (particle) of a population by moving it around the search space according to simple mathematical formula over the particle's position and velocity. PSO does not use the gradient of the problem being optimized, which means PSO does not require that the optimization problem be differentiable as is required by classic optimization methods.

Since magnetic materials behavior depends greatly on temperature as explained earlier, the parameters of the magnetic models that describe this behavior will also depend on temperature. In other words, the parameters of static and dynamic model will vary with the temperature according to the material. For this reason, magnetic properties variations under different temperatures need to be studied.

In fact the thermal aspect is of great importance in magnetic components modeling. To operate in the predefined temperature limits of magnetic components and to avoid their overheating, thermal modeling has become a routine in their design process. Thermal modeling allows designers to optimize their design, consider heat dissipation solutions and avoid temperature-related failures.

Thus after discussing magnetic modeling, the next section presents thermal modeling in general and thermal modeling of magnetic components in particular.

2.3 Thermal modeling

Thermal modeling of magnetic components is relatively recent, first works in this domain started in mid 90s by B. J. Swart and J.A. Ferreira [24]. The authors studied temperature rise in commercial magnetic components in relation with winding and core losses. They proposed increasing the exchange area of ferrites to lower core temperature. Other articles [40][41] also addressed thermal modeling until the work of P.R. Wilson in 2002 [42] proposing an equivalent thermal circuit to model a ferrite core. The model predicts core temperature rise by convection and radiation due to hysteresis losses (calculated by Jiles-Atherton model). Wilson coupled the magnetic and thermal models in order to vary JA parameters according to core temperature. So our work in thermal modeling is inspired by Wilson's to develop a complete thermal model of magnetic components and couple it with the magnetic model. The thermal model concept and magneto-thermal coupling are demonstrated in this chapter, but before that, a brief review on heat transfer and thermal elements is presented below.

2.3.1 Heat transfer

Basically, heat transfer is the flow of thermal energy driven by thermal non-equilibrium across a well-defined boundary. It is a process function where thermal flux is transferred from a region of high temperature to another region of lower temperature. Heat transfer is classified into various mechanisms or modes, such as thermal conduction, thermal convection and thermal radiation.

Conduction:

Conduction is the transport of thermal energy in solids and non-moving fluids due to short-range atomic interactions. As adjacent atoms or molecules collide, or as several electrons move from atom to atom in a disorganized way, thermal conduction occurs. Conduction can only take place within an object or material, or between two objects that are in contact. Heat transfer by conduction is stated by Fourier's law:

$$q = -k \cdot \frac{dT}{dx} \quad (2.32)$$

Equation (2.31) represents the one-dimensional form (x-direction) where q is the heat flux, T is the temperature and k is the thermal conductivity of the material.

Convection:

Convection is the transport of thermal energy between a solid surface and a moving fluid. Two types of heat convection can be distinguished, namely natural and forced convection. It is one of the major heat transfer modes, described by Newton's law of cooling (2.33) where h is the thermal convection coefficient.

$$q = h\Delta T \quad (2.33)$$

Radiation:

Thermal radiation is the emission of electromagnetic waves from matter having a temperature above absolute zero. It often contributes a small portion of the total heat transfer. The maximum flux emitted from a surface by radiation is given by Stefan-Boltzmann law:

$$q = \varepsilon \sigma T_s^4 \quad (2.34)$$

ε is radiation property of the surface called the emissivity, σ is the Stefan-Boltzmann constant and T_s is the surface temperature in Kelvin (K).

2.3.2 Thermal elements

Whenever two objects have different temperatures, there is a tendency for heat to be transferred from the hot region to the cold region, in an attempt to equalize the temperatures. For a given temperature difference, the rate of heat transfer varies, depending on the thermal resistance of the path between the hot and cold regions. The nature and magnitude of the thermal resistance depend on the mode of heat transfer involved. In general the **thermal resistance** is given by (2.35):

$$R_{th} = \frac{\Delta T}{q} \quad (2.35)$$

The ability of a system to store thermal energy is called the **thermal capacitance** measured in units of J/K. It can be calculated by the product of the mass of the system and the specific heat of the material ($C=m.c$). The thermal capacitance is related to the quantity of transferred thermal energy by (2.36):

$$q = C_{th} \frac{dT}{dt} \quad (2.36)$$

Based on these simple laws and definitions of thermal systems and heat transfer modes, the thermal modeling concepts and methods are explained in next section. The equivalent thermal model to describe magnetic components is detailed too.

2.3.3 Thermal model

As seen in first chapter, performance of the system containing magnetic components depends greatly on thermal aspect since different magnetic materials do not possess the same behavior under severe operating condition like temperature. For that reason it is of great interest to incorporate thermal behavior into simulation. This thermal behavior is investigated by the implementation of the magnetic component's thermal model. This model is able to evaluate temperature rise in both core and winding due to iron and copper losses respectively. The temperature rise is then injected to the magnetic model to take into account magnetic behavior variation due to thermal aspect or self-heating. So in fact the magnetic model is coupled with the thermal model.

Different approaches could be used to describe heat transfer and build a thermal model. Some, like the analytical and the numerical approaches give a detailed temperature distribution at each point of the component. However these approaches require different physical parameters (thermal convection coefficient, thermal conductivity, emissivity...) that are not always available and difficult to obtain. They require also large memory and long simulation time to solve heat transfer equations. Keeping in mind that the thermal model must be coupled with a magnetic one in a circuit simulation environment, a more appropriate approach is used called the “*Nodal analysis*” [43][44].

In nodal analysis, the system is modeled by an equivalent thermal circuit with different isothermal zones called nodes. The nodes are connected by thermal resistances. A heat source and a thermal capacitance are associated to each zone to model the quantity of heat dissipated and energy stored in each zone respectively, as described in Figure 2-4. This method operates on the principle that the power loss in the magnetic component can be instantaneously calculated by the magnetic model. The resulting power is then connected to a thermal network as a heat source. The solving of the network equations results in a change of temperature which is then used to control the electrical and magnetic properties of the device, providing dynamic self-heating and behavior variation depending on temperature.

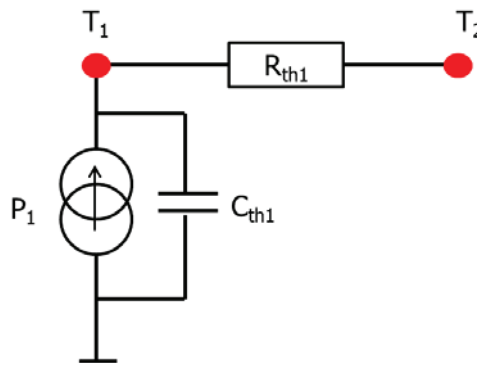


Figure 2-4: Nodal analysis

Considering a widely used magnetic component, an inductor, we aim to determine the average temperature of the magnetic core and winding. To keep a simple model, the temperature is assumed to be uniform in the magnetic material and in the copper. Also the thermal resistances are considered constants. Under these assumptions, the model will form a relatively simple, but sufficiently realistic, thermal equivalent circuit. The thermal circuit has two isothermal zones or two nodes, the core and winding, as shown in Figure 2-5. Core and winding losses are modeled by heat flow sources (equivalent to current sources in electrical domain). Ambient temperature is modeled by a temperature source (equivalent to voltage source in electrical domain). Thermal capacitances model stored energy in both magnetic core and winding. Heat transfer between nodes is modeled by thermal resistances.

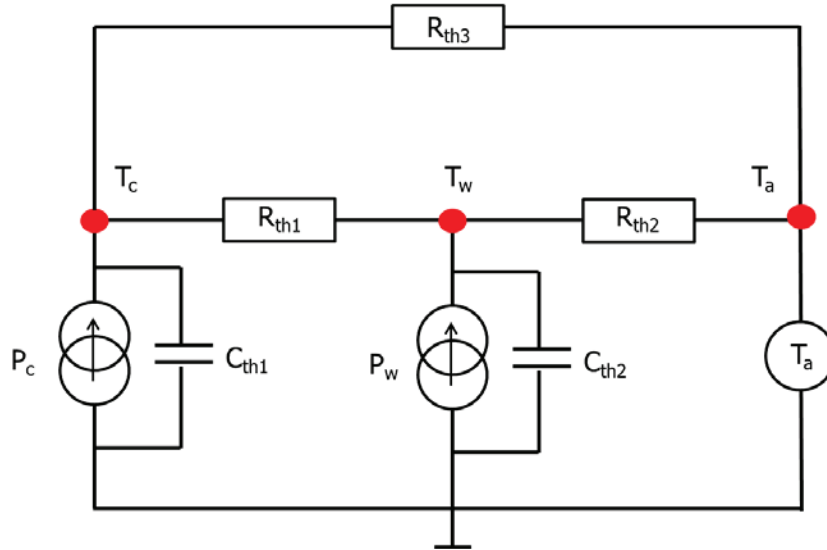


Figure 2-5: thermal model of an inductor (thermal equivalent circuit)

P_c	\rightarrow	core losses
P_w	\rightarrow	copper losses
C_{th1}	\rightarrow	energy stored in core
C_{th2}	\rightarrow	energy stored in winding
R_{th1}	\rightarrow	core-winding heat transfer
R_{th2}	\rightarrow	winding-ambient heat transfer
R_{th3}	\rightarrow	core-ambient heat transfer

Normally the heat transfer modes for a magnetic core are the thermal conduction, the thermal convection to the atmosphere and radiated emissions. As we assumed uniform temperature in the core, the thermal conduction between the center of the core and the core surface is neglected. Also the radiation of heat from the core is generally disregarded as it can be much smaller than the other forms of heat transfer, but can be included in a model if necessary. Thus the main heat transfer or dissipated energy from the core is by **Convection**.

After finding the equivalent thermal network of an inductor, the next step is to determine the thermal elements (thermal resistances and capacitances). These elements can be obtained experimentally (using the test bench presented in chapter 1) and by calculation. The approach of finding these elements is explained in the next section.

2.3.4 Parameters identification

Considering the thermal circuit of figure 5, the differential equations at the nodes T_c and T_w are presented by the (2.37) and (2.38) respectively.

$$C_{th1} \frac{dT_c}{dt} = P_c - \frac{T_c - T_w}{R_{th1}} - \frac{T_c - T_a}{R_{th3}} \quad (2.37)$$

$$C_{th2} \frac{dT_w}{dt} = P_w - \frac{T_w - T_c}{R_{th1}} - \frac{T_w - T_a}{R_{th2}} \quad (2.38)$$

The core losses P_c and winding losses P_w are given by magnetic B - H measurements, so their values are known. The core temperature T_c and winding temperature T_w are measured using the self-heating measurement approach presented in section 1.4.4. Then to calculate thermal resistances, the steady state is considered where the thermal capacitances are fully charged. The circuit in this case is reduced to resistive only as shown in Figure 2-6.

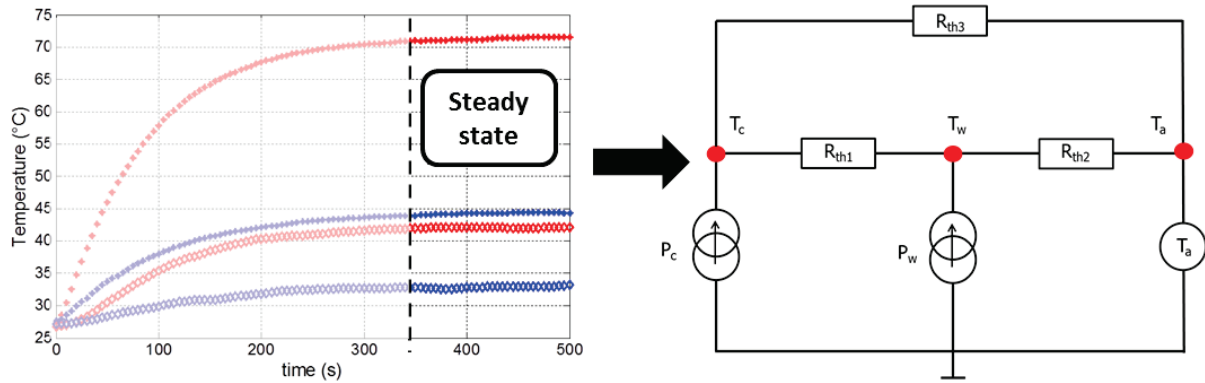


Figure 2-6: Steady state analysis

In the steady state the model's equations become as shown by equation (2.39), (2.40) and (2.41). The system of 3 equations with 3 unknowns is solved to get the values of R_{th1} , R_{th2} , and R_{th3} . The resistances values are then substituted in equations (2.37) and (2.38) to find the values of thermal capacitances C_{th1} and C_{th2} .

$$P_c = \frac{T_c - T_w}{R_{th1}} + \frac{T_c - T_a}{R_{th3}} \quad (2.39)$$

$$P_w = \frac{T_w - T_c}{R_{th1}} + \frac{T_w - T_a}{R_{th2}} \quad (2.40)$$

$$\frac{T_c - T_a}{R_{th3}} = \frac{T_c - T_w}{R_{th1}} + \frac{T_w - T_a}{R_{th2}} \quad (2.41)$$

Thus to summarize, the core and winding temperatures (T_c and T_w) are measured every 5 seconds to obtain their temporal variation shown in Figure 2-6. Their constant value at steady state is used with the measured core and winding losses (P_c and P_w) to find the three unknown thermal resistances R_{th1} , R_{th2} , and R_{th3} . Then equations (2.37) and (2.38) are solved in MATLAB including both temperature and time vectors to find the two unknown thermal capacitances C_{th1} , and C_{th2} . Using this approach, all parameters of the thermal model are obtained and the model can be implemented in circuit simulation.

2.4 Magneto thermal coupling

As we clearly see, on one hand the thermal model needs the losses of the magnetic component as inputs to calculate the component temperatures. On the other hand these temperatures are needed in the magnetic model to vary magnetic properties as function of temperature. For these reasons, it is of great importance to couple both models in circuit simulation. The process of magneto thermal coupling is clarified in Figure 2-7.

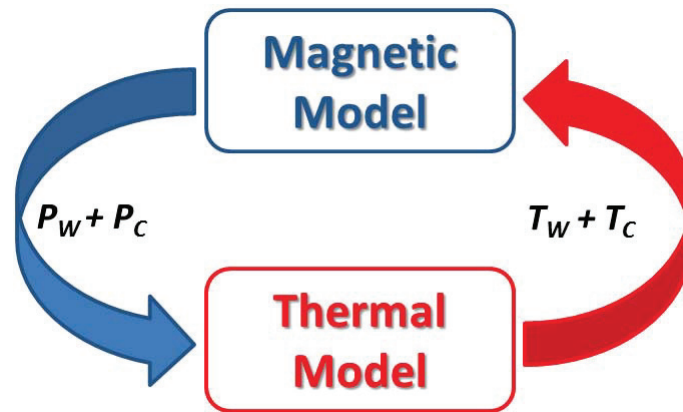


Figure 2-7: Magneto-thermal coupling

Indeed, core losses are estimated in the magnetic model by integrating the total magnetic field over the flux density. Winding losses are calculated using Joule's law. These losses are injected to the heat flow sources of the thermal model to calculate core and winding temperatures, which are in turn injected to the magnetic model. This feedback allows considering temperature effects on the magnetic component behavior.

2.5 Conclusion

Concerning magnetic modeling, a review on static and dynamic hysteresis models of magnetic materials was presented in this chapter. Advantages and inconveniences of each model were addressed. The four models Jiles-Atherton, Chan-Vladirimescu, Preisach-Néel and Hodgdon models available in circuit simulators were compared too.

Concerning thermal modeling of magnetic components, heat transfer and thermal elements are explained briefly. Then a thermal model of an inductor based on thermal equivalent circuit concept and nodal analysis is presented. The approach of model's thermal parameters identification from self-heating measurements was discussed as well.

Implementation, simulation and validation of both magnetic and thermal models side by side are discussed in chapter 3.

2.6 References

- [1] Lord Rayleigh, “XXV. Notes on electricity and magnetism.—III. On the behaviour of iron and steel under the operation of feeble magnetic forces,” *Philos. Mag. Ser. 5*, vol. 23, no. 142, pp. 225–245, Mar. 1887.
- [2] O. Frohlich, “Investigation of dynamoelectric machines and electric power transmission and theoretical conclusions therefrom,” *Electrotechn. Z*, vol. 2, pp. 134–141, 1881.
- [3] J. H. Chan, a. Vladimirescu, X.-C. Gao, P. Liebmann, and J. Valainis, “Nonlinear transformer model for circuit simulation,” *IEEE Trans. Comput. Des. Integr. Circuits Syst.*, vol. 10, no. 4, pp. 476–482, Apr. 1991.
- [4] M. L. Hodgdon, “APPLICATIONS OF A THEORY OF FERROMAGNETIC HYSTERESIS,” *IEEE Trans. Magn.*, vol. 24, no. 1, pp. 218–221, 1988.
- [5] C. H. Lee, F. Reitich, M. R. Jolly, H. T. Banks, and K. Ito, “Piecewise linear model for field-responsive fluids,” *Magnetics, IEEE Transactions on*, vol. 37, no. 1, pp. 558–560, 2001.
- [6] F. Preisach, “Über die magnetische Nachwirkung,” *Zeitschrift für Phys.*, vol. 94, no. 5–6, pp. 277–302, 1935.
- [7] D. C. Jiles and D. L. Atherton, “Theory of ferromagnetic hysteresis,” *J. Appl. Phys.*, pp. 2115–2120, 1984.
- [8] M. Akbaba, “A modified Froelich’s type equation for accurate modeling of magnetising characteristic of magnetic cores,” *Electr. Mach. power Syst.*, vol. 19, no. 3, pp. 303–311.
- [9] M. L. Hodgdon, “MATHEMATICAL THEORY AND CALCULATIONS OF MAGNETIC HYSTERESIS CURVES,” *IEEE Trans. Magn.*, vol. 24, no. 6, pp. 3120–3122, 1988.
- [10] C. Boley and M. L. Hodgdon, “MODEL AND SIMULATION OF HYSTERESIS IN MAGNETIC CORES,” vol. 25, no. 5, pp. 3922–3924, 1989.
- [11] A. V. Krasnosel’skii, Mark A., Pokrovskii, *Systems with Hysteresis*. 1983, p. 410.
- [12] I. D. Mayergoyz, “MATHEMATICAL MODELS OF HYSTERESIS,” no. 5, pp. 5–10, 1986.
- [13] T. Doong and I. D. MAYERGOYZ, “On numerical implementation of hysteresis models,” *IEEE Trans. Magn.*, vol. 21, no. 5, pp. 1853–1855, 1985.
- [14] F. Henrotte, F. Delinc, and P. W. Legros, “Modeling of ferromagnetic materials in 2D finite element problems using Preisach’s model,” vol. 28, no. 5, pp. 2614–2616, 1992.
- [15] P. R. Wilson, “MODELING AND SIMULATION OF MAGNETIC COMPONENTS IN ELECTRIC CIRCUITS,” 2001.
- [16] G. Gruosso and A. Brambilla, “Magnetic core model for circuit simulations including losses and hysteresis,” no. March, pp. 309–334, 2008.
- [17] D. C. Jiles, J. B. Thoeke, and M. K. Devine, “Numerical determination of hysteresis parameters for the modeling of magnetic properties using the theory of ferromagnetic hysteresis,” *IEEE Trans. Magn.*, vol. 28, pp. 27–35, 1992.

- [18] D. C. Jiles, “Modelling the effects of eddy current losses on frequency dependent hysteresis in electrically conducting media,” *IEEE Trans. Magn.*, vol. 30, pp. 4326–4328, 1994.
- [19] D. C. Jiles, “Frequency dependence of hysteresis curves in conducting magnetic materials,” *J. Appl. Phys.*, vol. 76, pp. 5849–5855, 1994.
- [20] D. C. Jiles and J. B. Thoeke, “Theory of ferromagnetic hysteresis: Determination of model parameters from experimental hysteresis loops,” *IEEE Trans. Magn.*, vol. 25, pp. 3928–3930, 1989.
- [21] J. V. Leite, N. Sadowski, and P. Kuo-peng, “Minor Loops Calculation with a Modified Jiles-Atherton Hysteresis Model,” vol. 8, no. 1, pp. 49–55, 2009.
- [22] J. V. Leite, S. L. Avila, N. J. Batistela, W. P. Carpes, N. Sadowski, P. Kuo-Peng, and J. P. a. Bastos, “Real Coded Genetic Algorithm for Jiles–Atherton Model Parameters Identification,” *IEEE Trans. Magn.*, vol. 40, no. 2, pp. 888–891, Mar. 2004.
- [23] N. C. Pop and O. F. Caltun, “Jiles – Atherton Magnetic Hysteresis Parameters Identification,” vol. 120, no. 3, 2011.
- [24] G. Bertotti, “Dynamic Generalization of the Scalar Preisach Model of Hysteresis,” vol. 28, no. 5, pp. 2599–2601, 1992.
- [25] Y. Yu, Z. Xiao, N. G. Naganathan, and R. V. Dukkipati, “Dynamic Preisach modelling of hysteresis for the piezoceramic actuator system,” *Mech. Mach. Theory*, vol. 37, no. 1, pp. 75–89, Jan. 2002.
- [26] M. Kuczmann, “Dynamic Preisach hysteresis model,” vol. 1, no. 1, pp. 1–5, 2010.
- [27] D. C. Jiles, “Frequency dependence of hysteresis curves in ‘non-conducting’ magnetic materials,” *IEEE Trans. Magn.*, vol. 29, no. 6, pp. 3490–3492, 1993.
- [28] M.-A. Raulet, F. Sixdenier, B. Guinand, L. Morel, and R. Goyet, “Limits and rules of use of a dynamic flux tube model,” *Int. J. Comput. Math. Electr. Electron. Eng.*, vol. 27, no. 1, pp. 256–265, 2008.
- [29] M. A. Raulet, B. Ducharne, J. P. Masson, and G. Bayada, “The magnetic field diffusion equation including dynamic hysteresis: A linear formulation of the problem,” in *IEEE Transactions on Magnetism*, 2004, vol. 40, pp. 872–875.
- [30] G. Bertotti, “General properties of power losses in Soft ferromagnetic Materials.” 1988.
- [31] H. Skarrie, “Design of Powder Core Inductors,” Lund Institute of Technology, Lund University, SWEDEN, 2001.
- [32] S. Cundeva, “A transformer model based on the Jiles-Atherton theory of ferromagnetic hysteresis,” *Serbian J. Electr. Eng.*, vol. 5, no. 1, pp. 21–30, 2008.
- [33] A. Raghunathan, Y. Melikhov, J. E. Snyder, and D. C. Jiles, “Modeling of two-phase magnetic materials based on Jiles–Atherton theory of hysteresis,” *J. Magn. Magn. Mater.*, vol. 324, no. 1, pp. 20–22, Jan. 2012.

- [34] A. Stancu, O. Caltun, and P. Andrei, "Models of Hysteresis in Magnetic Cores," *J. Phys.*, vol. 7, no. 1 997, pp. 4–5, 1997.
- [35] A. Raghunathan, Y. Melikhov, J. E. Snyder, and D. C. Jiles, "Modeling the temperature dependence of hysteresis based on jiles-atherton theory," in *IEEE Transactions on Magnetics*, 2009, vol. 45, pp. 3954–3957.
- [36] a. Raghunathan, Y. Melikhov, J. E. Snyder, and D. C. Jiles, "Theoretical Model of Temperature Dependence of Hysteresis Based on Mean Field Theory," *IEEE Trans. Magn.*, vol. 46, no. 6, pp. 1507–1510, Jun. 2010.
- [37] A. Ladjimi and M. Rachid, "Modeling of Thermal effects on Magnetic Hysteresis using the Jiles-Atherton Model," no. 4, pp. 253–256, 2012.
- [38] J. C. Lagarias, J. A. Reeds, M. H. Wright, and P. E. Wright, "Convergence Properties of the Nelder--Mead Simplex Method in Low Dimensions," *SIAM Journal on Optimization*, vol. 9, pp. 112–147, 1998.
- [39] J. Kennedy and R. Eberhart, "Particle swarm optimization," *Proc. ICNN'95 - Int. Conf. Neural Networks*, vol. 4, 1995.
- [40] J. C. S. Fagundes, A. J. Batista, and P. Viarouge, "Thermal modeling of pot core magnetic components used in high frequency static converters," *IEEE Trans. Magn.*, vol. 33, 1997.
- [41] W. G. Odendaal and J. A. Ferreira, "A thermal model for high-frequency magnetic components," *IEEE Trans. Ind. Appl.*, vol. 35, pp. 924–931, 1999.
- [42] P. R. Wilson, S. Member, J. N. Ross, A. D. Brown, and S. Member, "Simulation of Magnetic Component Models in Electric Circuits Including Dynamic Thermal Effects," vol. 17, no. 1, pp. 55–65, 2002.
- [43] U. V. Wali, R. N. Pal, and B. Chatterjee, "ON THE MODIFIED NODAL APPROACH TO NETWORK ANALYSIS.," *Proc. IEEE*, vol. 73, pp. 485–487, 1985.
- [44] L. M. Wedepohl, "Modified nodal analysis: an essential addition to electrical circuit theory and analysis," *Engineering Science and Education Journal*, vol. 11. p. 84, 2002.

Chapter 3

3. Virtual Prototyping and Developed Model

3.1 Introduction

Virtual prototyping is essential in the development of new power electronics devices like static power converters [1], [2], [3]. Circuit simulators allow the optimization of complex circuit prototypes by associating models of passive and active components [4], [5]. Indeed modeling and simulation allow the prior knowledge of the system's behavior using circuit simulators to optimize complex circuit prototypes. Individual components models exist and are associated together to form a complete system design. Therefore we are able to predict the realistic behavior of the whole system under variable operating conditions.

There are several forms of creating component models of real devices ranging from ideal models using approximate equations to complex models including detailed underlying physical behavior. The modeling approaches fall into two main categories: behavioral and structural. Behavioral modeling can take the form of direct implementation of model equations using Hardware Description Languages to describe the relationship between input and output signals. Structural modeling involves interconnecting different blocks together to build a close physical representation of the actual system and perform the desired operations.

Our work is based mainly on behavioral modeling of magnetic components, but also takes advantage of structural modeling to separate static and dynamic core models in addition to windings models. In fact the developed magnetic component model consists of several blocks connected together (structural modeling) for which each block is described using a Hardware Description Language (behavioral modeling). The complete developed model is explained later in this chapter after a brief review on magnetic component modeling for circuit simulators including employed theory and techniques.

3.2 Magnetic component modeling for circuit simulators

In circuit simulation, behavioral block models of individual components are connected and the resulted equations are solved to determine the function of the circuit. Concerning magnetic components models, there exist some ideal models excluding saturation, hysteresis and dynamic effects. This approach can be extended to include materials saturation and nonlinear behavior. Another more accurate approach is to model each winding as an interface between the electrical and magnetic domains, and define core models for the magnetic material (as the models presented in chapter 2). In this approach each model is described using a modeling language and are implemented in a simulation software that supports this language. Also each model has its unique variables, connections and equations. Modeling and simulation techniques, simulation software, and modeling languages are discussed below.

3.2.1 Modeling Theory and Techniques

The term “model” is derived from the Latin word *modulus*, which means measure, rule, pattern, or example to be followed. In electrical engineering, a model is a set of equations or relations, which appropriately describes the interactions between different quantities of a physical or engineered component or system. Models help in the design and optimization of systems and are used to simulate the behavior of the component or system that they represent.

In circuit simulation, a model represents a physical element such as a resistor, capacitor or inductor. The model consists of a set of equations, connection points to other elements in the circuit and parameters that characterize the exact behavior of the physical element. Number of these parameters, connections and equations increase with the complexity of the elements. If we consider a simple element, like a resistor for example, a resistor model would have two connection points (or terminals), one parameter the resistance R , and at least one equation as shown in Figure 3-1.

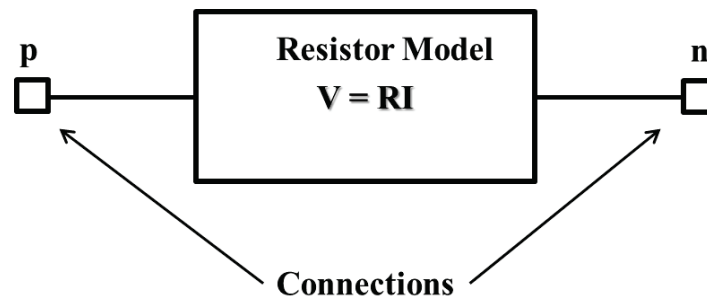


Figure 3-1: Resistor model example.

Generally, analogue models are described using non-linear ordinary differential equations (ODEs), and these provide the simultaneous fundamental equations to the matrix to be solved by the simulator. Parameters and Sequential variables may use sequential statements (like if-then-else type expressions) that use a discrete logic solver. Logic methods are used to handle events, changes, scheduling and conflict resolution.

There are two general types of connection used in analogue simulation: signal flow and conserved energy. Signal flow is the classical control system definition, where the signal has a single value only. The model has an input pin “in”, and an output pin “out”. Considering a simple gain block as an example (see Figure 3-2), the output will always be the input times the gain. In contrast, the conserved energy connections have two values or aspects. These are the effort-like and flow-like aspects, called the “across” and “through” quantities respectively. It is useful to explain this concept using practical examples, in this case the resistor shown in Figure 3-2. The voltage across the resistor is defined as the potential difference between the pins “p” and “n”. Therefore the voltage (v) is defined as an across variable as it is literally across the component pins. The current (i) flows through the pins and is therefore defined as a through variable. At the connection pin “p”, there is both a potential difference between the pin and ground, and a current through the pin. The current can pass in both directions (from “n” to “p” or from “p” to “n”) as the voltage can be positive or negative between “n” and “p”. This connection type becomes important when models are connected together in a circuit, as the conserved energy case will be dependent on impedances and loading.

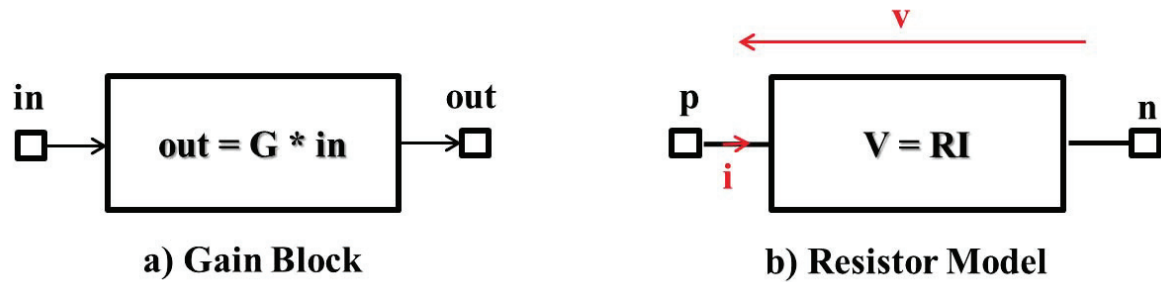


Figure 3-2: a) Signal flow (gain block) and b) conserved energy models (Resistor model).

Systems and models are divided into different domains according to their physical nature, like Mechanical, Fluidic, Electrical, Magnetic and Thermal systems. Each of these systems can be modeled using behavior modeling as in the case of electrical system (Resistor), but each has its proper across and through quantities (similar to voltage and current). For example a mechanical system has displacement and force as across and through quantities respectively. Fluidic systems have pressure (across) and flow rate (through), etc. For our applications in this thesis we consider only electric, magnetic and thermal systems. Modeling of these three systems is explained below.

3.2.1.1 Electrical System Modeling

Modeling of electrical systems is best approached by thinking separately about the element laws and the interaction laws. The interactions laws are Kirchhoff's Voltage Law (KVL) and Kirchhoff's Current Law (KCL). The element laws are relationships for individual components such as resistors (Ohm's law $V = RI$), capacitors, inductors...Electrical connections or nets have two variables, the voltage or potential difference (across quantities) and current (through quantity). Kirchhoff's laws are used by circuit simulators to solve for these variables at junctions in schematics using standard matrix techniques. An electrical system may be analogous to magnetic, thermal or other systems. Due to their ease of study and implementation, electrical circuits are usually used as analogs of thermal and magnetic circuits.

3.2.1.2 Thermal System Modeling

Thermal modeling uses the same basic construction as electrical with some basic differences. The through variable is defined as Heat Flow (Q in Watts) and the across variable is temperature (T in degree Celsius or Kelvin). This makes sense from a physical point of view, as the heat flows through the physical elements, and this causes a temperature difference between points. Modeling thermal networks in circuit simulators consists of assigning thermal connections between thermal elements (thermal resistances and capacitances). The temperature is equivalent to voltage and the heat flow is equivalent to the current in electric circuits.

Considering the heat dissipation of a power electronic component (chip or IC), for example, the heat path from the chip (die) to the case (package) and then to a heat sink can be modeled with the equivalent circuit diagram shown in Figure 3-3. In this case, the heat flow source $Q(t)$ represents the power dissipation occurring in the chip and evacuated to the

ambient through thermal resistances ($R\theta_{jc}$, $R\theta_{ch}$, and $R\theta_{ha}$) due to temperature difference ($T_j > T_{amb}$).

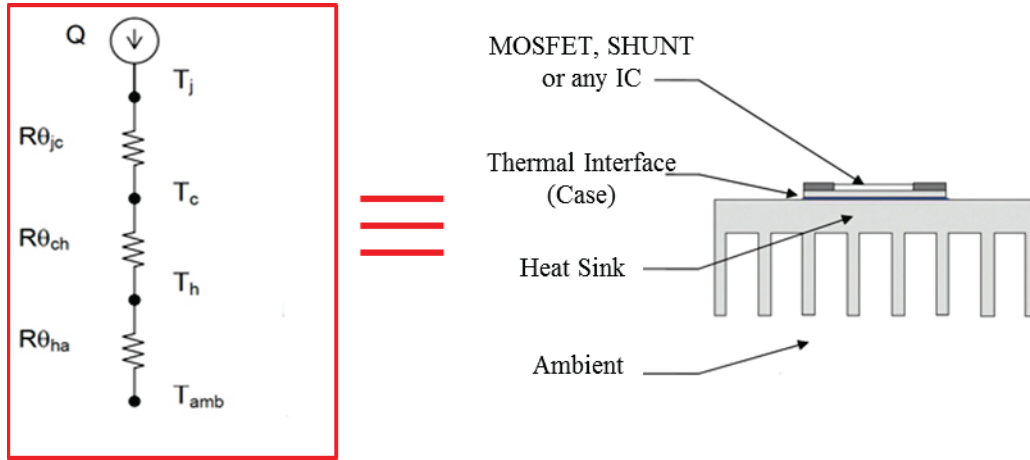


Figure 3-3: IC on heat sink equivalent thermal circuit.

3.2.1.3 Magnetic System Modeling

Magnetic modeling again uses the same basic construction as electrical with some differences. The through variable is defined as Flux (ϕ in Wb) and the across variable is Magneto Motive Force (MMF in Ampere turns). This makes sense from a physical point of view, as the flux flows through the magnetic elements, and this causes a magnetic field difference between points. The Magneto Motive Force is equivalent to voltage and the Flux is equivalent to the current in electric circuits.

Modeling magnetic networks in circuit simulators is a case of assigning magnetic connections between magnetic lumped elements. There exist several magnetic equivalent circuit models named after the magnetic elements (reluctances, inductances, or other lumped elements) used in the magnetic networks. For example, an E-core two-winding transformer presented in Figure 3-4 can be modeled by an equivalent magnetic reluctance model. In this case, the Magneto Motive Force source (MMF_1) represents the total MMF due to the current I_1 flowing in the first winding. Similarly for MMF_2 that is due to current I_2 flowing in the secondary winding. The magnetic path is modeled by magnetic reluctances (analogous to electric resistors) to represent different parts of physical core.

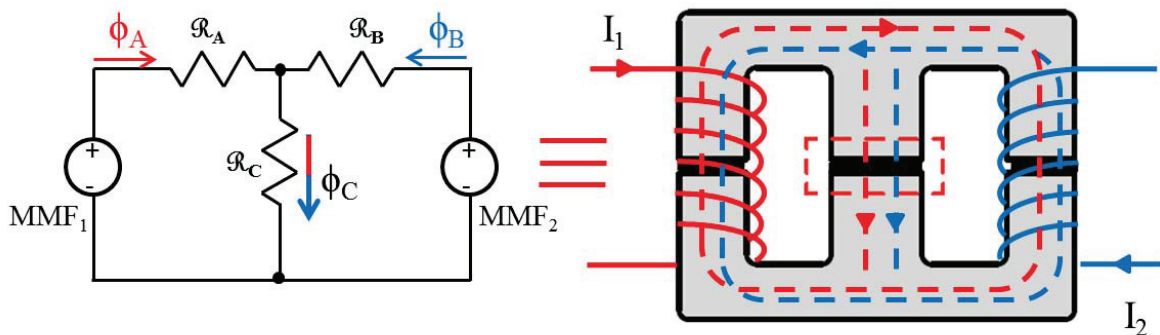


Figure 3-4: E-core two-winding transformer equivalent magnetic circuit.

The reluctance model is considered here for simplicity only in order to explain the analogy between magnetic and electric circuits. This model is ideal and does not take into account magnetic saturation or hysteresis. However there exists similar but more advanced models as the flux tube model presented in [6] which replaces the reluctance by a more complex magnetic lumped element (flux tube). This last model takes into account nonlinear and hysteresis behavior of magnetic components.

3.2.2 Multi/Mixed domain modeling

In systems modeling and simulation, it is important to ensure connections between different models of the design. When a complex system design contains components of different physical natures (like electromagnetic or electromechanical systems), electric simulators become insufficient. In this case multi-domain simulators and modeling languages are used instead [7][8][9]. The advantages of multi-domain modeling are the ability to describe the global behavior of components more accurately and providing coupling between them.

The power of multiple domain modeling becomes apparent when different technologies require to be simulated in the same circuit. For example, if an inductor is to be modeled, one of the two approaches (electrical or mixed domain) could be taken. If the electrical route is taken, then the inductor is modeled directly as an electrical inductor. The information available to the engineer from the model is purely the electrical information such as the voltage, current and power. On the other hand, if a mixed domain model is used, with a winding and core model in the magnetic domain, the engineer has access to the electrical data as before, but also the Flux, Flux Density, MMF and Magnetic Field Strength.

If we consider a winding model, it has electrical connections to the circuit with voltages and currents, but there are also the magnetic variables, flux and magnetic field in the magnetic domain. The example of a winding has four connections as shown in Figure 3-5.

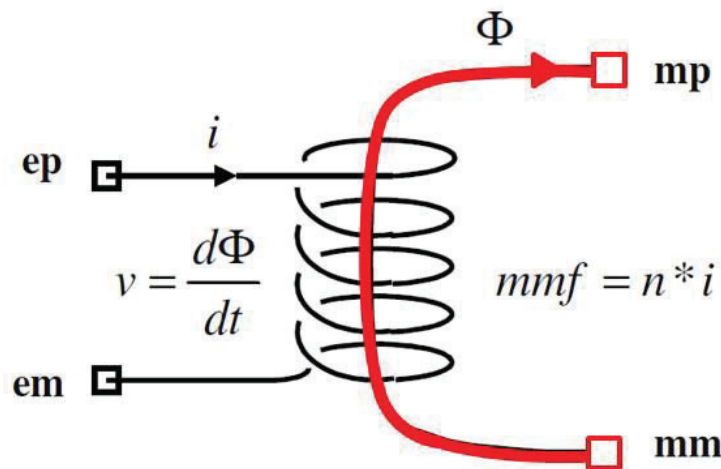


Figure 3-5: Winding model concept and connections.

The connections “ep” and “em” are electrical (voltage & current) while the connections “mp” and “mm” are magnetic (flux & MMF). The transfer from electrical to magnetic is straightforward. The MMF is derived from the current in the winding using Ampere’s law, and the voltage is derived from the flux using Faraday’s law. This has important implications with regard to electromagnetic modeling. The winding model is a part of our developed magnetic component model and it is completely explained later in this chapter.

3.2.3 VHDL-AMS modeling language

Electronic circuits fall into two main areas, analogue and digital. Analogue simulation using digital computers is based on approximating the continuous time behavior of the electronics circuit, solving non-linear differential equations using numerical integration methods (*Euler Integration, Trapezoidal Integration...*). At each time-step, the analogue simulation requires the complete system to be solved. If the time-steps are small enough it is effectively continuous. This approach is usually very accurate but can be time consuming and the simulation time increases with the size of the system.

Digital simulation relies on an event-based approach. Rather than solve differential equations, events are scheduled at certain points in time, with discrete changes in level. Resolution of multiple events and connections is achieved using logical methods. With the digital simulation method, variables only need to change if an event occurs, in general leading to much faster simulations. Using logical variable resolution rather than numerical techniques as in the analogue case is also generally faster and simpler to implement.

Developments in simulation technology combine the two techniques into a form of mixed-signal simulation that can take advantage of the relatively high accuracy of the analogue simulation and the high speed of the digital simulation [10], [11]. One of the best-known modeling languages that support Mixed-Signal is the VHDL-AMS [12].

VHDL (Very High Speed Integrated Circuit Hardware Description Language) was originally developed by the US Department of Defense to simulate the behavior of ASIC devices (IEEE Standard 1076-1987) [13]. It had quickly developed to implement complex logic designs into programmable logic devices (e.g. FPGA type devices). In the early 1990s the need to simulate systems consisting of a combination of analogue and digital signals lead to the extension of VHDL language in 1999 to the IEEE 1076.1 standard for the simulation of *analogue and mixed systems* known as VHDL-AMS.

In VHDL-AMS we can define different physical discipline or energy domains such as electrical, thermal, magnetic...represented by the Nature. Each nature has two aspects related to physical effects:

- Across: effort-like effects (voltage, velocity, temperature, etc.)
- Through: flow-like effects (current, force, heat flow rate, etc.)

A VHDL-AMS design description consists of an entity declaration and one or more architectures (Figure 3-6).

The ENTITY declaration defines the inputs to and outputs from the model (Describes the model interface to the outside environment). It contains constants, terminals and any generic parameters used by the different implementations. Constants are objects used for data storage. Terminals of a specified nature represent continuous, conservative ports of the model.

Each ARCHITECTURE defines a different implementation or behavior of a given design unit. For analog modeling, quantities are routinely used and declared in the ARCHITECTURE. Quantities represent an unknown (continuous-time waveform) in the set of Differential Algebraic Equations (DAEs) implied by the text of the model. Different “*sequential statements*”, “*concurrent statements*” and “*simultaneous statements*” may be used to describe the behavior of the model [14].

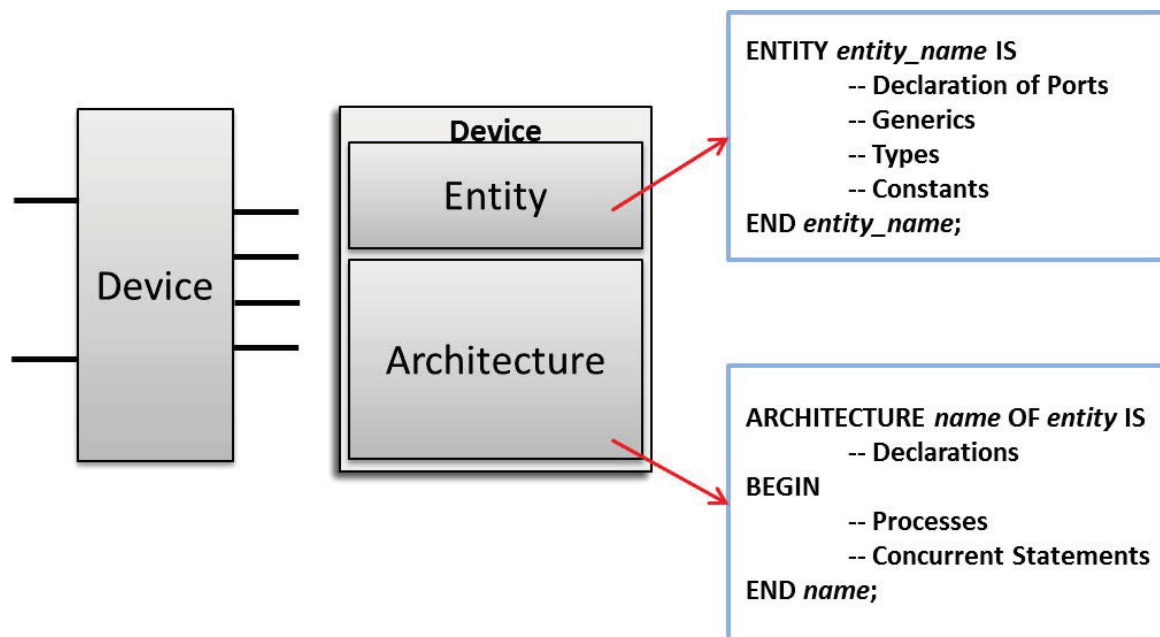


Figure 3-6: VHDL-AMS entity and architecture.

Sequential and concurrent statements are available in both VHDL and VHDL-AMS, but simultaneous statements are available only in VHDL-AMS. Sequential are used for signal assignment, ‘delays’, ‘loops’, ‘wait’ instructions, condition instructions etc. They are executed in the order in which they appear within the process or subprogram. Concurrent statements are used to define processes that are executed concurrently with each other. They are also used in ‘assert’ instructions (report messages for predefined conditions) ‘generate’ instructions and ‘call’ instructions

Simultaneous statements express relationships between quantities where the left-hand side and right-hand side are symmetrical and separated by “==” sign. This sign indicates that the equation is continuously evaluated during simulation, and equality is maintained between the expressions on either side of the “==” sign at all times. The order of simultaneous statements does not matter but one quantity must appear in each statement at least, with scalar sub elements of a floating point type. Statements may involve quantities, constants, signals, and (possibly user-defined) functions.

3.2.4 Circuit simulation software

Circuit simulators, first began to appear in early 1970's with the explosive growth of the integrated circuit market that precipitated the rise of importance of circuit simulation. With integrated circuits, prototypes were expensive to build and difficult to troubleshoot. Circuit simulators were necessary to evaluate designs before they were fabricated. As designs became larger and more complicated, the need to use circuit simulators increased [15].

These simulators or so-called CAD tools (*Computer Aided Design*) or circuit analysis programs provide a simple, cost-effective means of confirming the intended operation prior to circuit construction. They also allow testing and verifying new ideas that could lead to improved circuit performance. Circuit simulation software use behavioral models to replicate the behavior of actual device or system.

Circuit simulators may include analog simulation, digital simulation, or a combination of both. These including both types of simulation are called “*mixed-signal*” or “*mixed-mode*” circuit simulators. From another point of view, simulation software combining different physical disciplines or energy domains (electric, magnetic, thermal, mechanical...) are called “*multi-domain*” simulators. One of the known multi-domain circuit simulators is SIMPLORER that supports VHDL-AMS and thus mixed-signal modeling. All simulations in this thesis are simulated using Simplorer (versions 7.0, 8.0, and 11.0).

Simplorer is multi-domain simulation software [16] allowing virtual prototyping of different physical domains of a system including the electrical, digital, mechanical, thermal and magnetic (Figure 3-7). It enables modeling, simulation, analysis and optimization of complex systems including electromechanical, electromagnetic, and power designs. This enables engineers to investigate system functionality and performance and to verify overall design. The result is a reduction in development time and cost, increased system reliability and performance optimization.

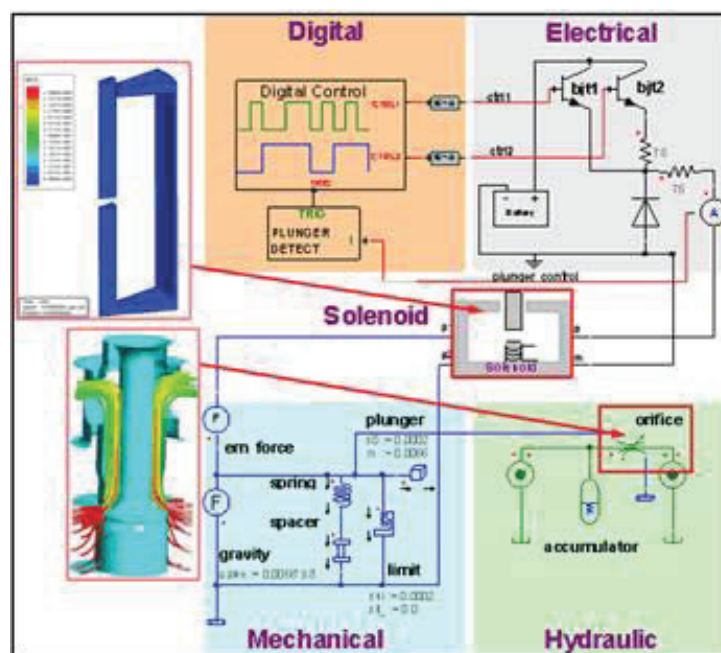


Figure 3-7: Multi-Domain ANSYS Simplorer [16].

Simplorer offers multiple modeling techniques including circuits, block diagrams, state machines, equation level, and modeling languages such as VHDL-AMS, C/C++, and SML (Simplorer Standard Language). These can be used concurrently to model analog, digital, and mixed signal multi-domain designs.

Simplorer supports the IEEE standard (1076.1) VHDL-AMS modeling language for mixed signal and multi-domain systems. It provides both continuous-time and event-driven modeling semantics, and is suitable for analog, digital, and mixed analog/digital circuits. The three primary simulation modes **Transient Analysis**, **DC analysis** and **AC analysis** are supported by Simplorer in addition to other modes like Monte Carlo analysis, Fourier analysis, distortion analysis...

The DC Analysis calculates the state of a circuit with fixed (non-time varying) inputs after an infinite period of time. DC analysis is useful to determine the operating point (Q point) of a circuit, power consumption, output voltage of power supplies, transfer functions, and noise margin.

The AC Analysis mode computes the complex values of the node voltages of a linear circuit as a function of the frequency of a sinusoidal signal applied at the input. AC Analysis uses phasor analysis to calculate the frequency response of a circuit. The analysis is useful for calculating the gain, cut-off frequency, input and output impedance, and noise of a circuit as a function of frequency.

The Transient Analysis mode computes the voltage waveforms at each node of the circuit as a function of time. This is a large-signal analysis: no restriction is put on the amplitude of the input signal. Transient analysis is the most powerful analysis capability of a simulator because the transient response is so hard to calculate analytically. Transient analysis is also the most CPU intensive and can require more CPU time as a DC or AC analysis.

In this thesis only Transient analysis is used in simulation to study the dynamic response of models subjected to time varying excitations. These models and the complete magnetic component model are presented in the next section.

3.3 Developed Model

The developed non-linear dynamic model of magnetic components for use in circuit simulators is presented in this section. It includes the material's nonlinear hysteresis behavior with accurate modeling of winding and core losses in addition to thermal effects that are not taken into account by existing models in circuit simulators. The model is based on the principle of separation of static and dynamic contributions as well as Bertotti's theory [17]. VHDL-AMS is used as a modeling language due to its multi-domain modeling feature, allowing coupling with a thermal model. The thermal model is represented by a temperature source for static thermal conditions or by an equivalent thermal circuit for self-heating conditions.

As mentioned before the model is based on both behavioral and structural modeling of magnetic components. Based on structural modeling approach, the developed model consists of several blocks connected together to separate static and dynamic magnetic models as well as windings models. Based on behavioral modeling, static and dynamic behavior of magnetic components is modeled using a Hardware Description Language (HDL). Actually, the blocks constituting the component model are described using VHDL-AMS. The model structure including these behavioral blocks is presented below.

3.3.1 Model Structure

In the interest of precision and in order to be adaptable for different kinds of magnetic materials, the magnetic component model adopts a structural modeling approach. As a consequence the model consists of 3 major blocks as shown in Figure 3-8: a winding allowing the coupling between electrical and magnetic domains using Ampere's and Faraday's laws, a static model to describe the static hysteresis behavior of the magnetic material and a dynamic model to add dynamic effects in the core (eddy currents and walls motion). VHDL-AMS language is chosen to describe each block behavior due to its multi-domain modeling feature and since it is supported by several circuit simulators. The result is a complete magnetic component model including electrical, magnetic and thermal domains shown in Figure 3-8.

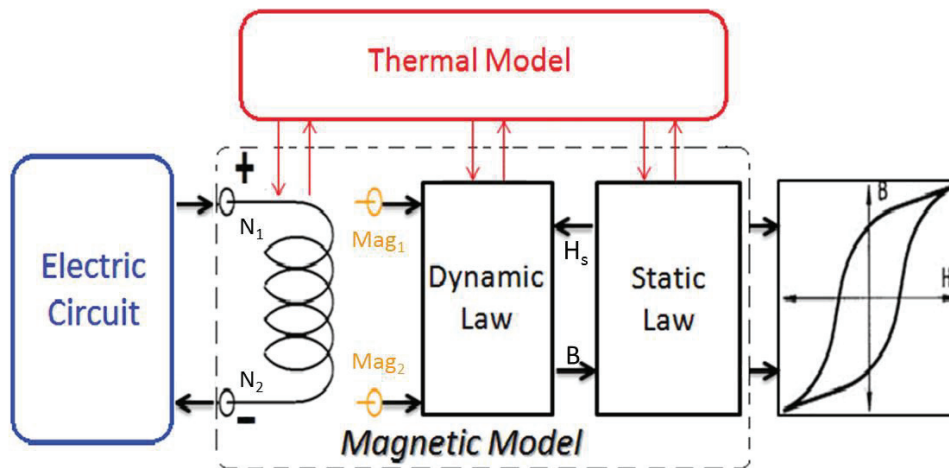


Figure 3-8: Magnetic Component Structure.

Figure 3-8 represents the structure of an inductor, connected to the electric circuit by positive and negative *electric* terminals of the winding. *Magnetic* terminals of the winding are connected to the dynamic model block to relate magnetic flux and MMF through and across the magnetic terminals according to dynamic model equations. The dynamic model block is connected to a static model block by input/output ports (I/O). The output flux density B of the dynamic block is an input to the static block which is used to calculate the corresponding static field H_s . Then the static field H_s calculated by the static block is an input to the dynamic block which is needed to calculate the total magnetic field H . All three blocks are connected to the thermal model to take temperature into account in each model and to retrieve winding and core losses as inputs to the thermal model. A detailed description of model structure and each block function and connections is presented below.

3.3.1.1 Winding Block

The winding block model shown in Figure 3-9 represents a coupling element between electric and magnetic circuit. It converts electrical energy into magnetic energy and vice versa (bidirectional energy flow). The model has electrical pins, N1 and N2 (across: v , through: i) and magnetic pins, Mag1 and Mag2 (across: MMF, through: flux). It has two global parameters, the number of turns (N) for coupling quantity between magnetic and electric domains and the winding resistance (R) shown in Table 1.

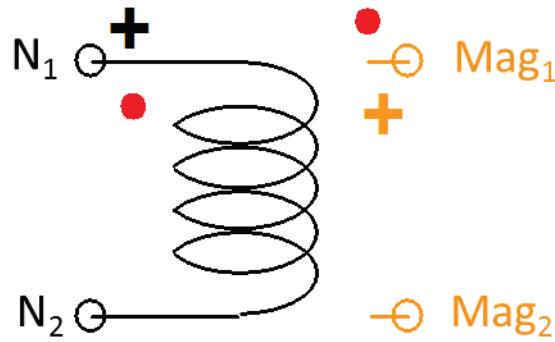


Figure 3-9: Winding Model Block.

Conservative Pins		
Name	Description	Nature/Data Type
N ₁	Positive node Pin 1 (with red point)	electrical
N ₂	Negative node Pin 2	electrical
Mag ₁	Positive node Pin 1 (with red point)	magnetic
Mag ₂	Negative node Pin 2	magnetic
Parameters		
Name	Description	Nature/Data Type
R	Resistance (Ohm)	real
N	Number of turns	real

Table 1: Pins and parameters of winding model block.

The winding model is described by the following two equations:

$$v(t) = -N \cdot \frac{d\phi}{dt} + R \cdot i(t) \quad (3.1)$$

$$MMF = N \cdot i(t) \quad (3.2)$$

3.3.1.2 Dynamic Model Block

The dynamic model is the center of the component model representing the overall behavior of the core magnetic material. It describes the total magnetic field H variation as function of flux density (or vice versa) or simply the BH loop.

This total field is the sum of static field calculated by the static model and the dynamic fields due to eddy current and excess losses calculated by the dynamic model (loss separation). Thus the dynamic model is connected to the static model such that the flux density B is a model output and the corresponding static field H_s (calculated by the static block) is a model input as shown in Figure 3-10.

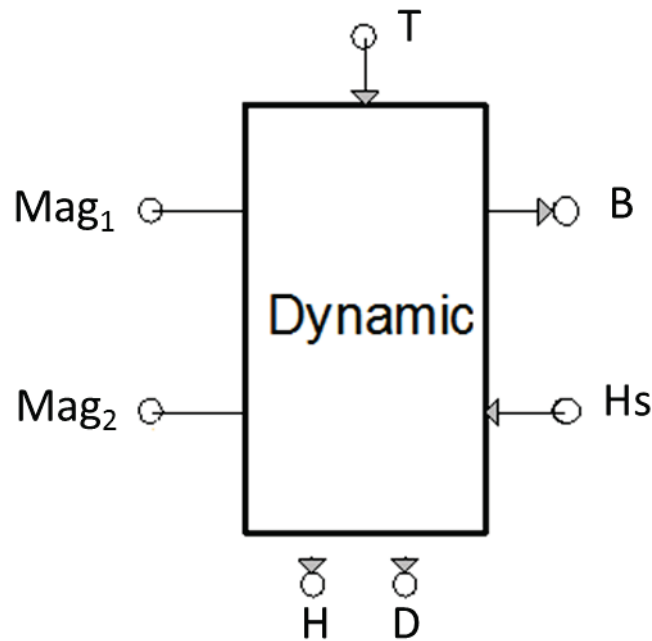


Figure 3-10: Dynamic Model Block.

Conservative Pins		
<i>Name</i>	<i>Description</i>	<i>Nature/Data Type</i>
Mag1	Positive node Pin 1	Magnetic
Mag2	Negative node Pin 2	Magnetic
T	In - Temperature	Thermal
Hs	In - Static magnetic field	real
B	Out - Flux density	real
D	Out - Derivative of flux density	real
H	Out - Total magnetic field	real

Parameters		
<i>Name</i>	<i>Description</i>	<i>Nature/Data Type</i>
s	Magnetic cross section	real
l	Magnetic mean length	real
Delta	Sign parameter	real
a1, a2, a3...	Dynamic model parameters (depend on choice of model)	real

Table 2: Pins and parameters of dynamic model block.

The dynamic model has magnetic pins, Mag1 and Mag2 (across: MMF, through: flux) that are directly connected to the winding model. An input thermal pin (T) is used to set the temperature of the model. Two output pins D and H, representing the time Derivative of Flux density and Total magnetic field respectively are available for total core losses calculations. The dynamic model includes geometrical parameters as magnetic cross-section (s) and mean-length (l), along with dynamic model parameters that are dependent of the chosen model. A summary of these pins and parameters are presented in Table 2.

3.3.1.3 Static Model Block

The static model describes the static hysteresis behavior of magnetic materials. It may be composed by one of the physical or mathematical static magnetic models explained in previous chapter (Polynomial model, Jiles-Atherton model, Presiach-Néel model...). This block model is connected to the dynamic model such that the flux density is a model input and the calculated static field is a model output as shown in Figure 3-11 (inverse to dynamic model).

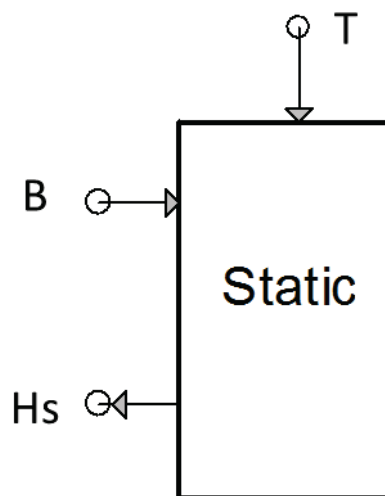


Figure 3-11: Static Model Block.

The static model has also an input thermal pin (T) to take temperature into account. The model includes the Relative permeability (μ_r) as parameter, in addition to static model parameters that are dependent of the chosen model. A summary of these pins and parameters are presented in Table 3.

Conservative Pins		
<i>Name</i>	<i>Description</i>	<i>Nature/Data Type</i>
T	In - Temperature	Thermal
B	In - Flux density	real
Hs	Out - Static magnetic field	real
Parameters		
<i>Name</i>	<i>Description</i>	<i>Nature/Data Type</i>
μ_0	Vacuum permeability	Constant
b1, b2, b3...	Static model parameters (depend on choice of model)	real

Table 3: Pins and parameters of static model block.

3.3.1.4 Thermal Model Block

The thermal model consists either of a simple temperature source for modeling component's behavior under different operating temperatures (static conditions) or of an equivalent thermal circuit including thermal resistances and capacitances for modeling the self-heating of the magnetic component (dynamic conditions).



Figure 3-12: Temperature source component.

For static thermal conditions, the temperature source shown in Figure 3-12 is connected to all blocks of the component model. This component (T1) represents an ideal temperature source which supplies the defined temperature (θ) for an arbitrary heat flow. This source could be constant or time-controlled.

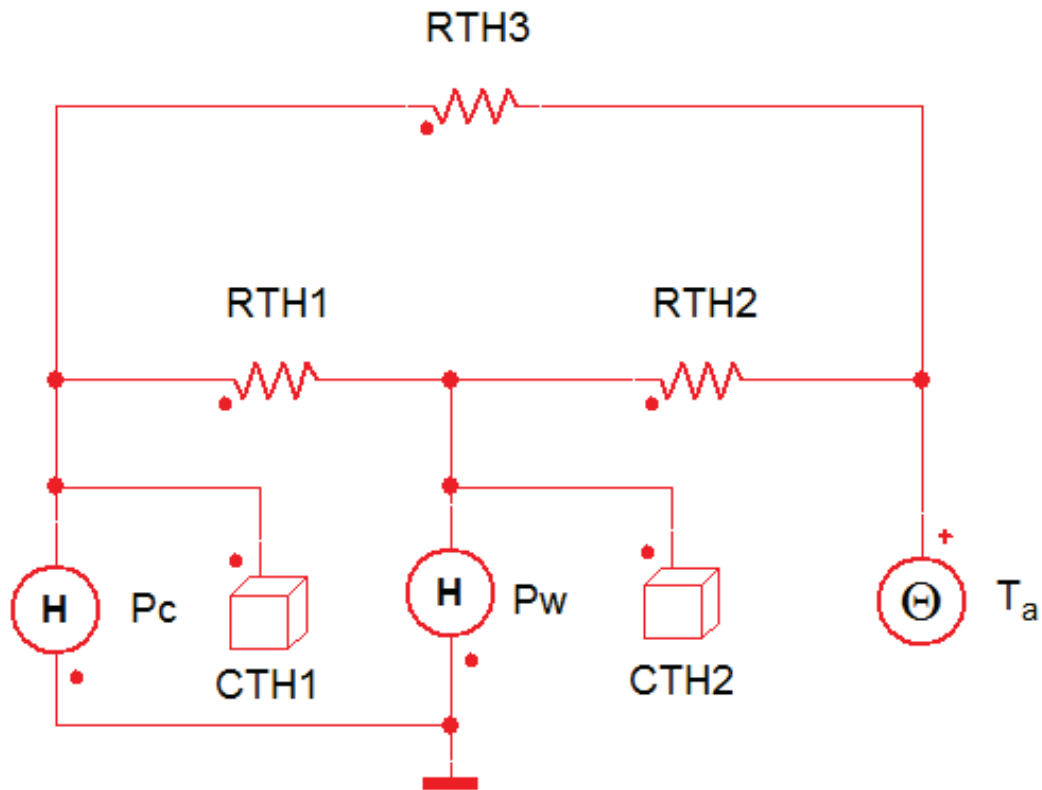


Figure 3-13 : Thermal model (equivalent circuit) of an inductor in Simpler

For self-heating modeling, a thermal model is needed and coupled with the other model blocks. As a thermal model we use an equivalent thermal circuit based on nodal analysis (explained in chapter 2). An inductor thermal equivalent circuit would be as shown in Figure 3-13. In this circuit core and winding losses are represented by the heat flow sources (P_c : core losses and P_w : winding losses) while thermal capacitances $CTH1$ and $CTH2$ represent the heat energy stored in both core and winding respectively. The thermal resistances $RTH1$, $RTH2$ and $RTH3$ correspond to heat transfer between core-winding, winding-ambient, and core ambient respectively.

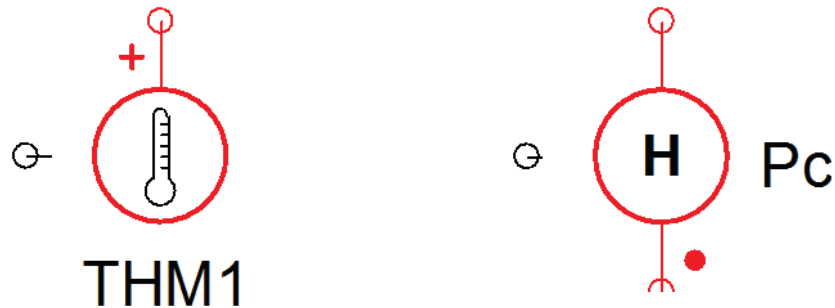


Figure 3-14: thermometer component (left) and heat flow source component (right)

The temperature at each node of thermal circuit can be measured using the thermometer component shown in Figure 3-14 (left). This is useful to inject measured temperatures into

other model blocks. The losses are injected to thermal model by the option “*use-pin*” available in heat flow sources. This allows adding a third pin to the source to control heat flow using losses value (in watts) calculated by the magnetic model, see Figure 3-14 (right).

3.3.2 Choice of Materials

In our work we study powder and nanocrystalline cores only due to their high performance in the domain of frequency and application considered. Nanocrystalline materials are mainly used in EMI filters and power electronics applications like switched mode power supplies and static converters. Among studied materials, nanocrystalline Nanophy cores N14E1, provided by Mecagis, are chosen due to their interesting properties including high saturation induction, low coercive field and high relative permeability. Furthermore, these materials are already available in our laboratory and have been used in EMI filter application in previous thesis [18][19]. Nevertheless, other nanocrystalline and powder cores are also used according to the application presented in next chapter.

The choices of static and dynamic materials laws are based on the choice of material and are explained below.

3.3.3 Choice of static and dynamic laws

3.3.3.1 Choice of static law

The choice of the static model is based on material static characterization. In order to describe the static behavior of the material we considered Jiles-Atherton model which is well-known, and widely used. Unfortunately Jiles-Atherton does not apply for the nanocrystalline material static behavior, since none of the parameters identification methods (PSO, simplex) gives a set of physical parameters values corresponding to the measured static hysteresis loop. The best result is shown in Figure 3-15. In addition, the variation of JA parameters as function of temperature may be complicated since it depends on the measurements done near 0 K [20].

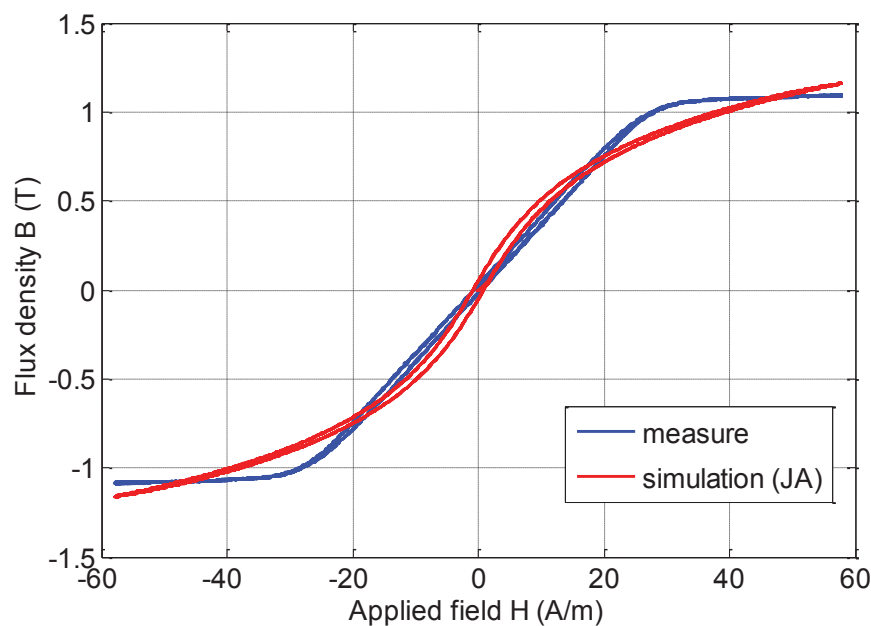


Figure 3-15: Measured and simulated static BH curves by Jiles-Atherton model at $f = 1$ Hz

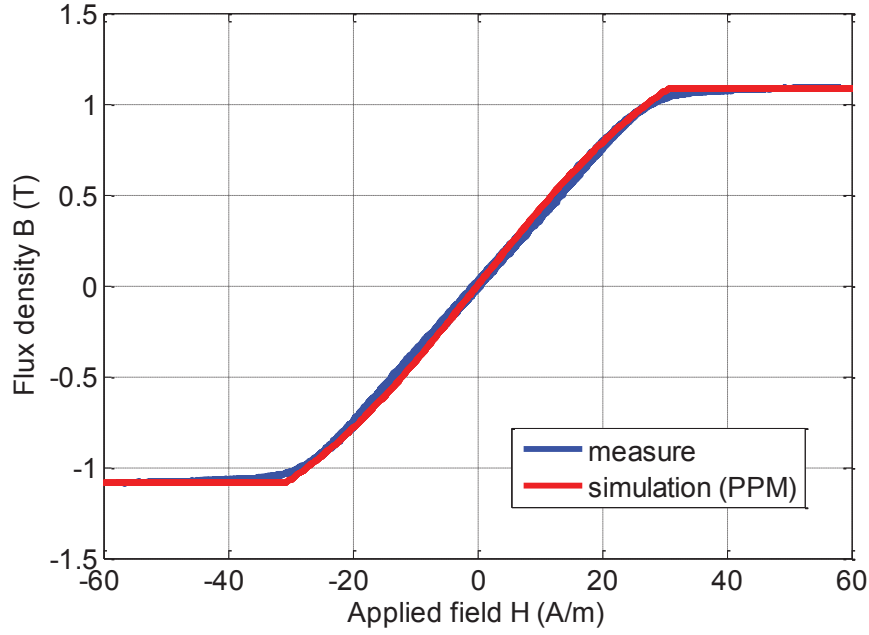


Figure 3-16: Measured and simulated static BH curves by Piecewise Polynomial model at $f = 1$ Hz

The nanocrystalline magnetic material used has a very thin static hysteresis loop (coercive field about 0.5A/m) and a piecewise linear behavior. Due to these characteristics, the physical model of Jiles-Atherton does not apply. In the aim to describe the linear static behavior of the material, the mathematical polynomial model presented in previous chapter in static models section is used (Figure 3-16). This reversible model is limited to materials with low coercive field. The model equations (3.3) are coded in VHDL-AMS and the code is available in the annex A.

$$B = \begin{cases} \mu_0(H - H_b) + P(H_b) & \text{if } H \geq +H_b \\ P(H) & \text{if } |H| < H_b \\ \mu_0(H + H_b) - P(H_b) & \text{if } H \leq -H_b \end{cases} \quad (3.3)$$

The precision and number of parameters of this model depend on the order n of the $P(H)$ function. For the N14E1 nanocrystalline material a polynomial of fifth order ($n=5$) is sufficient to represent its static behavior. In that case we have 4 parameters p_1 , p_3 , p_5 and H_b considering the even parameters are null due to the odd parity of the curve.

3.3.3.2 Choice of Dynamic law

Concerning the dynamic model, we started modeling using DSF [21] due to its advantages as simplicity, only one dynamic parameter, and short calculation time. However, due to high excess losses of the chosen material, this model is not very accurate in wide frequency applications. For that reason the Bertotti's model is used as the dynamic model (equation 3.4). The presence of a 2nd term of the flux derivative $(dB/dt)^{1/2}$ makes this model more accurate. Using this model we are able to model dynamic hysteresis loops of the nanocrystalline materials N14E1 with high precision (Mean Squared Error: $MSE < 1 \times 10^{-3}$) as shown in Figure 3-17.

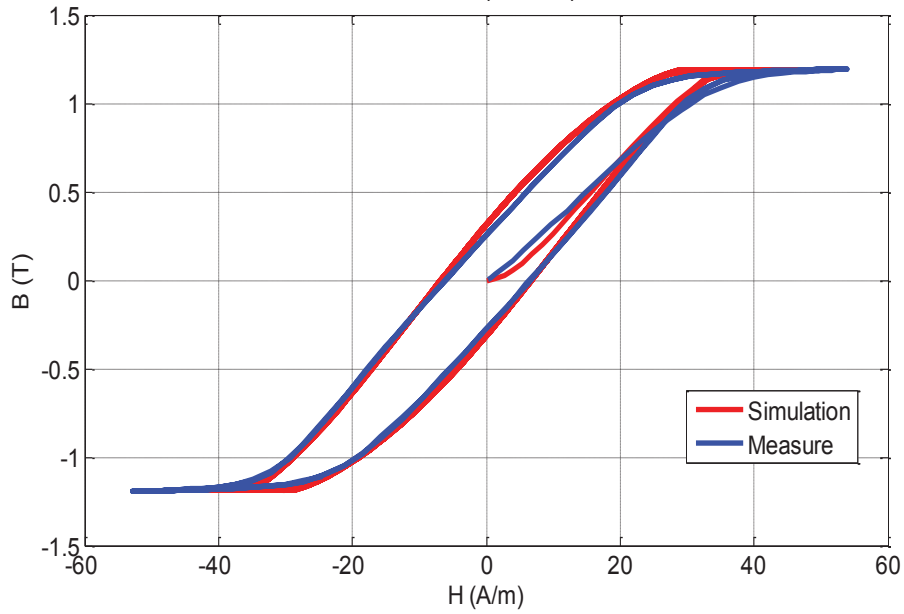


Figure 3-17 : Measured and simulated dynamic BH curves by Bertotti's model at $f = 10$ kHz

In fact this model, according to G. Bertotti, separates dynamic losses into eddy current losses and excess losses by two flux derivative terms in the general model equation (3.4). As a consequence it is more accurate but requires two dynamic parameters shown in equation (3.5). Equations of this dynamic model are also coded in VHDL-AMS and the code is available in annex B.

$$H_{total}(t) = H_s(B(t)) + \gamma \cdot \frac{dB(t)}{dt} + \alpha \cdot \delta \cdot \left| \frac{dB(t)}{dt} \right|^{\frac{1}{2}} \quad (3.4)$$

$$\gamma = \frac{\sigma \cdot d^2}{12} \quad \alpha = \sqrt{\sigma G V_0 S} \quad \delta = \text{sign}\left(\frac{dB}{dt}\right) \quad (3.5)$$

For ribboned nanocrystalline materials, the first dynamic parameter (γ) is related to the material's conductivity σ and ribbon thickness d . The second dynamic parameter (α) is a function of the characteristic field V_0 , a dimensionless coefficient G , and the magnetic cross section S .

A limitation of the Bertotti's model is that it does not take magnetic diffusion into account. It is quite accurate in a condition of no skin effect is considered. For this studied material, the skin effects remain negligible until a frequency of 100 kHz. Indeed at this frequency the skin depth δ estimated by equation (3.6) is about 9.8 μm compared to the 20 μm thickness of nanocrystalline ribbons. However this limiting frequency is much higher for low permeability materials that are used in the application presented in next chapter.

$$\delta = \sqrt{\frac{2\rho}{\omega\mu}} \quad (3.6)$$

According to the chosen static and dynamic materials laws (polynomial and Bertotti's), a total of 6 parameters (4 static and 2 dynamic) are needed for the complete component model. These static and dynamic parameters identification and variation as function of temperature are presented in next section.

3.3.4 Temperature dependence and parameters extraction

3.3.4.1 Static parameters

The parameters of the static model are identified from the static measurements using mathematical fitting. Their evolution as function of temperature is studied [22]. Since the trend of variation of these parameters is monotonic, a linear approximation can express this variation as function of temperature. This linear function is implemented in the model to calculate each parameter at any temperature.

For a polynomial model of 5th order, the central zone of the static hysteresis loop is modeled by the equation (3.7). The three parameters p_1 , p_3 and p_5 are identified for different temperatures up to 250 °C. The variations of these three parameters as function of temperature are presented in Figure 3-18. The 4th static parameter H_b variation is also studied and shown in Figure 3-18. The approximations of these four parameters, shown in dotted lines, are implemented in the static block model.

$$B(H) = p_5 \cdot H^5 + p_3 \cdot H^3 + p_1 \cdot H^1 \quad (3.7)$$

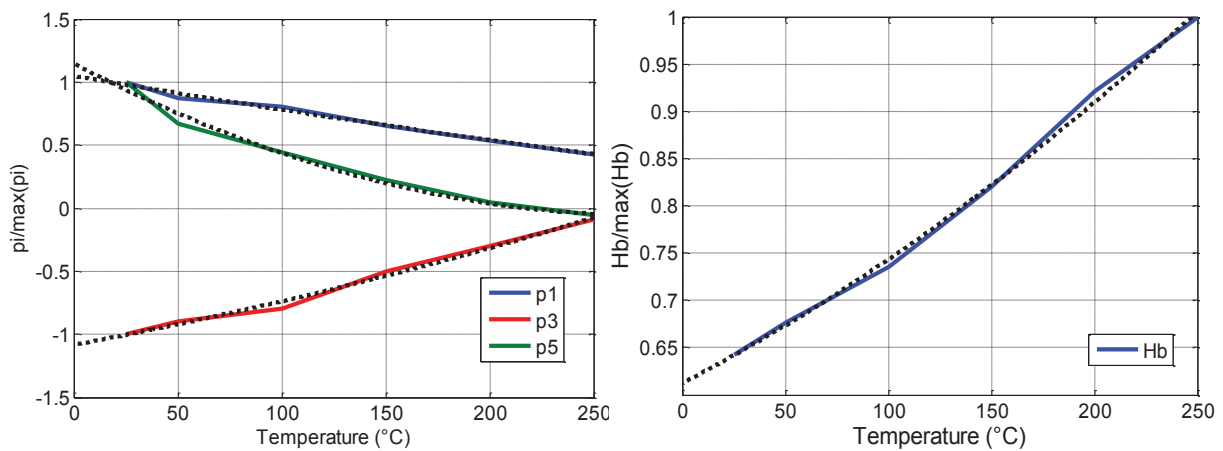


Figure 3-18: Static parameters variations with temperature (approximated by dotted curves)

3.3.4.2 Dynamic parameters

The dynamic parameters variation as function of temperature must be studied in order to associate thermal effects to the dynamic model. Since γ depends only on the material's conductivity and ribbon thickness, it is directly calculated from the electrical conductivity measurements using a four-point probes method [23]. Figure 3-19 illustrates the principle of four-point resistivity measurements for thin films. This measuring technique has four probes: two probes for passing a DC current through the sample and two other probes for measuring the induced voltage. If the probes are placed near the edges of the sample, the resistance of the film is the ratio of voltage to current. The resistivity ρ is calculated from the measured resistance R using (3.8) where l is the distance between probes and s is the film cross section.

$$R = \rho \frac{l}{s} \quad (3.8)$$

In contrast to the two-point method, the four point method uses the two additional probes to measure the voltage potential of the material surface. These probes do not carry any current, thus eliminating the parasitic resistances. A high quality four-point head is necessary to get repeatable and reliable resistivity values. Probes spacing is very important and different probes configuration lead to different calculation methods. When measuring samples with low resistivity, high currents are needed in the current probes to obtain good voltage readings.

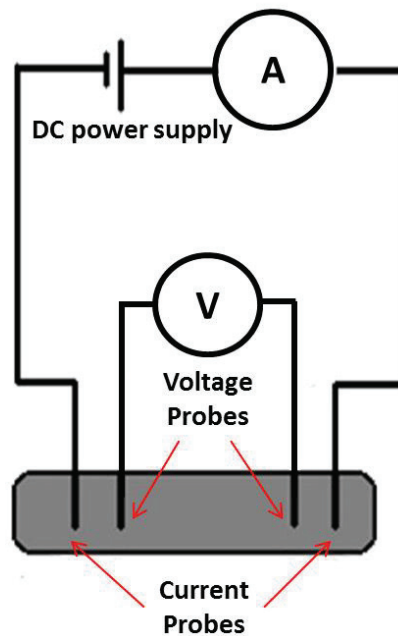


Figure 3-19: principle of four-point resistivity measurement technique

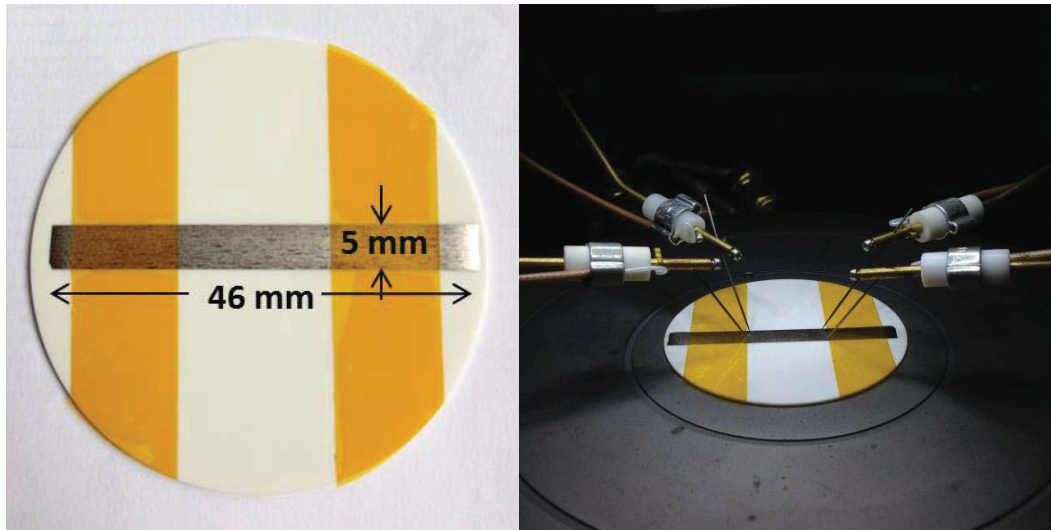


Figure 3-20: Resistivity measurement of a nanocrystalline ribbon

To measure the resistivity of the N14E1 nanocrystalline material, a 46 mm length sample of the 20 μm thick ribbon material is flattened and fixed on a ceramic support (Figure 3-20). Using the four point technique, the resistivity of the material is measured for temperatures between 25 $^{\circ}\text{C}$ and about 300 $^{\circ}\text{C}$. At 25 $^{\circ}\text{C}$ the measured resistivity is very close to 1.15 $\mu\Omega\cdot\text{m}$ value given by the manufacturer. As the temperature increases, the resistivity increases linearly as shown in Figure 3-21. This phenomenon is generally known in metals and modeled by mathematical formulas [24]. From resistivity measurements the dynamic parameter γ is calculated using (3.5) and its variation with temperature is shown in Figure 3-22.

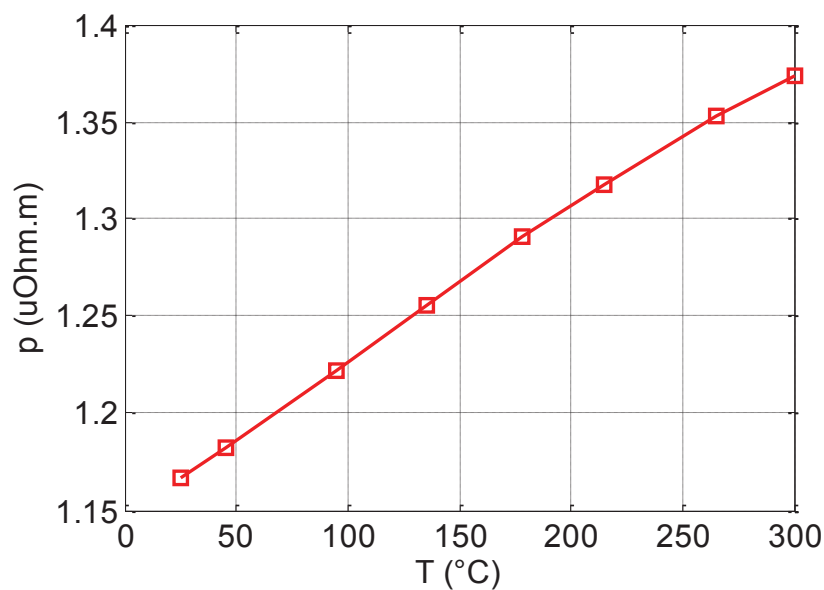
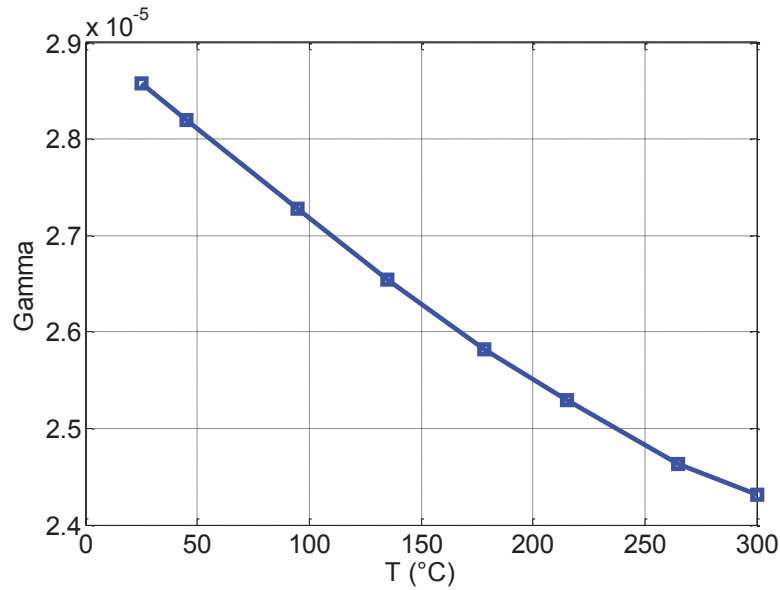
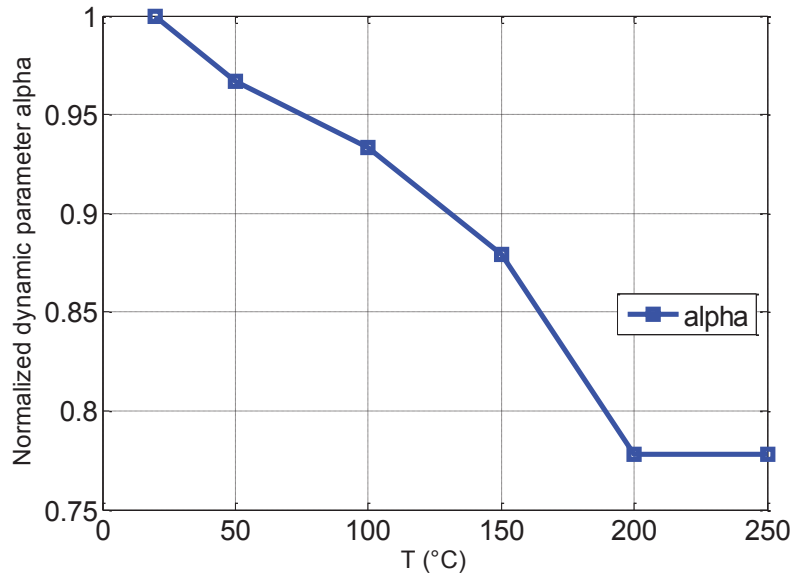


Figure 3-21 : Electric resistivity variation with temperature

Figure 3-22: Dynamic parameter γ variation with temperature

The other parameter α is extracted from mathematical fitting of equation (3.4) to the measured B-H loop at 10 kHz. It is calculated in order to have the same measured and simulated B-H loops at each temperature. The results are presented in Figure 3-23 showing normalized values of the second dynamic parameter α as function of temperature. The variation of α remain approximately linear up to 150 °C after this temperature its value decreases rapidly and remains constant after 200 °C.

Figure 3-23 : Dynamic parameter α variation with temperature

A Linear approximation of the dynamic parameters variation as a function of temperature is implemented in the dynamic model. Even if alpha variation is not perfectly linear, using such approximation leads to a maximum error of 5% in loss calculation at 200 °C compared to less than 1% at 25 °C. For higher precision, a higher degree polynomial could be used.

3.4 Simulation and Model Validation

To validate the developed model, a circuit identical to the test bench circuit used for measurements is simulated. The circuit used, is a RL circuit in series with a sinusoidal voltage source shown in Figure 3-24. Comparison between measured and simulated BH loops is presented for different temperatures and frequencies.

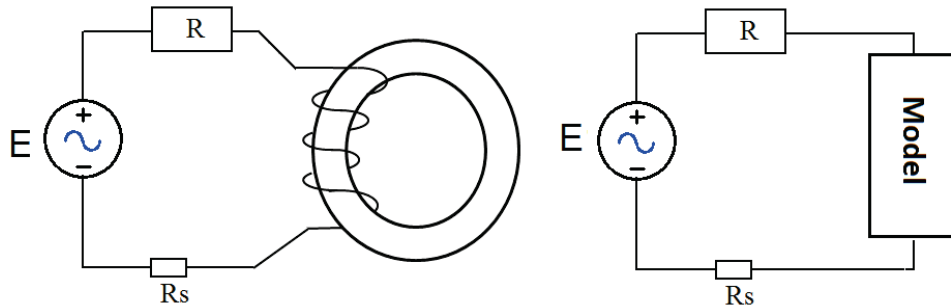


Figure 3-24 : Measurement (left) and simulation (right) circuits.

In circuit simulation, the schematic or “*sheet*” of Simplorer is shown in Figure 3-25 where the simple RL circuit is simulated. This sheet includes the whole magnetic component model including winding, dynamic, and static blocks along with the temperature source at the right in red. Some function blocks (like Moving average, Sum, and gain shown in yellow) are used in loss calculations. The temperature source is connected to both static and dynamic blocks (as shown in Figure 3-25) to take into account temperature effects on the material magnetic behavior. Various outputs are available from the circuit simulation, like the BH loop shown in blue at the bottom right, as well as currents, voltages, losses, and temperatures shown on the top.

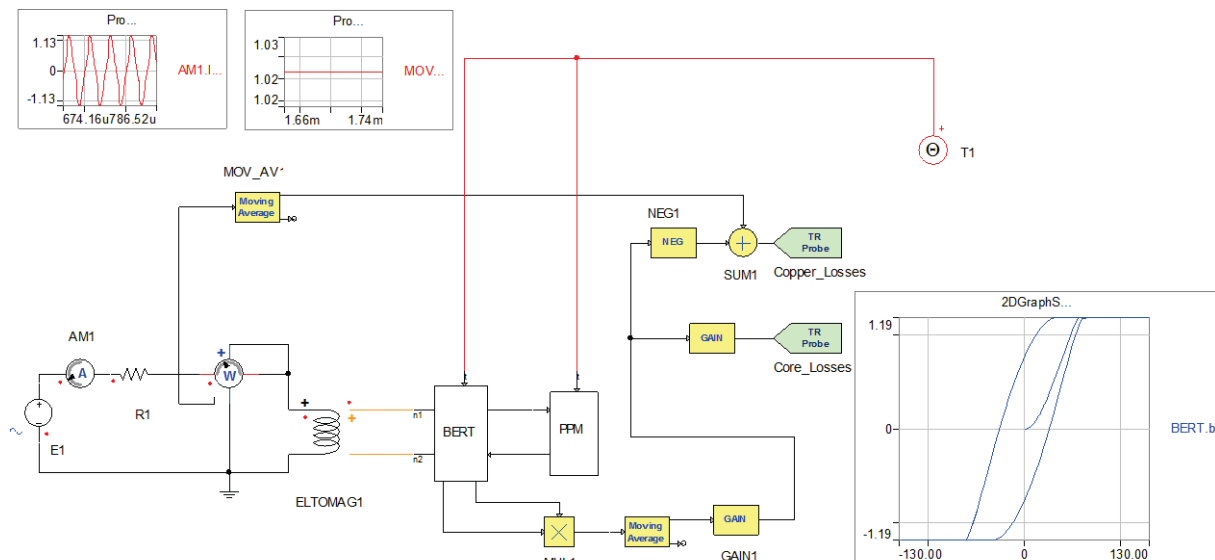


Figure 3-25 : Circuit simulation in Simplorer (schematic)

Results of circuit simulation are compared to measurements and are shown in Figure 3-26, Figure 3-27 and Figure 3-28.

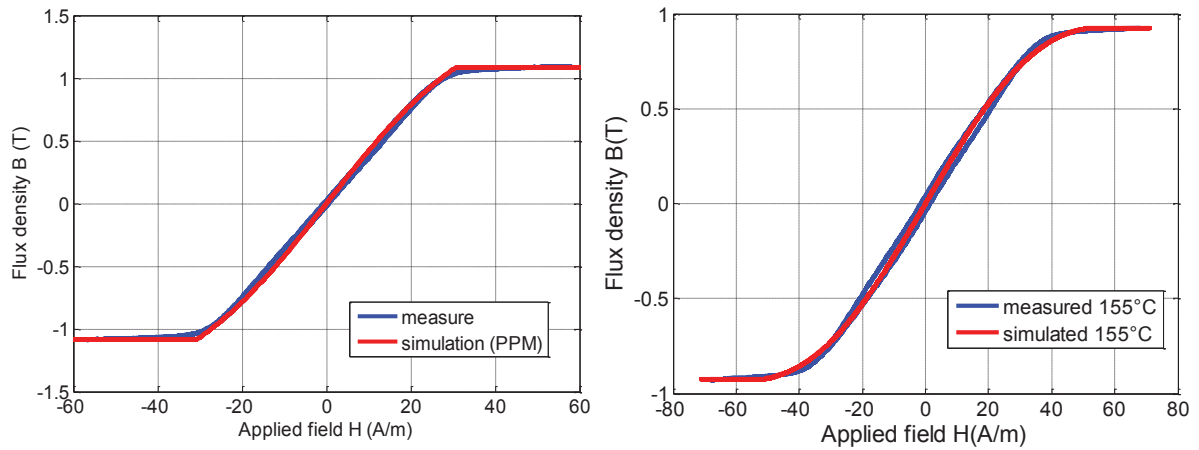


Figure 3-26: Measured and simulated static ($f = 1$ Hz) BH curves at $T = 25$ °C (left) and $T = 155$ °C (right)

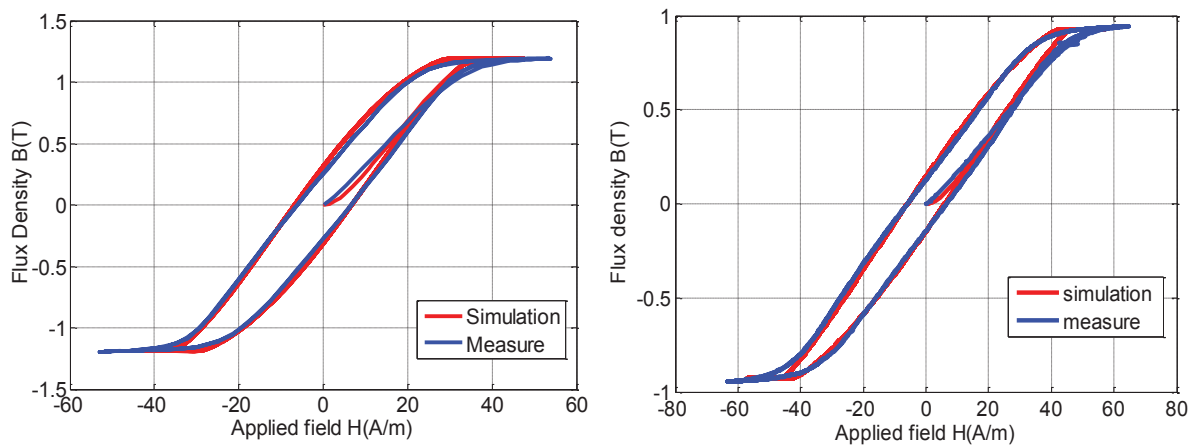


Figure 3-27: Measured and simulated dynamic ($f = 10$ kHz) BH curves at $T = 25$ °C (left) and $T = 155$ °C (right)

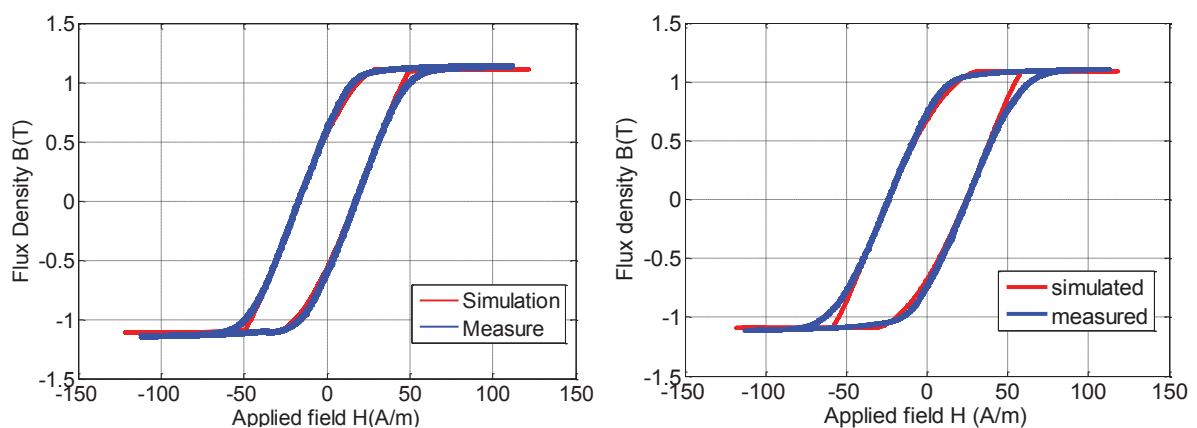


Figure 3-28: Measured and simulated dynamic BH curves at 20 kHz (left) and 40 kHz (right)

Figure 3-26 shows measured and simulated static loops at 25 °C (left) and 155 °C (right). Results indicate that the proposed static model, despite its simplicity, represents well the static behavior of the nanocrystalline material at both temperatures.

Figure 3-27 represents measured and simulated 10 kHz dynamic loops at 25 °C (left) and 155 °C (right). This shows a good correlation between the measured dynamic hysteresis loops and the simulated ones at both 25 °C and 155 °C.

To demonstrate the accuracy of the dynamic model, comparison between measured and simulated dynamic loops at 20 kHz and 40 kHz are shown in Figure 3-28. At both frequencies, the dynamic model represents accurately dynamic loops. Results are in good agreement.

Figure 3-29 summarize the results of simulated and measured minor loops at 25°C and 250°C for an applied flux density of 0.5T. Simulated and measured centered minor loops are in good agreement. We can notice that due to permeability decrease with temperature, a maximum magnetic field of 12 A/m and 25 A/m is reached at 25°C and 250°C respectively. Consequently the current flowing in the circuit at 250 °C is about double that the one flowing at 25 °C. This significant current increase may have negative effects on the circuit.

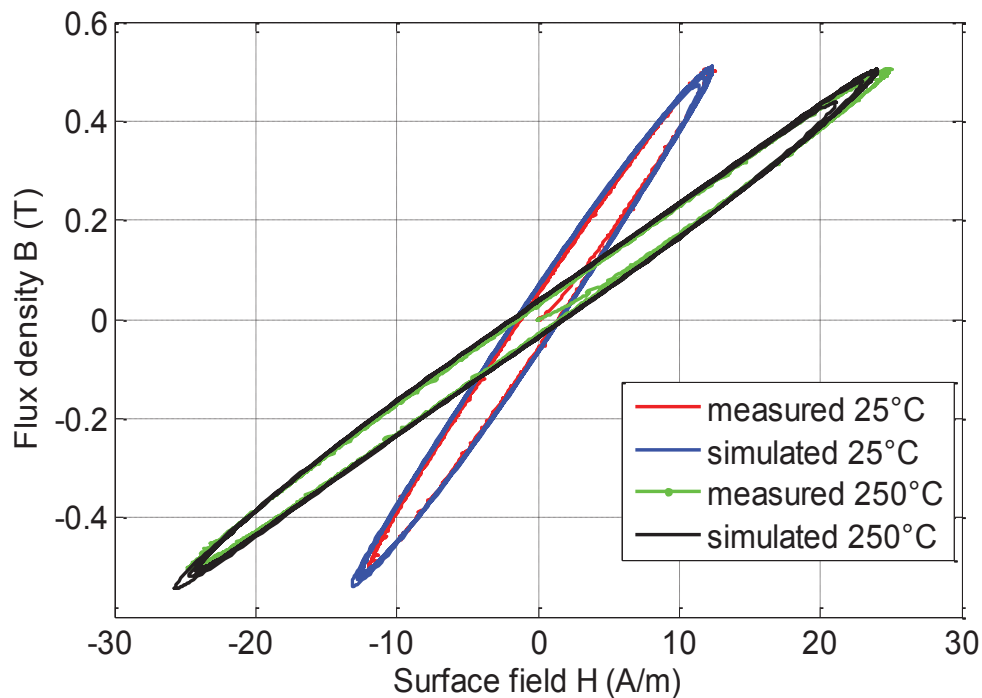


Figure 3-29: Measured and simulated field at 0.5T applied flux density at $f=10$ kHz.

In the aim of testing the magnetic component model reversibility and its accuracy for non-sinusoidal waveforms, a triangular magnetic flux density of 0.5 T is applied. Measured and simulated magnetic fields are compared. The results are presented in Figure 3-30 ensuring the model validity for a triangular waveform, triangular in particular. More details on this aspect are discussed in chapter 4 by the model implementation in a non-sinusoidal application (buck converter).

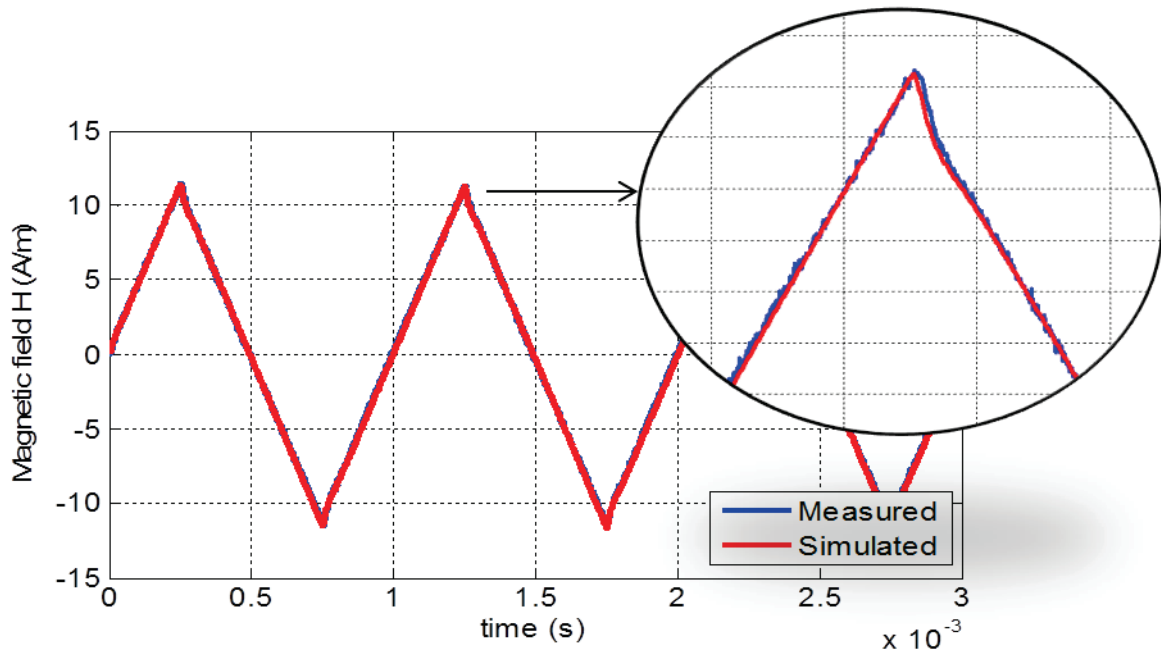


Figure 3-30: Measured and simulated magnetic fields for 0.5 T applied triangular flux density

To validate the thermal model and the magneto-thermal coupling in circuit simulation, the circuit shown in Figure 3-31 is simulated. This RL circuit includes both the magnetic component model and its corresponding thermal model. The coupling between magnetic and thermal models which allows taking into account self-heating conditions is clearly represented in the schematic. It is shown by the connection between magnetic block models and heat sources to compute the temperature rise caused by iron losses (forward). The connections between thermometers and magnetic block models allow injecting this temperature into the magnetic model to consider its effect on magnetic behavior (backward).

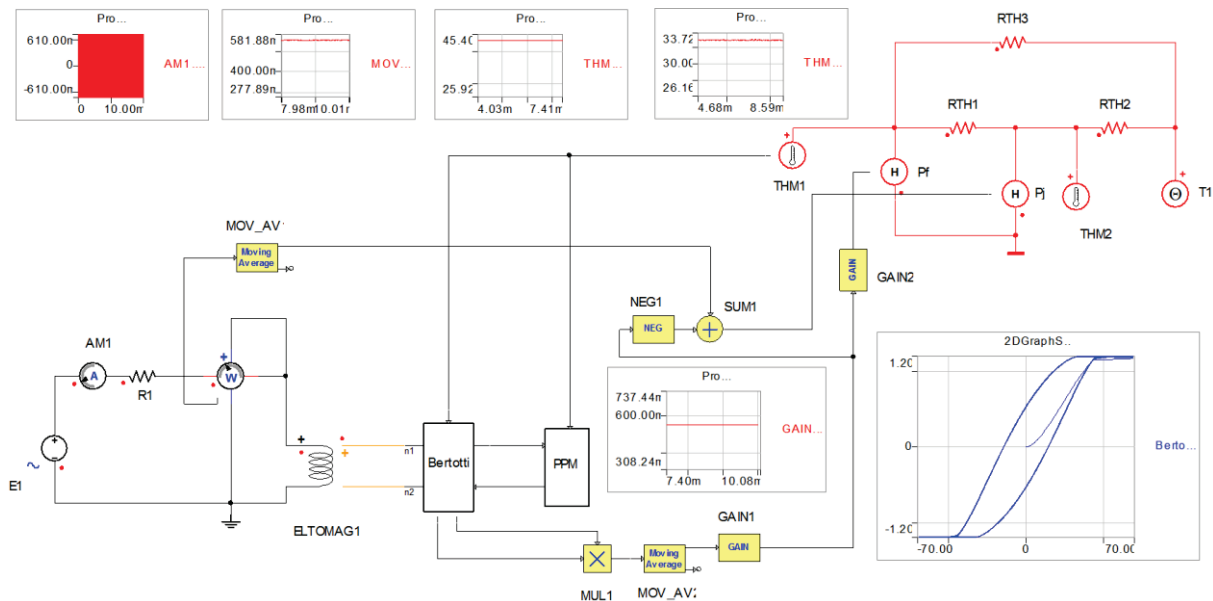


Figure 3-31 : Circuit simulation in Simplerer including thermal model

However before running circuit simulation, thermal model's parameters need to be defined. These parameters are identified from the thermal equivalent circuit equations (3.9) and (3.10) from temperature measurements at transient and steady states as explained in previous chapter. The values of these parameters for the modeled nanocrystalline core are represented in Table 4.

$$C_{th1} \frac{dT_c}{dt} = P_c - \frac{T_c - T_w}{R_{th1}} - \frac{T_c - T_a}{R_{th3}} \quad (3.9)$$

$$C_{th2} \frac{dT_w}{dt} = P_w - \frac{T_w - T_c}{R_{th1}} - \frac{T_w - T_a}{R_{th2}} \quad (3.10)$$

Thermal Parameters				
<i>RTH1</i>	<i>RTH2</i>	<i>RTH3</i>	<i>CTH1</i>	<i>CTH2</i>
96.8 °C/W	44.8 °C/W	70.4 °C/W	1.9 J/°C	1 J/°C

Table 4: Thermal parameters

The major heat transfer from the core material is by convection as stated in [25][26]. Due to the small dimensions of the core (thickness of 1.25 mm) and its ribbon structure, the temperature in the core is assumed to be homogenous. Thus no internal conduction is considered. To validate this assumption a thermal camera is used to verify the temperature distribution through the magnetic core. The thermal image represented in Figure 3-32 shows a constant temperature of 40.8 °C through the non-isolated part of the core in blue (the isolated part shown in brown is kept to avoid the collapse of the sample).

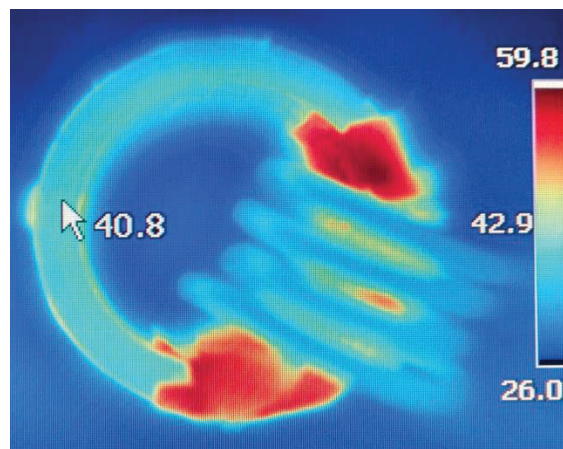


Figure 3-32: Thermal image of nanocrystalline core

The thermal parameters in Table 4 are identified from measurements. Moreover these values can be verified by calculation. Considering thermal convection heat transfer, the equivalent thermal resistance between the magnetic core and ambient can be calculated using thermal convection equations (3.12) and (3.12).

If the winding is neglected, the equivalent resistance of the thermal circuit R_{th} is also equal to $(R_{th1} + R_{th2}) // R_{th3}$. Taking the values of resistances identified from measurements R_{th} is found to be $47\text{ }^{\circ}\text{C}/\text{W}$ compared to $49\text{ }^{\circ}\text{C}/\text{W}$ value found by calculation (3.12)

$$P = h \cdot A \cdot \Delta T \quad (3.11)$$

$$\Rightarrow R_{th} = \frac{\Delta T}{P} = \frac{1}{h \cdot A} = 49.4\text{ }^{\circ}\text{C}/\text{W} \quad (3.12)$$

Where h and A are defined as follows by equations (3.13) and (3.14) while all equations parameters are presented in Figure 3-33.

$$h = k \cdot \left(\frac{\Delta T}{d} \right)^{0.25} = 45.828\text{ W}/\text{m}^2 \cdot ^{\circ}\text{C} \quad (3.13)$$

$$A = 2\pi \cdot d \cdot (R + r) + 2\pi \cdot (R^2 + r^2) = 441.8\text{ mm}^2 \quad (3.14)$$

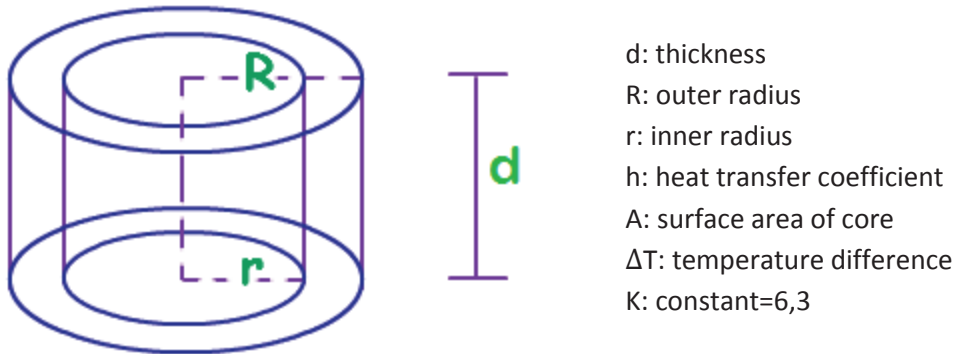


Figure 3-33: Core geometric parameters

The thermal model is then validated by comparing both measured core and winding temperatures to simulated ones for 20 kHz and 40 kHz. Results in Figure 3-34 show a good agreement between measured and simulated temperatures evolution as a function of time. Therefore the proposed thermal model describes completely the self-heating of the magnetic component in both transient and steady states. The core temperature exceeds $70\text{ }^{\circ}\text{C}$ for an applied 0.6 A - 40 kHz sinusoidal current. This temperature has non negligible effects on magnetic behavior which is taken into account thanks to the thermal model.

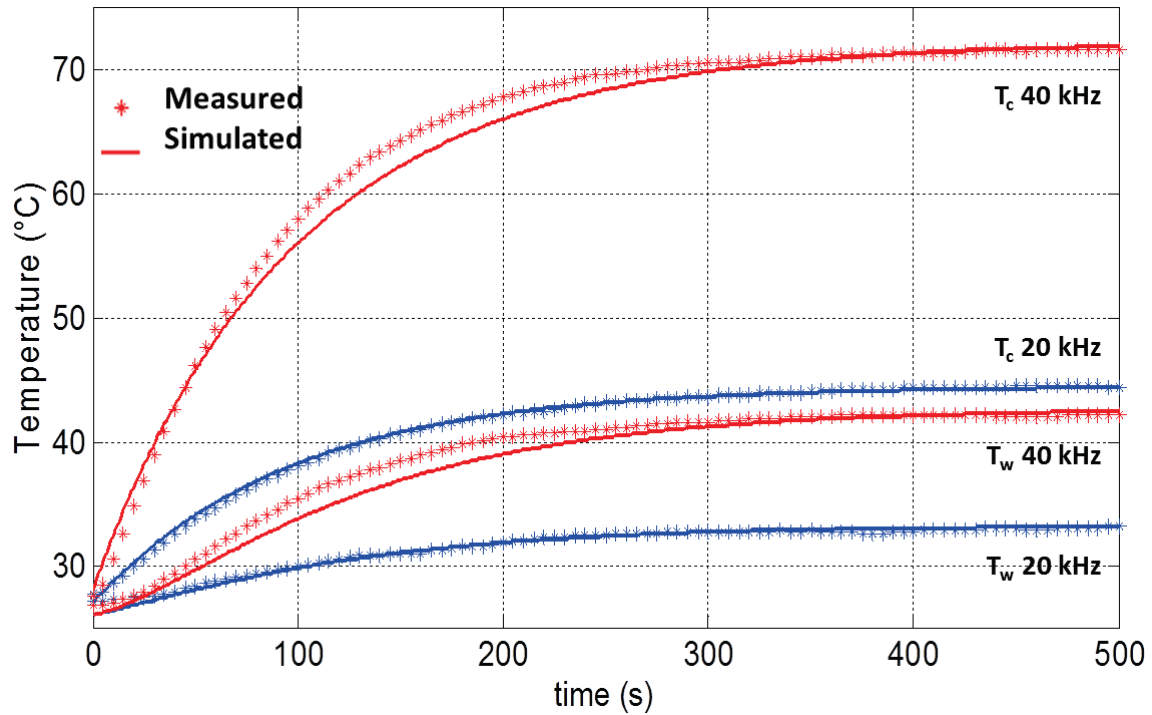


Figure 3-34: Measured and simulated core (T_c) and winding (T_w) temperatures.

3.5 Conclusion

In this chapter modeling techniques, VHDL-AMS modeling language and Simplorer circuit simulation software are detailed. The modular structure and the development of a temperature dependent magnetic component model and its implementation in the circuit simulation software “Simplorer” are presented. The approach is validated for a nanocrystalline material by choosing the appropriate static and dynamic laws and comparing measured and simulated B-H curves. Results are in a good agreement. Sinusoidal and non-sinusoidal (triangular) waveforms are tested. A thermal model is also presented and coupled with the magnetic model to take into account static and dynamic thermal effects.

The work on other materials and the magnetic component model implementation in power electronic application are presented in next chapter. The next chapter investigates the magnetic component behavior in a buck converter. Two core inductors, different frequencies and flux densities, DC bias and Temperatures effects are studied. Advantages of the model with respect to analytical losses formulas, as well as its limitations are discussed.

3.6 References

- [1] J. Biela, J. W. Kolar, A. Stupar, U. Drofenik, and A. Muesing, "Towards Virtual Prototyping and Comprehensive Multi-Objective Optimisation in Power Electronics," in *Power Conversion and Intelligent Motion Conference Europe, Nuremberg, Germany, May 4-6, 2010*, 2010.
- [2] Q. M. Li, F. C. Lee, and T. G. Wilson, "Design verification and testing of power supply system by using virtual prototype," *IEEE Trans. Power Electron.*, vol. 18, pp. 733–739, 2003.
- [3] F. Belloni and M. Riva, "Dynamic virtual test of power electronics converters," *2007 IEEE Instrum. Meas. Technol. Conf. IMTC 2007*, 2007.
- [4] P. G. Blanken, "A lumped winding model for use in transformer models for circuit simulation," *IEEE Trans. Power Electron.*, vol. 16, pp. 445–461, 2001.
- [5] C. Yue, V. M. Agostinelli, G. M. Yeric, and A. F. Tash, "Improved universal MOSFET electron mobility degradation models for circuit simulation," *IEEE Trans. Comput. Des. Integr. Circuits Syst.*, vol. 12, pp. 1542–1546, 1993.
- [6] F. Sixdenier, M. A. Raulet, R. Marion, R. Goyet, G. Clerc, and F. Allab, "Dynamical models for eddy current in ferromagnetic cores introduced in an FE-tuned magnetic equivalent circuit of an electromagnetic relay," *IEEE Trans. Magn.*, vol. 44, pp. 866–869, 2008.
- [7] Z. Jakopovic, V. Sunde, and Z. Bencic, "Electrothermal modeling and simulation with SIMPLORER," *IEEE Int. Conf. Ind. Technol. 2003*, vol. 2, 2003.
- [8] X. Li, S. Kher, and S. Lin, "Multi-domain system level behavioral hev library using VHDL-AMS," in *2013 IEEE International Electric Vehicle Conference, IEVC 2013*, 2013.
- [9] S. P. Levitan, J. A. Martinez, T. P. Kurzweg, A. J. Davare, M. Kahrs, M. Bails, and D. M. Chiarulli, "System simulation of mixed-signal multi-domain microsystems with piecewise linear models," *IEEE Trans. Comput. Des. Integr. Circuits Syst.*, vol. 22, pp. 139–154, 2003.
- [10] G. G. E. Gielen and R. a. Rutenbar, "Computer-aided design of analog and mixed-signal integratedncircuits," *Proc. IEEE*, vol. 88, pp. 1825–1852, 2000.
- [11] A. Vachoux, C. Grimm, and K. Einwich, "Analog and mixed signal modelling with SystemC-AMS," *Proc. 2003 Int. Symp. Circuits Syst. 2003. ISCAS '03.*, vol. 3, 2003.
- [12] E. Christen and K. Bakalar, "VHDL-AMS - a hardware description language for analog and mixed-signal applications," *IEEE Trans. Circuits Syst. II Analog Digit. Signal Process.*, vol. 46, pp. 1263–1272, 1999.
- [13] D. Damon and E. Christen, "Introduction to VHDL-AMS. 1. Structural and discrete time concepts," *Proc. Jt. Conf. Control Appl. Intell. Control Comput. Aided Control Syst. Des.*, 1996.
- [14] P. V. Nikitin and C. J. R. Shi, "VHDL-AMS based modeling and simulation of mixed-technology microsystems: a tutorial," *Integr. VLSI J.*, vol. 40, pp. 261–273, 2007.
- [15] K. S. Kundert and P. Foreword By-Gray, *The designer's guide to SPICE and Spectre*. Kluwer Academic Publishers, 1995.

- [16] “www.ansys.com › Products Overview › Electromagnetics.” .
- [17] G. Bertotti, “General properties of power losses in Soft ferromagnetic Materials.” 1988.
- [18] C. Thibaut, “Caractérisation et modélisation de matériaux magnétiques en hautes températures en vue d’une application au filtrage CEM,” UNIVERSITE CLAUDE BERNARD LYON 1, 2011.
- [19] R. Marion, “Contribution à la modélisation du magnétisme statique et dynamique pour le génie électrique,” Université de Lyon, 2010.
- [20] A. Raghunathan, Y. Melikhov, J. E. Snyder, and D. C. Jiles, “Modeling the temperature dependence of hysteresis based on jiles-atherton theory,” in *IEEE Transactions on Magnetics*, 2009, vol. 45, pp. 3954–3957.
- [21] M. Raulet and F. Sixdenier, “Limits and rules of use of a dynamic flux tube model,” ... *Comput. ...*, pp. 2–6, 2008.
- [22] T. Chailloux, M. Raulet, C. Martin, C. Joubert, F. Sixdenier, L. Morel, “Magnetic Behavior Representation Taking Into Account the Temperature of a Magnetic Nanocrystalline Material,” *IEEE Transactions on Magnetics* vol. 48, no. 2, pp. 455–458, 2012.
- [23] N. Bowler and Y. Huang, “Electrical conductivity measurement of metal plates using broadband eddy-current and four-point methods,” *Meas. Sci. Technol.*, vol. 16, no. 11, p. 2193, 2005.
- [24] L. S. Mazov, “High-field evidence for the Bloch-Gruneisen curve in the cuprates,” *Phys. Rev. B*, vol. 70, no. 5, p. 54501, 2004.
- [25] E. C. Snelling, “*Soft Ferrites: Application and Properties*”, 2nd edition. Butterworths, 1988.
- [26] P. R. Wilson, S. Member, J. N. Ross, A. D. Brown, and S. Member, “Simulation of Magnetic Component Models in Electric Circuits Including Dynamic Thermal Effects,” vol. 17, no. 1, pp. 55–65, 2002.

Chapter 4

4. Power Electronics Application

4.1 Introduction

In power electronics applications, magnetic components are often subjected to non-sinusoidal waveforms, variable frequencies and DC bias conditions. These operating conditions generate different losses in the core compared to sinusoidal losses provided by materials manufacturers [1], [2]. In the design stage, lack of precise losses diagnosis has unacceptable effects on system's efficiency, reliability and power consumption. Based on accurate components models, virtual prototyping is used to predict and improve system's behavior before realization.

DC-DC power converters are a good example of such system where electrical power need to be "efficiently" stepped up or down from a DC voltage level to another. Passive components especially magnetic ones play a key role in power converters [3], thus behavior and loss analysis of these components is essential [4]–[6]. Since magnetic core losses calculation is a delicate subject, analytical equations as Steinmetz (SE) [7] fail to precisely compute core losses due to limitation to sinusoidal excitation. Other improved formulas of SE like MSE [8], GSE [9], iGSE [10] and i2GSE [11] give better results but still limited due to their parameters variation as function of waveform, frequency and DC bias.

In this chapter the developed magnetic component model is tested for two different core inductors in a widely used power converter application, the buck converter, to ensure non-conventional excitation (square voltage with DC bias). Waveforms and losses of both powder and nanocrystalline cores inductors are simulated and compared to measured ones. The model is validated for different ripple currents, different loads and a relatively wide frequency range (10-100 kHz). DC bias is taken into account in both continuous and discontinuous conduction modes. Temperature effects on core losses for the nanocrystalline core inductor are also studied.

4.2 Buck Converter

The three basic DC-DC switching power supply topologies in common use are the buck, boost, and buck-boost. The power supply topology refers to how the switches, output inductor, and output capacitor are connected. Each topology has unique properties. The three basic converters use a pair of switches, usually one controlled (MOSFET for example) and one uncontrolled (diode), to achieve power flow from input to output. The converters also use one capacitor and one inductor to store and transfer energy from input to output and filter or smooth voltage and current.

The most common power converter topology is the buck converter, or so called a step-down power converter. It is a non-isolated SMPS (Switched Mode Power Supply) topology widely used throughout the industry to convert a higher input voltage into a lower output voltage. A simplified schematic of a buck converter is shown in Figure 4-1.

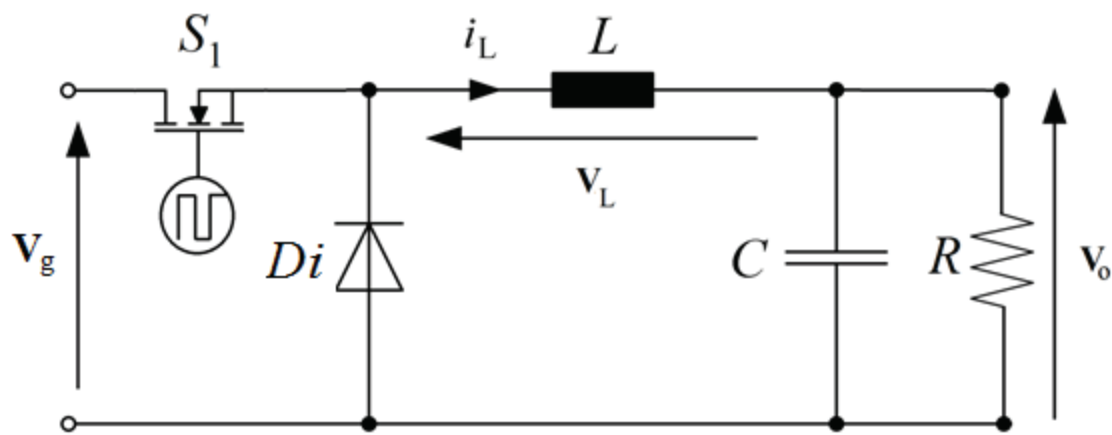


Figure 4-1: Buck converter circuit

The buck converter can have two distinct modes of operation: Continuous Conduction Mode (CCM) and Discontinuous Conduction Mode (DCM). Continuous inductor current mode is characterized by current flowing continuously in the inductor during the entire switching cycle in steady state operation. Discontinuous inductor current mode is characterized by the inductor current being zero for a portion of the switching cycle.

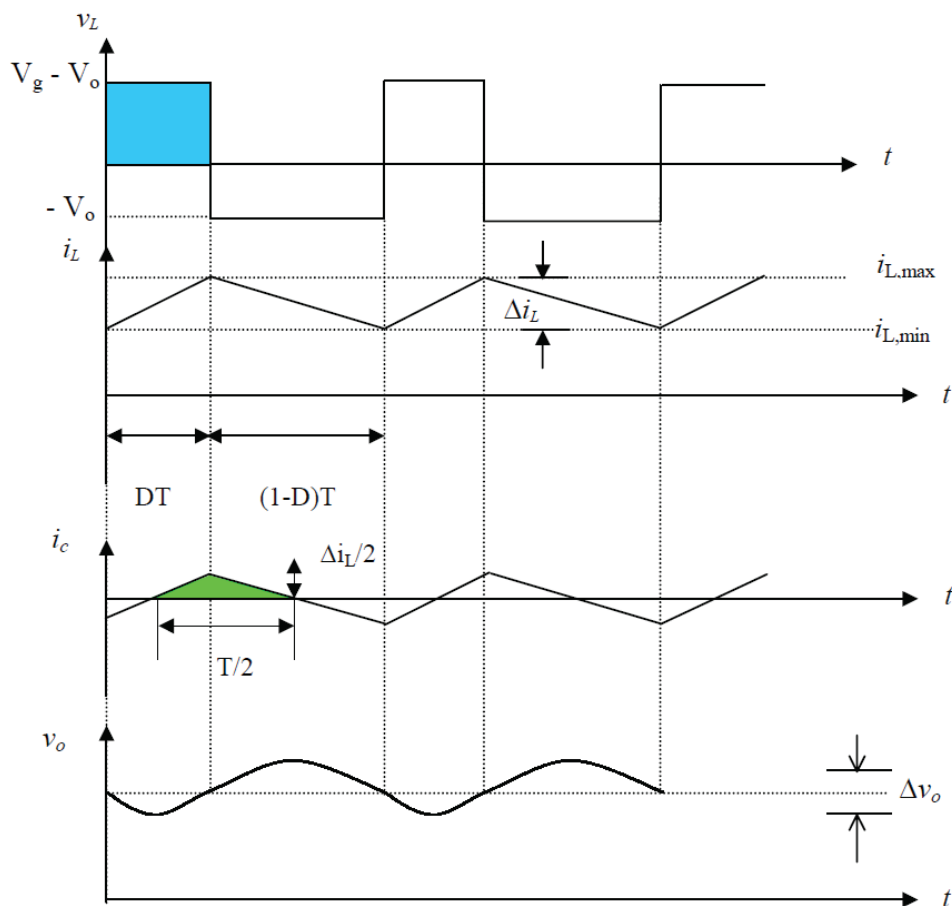


Figure 4-2: Buck voltages and currents waveforms

In continuous conduction mode, the buck converter assumes two states per switching cycle. The ON state is when the switch SI is ON and Diode Di is OFF. The OFF state is when switch SI is OFF and Diode Di is ON. When the switch is ON for a time duration DT , the switch conducts the inductor current and the diode becomes reverse biased. This results in a positive voltage $v_L(t) = v_{in}(t) - v_o(t)$ across the inductor. This voltage causes a linear increase in the inductor current i_L . When the switch is turned OFF, because of the inductive energy storage, i_L continues to flow. This current now flows through the diode, and $v_L(t) = -v_o(t)$ for a time duration $(1-D)T$ until the switch is turned on again (illustrated in Figure 4-2).

In this mode at steady state operation, the average inductor current I_L and ripple current Δi_L are calculated using (4.1) and (4.2) respectively

$$I_L = I_o = \frac{V_o}{R} \quad (4.1)$$

$$\Delta i_L = \frac{1}{L} \int_0^{t_{on}} v_L(t) dt = \frac{1}{L} (V_g - V_o) \times DT \quad (4.2)$$

The average output voltage V_o and the peak-peak output voltage ripple, Δv_o are calculated using (4.3) and (4.4) respectively.

The average inductor voltage over one period is zero:

$$\begin{aligned} \int_0^T v_L(t) dt &= \int_0^{t_{on}} v_L(t) dt + \int_0^{t_{off}} v_L(t) dt = 0 \\ (V_g - V_o) \times DT + (-V_o) \times (1-D)T &= 0 \\ \Rightarrow V_o &= DV_g \end{aligned} \quad (4.3)$$

And the ripple voltage is obtained from the capacitor current

$$\Delta v_o = \Delta v_C = \frac{1}{C} \int i_C(t) dt = \frac{\Delta i_L}{8fC} \quad (4.4)$$

A power stage operating in discontinuous conduction mode has three states during each switching cycle as opposed to two states for continuous conduction mode, both shown in Figure 4-3. The current starts at zero, reaches a peak value, and returns to zero during each switching cycle. It is very desirable for a power converter to stay in only one mode over its expected operating conditions, because the power converter frequency response changes significantly between the two modes of operation. Also, the input to output relationship for the discontinuous mode is quite different from that shown in equation (4.3) for the continuous mode.

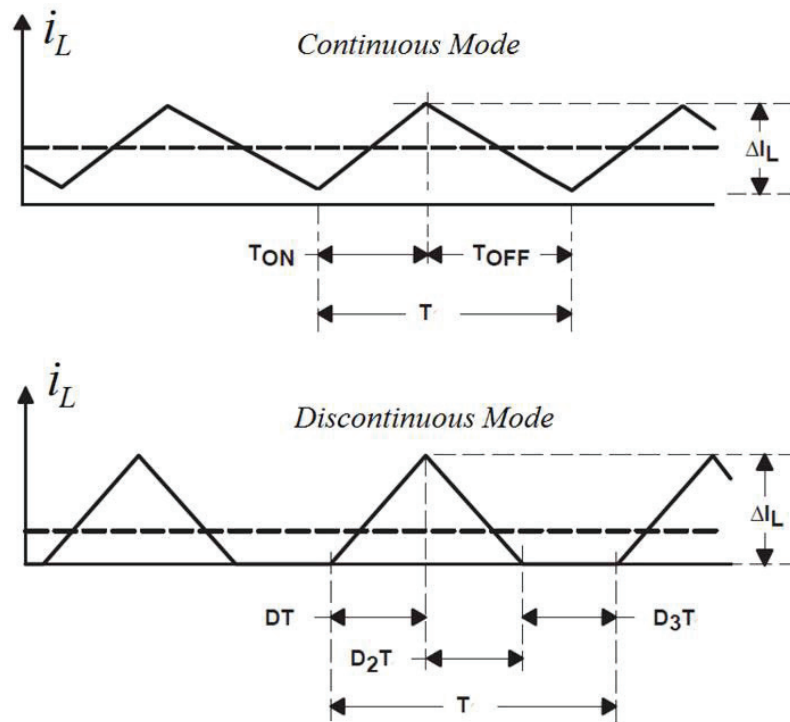


Figure 4-3: Continuous and Discontinuous Conduction modes

It is clear from the previous review on buck topology that inductors are important components in power converters. They are found in most power applications too. For each point of load application a specific design of these components is required.

In buck converter a PWM voltage is applied on the inductor and a DC bias depending on the load exists. This induces different losses compared to those provided by manufacturers based on sinusoidal flux density [12]. DC bias has also a significant effect on losses [13]. This would create a non-centered minor hysteresis loop. As a consequence core loss prediction becomes complex, and precise magnetic modeling is required. For these reasons the buck converter application is chosen to test the model under different operating conditions. Considering a buck converter circuit, the magnetic component model would replace the inductor as shown in Figure 4-4.

To validate the developed model, a special buck converter circuit is needed for measurements. This circuit must adapt to different voltages, frequencies and loads measurements. Inductor used in the circuit must be easily replaced too. Also, different connectors are necessary to measure voltages, currents and losses. The realized circuit and these measurements are discussed in the next section.

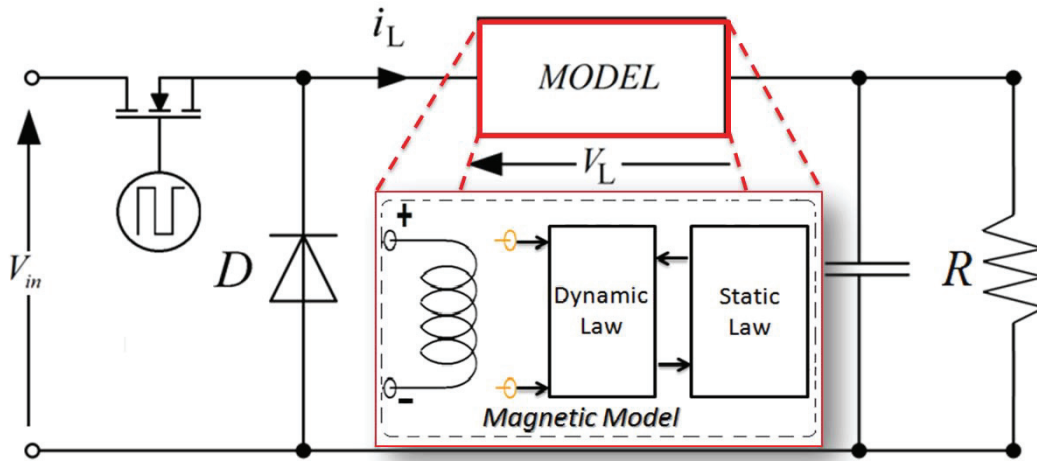


Figure 4-4: Buck converter circuit including the magnetic component model

4.3 Realized Circuit and Measurements

4.3.1 Buck Converter Circuit

In order to investigate magnetic component behavior in power applications, a 40 W buck converter is realized. The circuit design shown in Figure 4-5 allows different voltage levels and different frequencies by choosing the appropriate characteristics and power ratings of the MOSFET and the freewheeling diode. Inductors with 30 turns copper wire are used in the circuit and can be easily replaced by adding interchangeable connectors. Dedicated oscilloscope connectors are also added to the circuit to avoid measurement error and noise.

To measure precisely magnetic losses, a small shunt (200 mΩ) is added in series with the inductor and secondary turns are wound to the same core. The shunt allows precise current measurements, while open secondary side allows voltage measurement excluding coil losses. Iron losses calculations from primary current and secondary voltage are explained later in this chapter.

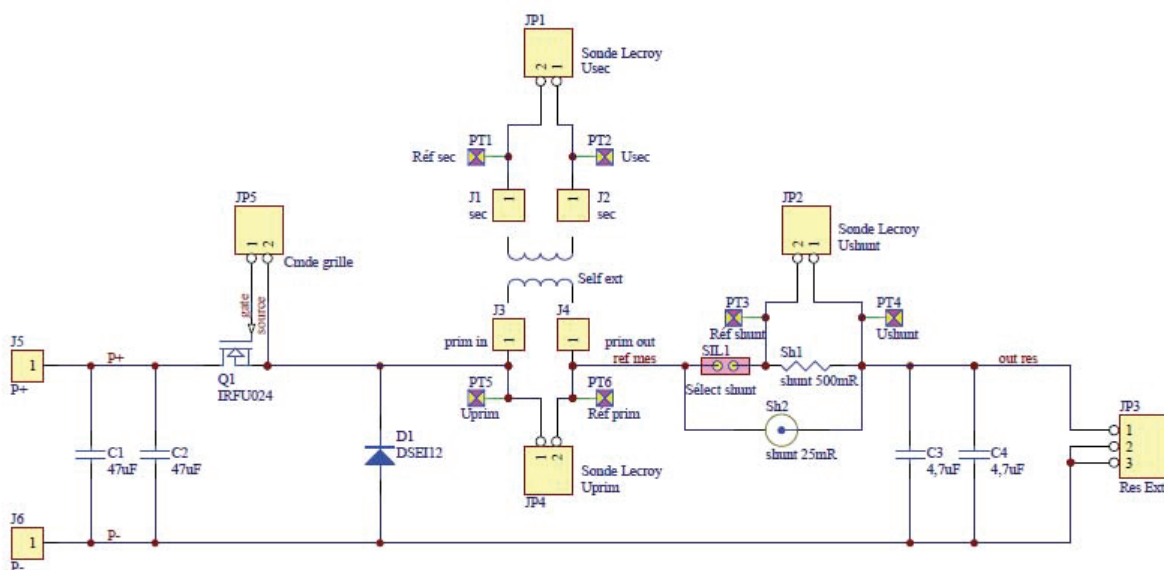


Figure 4-5: Circuit design of buck circuit

To study DC bias effects on magnetic losses, a set of 5 load circuits, consisting of ceramic cased power resistors, are used to vary DC current in the buck circuit. These resistive loads having values of 2, 3, 4.4, 5, and 6 ohms can be replaced using interchangeable connectors added to the buck circuit as shown below. The PCB layouts and realized circuits of both the buck and resistive loads are shown in Figure 4-6.

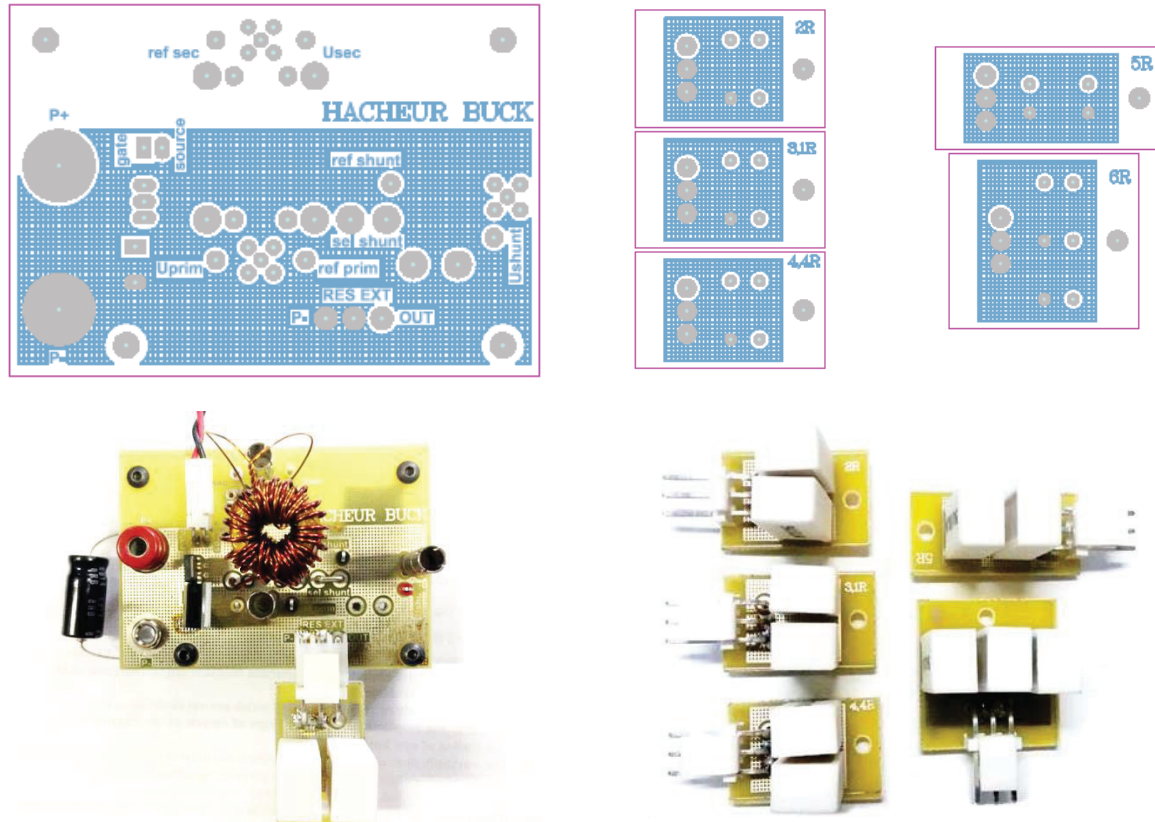


Figure 4-6: PCB layouts of buck and load circuits

The MOSFET is driven with an optically isolated gate driver circuit controlled by a function generator. This allows stable driving voltages with lower noise in addition to isolation. The buck and driver circuit are shown in Figure 4-7.

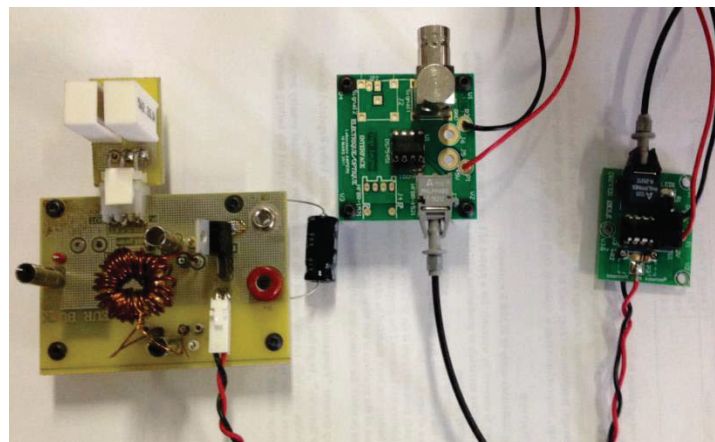


Figure 4-7: Buck with optically isolated gate driver circuit

4.3.2 Choice of Inductors and Magnetic Materials Characterization

Two toroid inductors cores (Figure 4-8) are chosen to be used in the buck converter application: A low permeability nanocrystalline core K44B200 provided by MECAGIS and a powder core HKBH Sendust provided by TOHO ZINK. The low permeability (down to $\mu_r=200$) nanocrystalline is a recent material resulting from magnetic field annealing or stress annealing of amorphous [14]. This material possesses high saturation induction, low losses and very good linearity. The Sendust (Fe-Si-Al) powder materials invented in Japan have relatively low cost and are used in commercial converters [15]. They are known for their low losses and stable performance with temperature. Characteristics of both inductors are presented in table 5.



Figure 4-8: Chosen Nanocrystalline and Powder cores inductors (including secondary windings)

Properties of Chosen Materials			
	<i>HKBH</i>	<i>NANO</i>	
Dext (mm)	10	16	
Dint (mm)	4,6	10	
S (mm ²)	9,45	18 (14 effective)	
lm (mm)	23	40	
N1	30	30	
N2	3	3	
μ_r	100	200	
Bs (T)	0,6	1,2	

Table 5: Properties of chosen inductors

The chosen materials are characterized before usage in application. Static and dynamic measurements are performed on test transformers of both nanocrystalline and powder cores. As in the case of previous characterized material, a sinusoidal current is applied to the primary winding, to create a magnetic field H and the flux density is calculated from the measured secondary voltage. Measurement results of the powder material are shown in Figure 4-9, while those of the nanocrystalline material are shown in Figure 4-10.

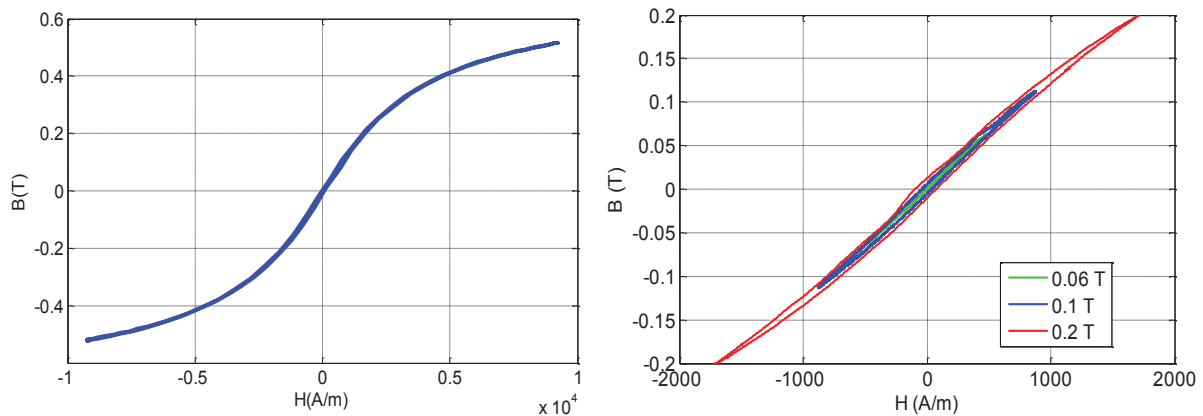


Figure 4-9: Static and dynamic characterization of the powder magnetic material (HKBH)

Figure 4-9 shows a major static loop on the left, having a reversible behavior and a relatively low coercive field. The thin static loop of the powder core has a polynomial behavior, but not a piecewise one. Figure 4-9 also shows 3 dynamic minor hysteresis loops at 30 kHz for 60, 100 and 200 mT applied flux densities. At this frequency hysteresis loops are wider than static ones. Loops enlargement is also function of applied flux density as we can notice dynamic loops area increase with applied flux density.

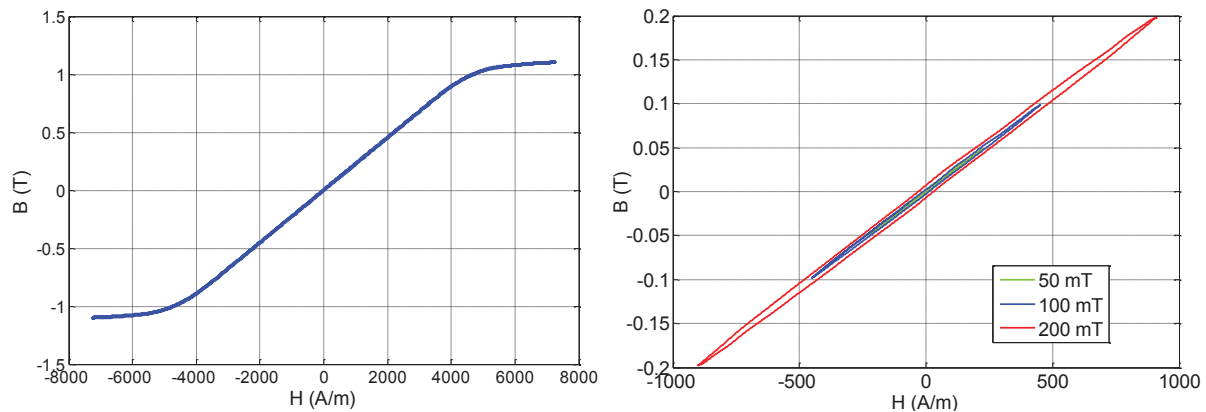


Figure 4-10: Static and dynamic characterization of the Nanocrystalline magnetic material (K44B200)

Figure 4-10 shows the major static loop (left) of the nanocrystalline material, having a reversible behavior and very low coercive field too. This static loop has a piecewise polynomial behavior, similar to that of high permeability N14E1 previously characterized. The 3 dynamic minor hysteresis loops measured at 30 kHz for 50, 100 and 200 mT applied flux densities are also shown in Figure 4-10 (right). The dynamic behavior for this nanocrystalline material is similar to that of the powder core, except the very good linearity signifying a better DC bias performance.

The dynamic loop area increase with applied flux density manifests by the increase of the wall motion parameter α (second parameter of the dynamic model). The parameter α , (extracted from mathematical fitting of the measured B-H loops to Bertotti's equation), variation could be due to increase of number of active magnetic objects (MO) with external field. Tracing the wall motion parameter α variation as a function of flux density level we find a linear variation for both powder and nanocrystalline materials as shown in Figure 4-11. Interpolation of α is inserted in the model to estimate iron losses at different flux density levels.

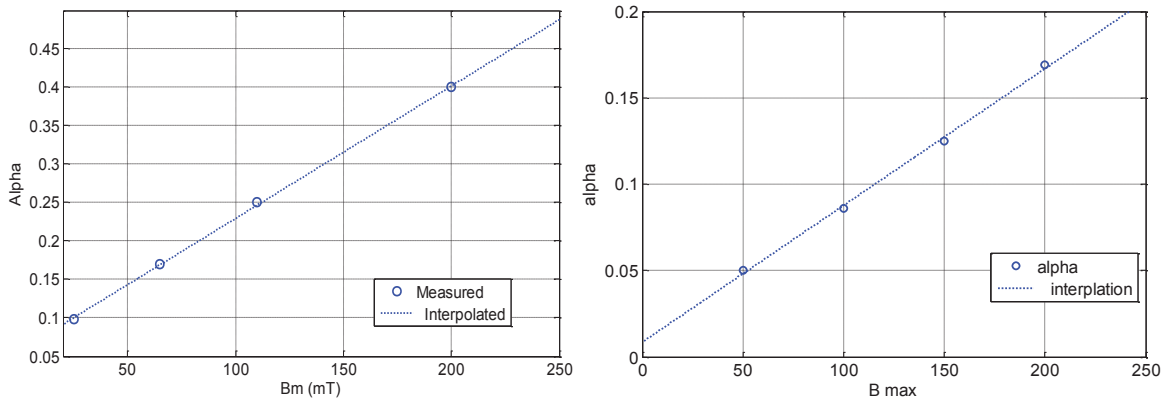


Figure 4-11: Parameter α variation with maximum flux density level for HKBH (left) and K44B200 (right)

The static and dynamic measurements permit the identification of models parameters similar to the procedure done for the N14E1 material in chapter 3. The only difference is that for powder cores the dynamic coefficient γ is proportional to the particle average size of powder constituting the core and is calculated according to [16]. For powder cores γ is calculated using equation 4.5, while equation 4.6 is used for nanocrystalline cores. Where σ_p is the material's conductivity and r_p is the average radius of powder particles (Annex C).

$$\text{Powder cores} \quad \gamma = \frac{\sigma_p r_p^2}{8} \quad (4.5)$$

$$\text{Nanocrystalline Cores} \quad \gamma = \frac{\sigma d^2}{12} \quad (4.6)$$

For both materials a polynomial of 5th order is considered for static model. The resulting static parameters are presented in table 6.

Static Parameters				
	P_1	P_3	P_5	H_b
HKBH	1.3096e-04	-3.5058e-12	6.4788e-20	9000
NANO	2.4038e-04	-1.444e-12	-5.12e-21	6000

Table 6: static parameters

4.3.3 Core Losses Measurements and Calculation

Core losses are calculated from both primary current and secondary voltage measurements. These measurements are performed by a 1.5 – 6 GHz bandwidth, 40 GS/s LECROY WavePro 7 Zi-A oscilloscope [17]. Knowing the primary current and secondary voltage, core losses are calculated using (4.7).

$$P = \frac{1}{T} \int_0^T \frac{N_1}{N_2} v_2(t) \cdot i_1(t) \cdot dt \quad (4.7)$$

4.3.3.1 Different waveforms

As mentioned before, losses under sinusoidal and non-sinusoidal excitation are not the same. To demonstrate that, Figure 4-12 presents losses measured in the powder core under sinusoidal and square voltage excitations. These measurements are carried out under a constant level magnetic flux density (100 mT) and for a frequency range between 40 and 100 kHz. Then datasheet losses are calculated using Steinmetz equation and parameters both provided by the constructor [18].

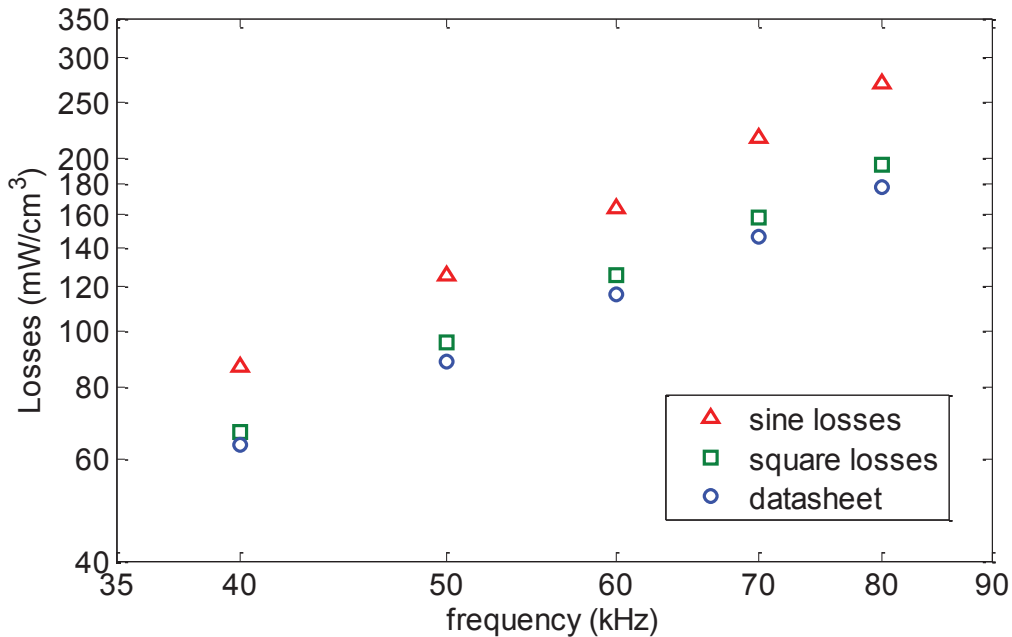


Figure 4-12: Measured sine and square losses and datasheet losses at B = 100 mT.

The data sheet losses calculated using the square waveform parameters provided by the manufacturer correspond to the measured ones. We can notice that these square losses at 50% duty cycle are lower than sine losses. However, for extreme duty cycles, square losses become higher than sine losses. This is due to the fact that losses are function of magnetic induction time derivative. Using sine losses for materials excited by other waveforms or vice versa is quite a drawback for systems design, regarding efficiency and power consumption.

4.3.3.2 Variable Induction and Variable Frequency

Furthermore core losses are function of applied induction level. For a given core cross-section and given number of turns, the applied induction is proportional to voltage over frequency ratio (V/f). Varying the input voltage of the buck converter at each frequency (in the 40 to 100 kHz frequency range), the core losses are measured for different induction levels (100, 150 and 200 mT). Results are shown in Figure 4-13.

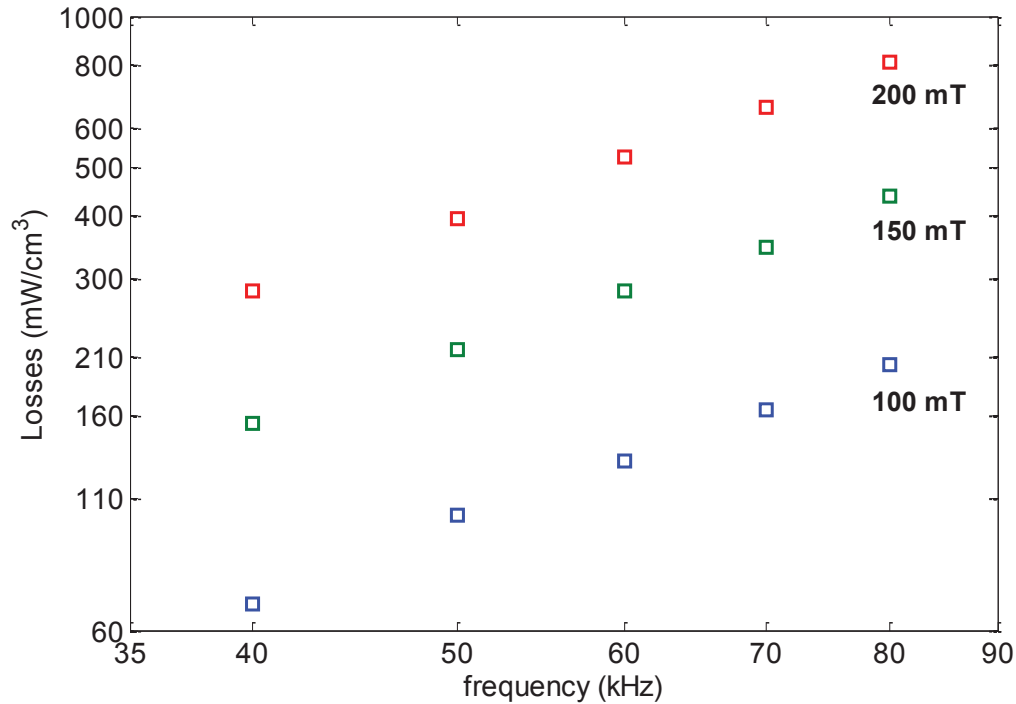


Figure 4-13: Measured core losses at different flux density levels in buck application

Figure 4-13 shows the core losses per unit volume in the powder core as function of frequency (log –log) at three induction levels, 100 mT in blue, 150 mT in green and 200 mT in red. Besides the increase of losses with frequency at a constant slope, clearly core losses increase with the applied induction level. We can notice that for a double induction level, losses are more than 4 times higher. The induction levels are chosen high enough to maintain the continuous conduction mode (CCM) of the buck converter. Thus Figure 4-13 shows results in CC mode only. Losses in discontinuous conduction mode (DCM) are discussed below.

4.3.3.3 Variable Load

To study DC bias effects on powder core magnetic losses, the realized set of 5 load circuits, consisting of ceramic cased power resistors, are used to vary DC current in the buck circuit. These resistive loads having values of 2, 3, 4.4, 5, and 6 ohms are connected and iron losses are measured simultaneously. Measurements done under fixed 5 V input voltage and 25 kHz frequency are shown in Figure 4-14. The low input voltage (5 V) is chosen to maintain low currents in order to pass from CCM to DCM. Similarly the choice of frequency (25 kHz) is to serve this purpose too since lower frequency means higher ripple current.

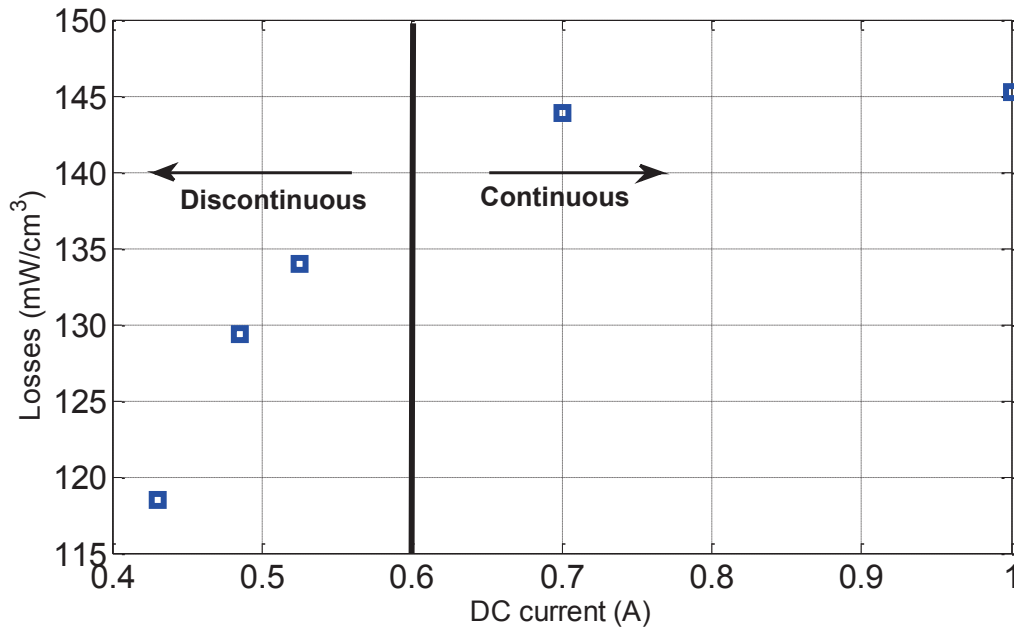


Figure 4-14: Measured core losses for variable load currents

On the one hand, for DC currents higher than 600 mA the inductor is in continuous current mode. The DC bias effect here is insignificant due to low hysteresis losses in the powder core material and a slight change in the DC current. This effect is explained in Figure 4-15: applying the same ΔB of 0.2T at 2 different DC levels B_{DC1} and B_{DC2} give two different ΔH values, and then two minor hysteresis loops with different areas. On the other hand, for DC currents lower than 600 mA the inductor operates in discontinuous conduction mode. In this case we still have the same flux density derivative (as voltage and frequency are the same) but with smaller ΔB and ΔH corresponding to the smaller ripple current ΔI (due to discontinuity). As a result we generate smaller minor B-H loops and thus lower losses. We can observe the losses decrease with DC current decrease.

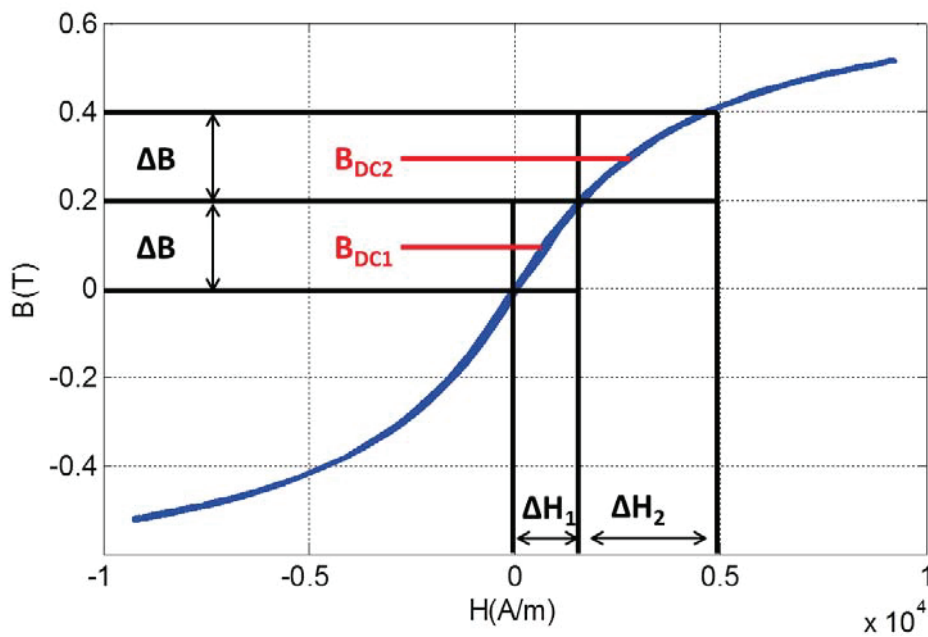


Figure 4-15: Effect of variable DC bias

Basically in the buck converter, a square voltage is applied on the inductor, creating a triangular magnetic induction B (the integral of square wave). This results a triangular magnetic field H (in the case of small signal and low hysteresis) in the core material which in turn induces the current in the winding of the inductor. In that case a normal asymmetric minor hysteresis loop is created as shown in Figure 4-16. As we change the load current I_{DC} and as long as we stay in continuous mode, H_{DC} will change linearly according to equation (4.8). Consequently B_{DC} will change but ΔB will not, neither do dB/dt , since voltage waveform, frequency and amplitude are kept the same.

$$H_{DC} = \frac{N}{l} \cdot I_{DC} \quad (4.8)$$

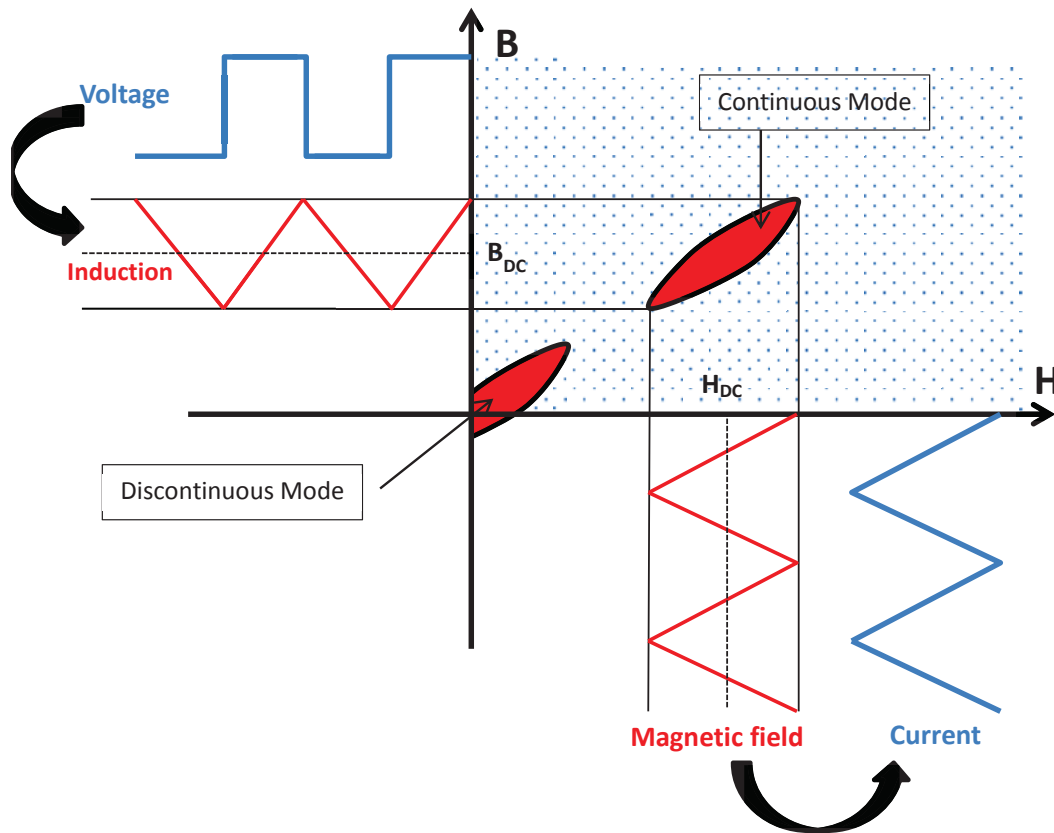


Figure 4-16: Minor loops in continuous and discontinuous conduction modes

Whereas when decreasing the DC current to a value less than $\Delta I/2$, we enter the discontinuous conduction mode (discontinuous current) in which current can't be negative (can't flow in opposite direction) so it becomes 0. As current is zero for a time Δt , H will become also zero for the same Δt and H will have a similar form to that of current shown in Figure 4-17.

B also follows the deformation to the triangular form by having a constant or zero value for a time Δt . In this case, both ΔH and ΔB are smaller and then they form a smaller BH minor loop (Figure 4-16) from a magnetic point of view, or a smaller area under negative power curve from an electrical point of view. Nevertheless the dB/dt is kept constant in this case too, due to the same reasons mentioned above (same voltage and frequency).

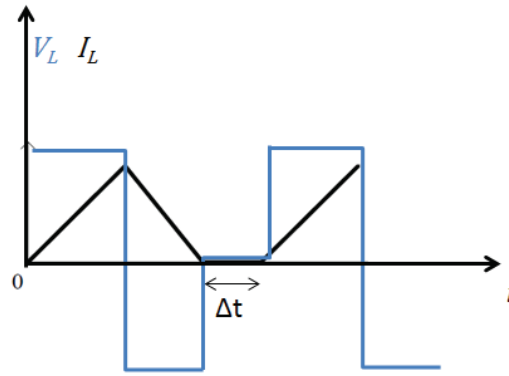


Figure 4-17: Inductor voltage and current in continuous and discontinuous conduction modes

The DC bias effect on the nanocrystalline core is not studied due to their good linear static behavior (see static hysteresis loop). Due to this linearity below saturation, DC bias has almost no effect on core losses for this particular material up to 1 Tesla. This gives such nanocrystallines an advantage in variable DC bias applications.

However, the studied nanocrystalline core is sensible to temperature, whereas temperature has negligible effects on the powder core. According to the constructor, the permeability of *HKBH* core varies about 2% at 160 °C. For that reason temperature effects are studied on the nanocrystalline core only and not the powder core. But before that, core losses comparisons in both materials alone and in application are presented below.

4.3.3.4 Materials comparison

Core losses per unit volume for both powder core *HKBH* and nanocrystalline core *K44B200* materials are compared under a 50 mT applied “sinusoidal” flux density. Results are shown in Figure 4-18 for frequencies up to 60 kHz. Figure 4-18 in log-log shows the expected increase of losses with frequency for both materials but with slightly different slopes. The powder core has the higher slope i.e. core losses increase with a higher rate with frequency. We can notice that the losses in powder material are relatively low, but they are about double the losses in nanocrystalline material.

Nonetheless when considering both materials (for the inductor) in the buck converter at a 4 V-40 kHz operating point or similar ($f/V=\text{constant}$), the loss difference between the two cores is much lower. In fact, as shown in Figure 4-19, the losses in mW at 40 kHz are 11 and 14 for nanocrystalline and powder respectively. Considering the same number of turns for both inductors, this is due to the smaller size of the powder core. When it comes to application, the core size is of great importance. Even though nanocrystallines have lower losses, they are limited to a minimum size of 10×7×5 mm due to fabrication process and fragility [19]. On the other hand powder cores can reach a size of 5×2×3 mm easily and even less [20].

In all cases, regarding the core power losses for these two materials, both are considered very good candidates for the buck converter application. In the given intermediate frequency range, they overcome ferrite materials and are used in commercial converters with efficiency higher than 92% [21].

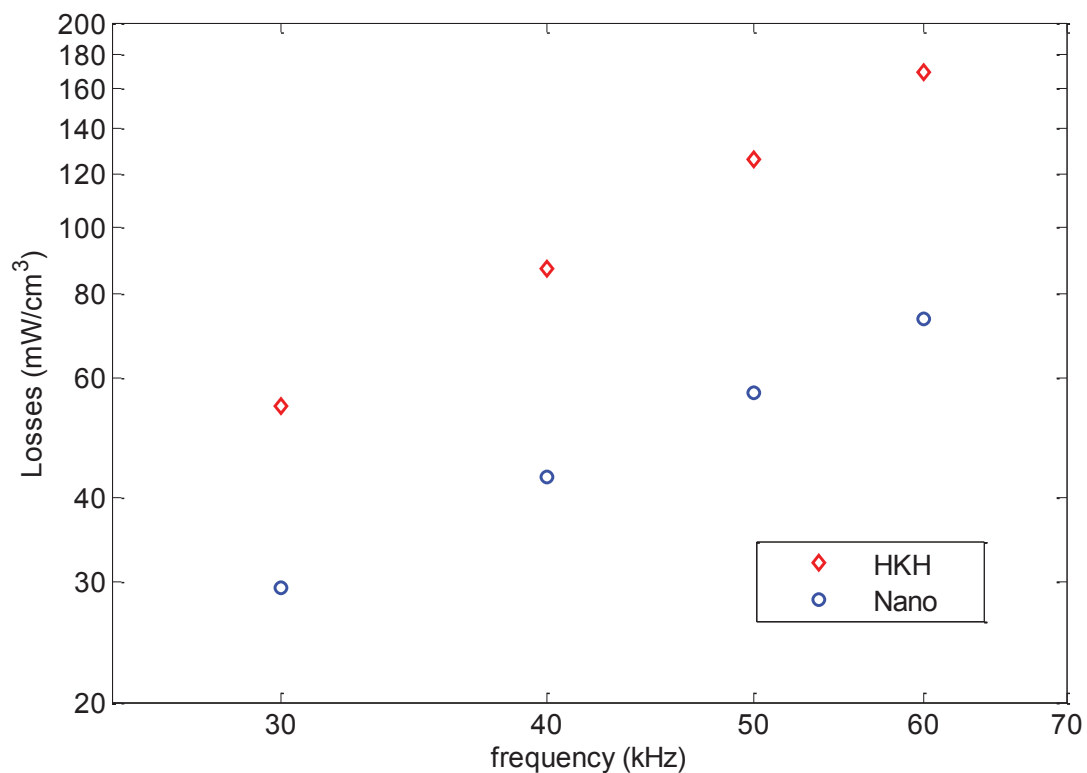


Figure 4-18: Core losses of both powder core HKBH and nanocrystalline core K44B200 materials under 50 mT applied “sinusoidal” flux density

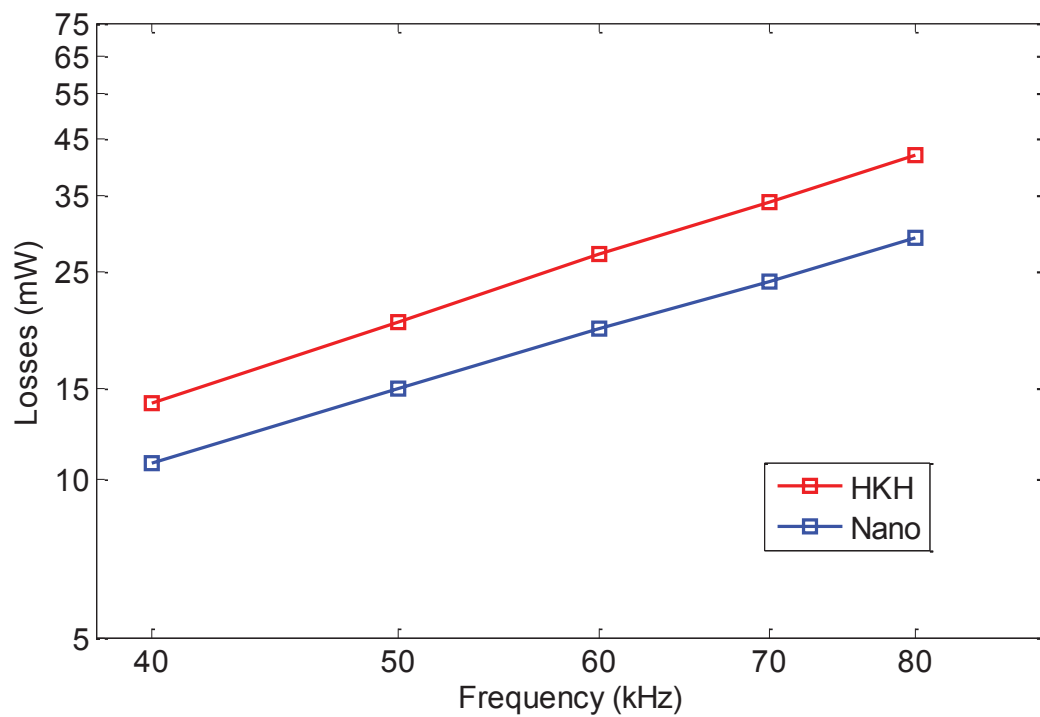


Figure 4-19: Core losses of both powder core HKBH and nanocrystalline core K44B200 materials in the buck converter at constant flux density operating points ($f/V=10k$)

4.3.3.5 Variable Temperature

To study the temperature influence on the nanocrystalline core in the application, a small setup shown in Figure 4-20 allowing the heating of the core is realized. While connected to the buck circuit, the used nanocrystalline core is placed under a hot air gun. The core is isolated from surroundings with a heat resistant silicon rubber cap. A thermocouple is also used to insure exact temperature readings. This setup grants temperatures up to 300 °C applied on the magnetic core during the normal operation of the buck converter (heat doesn't reach other components of the circuit).

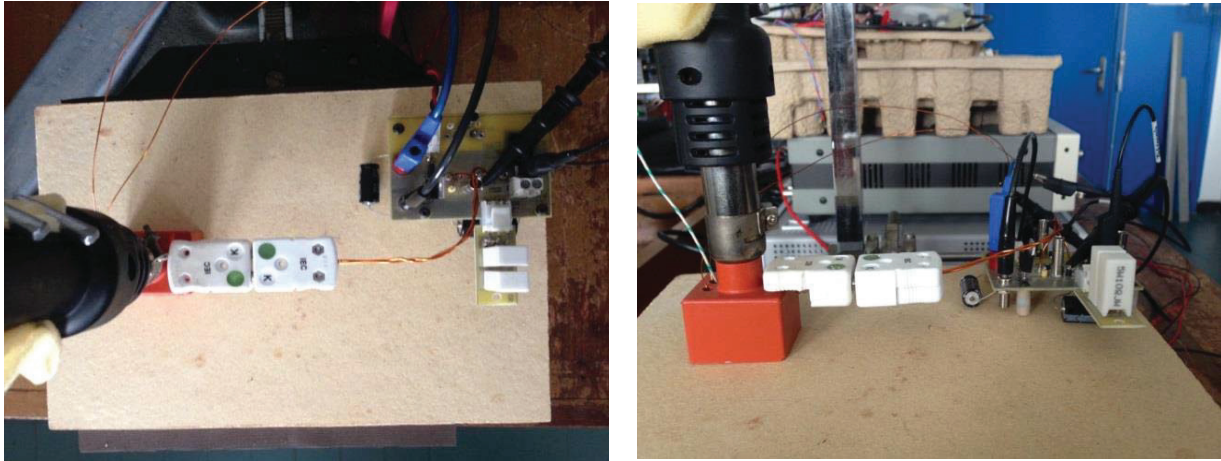


Figure 4-20: Setup for variable temperature measurements in buck converter

Using this setup, core losses are measured at different temperatures and frequencies are summarized in the 3D graph shown in Figure 4-21. Indeed core losses are measured in the 30 to 80 kHz frequency range at 5 temperature steps up to 200 °C (i.e. at 25, 50, 100, 150 and 200°C). Then these losses are traced as function of both frequency and temperature to form this plane shown in Figure 4-21.

From Figure 4-21 we can notice the effect of temperature on this material, namely on core losses which decrease with temperature. Between 25 °C and 200 °C core losses vary about 15% to 25% depending on the frequency. Clearly losses are lowest at 30 kHz-200 °C and highest at 80 kHz-25 °C.

This temperature influence maybe related to dynamic magnetic effects, as the losses would decrease due to resistivity increase (that is inversely related to the first dynamic coefficient γ). But since losses decrease about the same amount at each frequency (3 to 4 mW) the temperature influence is probably related to static magnetic effects. To clarify this point, static B-H measurements at different temperatures are performed on the nanocrystalline core. The results are shown in Figure 4-22.

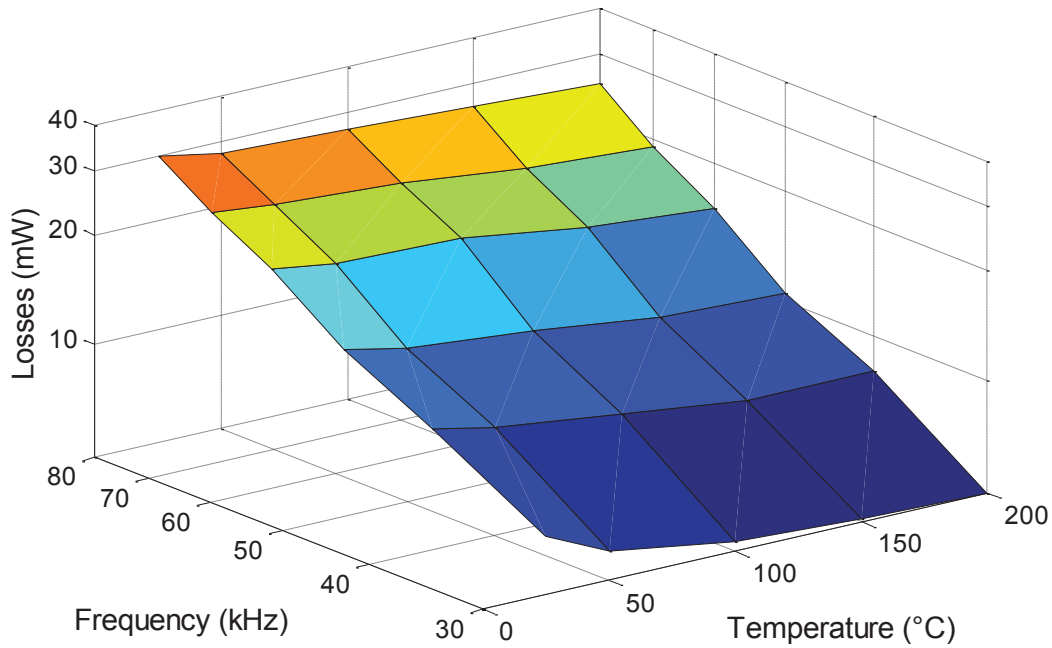


Figure 4-21: Core losses variation in the buck application for the nanocrystalline material as function of both frequency and temperature.

Figure 4-22 shows 3 static hysteresis loops under 0.75 T applied flux density at 3 different temperatures, 25 °C, 135 °C, and 230 °C. Contrary to the influence on high permeability nanocrystalline core studied before (N14E1), temperature affects the K44B200 core by increasing its permeability. Indeed it is clear from Figure 4-22 that the relative permeability increases with temperature to reach about 450 at 230 °C. This value is greater than double the initial value at 25 °C indicating the sensibility of these materials to temperature.

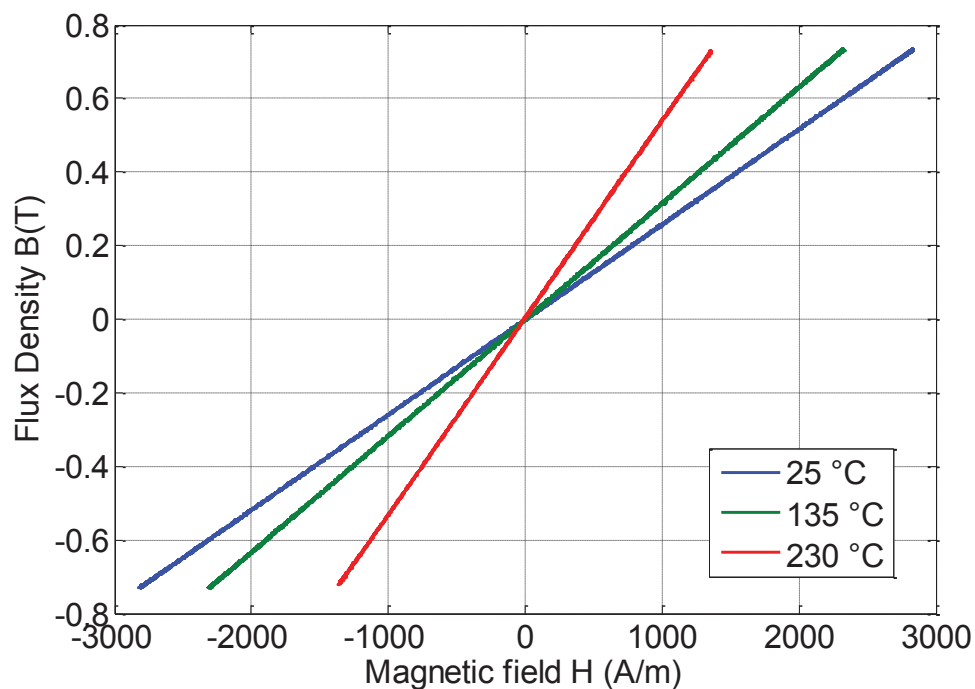


Figure 4-22: Measured flux density of nanocrystalline material as function of applied static field at different temperatures.

Moreover, this increase in permeability causes the decrease of minor loop area in the application and thus lower core losses. Again in this case we are applying the same ΔB at each temperature, but we obtain different ΔH values, and consequently different minor hysteresis loops with different areas. This explains the results of Figure 4-21 describing the core losses decrease with temperature.

After taking into account temperature in the buck application loss measurements, all variable conditions effects on core losses including variable induction, frequency, and DC bias are studied. Different core materials and dimensions are considered too.

Finally, one cannot conclude which is a better core for the buck converter application. There is a compromise between point of operation, size, frequency, and temperature. Table 7 summarizes the behavior of chosen magnetic core in the buck application. The powder core has a lower cost and a much better stability with temperature whereas the Nanocrystalline core has lower core losses and better stability with DC bias. Both materials have a very good performance in the intermediate frequency range and can operate up to 1 MHz without any problem.

Summary on Magnetic Cores		
	<i>HKBH</i>	<i>NANO</i>
Cost	**	*
DC bias	*	**
Core losses	*	**
Temperature	**	*
Frequency range	**	**
Available sizes and shapes	**	*

Table 7: Summary on magnetic materials performance in buck application

4.3.4 Copper Losses Measurements and Calculation

Concerning copper losses, they are studied for a combination of three different windings having different number of turns, different wire diameter and different lengths. In fact since the two studied powder and nanocrystalline cores have different sizes (precisely different core cross-section), their windings have different lengths even with the same number of turns. Then for the same core two windings with 20 and 30 turns are considered. And at last, two 30 turns winding with different wire diameters are also compared.

To calculate copper losses, the total power dissipated in the windings is considered to be the sum of DC and AC losses. Thus they are calculated using equation (4.9) where I_{DC} and R_{DC} are the DC current and resistance respectively. R_{DC} is derived from conductor resistivity and dimensions. R_{AC} is the AC resistance due to skin and proximity effects that increase with frequency. I_n is the current's n th harmonic. The AC resistance can be determined either by calculation [22], or by measurement using a coreless winding and an impedance analyzer.

$$P_w = P_{DC} + P_{AC} = R_{DC}I_{DC}^2 + \sum_n R_{ACn}I_n^2 \quad (4.9)$$

In our case we used the Agilent 4294A impedance analyzer [23] to trace the AC resistance as function of frequency. The three available coreless windings for measurement are presented in table 8. From the wire dimensions used to form the winding (shown in table 8), we can calculate the DC resistance by equation (4.10). It is the resistance of a cylindrical conductor where ρ is copper resistivity of value 16.8 nΩ.m, l is the length of the conductor and s is the conductor cross section. Calculating the DC resistance R_{DC} of the three windings W1, W2 and W3 using (4.10) we find 26.57 mΩ, 40.28 mΩ, and 17.54 mΩ respectively.

$$R_{DC} = \rho \frac{l}{s} \quad (4.10)$$

Windings			
	<i>1st Winding (W1)</i>	<i>2nd Winding (W2)</i>	<i>3rd Winding (W3)</i>
Length (cm)	31	47	82
Wire diameter (mm)	0.5	0.5	1
Wire cross-section (mm ²)	0.196	0.196	0.785
Number of turns	20	30	30
Core material (used for)	Powder	Powder	Nano

Table 8: Windings characteristics

To confirm these values and to find the winding resistances at different operating frequencies, measurements are carried out in the 40 Hz – 10 MHz frequency range. Resistances of W1, W2 and W3 are shown in Figure 4-23, Figure 4-24 and Figure 4-25 respectively. The variation of resistance as function of frequency is similar for the three windings. The effect of frequency remains negligible up to approximately 1 kHz then the winding resistance increase linearly with frequency. Above this frequency both skin effects and proximity effects manifest in the conductor (copper wire) to change its resistance.

From these figures we can deduce the DC resistance; it is the resistance value at low frequencies (40~50 Hz). For W1 we find a value of 26.82 mΩ, for W2 a value of 39.87 mΩ and for W3 a value of 18.49 mΩ. These measured values correspond to the calculated ones. Concerning AC resistances, their values at 100 kHz, for example, for the three windings W1, W2 and W3 are 287 mΩ, 408 mΩ and 745 mΩ respectively.

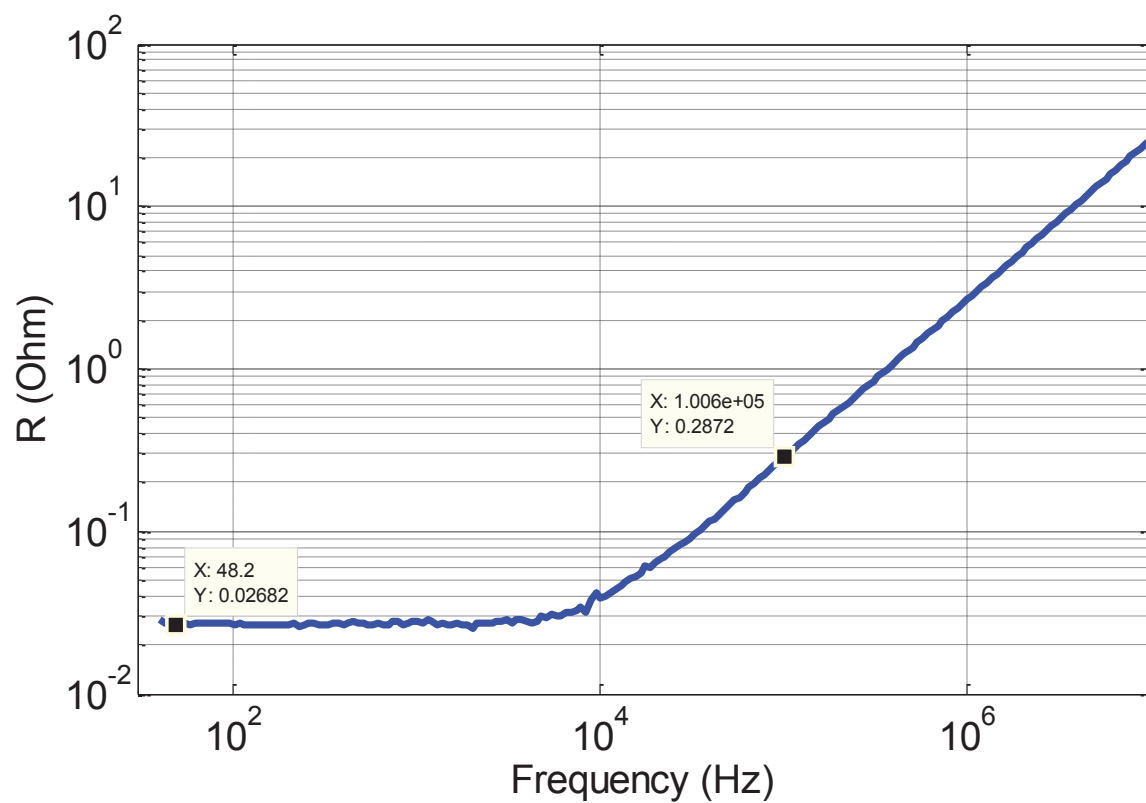


Figure 4-23: Measured AC resistance of W1 as function of frequency

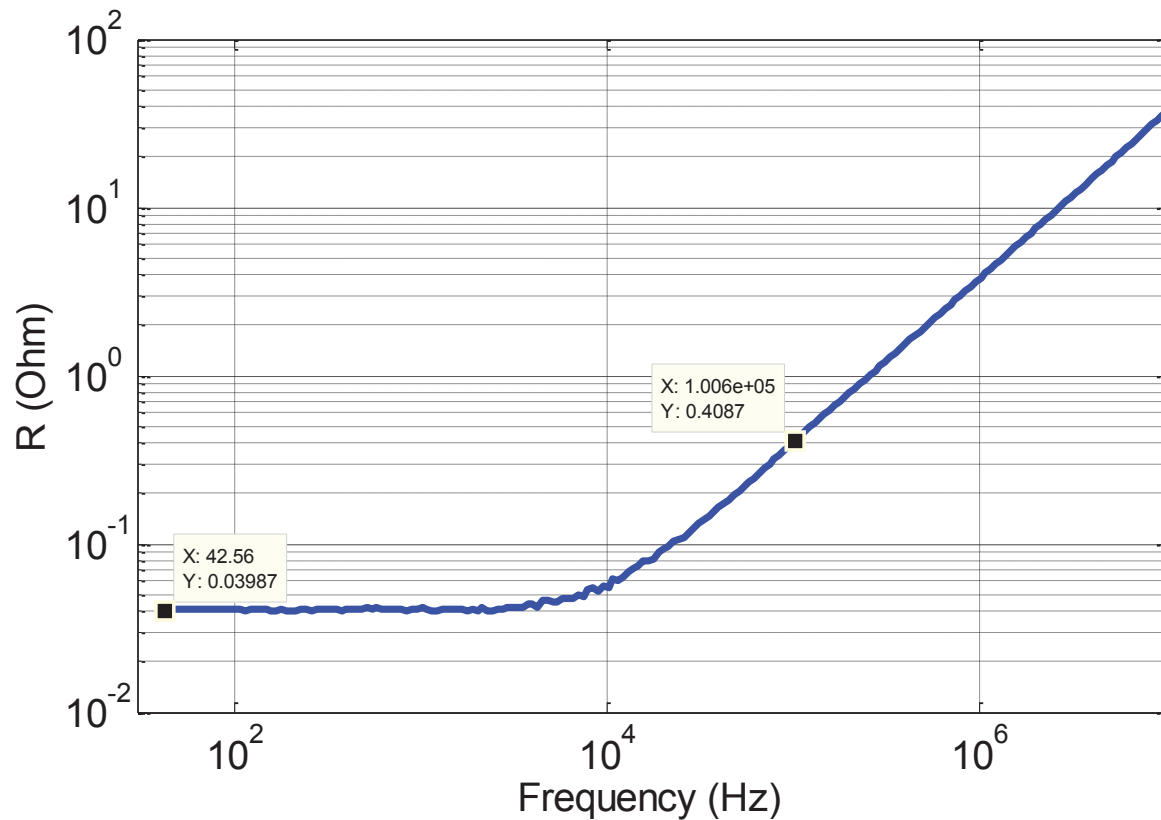


Figure 4-24: Measured AC resistance of W2 as function of frequency

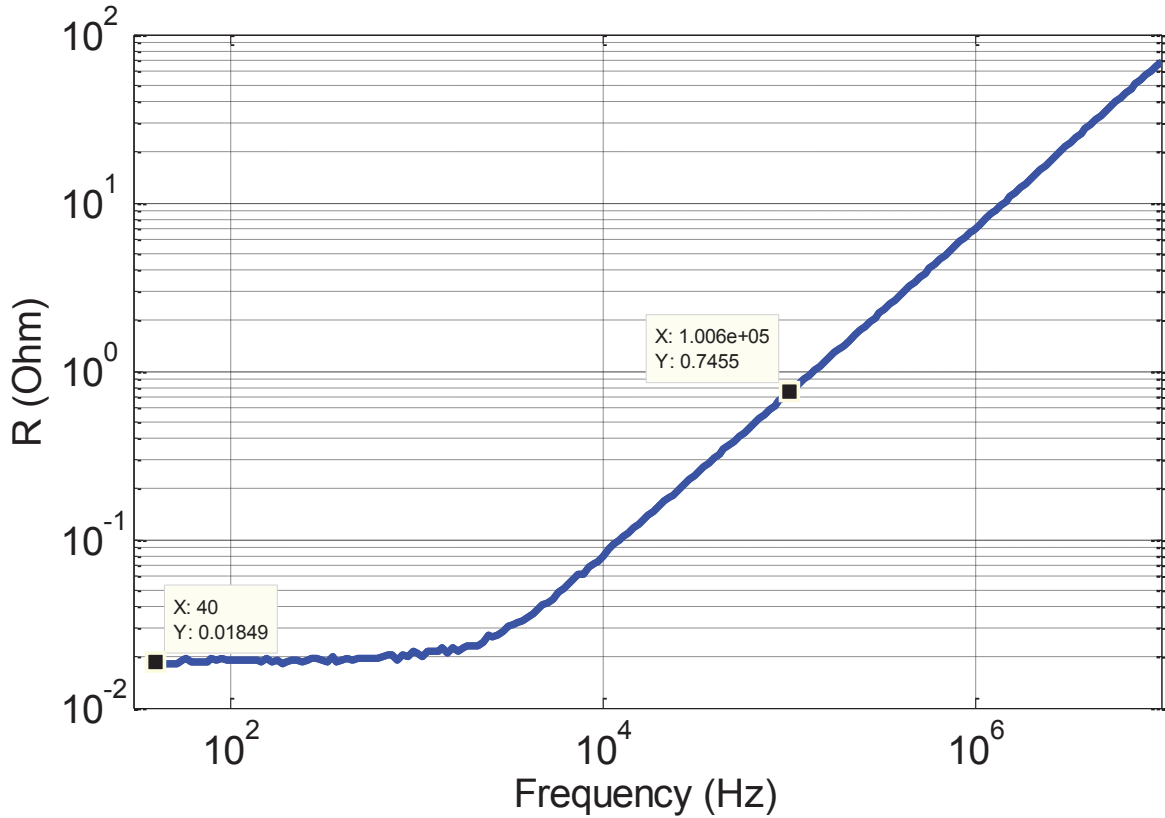


Figure 4-25: Measured AC resistance of W3 as function of frequency

Observing the measurement results of winding resistances, let us consider the 1st two windings W1 and W2 having 20 and 30 turns respectively. We can notice that these windings have a DC resistance ratio of 1.5 (R_{DC2}/R_{DC1}) which corresponds to their turn ratio or consequently length ratio. For the AC part, the AC resistances of both windings increase by the same rate with frequency. The AC curves have approximately the same slope.

Now considering the windings W2 and W3 having 0.5 and 1 mm diameter respectively. We can notice that the DC resistance of winding W3 is much lower than that of W2. This is due to the bigger diameter of the wire forming W3, and thus higher cross-section. However their AC behavior is totally different. The AC curve slope of W3 is higher than that of W2 leading to higher resistance of 758 mΩ for W3 compared to 408 mΩ for W2 at 100 kHz.

Eventually, the AC winding losses in the buck application are very low due to low AC current and to relatively low AC resistance for the operating frequency range (up to 100 kHz). For simplicity the winding losses can be limited to DC loss only (equation 4.11) since the AC copper losses don't exceed 3% of total winding losses. For example the DC winding losses for the used 30 turns winding W1 is found to be 39 mW at a DC current of 1A. The AC winding losses for the same winding at 100 kHz and 20% ripple current is 1.3 mW. However the accuracy in winding losses calculation is appreciated in other applications and for higher frequency range.

$$P_w = P_{DC} + P_{AC} \approx R_{DC} I_{DC}^2 \quad (4.11)$$

4.4 Model Implementation and Simulation Results

To validate the developed model in the buck converter application, a circuit identical to the buck circuit used for measurements is simulated in Simplorer as shown in Figure 4-26. The model replaced the inductor including both static and dynamic models (blocks) plus core dimensions. Winding resistance and number of turns are inserted to the winding block in the model. Simulations are run for different voltages, frequencies, and loads. Voltage, current, magnetic field and flux density waveforms are available from simulations. In addition, instantaneous and average core and winding losses are available too. Comparisons between measured and simulated waveforms and losses are presented below.

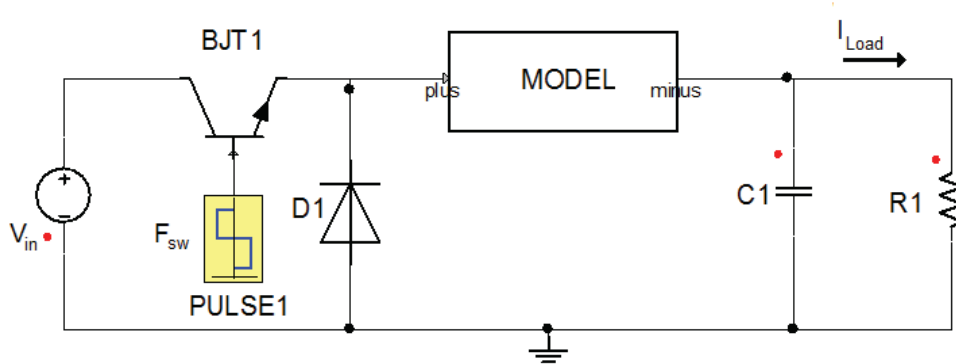


Figure 4-26: Buck converter simulation circuit

Simulated iron losses per unit volume (buck in continuous conduction mode) for different induction levels are compared to measured ones in the 40 to 100 kHz frequency range. Results for the *HKBH* powder core are shown in Figure 4-27. Simulations and measurements at the 3 induction levels of 100 mT, 150 mT and 200 mT are in good agreement. We note that only a single dynamic parameter “ α ” has to be identified from sinusoidal measurements. The other dynamic parameter γ is extracted from material’s resistivity and dimensions. Experiments confirm model’s loss prediction accuracy with a maximum error of 3% (MSE).

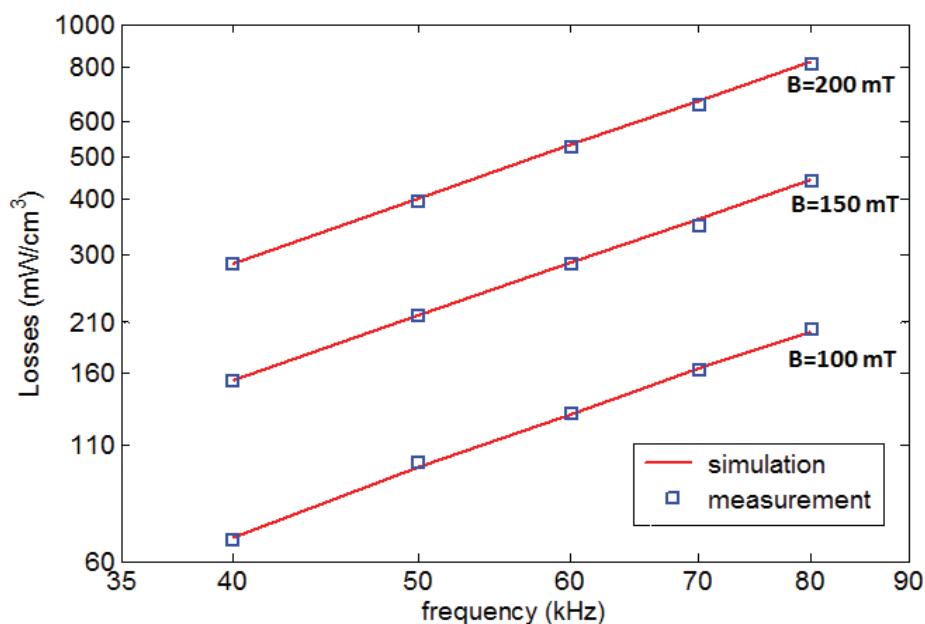


Figure 4-27: Measured and simulated core losses in powder core HKBH

Furthermore the exact inductor voltage and current of both continuous and discontinuous conduction modes available from circuit simulation are traced. Results in Figure 4-28 and Figure 4-29 show measured and simulated voltages and currents respectively at 50 kHz. Simulations and measurements are in good agreement as well.

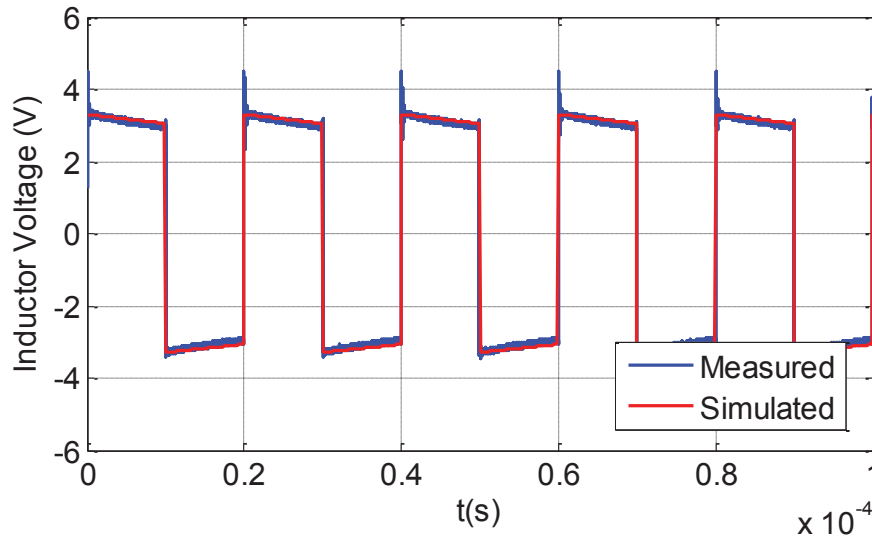


Figure 4-28: Measured and simulated inductor voltage at $f=50$ kHz

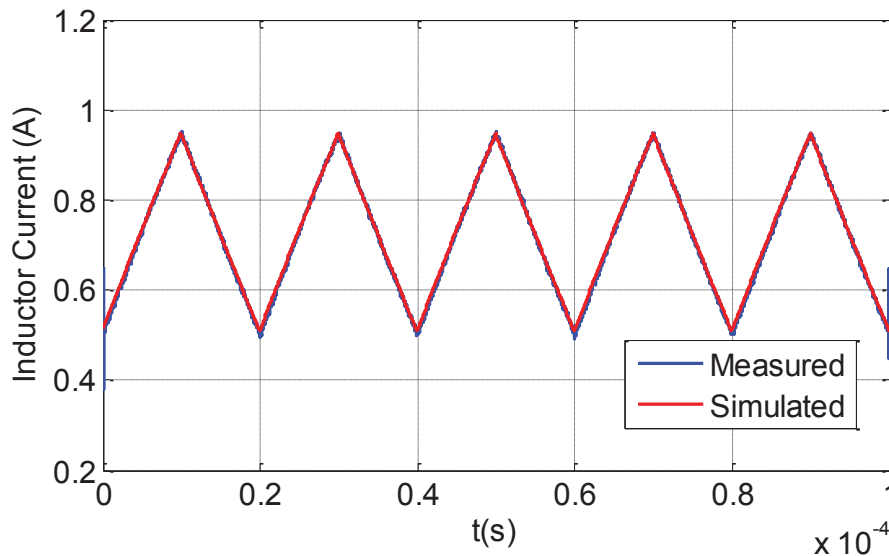


Figure 4-29: Measured and simulated inductor current at $f=50$ kHz

To test the model in the discontinuous conduction mode and under variable DC bias, simulations are carried out at different loads identical to those used in measurements. Under the same conditions, simulated and measured core losses per unit volume are compared and shown in Figure 4-30. Results show the agreement between simulations and measurements for the five different loads (2, 3, 4.4, 5, and 6 ohms). This indicates the model's efficacy for both continuous and discontinuous conduction modes of the buck converter.

Note that the high noise and damping in the discontinuous conduction mode measurements cause lower accordance between simulated and measured points in this mode. These measurements were one of the experimental challenges in our work.

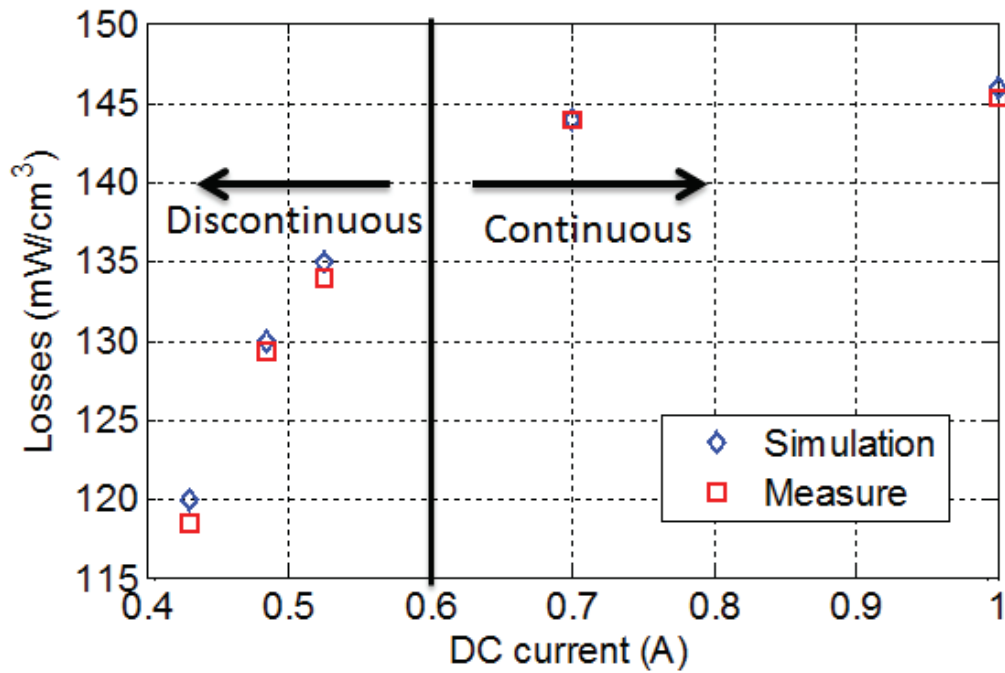


Figure 4-30: Simulated and measured core losses under variable load currents.

Similarly, the model is validated for the nanocrystalline core material in the buck converter. Properties, parameters and dimensions of the powder core are replaced by those of the nanocrystalline one. Simulations are then performed under different operating conditions. For instance, Figure 4-31 shows simulated and measured iron losses in the buck operating in continuous conduction mode for different frequencies in the 40 to 100 kHz range. These results of Figure 4-31 are at a magnetic flux density corresponding to the operating points of which $f/V=10k$. Simulations and measurements are also in good agreement for the nanocrystalline core.

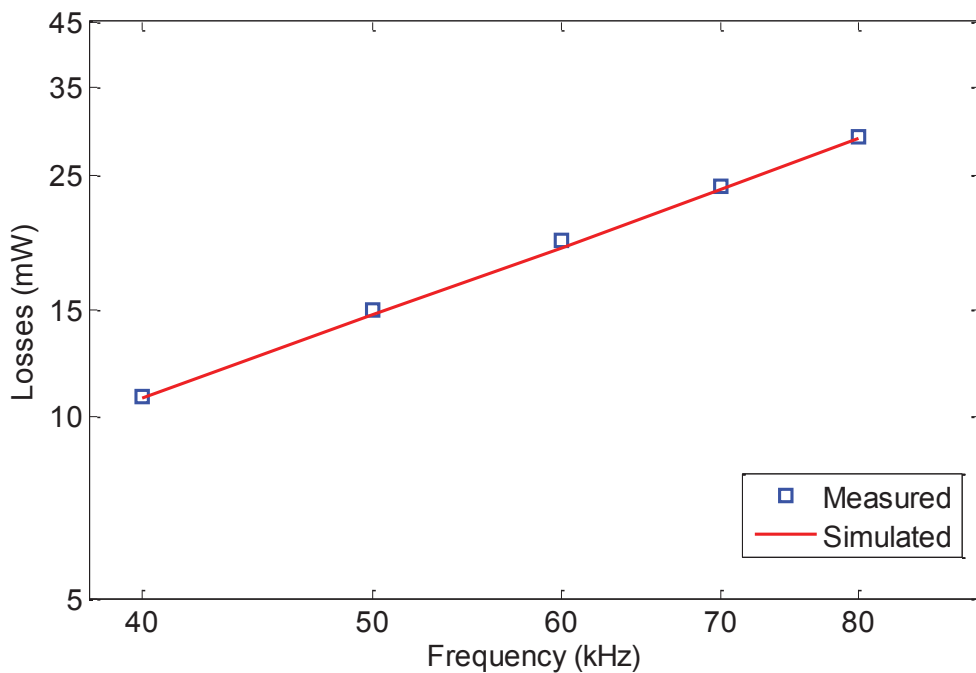


Figure 4-31: Measured and simulated core losses in nanocrystalline core K44B200

4.5 Other Results and Applications

Previously the validation of the developed magnetic component model in a homemade power converter buck application was discussed. The model was tested for different core inductors, different ripple currents, different loads and frequencies up to 100 kHz. However other efforts are done in the domain of application of the developed model.

Concerning other points of application, a commercial buck converter from TRAPOWPER is considered [21]. This 20×20 mm converter switches at a frequency of about 350 kHz at a variably duty cycle. This is an interesting application that takes the operating point to a frequency higher than that of the realized buck. This allows testing the model's performance for an already existing converter at high frequency for duty cycles different than 50%.

To go further in the domain of application, a small part of our work was dedicated to a different application. A two-winding transformer application was used in simulation including the developed component model. For the moment, the physical model could not be realized but is considered one of the perspectives. Nonetheless simulation results are presented and discussed in this section.

4.5.1 TRACOPWER commercial converter

The TRACOPOWER TSI-10N converter is low noise, high efficiency step-down converter. It has an adjustable output voltage from 1.8 to 3.3 V and supports input voltages between 4.75 and 13.6 V. The converter configuration and dimensions are shown in Figure 4-32 while its specifications are shown in table 9.

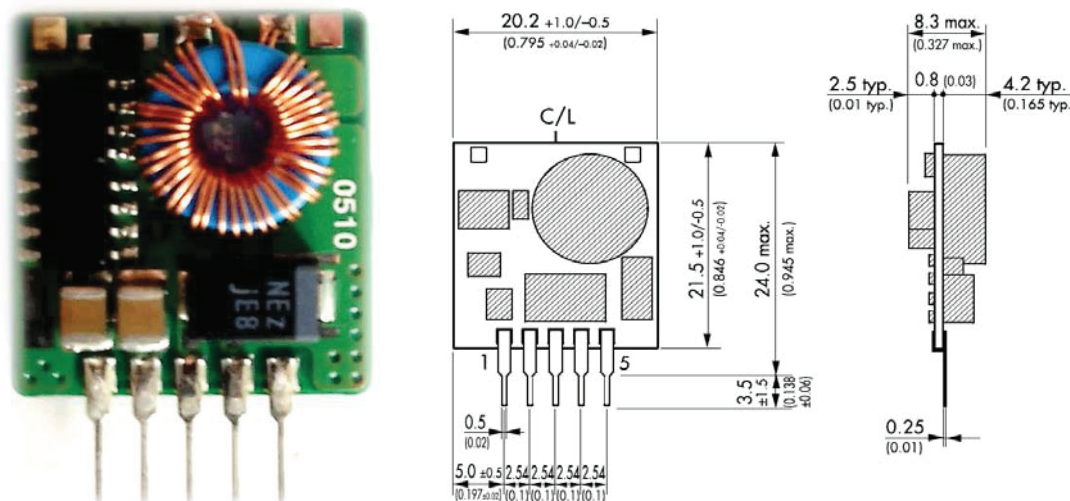


Figure 4-32: TRACOPOWER TSI-10N circuit and dimensions in mm

Converter Specifications				
Input voltage	Output voltage	Output current (max)	Efficiency	Switching frequency
4.75 – 13.6 V	1.8 – 3.3 V	2 A	92%	300-400 kHz

Table 9: TRACOPOWER TSI-10N converter specifications

Figure 4-32 shows the circuit of TSI-10N including the inductor (the magnetic component), occupying about 30% of its volume. The magnetic core used in this converter is the same powder core *HKBH* previously studied. This small (24×20 mm) low weight package (4 g) includes 5 connection pins. These pins are the input voltage (V_{in}), output voltage (V_{out}), Ground (GND), voltage adjustment (V_{adj}) and Remote pin (ON/OFF). This converter supports a maximum current of 2 A and has an efficiency of 92% at full load.

In order to measure inductor current, voltage and then core losses, some adjustments are made to the buck converter. The adjusted circuit shown in Figure 4-33 includes interchangeable connectors, special oscilloscope connectors and three ceramic cased power resistors used as load. Similar to the previous converter, a small shunt (500 m Ω) is added in series with the inductor and secondary turns are wound to the same core as well.

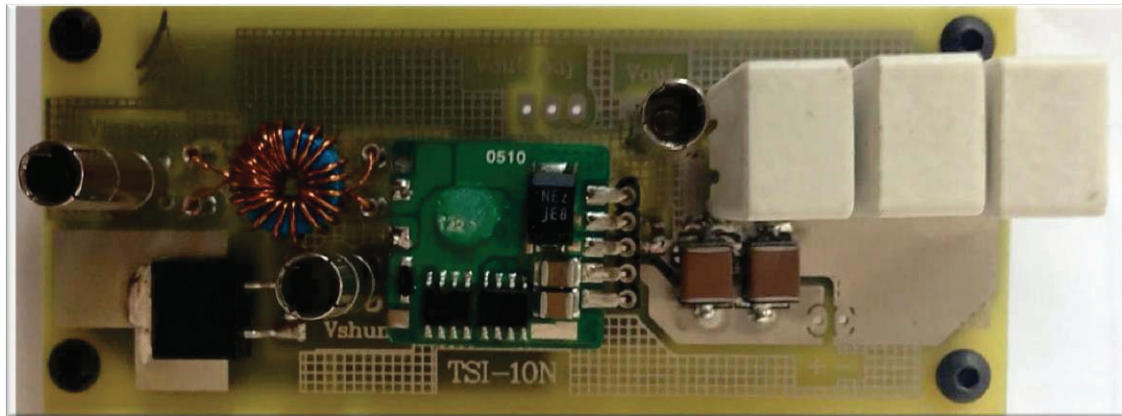


Figure 4-33: TSI converter adjusted circuit

The V_{adj} is left unconnected to ensure a maximum output voltage (3.3 Volts). The load is a three 10 Ω resistors connected in parallel to obtain 3.33 Ω . The result is an output current of 1 A. According to the input voltage, the regulator modifies its duty cycle to keep a constant output voltage. Two SMC 50 μ F/50V ceramic capacitors are added in parallel to the input voltage to form the 100 μ F input filtering capacitor recommended by the manufacturer. A small output capacitor of value 4.7 μ F is added as well.

The circuit of Figure 4-33 allows primary current and secondary voltage measurements which are performed using the LECROY oscilloscope. These measurements are used to obtain core losses as explained before. Other waveforms like input voltage, output voltage and inductor voltage are also available from the adjusted circuit. The output voltage is constant with very low ripple (50 mV maximum) and short transient response time (100 μ s). The inductor voltage has a low noise and damping.

Simulation of this circuit including the model is accomplished too. The measured inductor voltage and current are compared to simulated ones. Results are shown in Figure 4-34 and Figure 4-35 respectively.

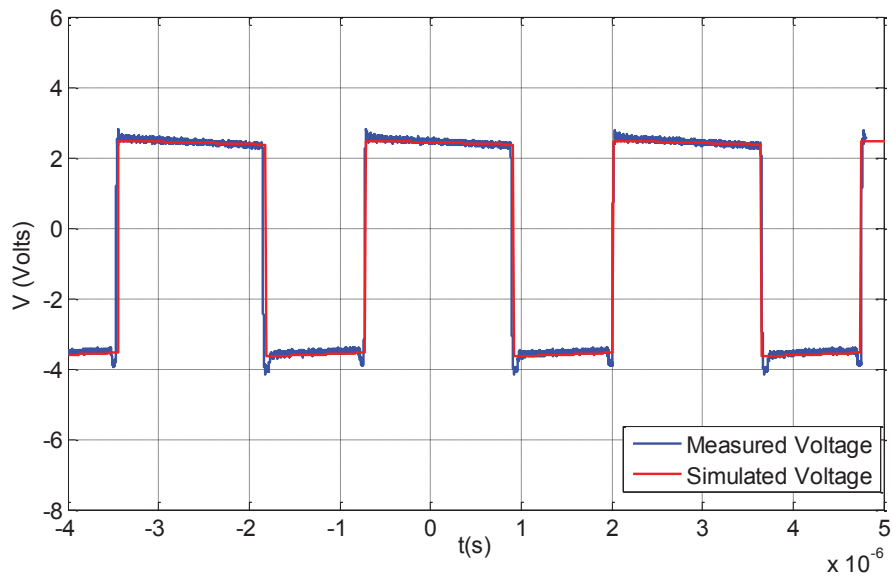


Figure 4-34: Measured and simulated inductor voltage

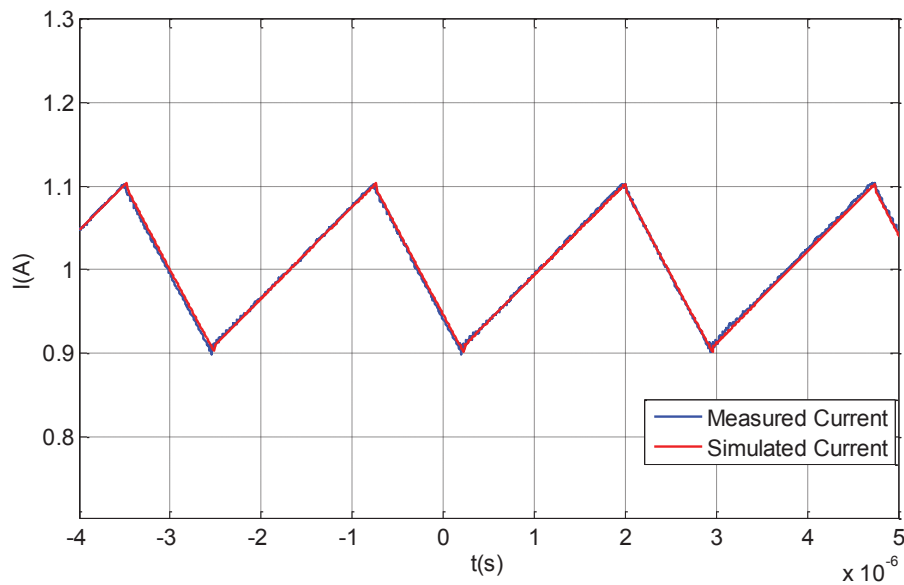


Figure 4-35: Measured and simulated inductor current

Figure 4-34 shows temporal variation of measured and simulated inductor voltages. We can notice the switching frequency of about 360 kHz with a duty cycle of about 65%. The measured voltage has much lower noise compared to other buck circuit realized at the laboratory. The simulated voltage corresponds to the measured one.

Figure 4-35 shows temporal variation of measured and simulated inductor currents. It's clear that the current also will have a 360 kHz switching frequency and a 65% duty cycle. We can deduce the inductor ripple current at this operating point having a value of about 20%. The simulated current and the measured one are in good agreement as well.

The secondary voltage is also measured and used to calculate the magnetic flux density $B(t)$. The magnetic field $H(t)$ is calculated from the measured primary current (inductor current). These two are used to trace the measured B-H loop which is compared to the simulated one. Both measured and simulated B-H loops are shown in Figure 4-36.

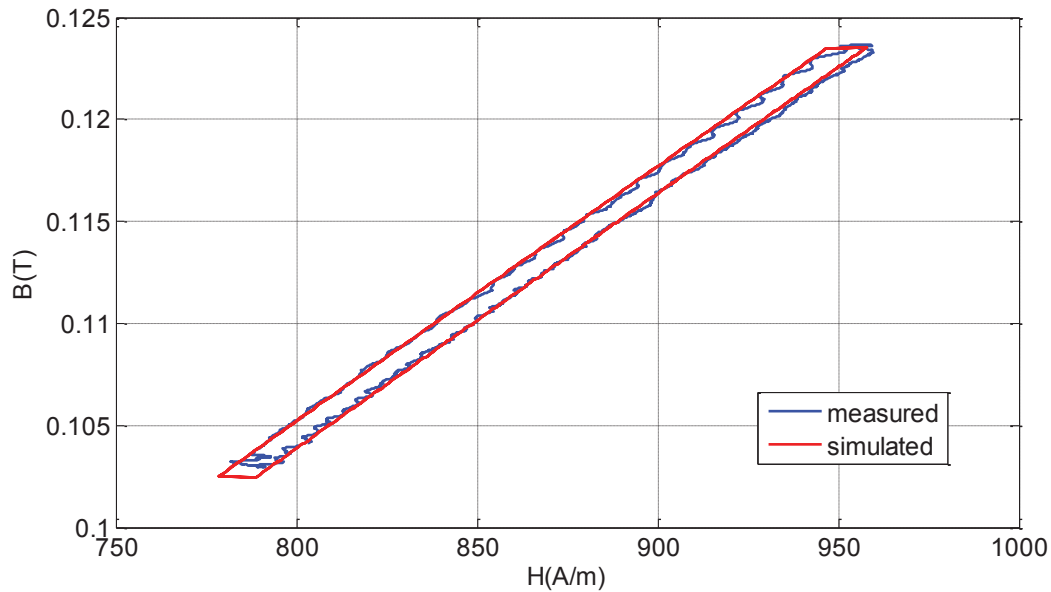


Figure 4-36: measured and simulated B-H loops

Figure 4-36 shows the agreement between measured and simulated B-H loops. The measured loop shows some deformations due to damping and measurements noise while the simulated loop corresponds to the ideal case (i.e. no damping and noise). It's clear that both loops are non-centered minor loops, with an average field of 870 A/m corresponding to the average output current. These B-H loops correspond to 12.2 mW measured core losses and 12.3 mW simulated core losses.

From measurements and simulations results of the small buck converter circuit, we can conclude the precision of the developed magnetic component model at higher frequencies. It is able to represent inductor's current and voltage waveforms in addition to the corresponding B-H loop. The duty cycle higher than 50%, particularly 65%, didn't affect the model's accuracy.

Besides the buck converter, there was an attempt to study the model in other applications. A different application, where magnetic components are widely used is the single-phase transformer. The developed model was implemented in a single-phase transformer circuit for simulation to test if the modeling approach is valid for more complex magnetic components or at least several windings applications. The simulation results for different operating points are discussed below.

4.5.2 Single phase transformer

A transformer is a static device consisting of two or more coupled windings, for inducing mutual coupling between circuits. Power transformers are used in the generation, transmission and distribution of electric power. Indeed, they are used in electric power systems to transfer power by electromagnetic induction between circuits at the same frequency, usually with changed values of voltage and current [24].

A single-phase two-winding transformer is nothing more than a primary and a secondary winding wound around the same magnetic core. Because the transformer has both primary and secondary windings, which have opposite current flowing, therefore, the MMF of primary winding is related to that of the secondary winding.

From a modeling point of view, the fact of having two windings will put additional constraints on the magnetic component model. The model must be able to take into account the MMF induced in the secondary winding and thus increase the primary current based on the value of secondary current (transformer's load). Clearly these constraints don't exist in the case of an inductor. For that reason, simulations of a two-winding transformer including the developed model were carried out and the corresponding circuit is shown in Figure 4-37.

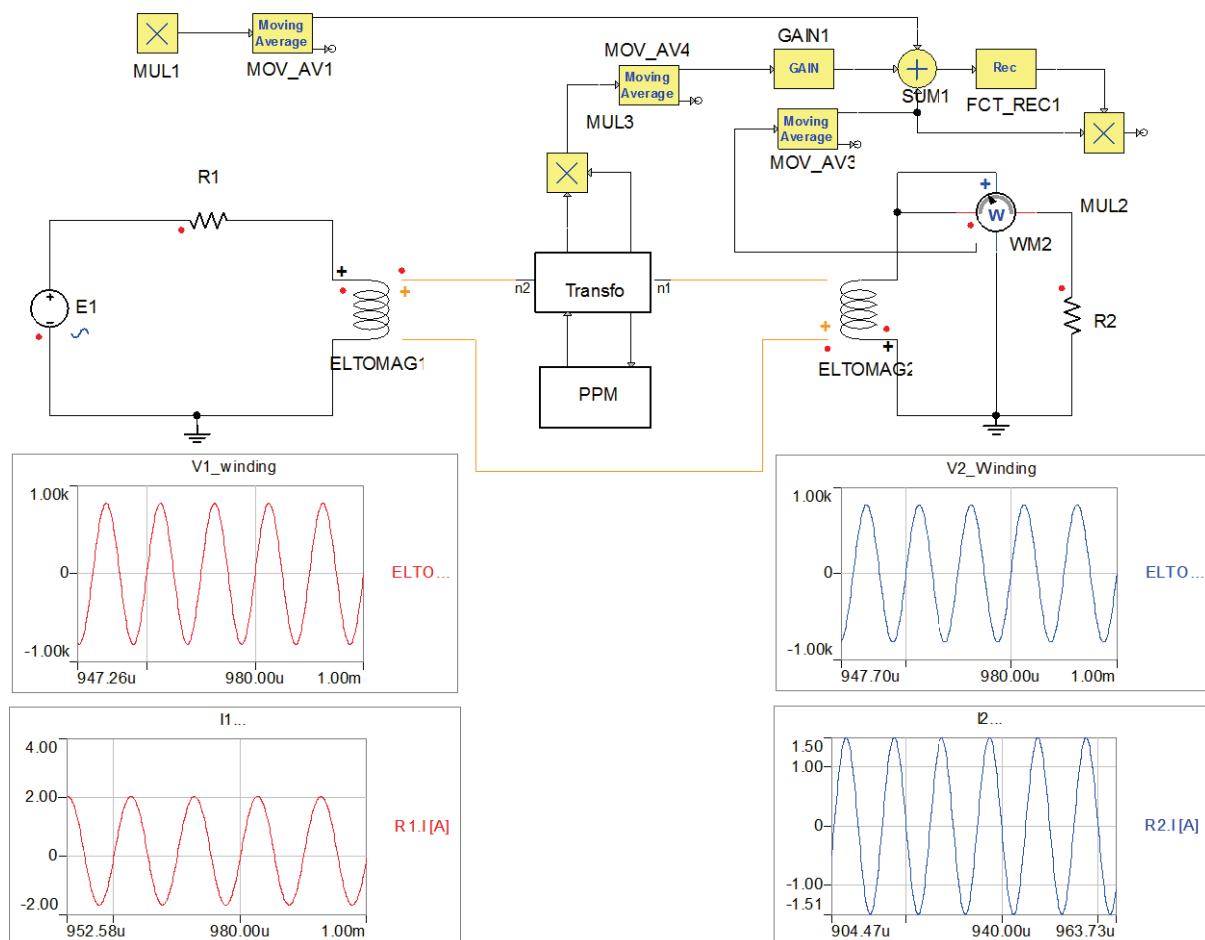


Figure 4-37: Simulation circuit of a two-winding transformer

The circuit in Figure 4-37 represents a single-phase two-winding transformer model. We can notice an additional winding compared to the previous inductor model. However we kept the same dynamic model (but is called here “Transfo”) and static “PPM” model as before. The model represents the same nanocrystalline core previously studied N14E1 but with much bigger size (120×108×20 mm). The primary winding have 20 turns whereas secondary winding have either 20, or 10 or 5 turns to vary the transformer turns ratio.

The primary winding is connected to a sinusoidal voltage source to apply a primary voltage V_1 . A variable resistive load is connected to the secondary winding. The primary and secondary currents are available from simulations. Core and winding losses are calculated too and the transformer’s efficiency is deduced.

The primary current (I_1) and the secondary current referred to the primary side ($N_2/N_1 \cdot I_2$) are simulated for load variation between 15% and 100%. These currents are traced in Figure 4-38. We notice that both currents increase linearly with load as expected due to higher load (lower resistance). However, the important observation is the constant difference between these currents for all load values. This difference as shown in equation (4.12) is related to the value of no-load current which is the sum of magnetization current and current supplying core losses.

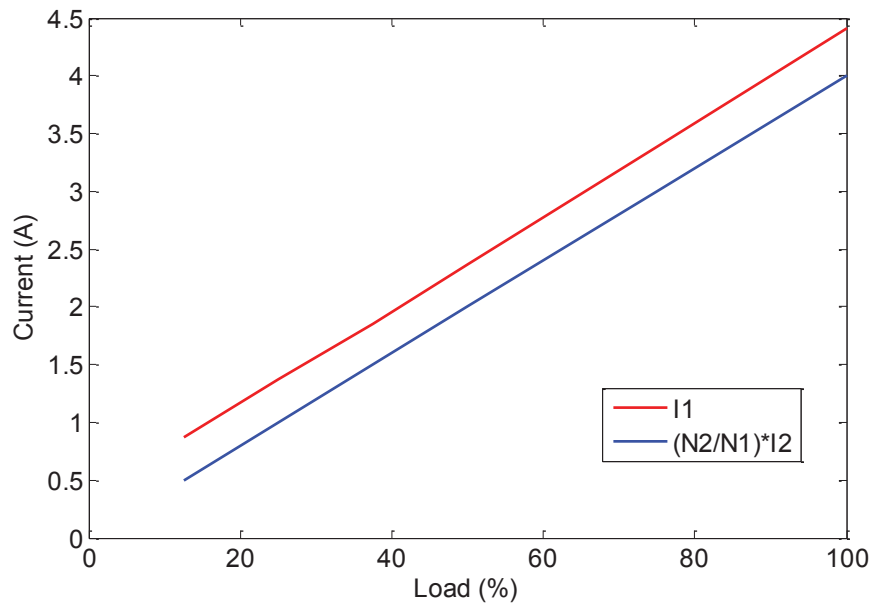


Figure 4-38: Primary current and secondary current referred to the primary side variation with load

$$MMF_{core} = MMF_{primary} + MMF_{secondary} \quad (4.12)$$

$$N_1 I_o = N_1 I_{primary} - N_2 I_{secondary}$$

$$I_o = I_{primary} - \frac{N_2}{N_1} I_{secondary} \quad (4.13)$$

Thus the total current drawn from the supply by the primary winding is the sum of the no-load current, I_o and the additional supply current, $N_2/N_1 \cdot I_2$ as a result of the secondary transformer loading. The no-load current (I_o) is function of core losses which are constant with loading, but increase with frequency, input voltage, core material and core size. Since the developed core model takes all these parameters into account, the transformer model becomes a realistic one. The actual primary current would be available from simulation to prevent underestimating transformer size and avoid overheating.

In addition to currents and voltages, core and copper losses are extracted from simulations. The variations of both core and copper losses as function of loading are presented in Figure 4-39. As frequency and input voltage (thus flux density) are kept the same, core losses are not affected by load variation. On the other hand, as copper losses are proportional to the square of the current, they increase quadratically with the load. These simulations are performed at 800 V input voltage and 100 kHz frequency.

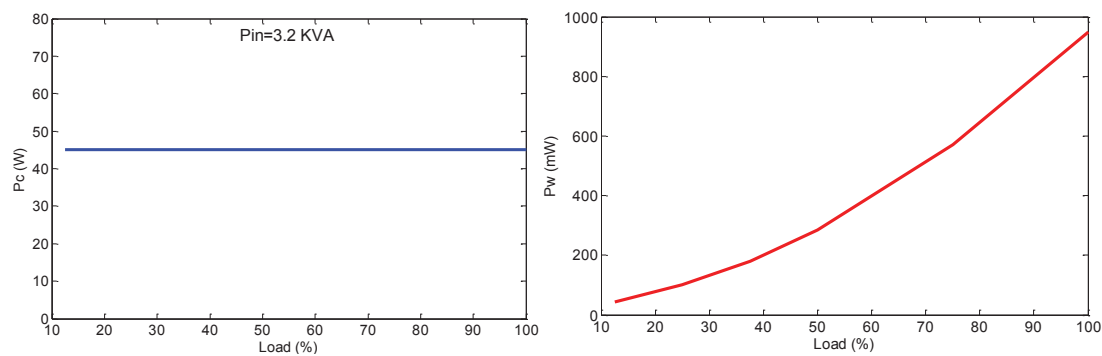


Figure 4-39: Core (left) and copper (right) losses as function of load

The transformer's efficiency, calculated from power losses and output power, is traced versus load in Figure 4-40. We can notice the exponential increase of efficiency with load percentage from 82% at 15% load to 97% at 100% resistive load.

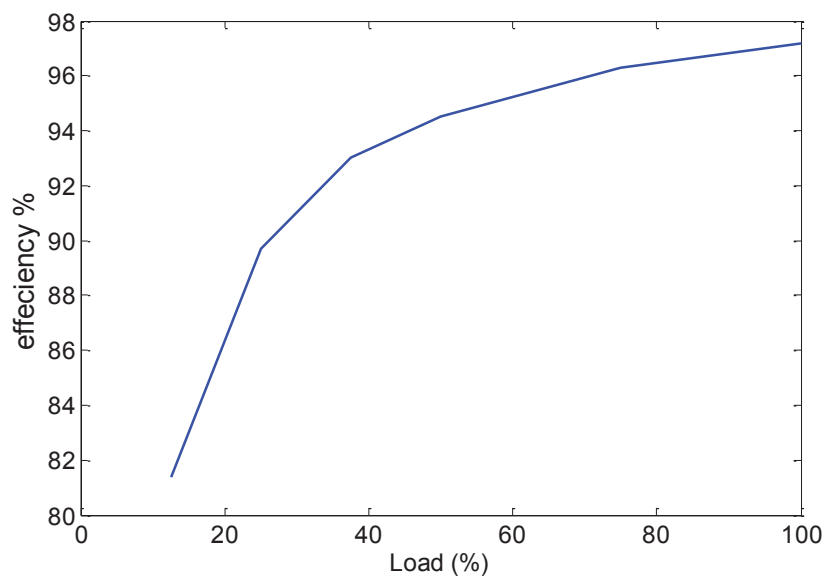


Figure 4-40: Converter efficiency as function of load

The value of copper losses is negligible compared to output power. This increase of efficiency with load percentage i.e. with secondary current is mainly due to core losses. Since core losses are constant, they have more effect on low output power at low secondary current (low load %) than on high output power at high secondary current (high load %).

The aim of these previous circuit simulations is to test the model in more than one winding application only. Thus they aren't profoundly analyzed but nevertheless they show that the model is adaptable for more complex applications. The developed transformer model could predict the actual primary current, power losses and efficiency. This becomes useful in the design stage of transformers serving the purpose of accurate virtual prototyping.

Finally the results on the two winding transformer are only simulated ones. Unfortunately they couldn't be validated with measurements due to time limitation. However these measurements are included in the perspectives for the next year research work. Besides this transformer circuit is considered relatively simple since no leakage is considered. These issues in addition to studies on other loads (inductive and capacitive) are also of our interest for future work.

4.6 Conclusion on Application

In this chapter the behavior of magnetic components in, a widely used power application, the buck converter is studied. A brief review on buck topology is demonstrated. Realization of a buck test circuit of variable voltage, switching frequency and load is exposed. Characterization of two candidate core materials, a Sendust powder core and a low permeability nanocrystalline core are presented.

The developed magnetic component model is tested for different core inductors. Simulations of a buck converter including the developed model are compared to measurements performed on the realized converter circuit. Indeed, waveforms and losses of a both powder core and nanocrystalline inductors are simulated and compared to measured ones. The model is validated for different ripple currents, different loads and a wide frequency range (10-100 kHz). DC bias is taken into account. Both continuous and discontinuous conduction modes are studied. Temperature effects on core losses for the nanocrystalline core inductor are also discussed.

The magnetic component model allows precise prediction of core and winding losses. Simulated inductor current and voltage correspond to measured ones. Model's parameters are extracted from magnetic material characterization under sinusoidal excitation. Experiments confirm model's loss prediction accuracy with a maximum error of 3% for non-sinusoidal waveforms.

Concerning simulation time, the model is quite fast. For example simulating the buck converter including the model for 200 periods at 80 kHz switching frequency takes only 5.4 seconds on a 3.1 GHz - 4Go RAM Computer. However coupling with the thermal model increases simulation time but remains less than 1 min.

In the domain of application, two other operating modes are discussed. First the developed model was tested in a commercial buck converter from TRAPOWERS at a 360 kHz switching frequency and a variably duty cycle. Then for a more complicated application, a single-phase two-winding transformer was used in simulation including the developed component model. For the small buck converter circuit, simulated inductor current, voltage and B-H loop correspond to the measured ones. The model is able to represent magnetic component behavior at higher frequencies and duty cycles. For the two-winding transformer, circuit simulations are performed to test the model in more than one winding application. The developed transformer model could predict the actual primary current, power losses and efficiency.

4.7 References

- [1] C. A. Baguley, U. K. Madawala, and B. Carsten, "The influence of temperature and core geometry on ferrite core losses under DC bias conditions," in *SPEEDAM 2008 - International Symposium on Power Electronics, Electrical Drives, Automation and Motion*, 2008, pp. 355–359.
- [2] W. C. Tsai, "A study on core losses of non-oriented electrical steel laminations under sinusoidal, non-sinusoidal and PWM voltage supplies," in *IEEE Region 10 Annual International Conference, Proceedings/TENCON*, 2007.
- [3] N. A. Spaldin, *Magnetic materials: fundamentals and applications*, 2nd Editio. Cambridge University Press, 2010.
- [4] P. R. Wilson and J. N. Ross, "Definition and application of magnetic material metrics in modeling and optimization," *IEEE Trans. Magn.*, vol. 37, no. 5, pp. 3774–3780, 2001.
- [5] W. Chandrasena, P. G. McLaren, U. D. Annakkage, R. P. Jayasinghe, D. Muthumuni, and E. Dirks, "Simulation of hysteresis and eddy current effects in a power transformer," *Electr. Power Syst. Res.*, vol. 76, pp. 634–641, 2006.
- [6] G. Gruosso and A. Brambilla, "Magnetic core model for circuit simulations including losses and hysteresis," no. March, pp. 309–334, 2008.
- [7] C. P. Steinmetz, "On the law of hysteresis," *Proceedings of the IEEE*, vol. 72, no. 2. pp. 197–221, 1984.
- [8] J. Reinert, a. Brockmeyer, and R. W. De Doncker, "Calculation of losses in ferro- and ferrimagnetic materials based on the modified Steinmetz equation," *Conf. Rec. 1999 IEEE Ind. Appl. Conf. Thirty-Forth IAS Annu. Meet. (Cat. No.99CH36370)*, vol. 3, pp. 2087–2092, 1999.
- [9] J. Li, T. Abdallah, and C. R. Sullivan, "Improved calculation of core loss with nonsinusoidal waveforms," *Conf. Rec. 2001 IEEE Ind. Appl. Conf. 36th IAS Annu. Meet. (Cat. No.01CH37248)*, vol. 4, pp. 2203–2210, 2001.

- [10] K. Venkatachalam, C. R. Sullivan, T. Abdallah, and H. Tacca, "Accurate prediction of ferrite core loss with nonsinusoidal waveforms using only Steinmetz parameters," *IEEE Work. Comput. Power Electron. 2002. Proceedings.*, 2002.
- [11] J. Muhlethaler, J. Biela, J. W. Kolar, and A. Ecklebe, "Improved core-loss calculation for magnetic components employed in power electronic systems," *IEEE Trans. Power Electron.*, vol. 27, pp. 964–973, 2012.
- [12] A. Boglietti, A. Cavagnino, M. Lazzari, and M. Pastorelli, "Predicting iron losses in soft magnetic materials with arbitrary voltage supply: An engineering approach," *IEEE Trans. Magn.*, vol. 39, pp. 981–989, 2003.
- [13] C. a. Baguley, B. Carsten, and U. K. Madawala, "The Effect of DC Bias Conditions on Ferrite Core Losses," *IEEE Trans. Magn.*, vol. 44, no. 2, pp. 246–252, Feb. 2008.
- [14] C. Miguel, A. Zhukov, J. J. Del Val, and J. Gonzalez, "Coercivity and induced magnetic anisotropy by stress and/or field annealing in Fe- and Co- based (Finemet-type) amorphous alloys," *Journal of Magnetism and Magnetic Materials*, vol. 294, pp. 245–251, 2005.
- [15] "[http://fr.rs-online.com/web/p/convertisseurs-dc-dc-non-isoles/4338359/.](http://fr.rs-online.com/web/p/convertisseurs-dc-dc-non-isoles/4338359/)" .
- [16] H. Skarrie, "Design of Powder Core Inductors," Lund Institute of Technology, Lund University, SWEDEN, 2001.
- [17] "[http://teledynelecroy.com/oscilloscope/.](http://teledynelecroy.com/oscilloscope/)" .
- [18] "TOHO ZINC, Soft magnetic materials of TOHO ZINC, HKBH datasheet."
- [19] Aperam Amilly Alloys, "Low Permeability Nanocrystalline μ Cores datasheets 095 015 B 200."
- [20] "MAGNETICS 0055174AY datasheet."
- [21] "Traco Power TSI-10N Series 10 Watt DC/DC Converter datasheet."
- [22] P. L. Dowell, "Effects of eddy currents in transformer windings," *Proceedings of the Institution of Electrical Engineers*, vol. 113. p. 1387, 1966.
- [23] Agilent Technologies, "4294A precision impedance analyzer 40 Hz - 110 MHz [http://www.home.agilent.com/.](http://www.home.agilent.com/)" .
- [24] J. J. Winders Jr., *Power Transformers: Principles and Applications*. CRC Press, 2002, p. 304.

Conclusion

In this thesis we introduce magnetic materials, their classifications and their applications with focus on soft magnetic materials used in power electronics. The two main categories of materials studied in our work are the iron powder and nanocrystalline materials. Powder cores have low permeability, intermediate saturation flux density and low hysteresis and DC losses. They allow assembling stable inductance and are slightly sensible to thermal aging. Nanocrystalline materials combine high saturation flux density, low losses and wide permeability range. Powder and nanocrystalline cores are mainly used in chokes, transformers, EMI filters and power conversion applications.

Each of studied materials has its specific hysteresis, dynamic and thermal behaviors. These behaviors were investigated by materials characterization for different frequencies and temperatures. These characterizations include static and dynamic B-H measurements and self-heating measurements. From these characterizations, magnetic properties, losses and frequency dependence are deduced as well as the influence of temperature on these materials.

Since different magnetic materials do not possess same behavior for the same thermal conditions, performance of the system containing magnetic components depends greatly on operating temperature range. Thus thermal effects on magnetic materials must be taken into account before introducing these materials in the field of application. To predict temperature influence on material's behavior and the trend of variation of magnetic models parameters as function of temperature, magnetic material characterization is essential.

Materials characterizations are then used to predict appropriate static and dynamic laws to describe the material's behavior and extract model's parameters. Static and dynamic magnetic modeling laws well known and widely used in electrical engineering are presented focusing on the models currently used in circuit simulation. In addition, principles of thermal modeling, thermal models and magneto-thermal coupling are explained. Modeling theory and techniques for circuit simulators including electrical, thermal, magnetic and mixed domains modeling techniques are discussed. Modeling languages and circuit simulation software namely VHDL-AMS and SIMPLORER used in the development of the complete magnetic component model are exposed.

The developed magnetic component model is a non-linear dynamic model for use in circuit simulators. It includes the material nonlinear hysteresis and dynamic behaviors with accurate modeling of winding and core losses in addition to thermal effects. The model is based on the principle of separation of static and dynamic contributions. In order to be adaptable for different kinds of magnetic materials, the magnetic component model consists of three major blocks: a winding block allowing the coupling between electrical and magnetic domains using Ampere's and Faraday's laws, a second block (static model) to describe the static hysteresis behavior of the magnetic material and a third block (dynamic model) to include dynamic effects in the core.

The choice of static and dynamic materials laws is based on the choice of materials. To describe the static behavior of the materials used in our work, a mathematical polynomial model is used. This model presented in chapter 2 is a reversible model limited to materials with low coercive field. Concerning material's dynamic behavior, Bertotti's model is used. This model is accurate and able to model dynamic hysteresis loops of the chosen materials. It separates dynamic losses into eddy current losses and excess losses by two flux derivative terms in the general model equation.

The parameters of the static model and their evolution as function of temperature are identified from the static measurements and using mathematical fitting. The dynamic parameter related to eddy currents is calculated from the electrical conductivity measured using a 4-point probes measurements. The second dynamic parameter related to walls motion effects is extracted from mathematical fitting of dynamic model equation to the measured B-H loop. Since the trend of variation of these parameters is monotonic, a linear approximation can express this variation as function of temperature. This linear function is implemented in the model to calculate each parameter at any temperature.

The magnetic component model is implemented in circuit simulation software "Simplorer" using VHDL-AMS modeling language. After the proper choice of static and dynamic material models and their parameters identifications, the component model is validated by modeling a Nanocrystalline-core inductor for different frequencies, temperatures and waveforms.

In the aim of testing the adaptability, reliability and accuracy of the developed model for use in power electronics applications, it is implemented in a buck converter application. The developed magnetic component model is tested for two candidate core materials, a Sendust powder core and a low permeability nanocrystalline core. Waveforms and losses of a both powder core and nanocrystalline inductors are simulated and compared to measured ones (maximum error of 3%). The model is validated for different current ripples, different resistive loads and a wide frequency range (10-100 kHz). DC bias is taken into account. Both continuous and discontinuous conduction modes are studied. Temperature effects on core losses for the nanocrystalline core inductor are also discussed.

In addition to the realized buck application, two other applications are discussed: a similar commercial buck converter from TRAPOWERR and a single-phase two-winding transformer. In the commercial buck converter the model was tested at 360 kHz switching frequency and a variably duty cycle. Simulated inductor current, voltage and B-H loop correspond to the measured ones. The model is able to represent magnetic component behavior at higher frequencies and duty cycles. In the two-winding transformer circuit simulations are performed to test the model in more than one winding application. The developed transformer model could predict the actual primary current, power losses and efficiency.

Finally the developed model is limited to negligible skin effects conditions, since the model doesn't take magnetic diffusion into account. Relaxation losses are partially taken into account (only dynamic) by the proposed component model. Both magnetic diffusion and relaxation losses effects will be studied in future work by implementing more complex static (relaxation) and dynamic (diffusion) material's laws. Also the post-doctoral work will be devoted for developing the transformer model and the experimental validation of simulations. A three phase transformer would be also one of our future perspectives.

Annexes

Annex A

VHDL-AMS Code (PPM)

```
LIBRARY ieee;
LIBRARY std;
LIBRARY basic_vhdlams;

----- VHDLAMS MODEL polynomial -----

USE basic_vhdlams.ALL;
USE std.ALL;
USE ieee.ALL;

----- ENTITY DECLARATION polynomial -----

ENTITY      polynomial IS

    generic (

        a1: real:= 0.0727);

    port (    QUANTITY B: in real;
              QUANTITY Hs: out real);

END ENTITY polynomial;

----- ARCHITECTURE DECLARATION arch_polynomial -----

ARCHITECTURE arch_polynomial OF polynomial IS

    CONSTANT uo: real:= 1.2566e-6;

    QUANTITY p1: real;
    QUANTITY p3: real;
    QUANTITY p5: real;
    QUANTITY B1: real;
    QUANTITY H1: real;
    QUANTITY T: real;

BEGIN

-----Static parameters-----

    T == 30.0;

    p1 == 0.05353 - (0.00013 * T);
    p3 == -1.492e-5 + (6.825e-8 * T);
    p5 == 1.79e-9 - (1.09e-11 * T);

    H1 == a1 * T + 29.52;
```



```

B1 == p1 * H1 + p3 * (H1)**3 + p5 * (H1)**5;

-----Static law-----

IF B > B1 USE Hs == B/uo - B1/uo + H1;
ELSE
  IF B < -B1 USE Hs == B/uo + B1/uo - H1;
  ELSE B == p1 * Hs + p3 * (Hs)**3 + p5 * (Hs)**5 ;
  END USE;
END USE;

END ARCHITECTURE arch_polynomial;

----- END VHDLAMS MODEL polynomial -----

```

Annex B

VHDL-AMS Code (BERTOTTI)

```
LIBRARY ieee;
LIBRARY std;
LIBRARY basic_vhdlams;

----- VHDLAMS MODEL BERTOTTI -----
USE basic_vhdlams.ALL;
USE std.ALL;
USE ieee.ALL;

----- ENTITY DECLARATION BERTOTTI -----
ENTITY DYN IS

    generic(
        s : real := 0.000009; -- Effective Area of Core
        l : real := 0.023); -- Effective Length of Core

    port(
        TERMINAL n1, n2 : MAGNETIC;
        QUANTITY B : out real;
        QUANTITY Hs : in real);

END ENTITY DYN;

----- ARCHITECTURE DECLARATION arch_BERTOTTI -----
ARCHITECTURE arch_DYN OF DYN IS

    QUANTITY MV ACROSS flux THROUGH n1 TO n2;

    ----- DYNAMIC PARAMETERS -----
    CONSTANT gamma: real := 1.531e-4; -- dynamic parameter 1
    CONSTANT alpha: real := 13.30e-2; -- dynamic parameter 2

    QUANTITY D: real;
    QUANTITY Hd: real;

    QUANTITY delta: real;

    ----- BEHAVIOUR -----
BEGIN

    B == flux/s;
    Hd == MV/l;

    D == B'dot;

    if Hs'dot > 0.0 use delta == 1.0;
        else delta == - 1.0;
        end use;

    Hd == Hs + gamma * D + alpha * delta*(delta*D)**0.5;

END ARCHITECTURE arch_DYN;

----- END VHDLAMS MODEL BERTOTTI -----
```

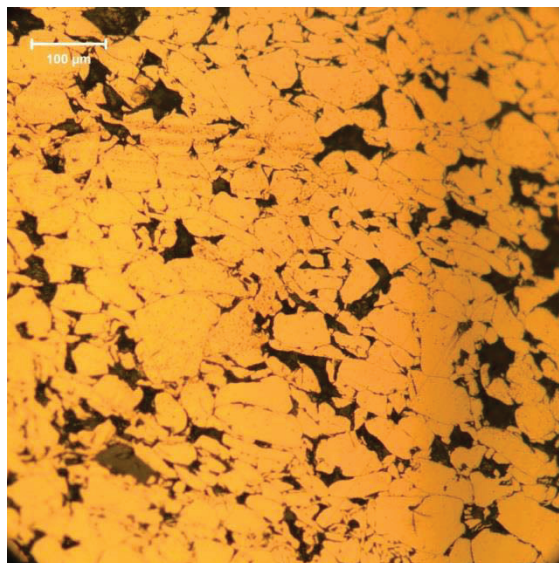
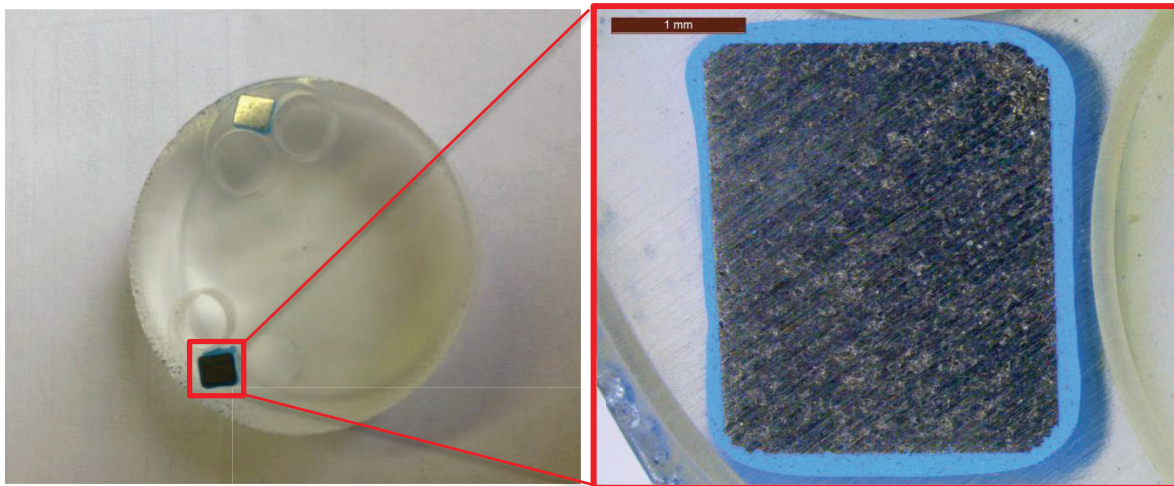
Annex C

Particle average size

The average particle size of a powder core is normally given by the manufacturer. However it may not be available for some cores as in the case of the powder core HKBH used in chapter 4. For this reason a specific procedure was followed to determine the average particle size of this core:

- The core is cut in half and placed in epoxy
- Smoothing of $1\mu\text{m}$ is applied
- Light microscopic images up to 100X were taken (images below)

From the obtained images, the average particle size is calculated using “*Hilliard Single-circle Procedure*”. This method consists of drawing a circle with a known radius on the image, calculating its perimeter and dividing it by the number of particles intercepted by the circle.



Résumé en Français

En génie électrique, la complexité croissante des dispositifs électroniques de puissance nécessite l'intervention d'une conception assistée par ordinateur. Aujourd'hui, le développement de systèmes électriques/électroniques est effectuée à l'aide de prototypes virtuels, au sein desquels les logiciels de simulation sont utilisés pour prédire le comportement des composants. Ceci permet de limiter le coût et le temps nécessaires à la réalisation de prototypes physiques.

Les composants magnétiques constituent une part majeure des appareils électroniques. Par conséquent la modélisation précise des matériaux magnétiques est nécessaire afin de prédire leur comportement réaliste dans des conditions d'exploitation variables. En fait, les caractéristiques non linéaires de ces matériaux et de leurs effets dynamiques et thermiques, ont une influence non négligeable sur les performances du système et doivent être prises en compte dans les simulations de circuits. En outre, la température induit des changements importants dans le comportement des composants et n'est pas prise en compte dans les modèles magnétiques existants.

Notre travail se déroule dans ce contexte, en proposant un modèle dynamique non-linéaire de composants magnétiques pour une utilisation dans les simulateurs de circuits. Il comprend les comportements d'hystérésis et dynamiques de matériaux, avec une modélisation précise des pertes fer et des pertes Joule, avec en plus des effets thermiques. Le langage VHDL-AMS est utilisé pour son aptitude à la modélisation multi-domaine, ce qui permet un couplage avec un modèle thermique. Le modèle du composant magnétique est implémenté dans le logiciel de simulation de circuits "Simplorer" et validé par la modélisation d'une inductance composé d'un noyau nanocristallin. Les effets de la fréquence, de la température et de la forme d'onde sont étudiés. Il est ensuite testé dans un convertisseur abaisseur, afin d'assurer une excitation non conventionnelle. Le modèle est validé pour différentes inductances, différentes ondulations de courant, différentes charges, une large gamme de fréquence (10 à 100 kHz) et pour des températures allant jusqu'à 200 °C.

Cette thèse se compose de quatre chapitres. Le premier chapitre présente les matériaux magnétiques actuellement utilisés dans les applications d'électronique de puissance. Puis les effets de la température sur ces matériaux et leur caractérisation à des fréquences et des températures variables sont étudiés. Le second chapitre concerne à la fois la modélisation magnétique et thermique, ainsi que le couplage qui les lie. Les lois magnétiques statiques et dynamiques, bien connues et largement utilisées, sont présentées. L'approche de la modélisation thermique et de la structure du modèle thermique est expliquée à l'aide des concepts d'éléments thermiques et de transfert d'énergie thermique. L'identification des paramètres de deux modèles magnétiques et thermiques est également présentée. Le travail sur le développement du modèle de composant magnétique est décrit dans le troisième chapitre. Nous expliquons la structure modulaire du modèle de composant magnétique et sa mise en œuvre dans le logiciel de simulation de circuits Simplorer, qui utilise le langage de modélisation VHDL-AMS. Le choix de ces deux lois statiques et dynamiques est expliqué. Les effets de la température sont introduits dans le modèle qui est validé pour un matériau nanocristallin, pour différentes températures et fréquences. Le quatrième chapitre est consacré à l'adaptabilité, la fiabilité et la précision du modèle développé pour utilisation dans des

applications d'électronique de puissance. Le comportement de composant magnétique dans un convertisseur abaisseur est étudié. Une conception de circuit à tension, fréquence et charge variables est réalisée. Pertes fer et pertes joules dans des conditions variables sont mesurées. Les résultats de mesures sont comparés à ceux simulés pour différents inducteurs, à des fréquences, des densités de flux, des composants continus et des températures variables.

Enfin une conclusion générale résume la thèse et clarifie nos perspectives pour les travaux futurs.

1. Les Matériaux magnétiques en électronique de puissance

1.1 Introduction

Les alimentations, transformateurs, moteurs électriques, téléphones mobiles, ordinateurs et de nombreux autres dispositifs s'appuient sur le magnétisme et les matériaux magnétiques. Le comportement magnétique d'un matériau dépend de sa structure, et en particulier de la configuration de ses électrons. La réponse d'un matériau magnétique à un champ magnétique appliqué H (A/m), spécifie si le matériau est magnétique ou non ainsi que de son type de magnétisme.

1.1.1 Les matériaux utilisés dans l'électronique de puissance

Basé sur leurs caractéristiques d'hystérésis, les matériaux magnétiques doux occupent différentes applications dans le domaine de l'électronique de puissance. Ils sont classés en trois principales catégories ayant des propriétés différentes (saturation, champ coercitif, perméabilité et résistivité). Ces trois principaux matériaux magnétiques sont les ferrites, les poudres de fer et les matériaux nanocristallins.

1.1.1.1 Les Ferrites

Les ferrites sont des matières céramiques chimiquement inertes ayant une structure cubique magnétique. Ce sont des matériaux cassants, stables et avec une haute résistivité. Les ferrites sont des oxydes métalliques ayant comme structure générale XFe_2O_4 , dans laquelle X est l'un des métaux de transition : Fe, Ni, Zn, Mn, Cu, Ba, Co et Mg. Ces métaux sont mélangés, broyés, et enfin pressés pour assurer la forme finale requise du noyau magnétique. Un chauffage jusqu'à 1300 °C est nécessaire pour fritter le matériau et assurer les propriétés magnétiques souhaitées.

1.1.1.2 Les Poudres de fer

Le noyau est constitué de petites particules de fer pur et/ou d'alliages métalliques, compactées puis enrobées d'une couche isolante mince. L'isolant réduit les courants de Foucault en augmentant la résistivité du matériau en vrac, et diminue la perméabilité en agissant comme de petits entrefers à l'intérieur du matériau du noyau. Pendant le compactage, des contraintes internes se produisent dans le matériau. Un traitement thermique est appliqué afin de diminuer ces contraintes et augmenter la résistance du matériau. Enfin les noyaux de poudre sont recouverts par un revêtement protecteur pour améliorer la résistance mécanique et l'isolation.

1.1.1.3 Les Nanocristallins

Les matériaux nanocristallins sont le résultat de processus de production high-tech à partir de matières premières à faible coût comme le silicium et le fer. Ce processus permet de produire une nouvelle génération de matériaux magnétiques doux qui possèdent des propriétés magnétiques intéressantes. Les nanocristallins sont formés par un ensemble de régions de structures cristallines cohérentes (les grains), ayant un diamètre moyen de grain de 1 à 50 nm. Ces régions présentent un ordre magnétique et sont noyées dans une matrice magnétique ou non. Les rubans d'alliages nanocristallins sont faits par solidification rapide, des techniques de dépôt et les réactions à l'état solide où le matériau initial peut être à l'état amorphe, puis

cristallisées. La composition de l'alliage, la structure cristalline, la morphologie et la microstructure déterminent les propriétés magnétiques du matériau. Les rubans produits sont ensuite utilisés pour former des noyaux toroïdaux fragiles qui sont recuits en présence d'un champ magnétique pour former des cristaux ultrafins.

Dans cette thèse, nous étudions les poudres et les nanocristallins seulement en raison de leur haute performance dans notre domaine d'application et la gamme de fréquence. En outre, les ferrites ont été largement étudiées contrairement aux matériaux nanocristallins et poudre. En fait les matériaux poudre fer et nanocristallins ont une meilleure densité de flux à saturation, des pertes d'hystérésis inférieures, et un effet de polarisation continue plus faible que les ferrites, mais les ferrites ont des pertes inférieures à très hautes fréquences en raison de leur haute résistivité. En ce qui concerne le comportement thermique, les ferrites ont une température de fonctionnement et de Curie inférieures. Les effets de la température sur les matériaux magnétiques sont présentés dans la section suivante.

1.2 Effets de la Température

La température influe sur le comportement magnétique du matériau en modifiant ses propriétés magnétiques. Une évolution non linéaire des paramètres magnétiques en fonction de la température existe. L'aimantation à saturation des matériaux magnétiques diminue avec la température, puis tombe à zéro à la température de Curie. Cependant, d'autres propriétés telles que le champ coercitif et la perméabilité peuvent varier différemment d'un matériau à l'autre.

Etant donné que les matériaux magnétiques différents n'ont pas même comportement pour la même température, la performance du système contenant des composants magnétiques dépend fortement de la température de fonctionnement. Ainsi les effets thermiques doivent être pris en compte avant d'introduire des matériaux dans l'application. Pour prédire l'influence de la température sur les matériaux et la tendance de la variation des paramètres magnétiques en fonction de la température, la caractérisation de matériaux magnétiques est nécessaire. A partir de cette caractérisation, les propriétés magnétiques, les pertes et la dépendance de fréquence sont également déduites.

1.3 Caractérisation des Matériaux Magnétiques

1.3.1 Principe de Caractérisation

Les matériaux magnétiques sont caractérisés en utilisant des méthodes différentes. Dans cette thèse, les caractérisations BH sont principalement utilisées. A partir d'un cycle BH mesuré les propriétés magnétiques macroscopiques telles que la perméabilité, la densité de flux à saturation, le magnétisme résiduel, et le champ coercitif peuvent être extraits. Les pertes magnétiques sont également disponibles. Les boucles d'hystérésis sont mesurées à différentes températures et fréquences pour étudier ces effets sur le comportement magnétique.

La caractérisation BH consiste à tracer la densité de flux magnétique B en fonction du champ magnétique appliqué H . Une structure de tore de matériau magnétique est considérée pour assurer un flux de fuite le plus faible. Le noyau sous test doit être muni de deux

enroulements. Le premier enroulement est alimenté avec un courant alternatif. Ce courant est directement proportionnel à H . Le second enroulement est utilisé pour mesurer la tension induite proportionnelle à B .

Afin de caractériser les matériaux magnétiques dans des conditions de fonctionnement variables, un banc d'essai expérimental est assemblé dans notre laboratoire permettant d'appliquer des formes d'ondes, niveaux d'induction, fréquences et températures variables. Le banc d'essai est représenté sur la Figure 1-1.

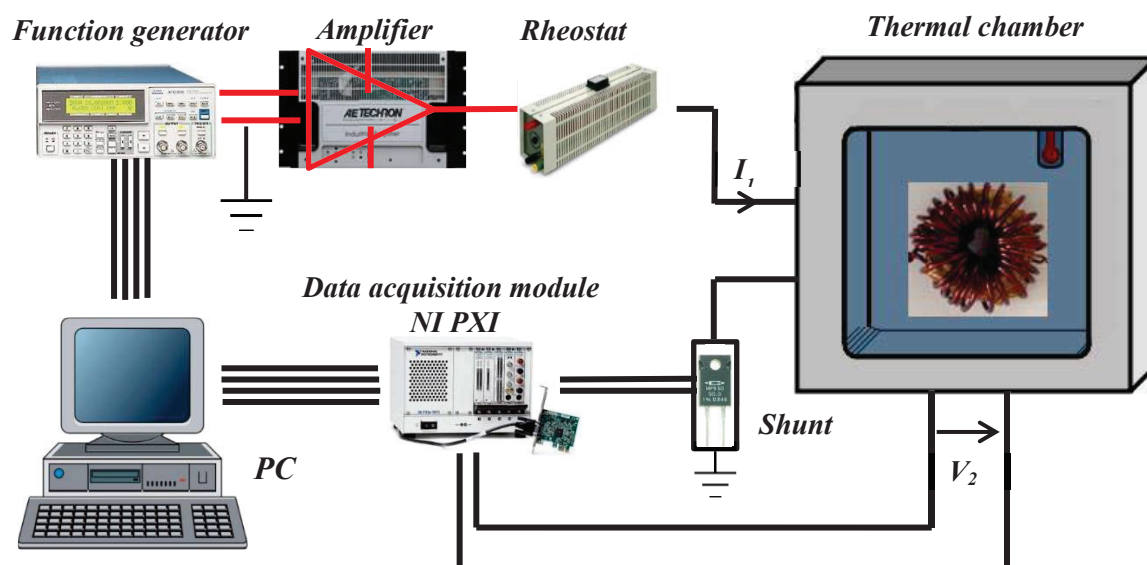
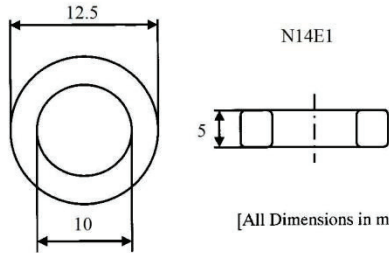


Figure 1-1: Banc de caractérisation BH

1.3.2 Les mesures à températures et fréquences variables

Le banc d'essai ci-dessus est utilisé pour caractériser différents matériaux avec différentes formes (ici nous avons utilisé seulement des tores). Parmi les matériaux étudiés, le nanocristalline Nanophy® N14E1, fourni par MECAGIS, est choisi en raison de ses propriétés intéressantes, dont la densité de flux à saturation élevée, son faible champ coercitif et sa perméabilité relative élevée, comme indiqué en Figure 1-2.

N14E1	
Relative permeability	30000
Losses (25 kHz, 0.2 T, 100°C)	3 W/kg
Saturation induction	1.2 T
Coercive field	5 to 10 mA/cm
Curie temperature	600 °C
Ribbon thickness	20µm
Resistivity	1.15µΩ.m
Max. operating temperature	150 °C



N14E1

[All Dimensions in mm]

Figure 1-2: Dimensions et propriétés du N14E1 [41].

Pour caractériser ce matériau, différentes mesures sont effectuées sur un transformateur d'essai pour des températures et des fréquences variables ayant les dimensions de la Figure

1-2. Un courant sinusoïdal est appliqué à l'enroulement primaire, pour créer un champ magnétique H et la densité de flux B est obtenue à partir de la tension secondaire mesurée sous des températures comprises entre 25 °C et 275 °C. Les résultats de mesures sont présentés dans la figure 1-3 montrant l'influence de la température et de la fréquence sur le comportement magnétique (jusqu'à 40 kHz) à 25 °C.

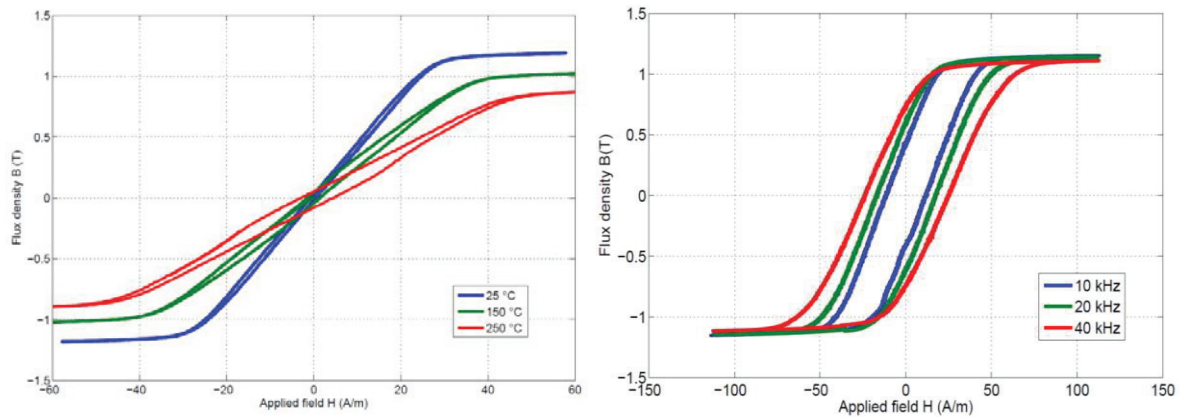


Figure 1-3: Densité de flux mesurée en fonction du champ appliqué à $f = 10$ Hz pour des températures différentes (à gauche) et à 25 °C pour différentes fréquences (à droite).

Nous remarquons que le champ coercitif statique augmente avec la température, mais reste relativement faible. Ce phénomène est généralement observé dans certains matériaux nanocristallins. L'augmentation de la température provoque une diminution de la densité de flux à saturation et de la perméabilité. Les Effets de la fréquence sont résumés par l'élargissement de cycles BH avec l'augmentation de la fréquence, ce qui signifie des pertes plus élevées à des fréquences plus élevées.

Les mesures effectuées dans cette section sont pour deux ou trois périodes de temps seulement pour éviter l'auto-chauffage des noyaux magnétiques. Ainsi, ils visent à étudier le comportement magnétique sous une température constante appliquée. Néanmoins l'auto-chauffant est un autre aspect de matériaux magnétiques qui est due à un fonctionnement de longue durée. Cet aspect est également important dans la caractérisation des matériaux magnétiques.

1.3.3 Mesure de l'auto échauffement

Lorsque les composants magnétiques fonctionnent en permanence, les pertes fer et pertes Joules causent l'auto-échauffement du composant magnétique. Les mesures d'auto-échauffement sont nécessaires pour le développement de modèles thermiques qui est une partie de notre travail.

Dans les mesures d'auto-échauffement, un inducteur de même matériau (N14E1) est alimenté par un courant sinusoïdal de 0,6 A à 20 A et 40 kHz pour assurer l'auto-échauffement. Puis l'évolution dynamique des températures de noyau (T_{core}) et d'enroulement ($T_{winding}$) est mesurée à l'aide d'un banc de test d'auto-échauffement. Ces températures et sont présentés en Figure 1-4.

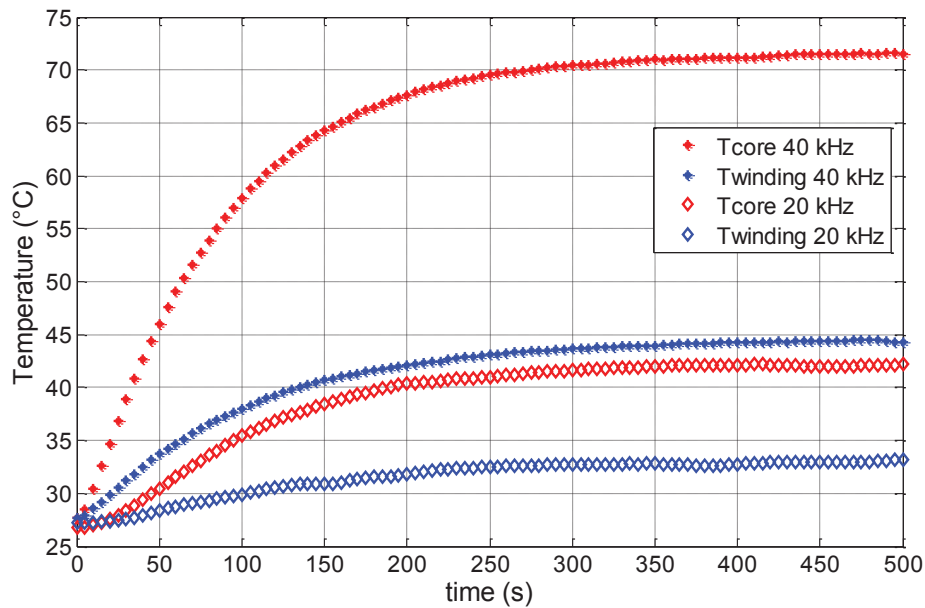


Figure 1-4: Mesures d'auto-échauffement: températures de noyau et enroulement en fonction du temps.

L'élévation de la température du noyau magnétique à cause de l'auto-échauffement a un effet non négligeable sur les propriétés magnétiques. Il faut noter qu'à plus haute fréquence les pertes magnétiques sont plus étendues et donc la température de noyau est plus élevée. Pour une meilleure performance thermique cet aspect doit être pris en compte avant d'introduire des matériaux dans leur application. Cet aspect est traité en intégrant un modèle thermique avec le modèle magnétique. Les deux modèles et leur couplage sont détaillés dans le prochain chapitre.

1.4 Conclusion

Dans ce chapitre, les matériaux magnétiques utilisés dans l'électronique de puissance et leurs propriétés sont présentés. Influence de la température sur ces matières est discuté. La caractérisation de matériaux magnétiques et les bancs de mesure disponibles sont également présentés dans ce chapitre.

Finalement, chaque matériau a son comportement hystérétique, dynamique et thermique. Les propriétés macroscopiques des matériaux magnétiques doux sont extraites de leurs boucles d'hystérésis mesurées à différentes températures et fréquences. La caractérisation des matériaux magnétiques permettent la prédiction des modèles statiques et dynamiques appropriées représentant ces comportements. En fait, cette étape est indispensable avant la modélisation.

Après l'introduction de matériaux magnétiques utilisés dans l'électronique de puissance, l'effet de la température et la caractérisation des matériaux dans ce chapitre, la modélisation magnétique et thermique des composants magnétiques sont expliqués dans le chapitre suivant.

2. Modélisation Magnétique et Thermique

2.1 Introduction

La modélisation est une étape impérative dans tout projet de conception d'ingénierie. Elle permet de voir les systèmes à réaliser à partir de plusieurs points de vue pour assurer leur performance souhaitée. La modélisation permet également de découvrir les erreurs antérieures et de réduire les défauts du système.

Avec la nécessité pour la gestion et la conversion efficace de l'énergie dans les circuits électroniques, il devient très important d'assurer que les composants magnétiques fonctionnent dans leurs limites de performance thermique, magnétique et électrique. A cet effet, les modèles standards et linéaires des composants magnétiques dans les simulateurs de circuit ne sont pas suffisants. Dans de nombreuses applications comme les alimentations à découpage et les convertisseurs de puissance, un modèle précis du matériau magnétique est nécessaire pour construire des inducteurs et des transformateurs.

Pour cette raison, dans ce chapitre, nous nous concentrerons sur la modélisation des matériaux magnétiques, par l'étude de modèles de matériaux magnétiques existants. Les modèles disponibles dans les simulateurs de circuits et leurs inconvénients sont présentés. La modélisation thermique y compris les concepts de transfert de chaleur et les réseaux thermiques sont également étudiés pour développer un modèle thermique dynamique dans le but d'un couplage magnéto-thermique.

2.2 Modélisation magnétique

Dans le but de modélisation précise de composants magnétiques, un modèle de matériau magnétique comprenant le noyau de la composante est essentiel. Le modèle de ce matériau décrit le comportement d'hystérésis dans des conditions de fonctionnement statique (modèle statique) en plus de le comportement dynamique à cause de courants de Foucault et des mouvements des parois (modèle dynamique). Basé sur l'hypothèse de la séparation des pertes, différents modèles de matériaux statiques et dynamiques existent, nous expliquons brièvement ci-dessous les plus connus en détaillant les modèles retenues pour notre application.

2.2.1 Modèles statiques d'hystérésis magnétiques

Un large choix de modèles magnétiques statiques existe pour décrire le comportement statique du matériau. Certains d'entre eux sont purement analytiques comme le modèle de Rayleigh, le modèle Fröhlich, le modèle Chan-Vladimirescu, et le modèle Hodgson. Ces modèles sont simples à mettre en œuvre mais n'ont aucun aspect physique, ne sont pas réversibles et ont de nombreuses limitations. Le modèle polynomial est réversible mais limité à des matériaux à faible champ coercitif. D'autres modèles sont fondés sur des considérations phénoménologiques et statistiques telles que Preisach-Néel qui a besoin d'une fonction de distribution et un grand nombre de données expérimentales. Il existe d'autres modèles magnétiques qui sont basés sur des principes physiques, plutôt que strictement mathématiques. Le plus connu est le modèle Jiles-Atherton introduit en 1983 en présentant quelques équations pour la magnétisation de matériaux ferromagnétiques.

2.2.1.1 Modèle Polynomial

Ce modèle statique ne représente pas le phénomène d'hystérésis dans les matériaux, c'est un modèle purement mathématique adapté aux matériaux de très faible champ coercitif. En fait, c'est une fonction polynomiale par morceaux. La saturation est modélisée par un polynôme d'ordre 1 de pente μ_0 et la zone centrale de la courbe d'hystérésis est modélisée par un polynôme d'ordre n , comme montre la Figure 2-1.

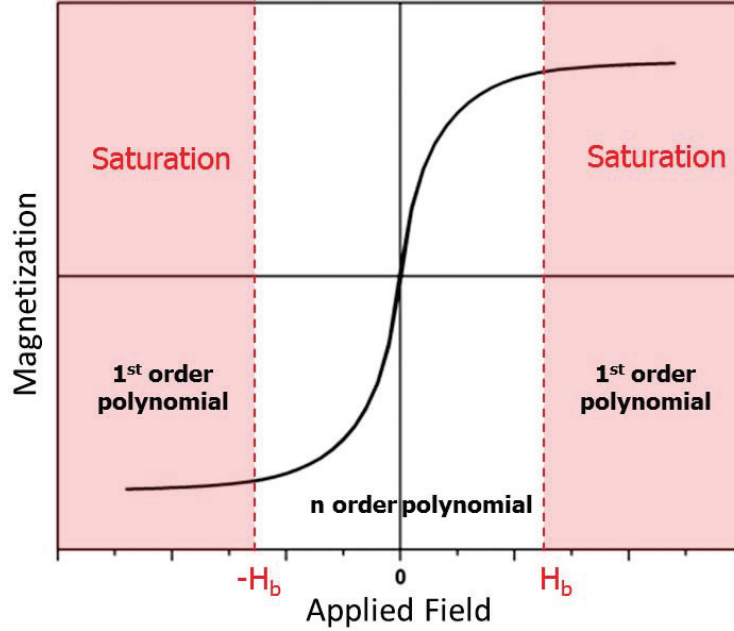


Figure 2-1: Modèle Polynomial

H_b est la valeur de H pour atteindre la saturation. Ce modèle est défini par les équations suivantes:

$$B = \begin{cases} \mu_0(H - H_b) + P(H_b) & \text{if } H \geq +H_b \\ P(H) & \text{if } |H| < H_b \\ \mu_0(H + H_b) - P(H_b) & \text{if } H \leq -H_b \end{cases} \quad (2.1)$$

Où P est un polynôme dans \mathbb{R} de telle sorte que :

$$P(X) = \sum_{i=0}^n p_i X^i \quad (2.2)$$

La précision et le nombre de paramètres de ce modèle dépendent de l'ordre n du polynôme central. Par exemple, pour $n = 5$, 4 paramètres (P_1 , P_3 , P_5 et H_b) sont tenus envisager même les paramètres sont nulles en raison de la parité impaire de la courbe. Il serait recommandé de choisir un ordre n en fonction du comportement statique de chaque matériau car différents matériaux peuvent nécessiter des polynômes à différents ordres.

2.2.2 Modèles dynamiques d'hystérésis magnétiques

Lorsque les matériaux magnétiques sont soumis à des champs magnétiques dynamiques, les pertes dues aux courants de Foucault et aux mouvements des parois sont induits. Ces

pertes augmentent avec la fréquence et ne sont pas prises en compte par les modèles magnétiques statiques. Ainsi les modèles dynamiques sont nécessaires pour représenter le comportement magnétique dynamique des matériaux. Concernant les modèles dynamiques, il n'y a pas un vaste choix, en raison du fait que les pertes magnétiques ne sont pas encore totalement comprises, en particulier les pertes anormales dues au mouvement des parois des domaines. Nous présentons ici certains de ces modèles : modèle dynamique de Preisach-Néel, modèle dynamique de Jiles-Atherton, et modèle de DSF (Dynamic Static Feedback Model)

2.2.2.1 Modèle de Bertotti

Ce modèle dynamique est basé sur le principe de la séparation des pertes entre contributions statiques et dynamiques. La théorie de Bertotti suppose que les pertes dynamiques sont la somme des deux pertes classiques et excédentaires.

G. Bertotti déclare dans sa théorie que le comportement à grande échelle des domaines magnétiques peut être décrit en termes d'objets magnétiques (MO). Chacun de ces objets magnétiques dynamiques, statistiquement indépendants correspond à un groupe de domaines magnétiques voisins. Le processus de magnétisation dans une section transversale du matériau peut être décrit en termes d'un nombre \tilde{n} d'objets magnétiques simultanément actifs. Cette quantité de \tilde{n} décrit par (2.3), est une fonction du champ H_{exc} et l'ensemble $\{P\}$ de paramètres caractérisant la structure de domaine et la microstructure du matériau.

$$\tilde{n}(H_{exc}, \{P\}) = \tilde{n}_0 + \frac{H_{exc}}{V_0} \quad (2.3)$$

ou les informations de la microstructure dans ce cas sont prises en compte par \tilde{n}_0 , qui représente le nombre de MO actif à $f \rightarrow 0$ et le champs magnétique V_0 caractérisant la distribution statistique des champs coercitifs locaux.

Cette théorie donne une interprétation naturelle de la dépendance des pertes excédentaires à la fois sur la polarisation maximale et la fréquence. Basée sur elle, le champ magnétique total est la somme du champ statique due à l'hystérésis et du champ dynamique due aux courants de Foucault et aux effets de mouvements de parois (2.4).

$$H_{total} = H_s + H_{eddy} + H_{excess} \quad (2.4)$$

$$H_{total}(t) = H_s(B(t)) + \gamma \cdot \frac{dB(t)}{dt} + \alpha \cdot \delta \cdot \left| \frac{dB(t)}{dt} \right|^{\frac{1}{2}} \quad (2.5)$$

Ou γ , α , et δ sont les coefficients liées aux courants de Foucault, aux mouvements des parois et une fonction signe, présenté en (2.6). γ dépend de la conductivité σ et l'épaisseur d du matériau pour les matériaux enrubannés. α est une fonction de champ caractéristique V_0 , un coefficient $G \approx 0,136$, et S la section magnétique.

$$\gamma = \frac{\sigma d^2}{12} \quad \alpha = \sqrt{\sigma G V_0 S} \quad \delta = \text{sign}\left(\frac{dB}{dt}\right) \quad (2.6)$$

2.2.3 Modèles disponibles dans les simulateurs de circuit

Le choix d'un modèle de matériau magnétique approprié pour une utilisation dans une simulation de circuit se résume à une variété de facteurs, y compris la facilité de mise en œuvre, la précision, la vitesse de la simulation et de la bonne convergence. Le modèle de Jiles-Atherton a été largement utilisé car il répond généralement à ces exigences. Il est mis en œuvre en utilisant des équations simples avec des paramètres significatifs liés aux aspects physiques. Le modèle de Preisach sert principalement dans l'analyse des éléments finis, mais n'a pas été largement utilisé pour la simulation de circuit. Le modèle Hodgdon serait particulièrement utile dans des applications dépendant de la fréquence.

Les modèles des matériaux magnétiques introduits dans la simulation de circuit sont : le modèle de Jiles–Atherton (*SPICE*, *Simplorer* and *Saber*), le modèle de Chan–Vladirimescu (*I-Spice*), le modèle de Preisach–Néel (*Saber*) et le modèle de Hodgdon (*Saber*).

Ces modèles sont principalement statiques, mais il n'y a pas de modèle dynamique mise en œuvre dans les simulateurs de circuits. En fait, certaines techniques ont été considérées pour inclure des courants de Foucault aux modèles mentionnés précédemment. Par exemple, dans *Simplorer*, une résistance est connectée en parallèle au modèle Jiles-Atherton pour avoir un circuit électrique équivalent à un modèle DSF. Mais, en général, les effets et les pertes dynamiques ne sont pas étudiées dans les simulateurs de circuits.

En conclusion, le modèle de Jiles-Atherton émerge comme le plus utilisé dans la simulation de circuit (disponible dans trois simulateurs commerciaux). Les avantages du modèle de JA sont l'aspect physiques et sa mise en œuvre pratique. Les inconvénients comprennent la modélisation des boucles mineures et l'extraction des paramètres. Le modèle Preisach–Néel est peu mise en œuvre en raison de l'extraction de paramètres, la dépendance de température et de la difficulté à mettre en œuvre. Le modèle Hodgdon a un avantage spécifique qui est la prise en compte de la fréquence et Chan-Valdirimrscu a un avantage spécifique qui est l'extraction de paramètres.

2.3 La modélisation thermique

La modélisation thermique des composants magnétiques est relativement récente. Les premiers travaux dans ce domaine ont commencé en milieu des années 90 par BJ Swart et JA Ferreira. Le concept de modèle thermique et le couplage magnéto-thermique sont démontrés dans ce chapitre.

2.3.1 Transfer de chaleur

Fondamentalement, le transfert de chaleur est le flux d'énergie thermique entraîné par un non équilibre thermique à travers une frontière bien définie. C'est un processus dans lequel le flux thermique est transféré d'une région de haute température à une autre région de température inférieure. Le transfert de chaleur est classé en plusieurs modes ou mécanismes, tels que la conduction thermique, la convection thermique et le rayonnement thermique.

2.3.2 Eléments Thermiques

Lorsque deux objets ont des températures différentes, il existe une tendance à la chaleur d'être transférée à partir de la zone chaude vers la zone froide, dans le but d'égaliser les

températures. Pour une différence de température donnée, le taux de transfert de chaleur varie en fonction de la résistance thermique du trajet entre les zones chaudes et froides. La nature et la valeur de la résistance thermique dépendent du mode de transfert de chaleur associé. La capacité d'un système de stockage d'énergie thermique est appelée la capacité thermique mesurée en J/K. Elle peut être calculée par le produit de la masse du système et de la chaleur spécifique du matériau ($C = mc$).

2.3.3 Modèle Thermique

Comme le montre le premier chapitre, la performance du système contenant des composants magnétiques dépend en grande partie des aspects thermiques. Pour cette raison, il est d'un grand intérêt à intégrer le comportement thermique des composants en simulation. Ce comportement thermique est étudié par la mise en œuvre du modèle thermique du composant magnétique. Ce modèle est en mesure d'évaluer l'élévation de température dans le noyau magnétique et les enroulements.

Le modèle thermique développée dans cette thèse est basée sur l'approche d'analyse nodale. Dans l'analyse nodale, le système est modélisé par un circuit équivalent thermique avec différentes zones isothermes appelés nœuds. Considérant un composant magnétique largement utilisé, un inducteur, le circuit thermique dispose de deux zones isothermes ou deux nœuds, le noyau et l'enroulement, comme montre le Figure 2-2. Les pertes fer et pertes Joules sont modélisées par des sources de flux de chaleur. La température ambiante est modélisée par une source de température. Les capacités thermiques représente l'énergie stockée dans le noyau magnétique et l'enroulement. Le transfert de chaleur entre les nœuds est modélisé par les résistances thermiques.

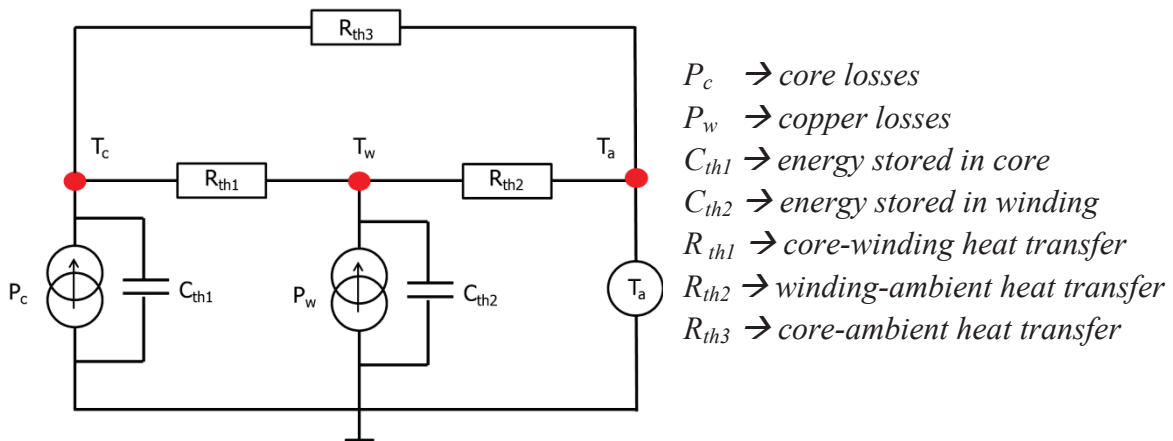


Figure 2-2: Modèle thermique d'un inducteur (circuit thermique équivalent)

Normalement, les modes de transfert de chaleur pour un noyau magnétique sont la conduction thermique, la convection thermique à l'air et les émissions rayonnées. Comme nous supposons la température uniforme dans le noyau, la conduction thermique entre le centre et la surface du noyau est négligée. De plus, le rayonnement de la chaleur du noyau est généralement ignoré car il est négligeable par rapport aux autres formes de transfert de chaleur, mais peut être inclus dans un modèle si nécessaire. Ainsi, le transfert de chaleur principal ou énergie dissipée à partir du noyau se fait par convection.

Après avoir trouvé le réseau thermique équivalent d'une inductance, l'étape suivante consiste à déterminer les éléments thermiques (résistances et capacités thermiques). Ces éléments peuvent être obtenus expérimentalement (en utilisant le banc d'essai présenté dans le chapitre 1) et par le calcul. L'approche pour l'identification de ces éléments est expliquée dans la section suivante.

2.3.4 Identification de Paramètres

Considérant le circuit thermique de la figure 2-2, les équations différentielles aux nœuds T_c et T_w sont présentés par (2.7) et (2.8) respectivement.

$$C_{th1} \frac{dT_c}{dt} = P_c - \frac{T_c - T_w}{R_{th1}} - \frac{T_c - T_a}{R_{th3}} \quad (2.7)$$

$$C_{th2} \frac{dT_w}{dt} = P_w - \frac{T_w - T_c}{R_{th1}} - \frac{T_w - T_a}{R_{th2}} \quad (2.8)$$

Les pertes fer P_c et pertes Joules P_w sont donnés par des mesures magnétiques (cycle BH). La température de noyau T_c et la température d'enroulement T_w sont évalués selon la méthode de mesure auto-échauffement présenté dans la section 1.4.4. Ensuite, pour calculer les résistances thermiques, le régime permanent est considéré où les capacités thermiques sont complètement chargées. Dans ce cas-là le système d'équations (2.9) (2.10) (2.11) est résolu pour obtenir les valeurs de R_{th1} , R_{th2} , et R_{th3} . Les valeurs des résistances sont alors substituées dans les équations (2.7) et (2.8) pour trouver les valeurs des capacités thermiques C_{th1} et C_{th2} .

$$P_c = \frac{T_c - T_w}{R_{th1}} + \frac{T_c - T_a}{R_{th3}} \quad (2.9)$$

$$P_w = \frac{T_w - T_c}{R_{th1}} + \frac{T_w - T_a}{R_{th2}} \quad (2.10)$$

$$\frac{T_c - T_a}{R_{th3}} = \frac{T_c - T_w}{R_{th1}} + \frac{T_w - T_a}{R_{th2}} \quad (2.11)$$

2.4 Couplage Magnétothermique

Comme on le voit clairement, d'une part, le modèle thermique a besoin des pertes du composant magnétique comme entrées pour calculer la température des éléments constitutifs. D'autre part ces températures sont nécessaires pour le modèle magnétique pour faire varier les propriétés magnétiques en fonction de la température. Pour ces raisons, il est d'une grande importance de coupler les deux modèles dans la simulation de circuit. Le processus de couplage magnétothermique est clarifié dans la Figure 2-3.

En effet, les pertes fer sont estimées dans le modèle magnétique en intégrant le champ magnétique total et la densité de flux. Les pertes dans le cuivre sont calculées en utilisant la loi de Joule. Ces pertes sont injectées aux sources de flux de chaleur du modèle thermique

pour calculer les températures du noyau et de l'enroulement, qui sont à leur tour injectés au modèle magnétique. Cette rétroaction permet de considérer les effets de la température sur le comportement du composant magnétique.

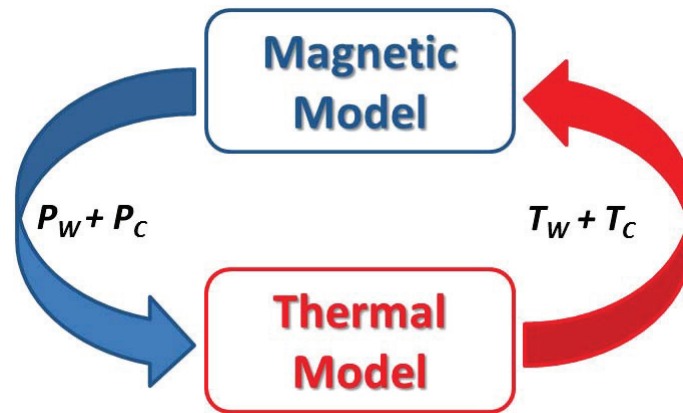


Figure 2-3: Couplage Magnétothermique

2.5 Conclusion

En ce qui concerne la modélisation magnétique, les modèles d'hystérésis statiques et dynamiques des matériaux magnétiques ont été présentés dans ce chapitre. Les Avantages et les inconvénients de chaque modèle sont adressés. Les quatre modèles Jiles-Atherton, Chan-Vladirimescu, Preisach-Néel et modèles Hodgdon disponibles dans les simulateurs de circuits ont été comparés également.

En ce qui concerne la modélisation thermique des composants magnétiques, le transfert de chaleur et les éléments thermiques sont expliquées brièvement. Ensuite, un modèle thermique de l'inducteur basé sur conception de circuit équivalent et l'analyse nodale est présentée. L'approche de l'identification des paramètres thermiques de modèle à partir des mesures d'auto-échauffement a été discutée.

3. Prototypage virtuel et modèle développé

3.1 Introduction

Le prototypage virtuel est essentiel dans le développement de nouveaux dispositifs électroniques de puissance comme les convertisseurs statiques de puissance. Simulateurs de circuits permettent l'optimisation de prototypes de circuits complexes en associant des modèles de composants passifs et actifs. Les modèles de composants individuels existent et sont associés entre eux pour former un modèle de système complet. Par conséquent, nous serons capables de prédire le comportement réaliste de l'ensemble du système dans des conditions de fonctionnement variables.

Notre travail est principalement basé sur la 'modélisation comportementale' des composants magnétiques, mais prend avantage de la modélisation structurelle également pour séparer les modèles statiques, dynamiques, et le modèle d'enroulement.

3.2 Modèle Développé

Le modèle dynamique non linéaire développé des composants magnétiques pour une utilisation dans les simulateurs de circuit est présenté dans cette section. Il inclut le comportement d'hystérésis non linéaire du matériau avec une modélisation précise des pertes fer et pertes joules plus les effets thermiques qui ne sont pas pris en compte par les modèles existants dans les simulateurs de circuits. Le modèle est basé sur le principe de la séparation des contributions statiques et dynamiques ainsi que la théorie de Bertotti. VHDL-AMS est utilisé comme un langage de modélisation en raison de sa fonction de modélisation multi-domaine, permettant le couplage avec un modèle thermique.

3.2.1 Structure de Modèle

Pour garantir une bonne précision et afin d'être adaptable à différents types de matériaux magnétiques, le modèle de composant magnétique adopte une approche structurale de modélisation. En conséquence, le modèle se compose de 3 blocs majeurs, comme indiqué sur la Figure 3-1: un enroulement permettant le couplage entre les domaines électriques et magnétiques, un modèle statique pour décrire le comportement statique du matériau magnétique et un modèle dynamique pour tenir compte des pertes classiques et excédentaires. Le langage de programmation VHDL-AMS est utilisé en raison de sa fonctionnalité de modélisation multi-domaine de plus il est mis en œuvre dans plusieurs simulateurs de circuits. Le modèle de composant magnétique obtenu est complet et permet de coupler les domaines électriques, magnétiques et thermiques présenté par la Figure 3-1. Une description de la structure du modèle et de chaque bloc sont présentées ci-dessous.

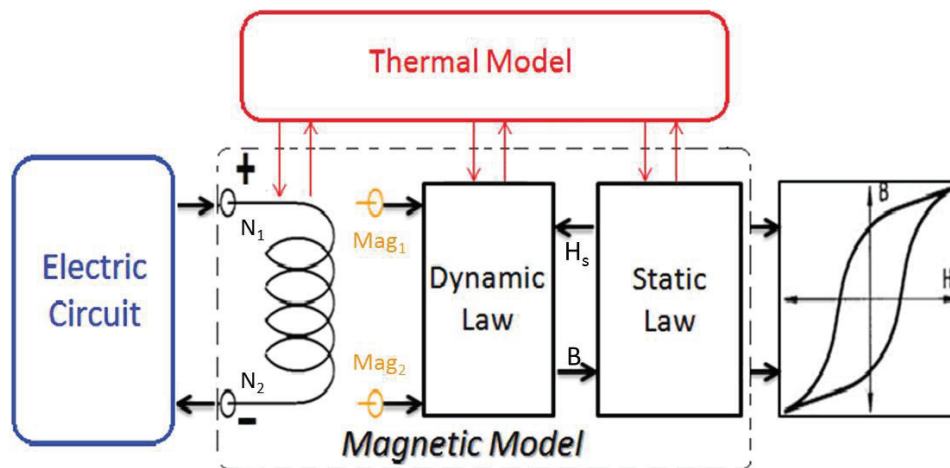


Figure 3-1: Structure du modèle de composant magnétique.

3.2.1.1 Modèle d'enroulement

Le modèle d'enroulement (Figure 3-2) représente un élément de couplage entre le circuit électrique et magnétique. Il convertit l'énergie électrique en énergie magnétique et vice versa (flux d'énergie bidirectionnel). Le modèle a des bornes électriques, n1 et n2 et des bornes magnétiques, Mag1 et Mag2. Il dispose de deux paramètres globaux, le nombre de tours (N) pour la quantité de couplage entre les domaines magnétiques et électriques et la résistance de l'enroulement (R)

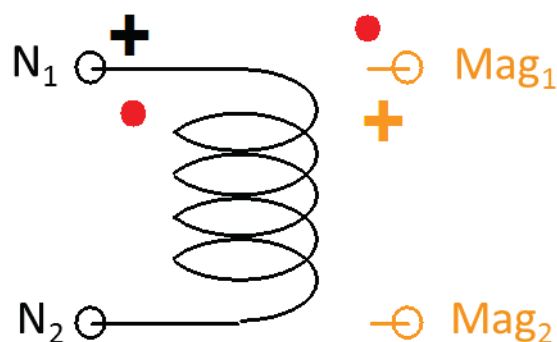


Figure 3-2: Modèle d'enroulement.

Le modèle d'enroulement est décrit par les deux équations suivantes:

$$v(t) = -N \cdot \frac{d\phi}{dt} + R \cdot i(t) \quad (3.1)$$

$$MMF = N \cdot i(t) \quad (3.2)$$

3.2.1.2 Modèle de Bloc Dynamique

Le modèle dynamique est le centre du modèle de composant représentant le comportement global du matériau magnétique de noyau. Il décrit la variation de champ magnétique H totale en fonction de la densité de flux ou vice versa (ou simplement le cycle BH).

Ce champ total est la somme du champ statique calculée par le modèle statique et des champs dynamiques dues aux pertes par courants de Foucault et des pertes excédentaires calculées par le modèle dynamique (principe de séparation des pertes). Ainsi, le modèle dynamique est connecté au modèle statique de telle sorte que la densité de flux B soit une sortie de modèle et le champ statique H_s correspondant (calculé par le bloc statique) soit une entrée de modèle comme représenté sur la Figure 3-3.

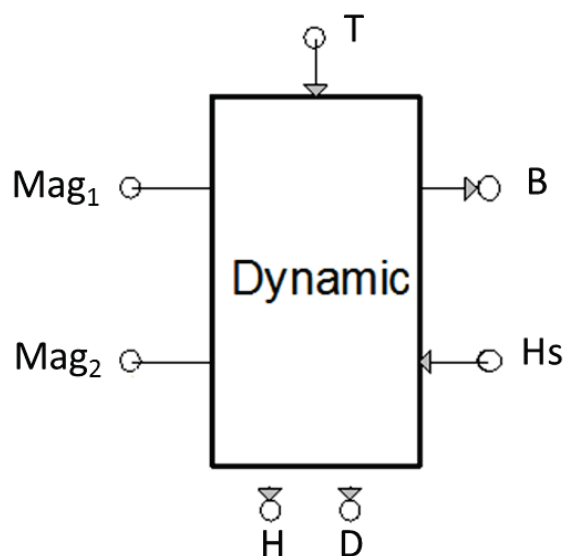


Figure 3-3: Modèle de Bloc Dynamique.

Le modèle dynamique a des bornes magnétiques, Mag1 et Mag2 qui sont directement reliés au modèle d'enroulement. Une borne thermique d'entrée (T) est utilisée pour régler la température du modèle. Deux bornes de sortie D et H, représentant respectivement la dérivée de la densité de flux et le champ magnétique total sont disponibles pour calculer les pertes fer. Le modèle dynamique comprend des paramètres géométriques comme la section magnétique (s) et longueur moyen (l), ainsi que des paramètres des modèles dynamiques qui dépendent du modèle choisi.

3.2.1.3 Modèle de Block Statique

Le modèle décrit le comportement statique d'hystérésis statique de matériaux magnétiques. Il est composé par l'un des modèles magnétiques statiques physiques ou mathématiques expliqués dans le chapitre précédent. Ce modèle de bloc est relié au modèle dynamique de telle sorte que la densité de flux soit une entrée du modèle et le champ statique calculé soit une sortie de modèle comme représenté sur la Figure 3-4.

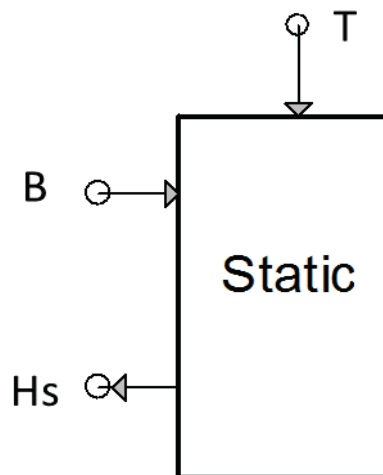


Figure 3-4: Modèle de bloc statique.

Le modèle statique a également une borne d'entrée thermique (T) pour prendre en compte la température. Le modèle comprend la perméabilité initiale (μ_0) comme paramètre, en plus des paramètres du modèle statique qui dépendent du modèle choisi.

3.2.1.4 Modèle Bloc Thermique

Le modèle thermique est constitué soit d'une source de température simple pour modéliser le comportement du composant à des températures d'exploitation différentes ou d'un circuit thermique équivalent, comprenant des résistances et des capacités thermiques pour modéliser l'auto-échauffement de la composante magnétique, Figure 3-5.

Pour les conditions thermiques statiques, la source de température est connectée à tous les blocs du modèle de composant. Alors que pour la modélisation auto-échauffement, un modèle thermique couplé avec les autres blocs de modèle est nécessaire. Comme un modèle thermique, nous utilisons un circuit thermique équivalent basé sur l'analyse nodale (expliqué dans le chapitre 2).

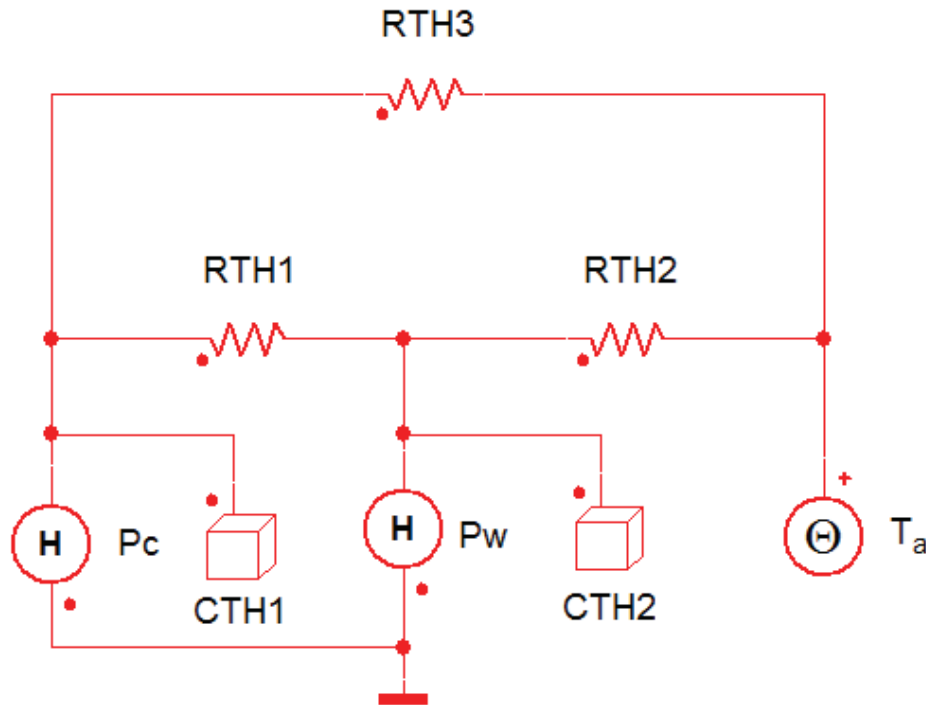


Figure 3-5 : Modèle thermique d'un inducteur dans Simplorer

3.2.2 Choix de Matériau

Dans notre travail, nous étudions les matériaux poudre fer et nanocristallins seulement en raison de leur haute performance dans le domaine de fréquence et de l'application considérée. Les matériaux nanocristallins sont principalement utilisés dans les filtres CEM et des applications d'électronique de puissance comme les alimentations à découpage et de convertisseurs statiques. Parmi les matières étudiées, les noyaux nanocristallins Nanophy N14E1, fourni par MECAGIS, sont choisis en raison de leurs propriétés intéressantes, comme l'induction de saturation élevée, le faible champ coercitif et la perméabilité relative élevée. En outre, ces matériaux sont déjà disponibles dans notre laboratoire et ont été utilisés dans l'application du filtre CEM dans une thèse précédente.

3.2.3 Choix des modèles statique et dynamique

3.2.3.1 Choix de modèle statique

Le choix du modèle statique s'appuie sur la caractérisation statique du matériau. Le matériau magnétique nanocristallin utilisé a une très mince boucle d'hystérésis statique (champ coercitif environ 0,5 A/m) et un comportement linéaire par morceaux. Grâce à ces caractéristiques, le modèle physique de Jiles-Atherton ne s'applique pas. Dans le but de décrire le comportement statique linéaire du matériau, le modèle mathématique polynomiale présenté dans le chapitre précédent dans la section modèles statique est utilisé (Figure 3-6).

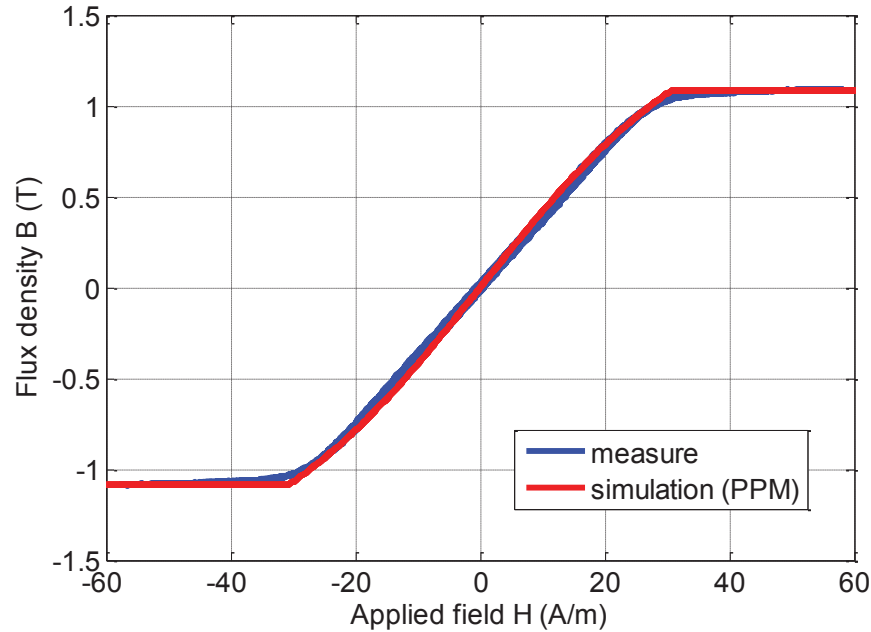


Figure 3-6: Courbes BH statiques mesurées et simulées par le modèle polynomiale par morceaux $f = 1$ Hz

3.2.3.2 *Choi de modèle dynamique*

Concernant le modèle dynamique, nous avons commencé la modélisation en utilisant DSF en raison de ses avantages comme la simplicité, un seul paramètre dynamique, et peu de temps de calcul. Toutefois, en raison des pertes excédentaires élevées du matériau choisi, ce modèle n'est pas très précis sur toute la plage de fréquence. Pour cette raison, le modèle de Bertotti est utilisé comme modèle dynamique. En utilisant ce modèle, nous sommes capables de modéliser les boucles d'hystérésis dynamiques du N14E1 avec une grande précision (erreur quadratique moyenne: $MSE < 1 \times 10^{-3}$) comme indiqué dans la Figure 3-7.

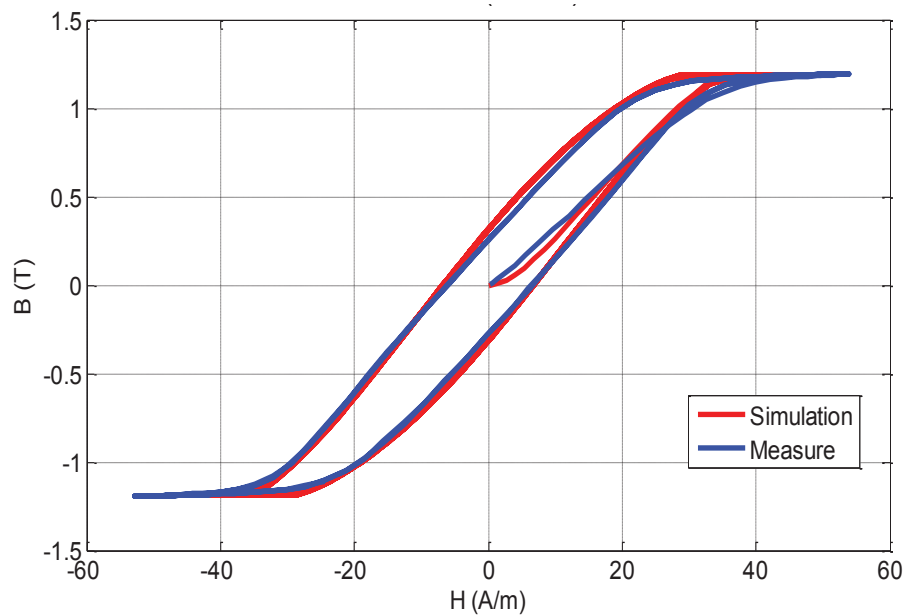


Figure 3-7 : Courbes BH dynamiques mesurées et simulées par le modèle de Bertotti $f = 10$ kHz

En fait ce modèle, selon G. Bertotti, sépare les pertes dynamiques entre pertes par courants de Foucault et les pertes excédentaires par deux termes dérivés de flux dans l'équation de modèle général. En conséquence, il est plus précis mais nécessite deux paramètres dynamiques.

Selon les lois de matériaux statiques et dynamiques choisis (polynômes et Bertotti), un total de 6 paramètres (4 statiques et 2 dynamiques) sont nécessaires pour le modèle complet de composant. L'identification des paramètres statiques et dynamiques et leur variation en fonction de la température sont présentées dans la section suivante.

3.2.4 Dépendance sur la température et l'extraction des paramètres

3.2.4.1 Paramètres Statiques

Les paramètres du modèle statique sont identifiés à partir des mesures statiques à l'aide de fitting mathématique. Leur évolution en fonction de la température est étudiée. Étant donné que la tendance de la variation de ces paramètres est monotone, une approximation linéaire peut exprimer cette variation en fonction de la température. Cette fonction linéaire est mise en œuvre dans le modèle pour le calcul de chaque paramètre à chaque température.

Pour le modèle polynomial de 5^{ème} ordre, les trois paramètres p_1 , p_3 et p_5 sont identifiées pour différentes températures allant jusqu'à 250 °C. Les variations de ces trois paramètres en fonction de la température sont présentés en Figure 3-8. La variation du 4^{ème} paramètre statique H_b est également étudiée et représenté dans la Figure 3-8. Les approximations de ces quatre paramètres sont implémentées dans le modèle de bloc statique.

$$B(H) = p_5 \cdot H^5 + p_3 \cdot H^3 + p_1 \cdot H^1 \quad (3.3)$$

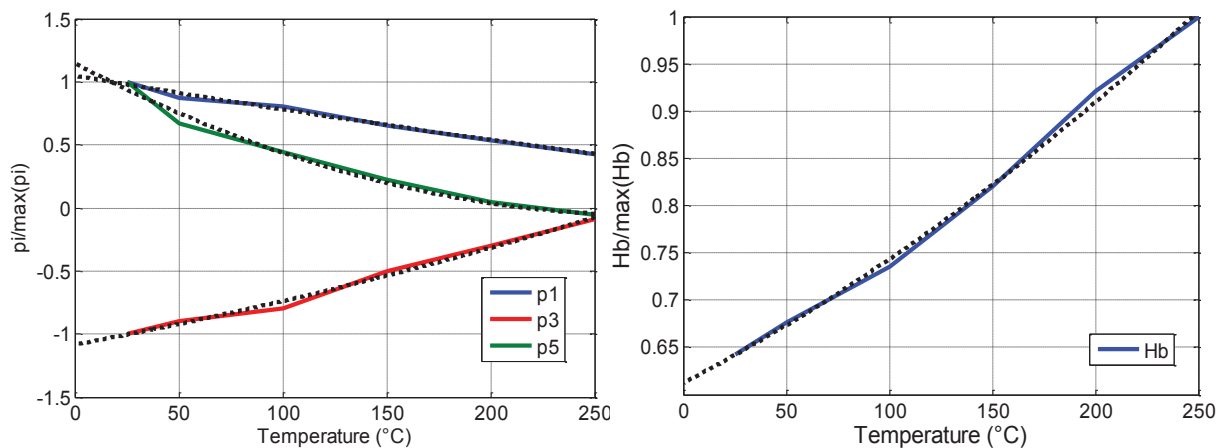


Figure 3-8: Variations des paramètres statiques avec la température (approchées par des courbes en pointillés)

3.2.4.2 Paramètres Dynamiques

La variation des paramètres dynamiques en fonction de la température doit être étudiée afin d'associer les effets thermiques du modèle dynamique. Comme γ ne dépend que de la conductivité et de l'épaisseur de ruban du matériau, il est directement calculé à partir des mesures de conductivité électrique en utilisant la méthode de quatre pointes. Cette technique de mesure comporte quatre sondes: deux sondes pour le passage d'un courant continu à travers l'échantillon et les deux autres sondes de mesure de la tension induite. La résistance du film

est le rapport entre la tension et le courant. La résistivité ρ est calculée à partir de la résistance de mesure R .

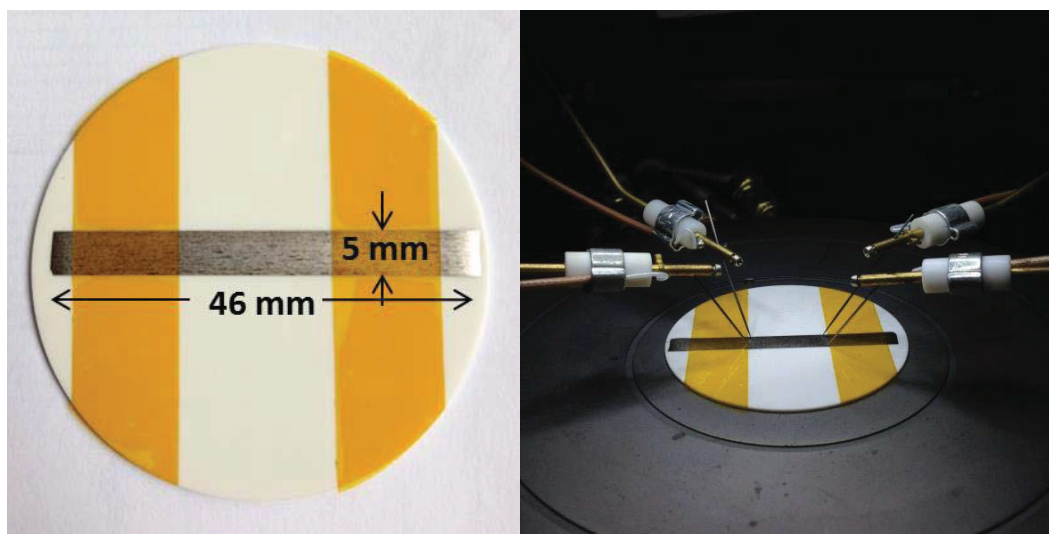


Figure 3-9: La mesure de la résistivité d'un ruban nanocristallin

Pour mesurer la résistivité du matériau nanocristallin N14E1, un échantillon de ruban du matériau d'épaisseur $20\text{ }\mu\text{m}$ est aplati et fixé sur un support en céramique (Figure 3-9). En utilisant la technique à quatre points, la résistivité du matériau est mesurée à des températures comprises entre $25\text{ }^{\circ}\text{C}$ et environ $300\text{ }^{\circ}\text{C}$. A $25\text{ }^{\circ}\text{C}$, la résistivité mesurée est très proche de valeur donnée par le constructeur ($1,15\text{ }\mu\Omega\cdot\text{m}$). Lorsque la température augmente, la résistivité augmente linéairement. A partir des mesures de résistivité le paramètre dynamique γ est calculé et sa variation avec la température est représentée par la Figure 3-10.

L'autre paramètre α est extrait par le fitting mathématique de l'équation de Bertotti avec un cycle BH mesuré à 10 kHz . Il est calculé de façon à avoir le même cycle BH mesurés et simulés à chaque température. Les résultats sont présentés sur la Figure 3-10 représentant les valeurs normalisées du deuxième paramètre α dynamique en fonction de la température. La variation de α reste approximativement linéaire jusqu'à $150\text{ }^{\circ}\text{C}$ après cette température sa valeur diminue rapidement puis reste constante et après $200\text{ }^{\circ}\text{C}$.

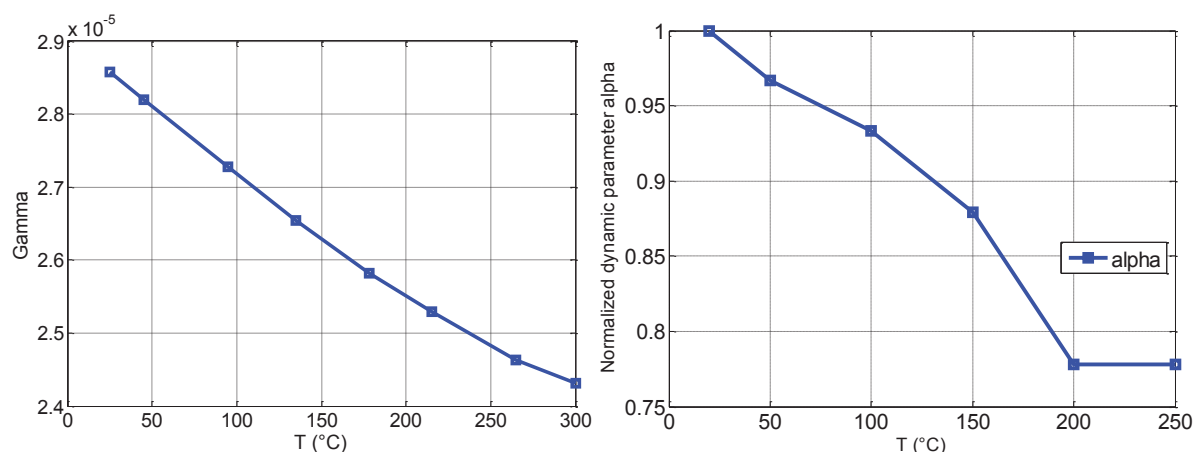


Figure 3-10: Variation des paramètres dynamiques γ (à gauche) et α (à droite) avec la température

Une approximation linéaire de la variation des paramètres dynamiques en fonction de la température est mise en œuvre dans le modèle dynamique. Même si la variation d' α n'est pas parfaitement linéaire, cette approximation conduit à une erreur maximale de 5% dans le calcul des pertes à 200 °C comparativement à moins de 1% à 25 °C. Pour plus de précision, un polynôme de degré plus élevé pourrait être utilisé.

3.3 Simulation et Validation de Modèle

Pour valider le modèle développé, un circuit identique au circuit de banc d'essai utilisé pour la mesure est simulé. La comparaison entre les cycles BH mesurés et simulés est présentée pour différentes températures et fréquences. Les résultats sont présentés dans la Figure 3-11 et la Figure 3-12.

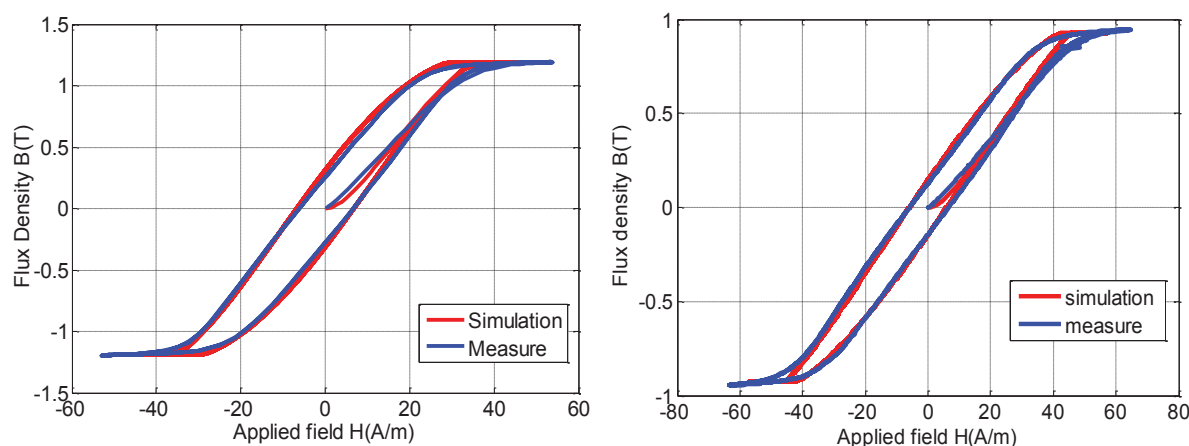


Figure 3-11: Courbes BH dynamique ($f = 10$ kHz) mesurée et simulée à $T = 25$ °C (à gauche) et $T = 155$ °C (à droite)

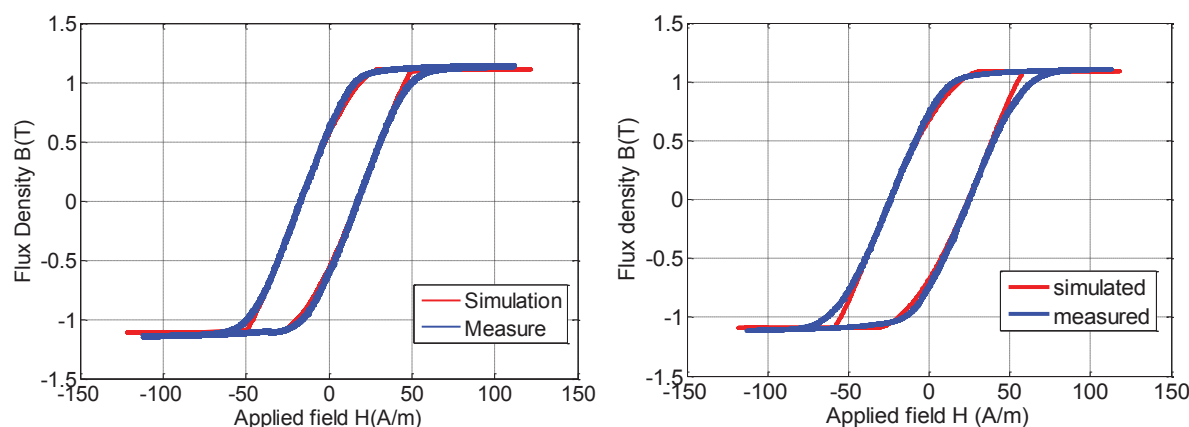


Figure 3-12: Courbes BH dynamiques mesurées et simulées à 20 kHz (à gauche) et 40 kHz (à droite)

La Figure 3-11 représente les cycles dynamiques mesurés et simulés à 25 °C (à gauche) et 155 °C (à droite). Cela montre une bonne corrélation entre les boucles d'hystérésis dynamique mesurées et celles simulées en fonction de la température.

Pour valider le modèle thermique et le couplage magnétothermique dans l'environnement de simulation de circuit, un circuit de RL qui comprend à la fois le modèle du composant magnétique et son modèle thermique correspondant est simulé.

Le modèle thermique est ensuite validé en comparant les deux températures mesurées (de noyau et de bobinage) à celles simulées pour 20 kHz et 40 kHz. Les résultats en Figure 3-13 montre un bon accord entre les évolutions des températures mesurées et simulées en fonction du temps. Par conséquent, le modèle thermique proposé décrit complètement l'auto-échauffement du composant magnétique dans les deux régimes transitoires et permanents. La température de noyau dépasse 70 °C pour un courant sinusoïdal de 0,6 A appliqué à 40 kHz. Cette température a des effets non négligeables sur le comportement magnétique qui est prise en compte grâce au modèle thermique.

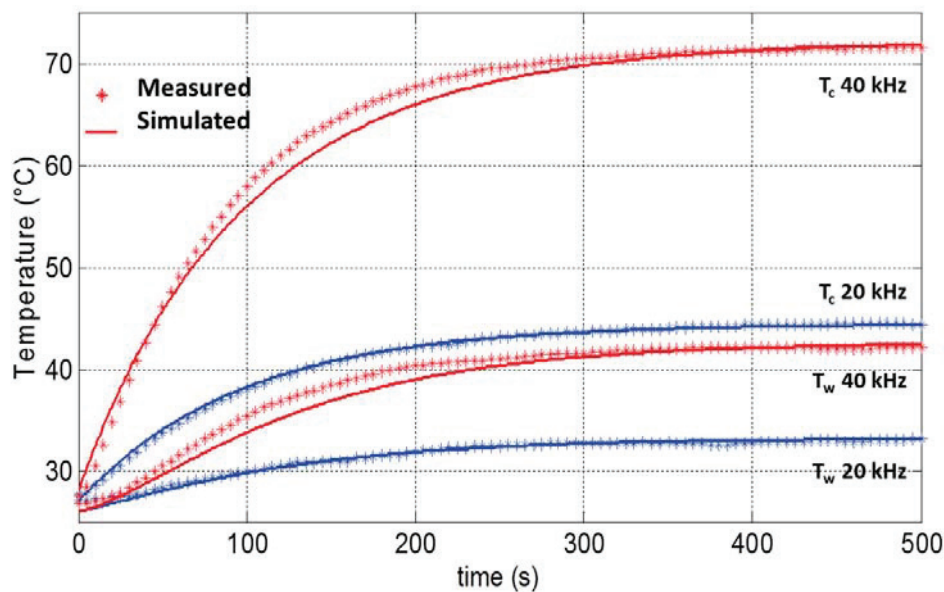


Figure 3-13: Températures de noyau (T_c) et d'enroulement (T_w) Mesurées et simulées.

3.4 Conclusion

Dans ce chapitre, la structure modulaire et le développement d'un modèle de composant magnétique dépendant de la température et sa mise en œuvre dans le logiciel de simulation de circuit "Simplorer" sont présentés. La méthode est validée pour un matériau nanocristallin en choisissant les lois statiques et dynamiques appropriées et en comparant les courbes BH mesurées et simulées. Les résultats sont en bon accord. Un modèle thermique est également présenté et couplé avec le modèle magnétique pour tenir compte des effets thermiques statiques et dynamiques.

4. Application d'Electronique de Puissance

4.1 Introduction

Dans les applications d'électronique de puissance, les composants magnétiques sont souvent soumis à des formes d'onde non-sinusoïdales, des fréquences variables et à des conditions de polarisation. Ces conditions de fonctionnement génèrent différentes pertes dans le noyau magnétique par rapport à des pertes sinusoïdales données par le fabricant. Dans la phase de conception, le manque d'un diagnostic précis des pertes a des effets inacceptables sur l'efficacité, la fiabilité et la consommation d'énergie du système.

Les composants passifs et ceux magnétiques en particulier jouent un rôle clé dans les convertisseurs de puissance, donc l'analyse du comportement et des pertes de ces composants est essentiel. Comme le calcul des pertes dans un noyau magnétique n'est pas évident, les équations analytiques de Steinmetz (SE) ne parviennent pas à calculer les pertes précisément en raison de sa limitation à une excitation sinusoïdale.

Dans ce chapitre, le modèle de composant magnétique développé est testé pour deux inducteurs en deux matériaux différents (poudre et nanocristallins) dans une application de convertisseur de puissance. Les formes d'onde et les pertes dans les deux noyaux sont simulées et comparées à celles mesurées. Le modèle est validé pour différents courants d'ondulation et une gamme de fréquences relativement large (10 à 100 kHz). La polarisation continue est prise en compte dans les deux modes de conduction continue et discontinue. Les effets de la température sur les pertes fer pour l'inducteur avec un noyau en nanocristalline sont également étudiés.

4.2 Convertisseur Abaisseur

Les trois convertisseurs DC-DC les plus utilisés sont l'abaisseur, l'élévateur et l'abaisseur-élévateur. Chaque topologie possède des propriétés uniques. La topologie de convertisseur de puissance la plus commune est le convertisseur abaisseur. C'est un SMPS (Switched Mode Power Supply) non-isolés largement utilisé dans l'industrie pour convertir une tension d'entrée en une tension de sortie inférieure.

Le convertisseur abaisseur peut avoir deux modes de fonctionnement : le mode de conduction continue et le mode de conduction discontinue. Le mode continu est caractérisé par un courant continu circulant dans la bobine d'inducteur pendant l'ensemble du cycle de fonctionnement en régime permanent. Le mode discontinue est caractérisé par un courant nul pendant une partie du cycle de fonctionnement.

Dans un convertisseur abaisseur une tension carrée est appliquée sur l'inducteur et une polarisation de courant continue en fonction de la charge existe. Ceci induit des pertes différentes par rapport à celles fournies par les fabricants données pour une densité de flux sinusoïdal. La polarisation a également un effet significatif sur les pertes. Cela créerait une boucle d'hystérésis mineure non-centrée. Comme conséquence la prédiction des pertes fer devient complexe, et la modélisation magnétique précise est nécessaire. Pour ces raisons, l'application de convertisseur abaisseur est choisie pour tester le modèle dans différentes

conditions d'exploitation. Considérant un circuit convertisseur abaisseur, le modèle de composante magnétique remplacerait l'inducteur comme représenté sur la Figure 4-1.

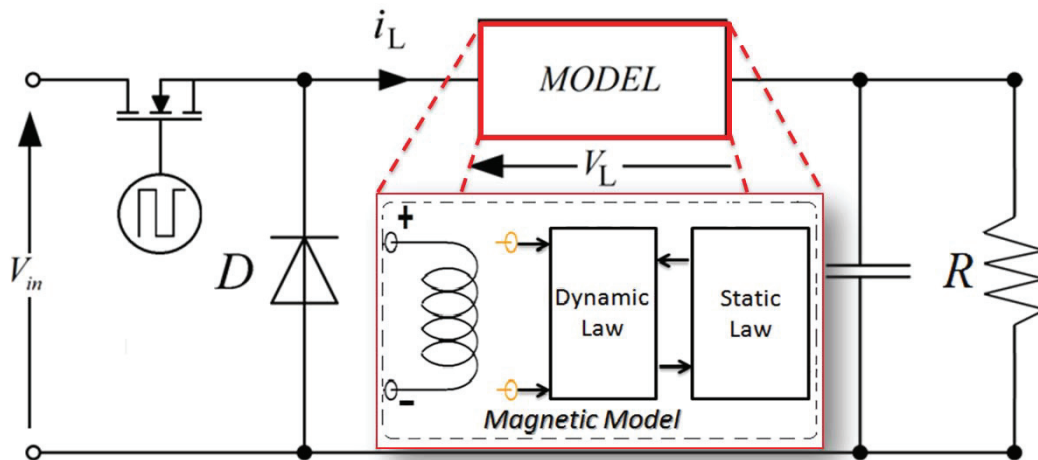


Figure 4-1: Circuit de convertisseur abaisseur comprenant le modèle de composant magnétique

Pour valider le modèle développé, un circuit de convertisseur abaisseur est nécessaire pour les mesures. Le circuit réalisé et ces mesures sont discutés dans la section suivante.

4.3 Circuit réalisé et mesures effectuées

4.3.1 Circuit de Convertisseur Abaisseur

Afin d'étudier le comportement des composants magnétiques dans les applications de puissance, un convertisseur abaisseur de 40 W est réalisé. La conception du circuit permet de faire varier les différents niveaux de tension et les fréquences de commutation. Des inducteurs avec 30 spires de fil de cuivre sont utilisés dans le circuit et peuvent être facilement remplacés via des connecteurs interchangeables. Des connecteurs d'oscilloscope dédiés sont également ajoutés au circuit pour éviter le bruit et les erreurs de mesures.

Pour mesurer avec précision les pertes magnétiques, un shunt (200 mΩ) est ajouté en série avec l'inducteur et des spires secondaires sont enroulées sur le même noyau. Le shunt permet des mesures précises du courant, tandis que les spires secondaires permettent la mesure de la tension induit sans ajouter les pertes de bobine. Le circuit du convertisseur est montré dans la Figure 4-2.

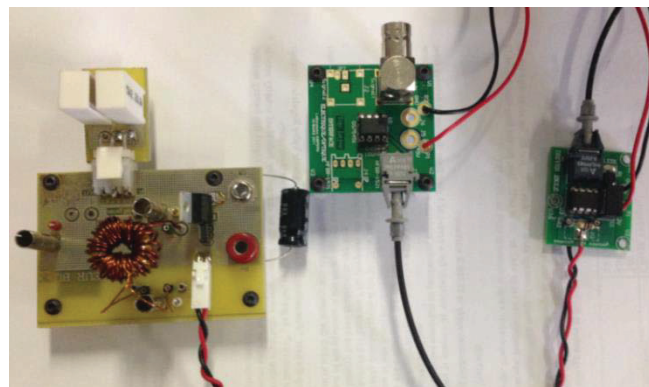


Figure 4-2: Convertisseur abaisseur avec circuit de commande de grille isolée optiquement

4.3.2 Choix d'inductances et la caractérisation de leurs matériaux magnétiques

Deux inductances de noyaux toroïdaux sont choisies pour être utilisées dans l'application abaisseur: Un noyau nanocristallin K44B200 de faible perméabilité fourni par MECAGIS et un noyau poudre Sendust HKBH fourni par TOHO ZINK. Le nanocristallin à faible perméabilité est un matériau récent résultant d'un recuit sous traction mécanique des amorphes. Ce matériau possède une induction à saturation élevée, de faibles pertes et une très bonne linéarité. Les Sendust (Fe-Si-Al), matériaux de poudre, ont un coût relativement faible et sont utilisés dans les convertisseurs commerciaux. Ils sont connus pour leurs faibles pertes et une performance stable avec la température.

Les matériaux choisis sont caractérisés avant utilisation dans l'application. Les mesures statiques et dynamiques sont effectuées sur des transformateurs d'essai de deux noyaux nanocristallin et poudre. Les résultats de mesure de la matière en poudre sont présentés dans la Figure 4-3, tandis que ceux du matériau nanocristallin sont présentés dans la Figure 4-4.

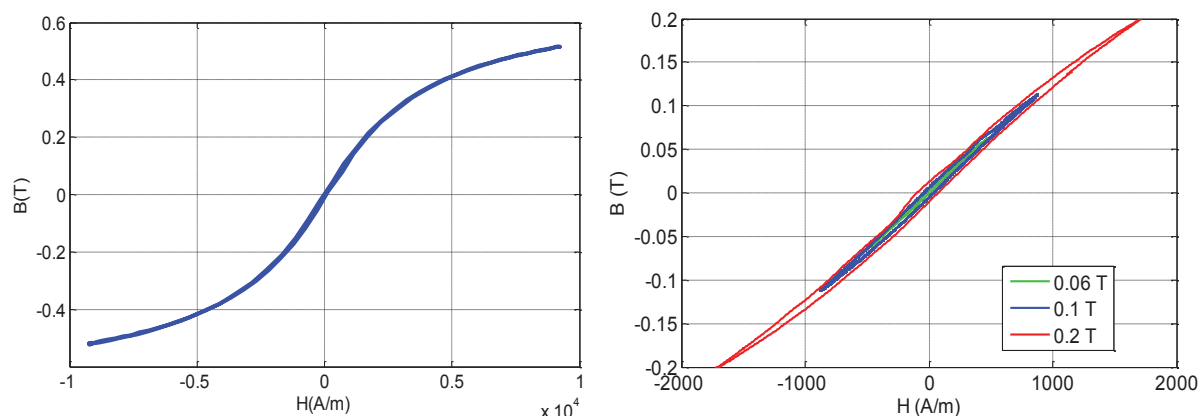


Figure 4-3: Caractérisation statique et dynamique de la matière magnétique en poudre (HKBH)

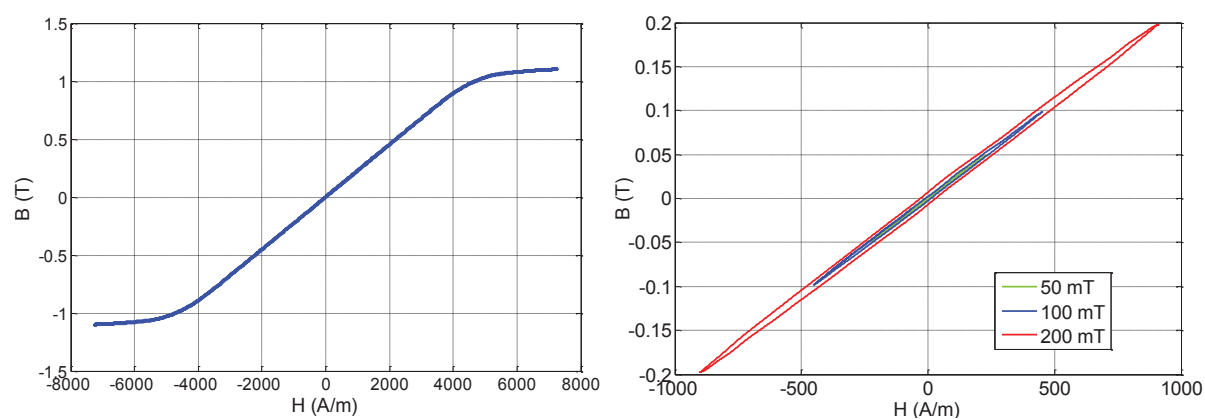


Figure 4-4: Caractérisation statique et dynamique du matériau magnétique nanocristallin (K44B200)

Les mesures statiques et dynamiques permettent l'identification des paramètres des modèles avec la même procédure faite pour le matériau N14E1 au chapitre 3.

4.3.3 Mesure et Calcul des Pertes Fer

Les pertes fer sont calculées à partir de mesures de courants primaires et de tensions secondaires. Ces mesures sont réalisées par un oscilloscope LECROY WavePro 7 Zi-A de une bande passante 1,5 - 6 GHz, 40 GS/s. Connaissant le courant primaire et la tension secondaire, les pertes fer sont calculées à l'aide de (4.1).

$$P = \frac{1}{T} \int_0^T \frac{N_1}{N_2} v_2(t) \cdot i_1(t) \cdot dt \quad (4.1)$$

4.3.3.1 Forme d'onde Différente

Comme mentionné précédemment, les pertes résultant de l'excitation sinusoïdale et non sinusoïdale ne sont pas les mêmes. Pour démontrer ça, la Figure 4-5 présente les pertes mesurées dans le noyau de poudre sous excitations de tension sinusoïdales et carrées. Ces mesures sont réalisées sous un niveau de densité magnétique de flux constant (100 mT) et pour une gamme de fréquence comprise entre 40 et 100 kHz. Puis les pertes sont calculées selon l'équation de Steinmetz et les paramètres correspondant fournis par le constructeur.

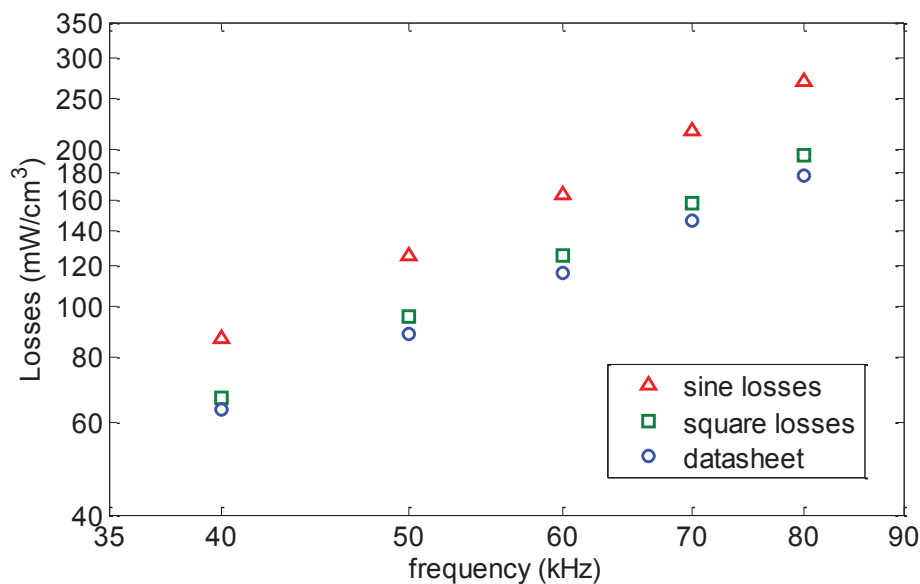


Figure 4-5: Pertes mesurées (carrés, sinus et datasheet) à B = 100 mT.

Les pertes fer calculées à l'aide des paramètres fournies par le fabricant pour les formes d'onde carrées correspondent à celles mesurées. Nous pouvons remarquer que ces pertes obtenus sous une excitation carrée avec un rapport cyclique de 50% sont inférieures aux pertes sinusoïdales.

4.3.3.2 Induction et fréquence variables

En outre les pertes fer sont fonction du niveau d'induction appliquée. Pour une section magnétique donnée et nombre de spires donné, l'induction appliquée est proportionnelle au rapport tension - fréquence. En variant la tension d'entrée du convertisseur abaisseur à chaque fréquence (dans la gamme de fréquences de 40 à 100 kHz), les pertes fer sont mesurées pour différents niveaux d'induction. Les résultats sont présentés dans la Figure 4-6.

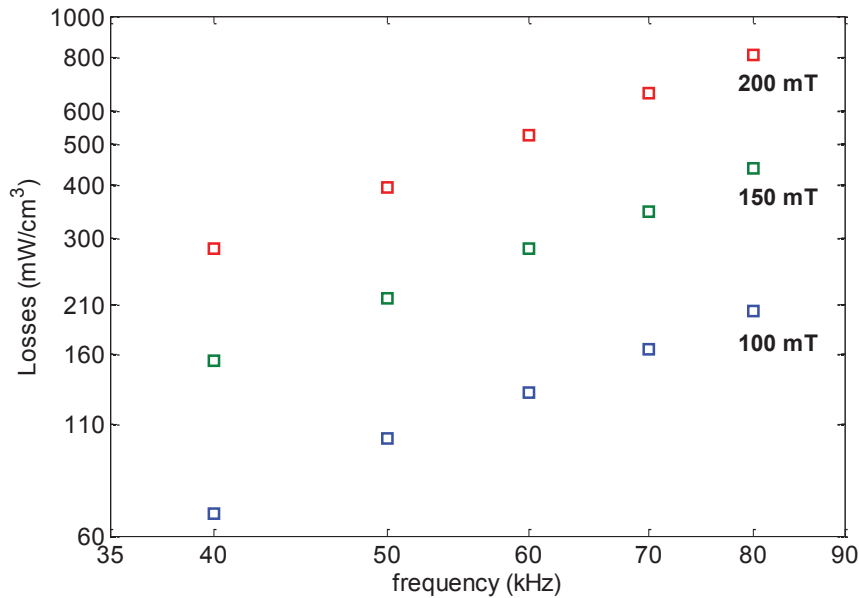


Figure 4-6: Pertes fer mesurées à différents niveaux de densité de flux dans l'application

La Figure 4-6 montre les pertes dans le noyau en poudre par unité de volume en fonction de la fréquence à trois niveaux d'induction. Outre l'augmentation des pertes avec la fréquence, les pertes augmentent nettement avec le niveau d'induction appliqué aussi. Nous pouvons remarquer que pour un niveau d'induction double, les pertes sont quatre fois plus élevées.

4.3.3.3 Charge Variable

Pour étudier les effets de la polarisation sur les pertes magnétiques de poudre fer, cinq circuits de charge, comprenant des résistances de puissance tubé en céramique, sont utilisés pour faire varier le courant continu dans le circuit de convertisseur. Ces charges résistives ayant des valeurs de 2, 3, 4, 4, 5, et 6 ohms sont connectées et les pertes fer sont mesurées simultanément. Les mesures effectuées sous tension d'entrée fixe de 5 V et de fréquence de 25 kHz sont présentées dans la Figure 4-7.

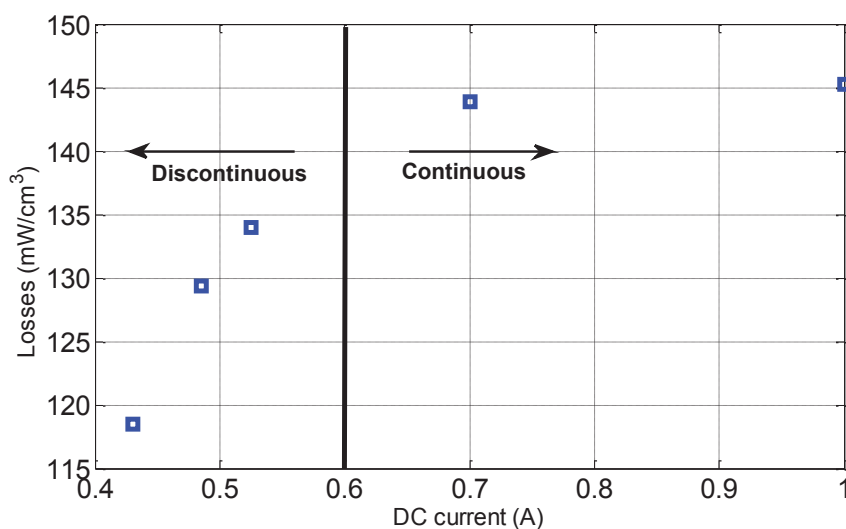


Figure 4-7: Pertes fer mesurées pour des courants de charge variables

L'effet de la composante continue sur les matériaux nanocristallin n'est pas étudié en raison de leur bon comportement statique linéaire (voir boucle d'hystérésis statique). Du fait de cette linéarité en dessous de la saturation, la polarisation continue n'a presque aucun effet sur les pertes fer pour ce matériau particulier jusqu'à 1 Tesla. Cela donne aux matériaux nanocristallins un avantage dans les applications avec des polarisations continues variables.

Cependant, le noyau nanocristallin étudié est sensible à la température, tandis que la température a des effets négligeables sur le noyau de poudre. Selon le constructeur, la perméabilité du noyau HKBH varie d'environ 2% à 160 °C. Pour cette raison, les effets de température sont étudiés seulement sur le noyau nanocristallin et non pas sur le noyau de poudre.

4.3.3.4 Température Variable

Pour étudier l'influence de la température sur le noyau nanocristallin dans l'application, une petite configuration permettant le chauffage de matériau est réalisée. Bien relié au circuit de Buck, le noyau nanocristallin utilisée est placé sous une source à air chaud. Le noyau est isolé du milieu avec de capuchon de silicium résistant à la chaleur. Un thermocouple est également utilisé pour assurer les mesures de température précises. Cette configuration permet des températures allant jusqu'à 300 °C appliqués sur le noyau magnétique pendant le fonctionnement normal du convertisseur abaisseur.

Les Pertes fer sont mesurées à différentes températures et fréquences et sont résumés dans le graphique 3D de Figure 4-8. En effet les pertes fer sont mesurées dans la gamme de fréquences de 30 à 80 kHz à 5 niveaux de température (25, 50, 100, 150 et 200 °C).

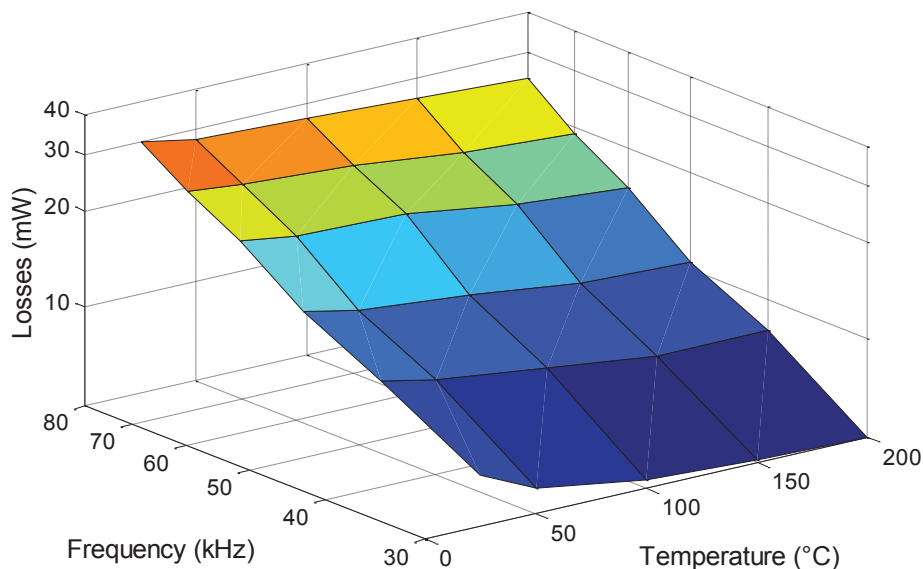


Figure 4-8: variation des pertes fer dans l'application pour le matériau nanocristallin en fonction de la fréquence et de la température

Sur la Figure 4-8 nous pouvons remarquer l'effet de la température sur ce matériau, à savoir que les pertes fer diminuent avec la température. Entre 25 °C et 200 °C, les pertes dans le noyau varient de 15% à 25% en fonction de la fréquence.

Enfin, on ne peut pas conclure qui est un meilleur noyau pour l'application de convertisseur abaisseur. Il existe un compromis entre le point de fonctionnement, la dimension, la fréquence et la température. Le tableau 1 résume le comportement du noyau magnétique sélectionné dans l'application de Buck. Le noyau de poudre a un coût inférieur et une bien meilleure stabilité avec la température alors que le noyau nanocristallin a des pertes fer inférieures et une meilleure stabilité à la polarisation DC. Les deux matériaux ont une très bonne performance dans la gamme de fréquence intermédiaire et peuvent fonctionner jusqu'à 1 MHz sans aucun problème.

Summary on Magnetic Cores		
	<i>HKBH</i>	<i>NANO</i>
Cost	**	*
DC bias	*	**
Core losses	*	**
Temperature	**	*
Frequency range	**	**
Available sizes and shapes	**	*

Table 1: Résumé sur la performance des matériaux magnétiques dans l'application abaisseur

4.4 Implémentation de Modèle et Résultats de Simulation

Pour valider le modèle développé dans l'application de convertisseur abaisseur, un circuit identique au circuit de Buck utilisé pour les mesures est simulé dans Simplorer comme indiqué dans la Figure 4-9. Le modèle de l'inducteur comprend les deux modèles statiques et dynamiques.

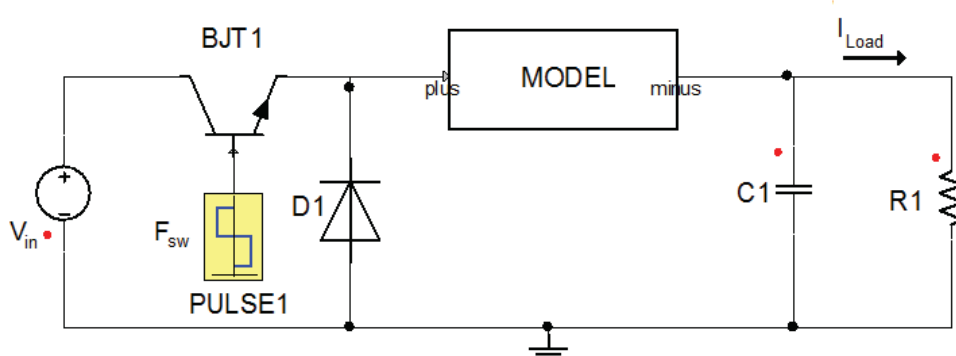


Figure 4-9: Circuit de simulation du convertisseur abaisseur

Les simulations sont exécutées pour différentes tensions, fréquences, et charges. La tension, le courant, le champ magnétique et la densité de flux sont disponibles à partir de la simulation. En outre, les pertes instantanées et moyenne et dans le cuivre et noyau sont également disponibles. Les comparaisons entre les formes d'onde et les pertes mesurées et simulées sont présentées à la Figure 4-10.

Les pertes fer par unité de volumes simulées (mode de conduction continue) pour les différents niveaux d'induction sont comparées à celles mesurées dans la gamme de fréquences de 40 à 100 kHz. Les résultats pour le noyau de poudre de HKBH sont présentés dans le Figure 4-10. Les simulations et les mesures aux trois niveaux de 100 mT, 150 mT et 200 mT induction sont en bon accord. Nous notons qu'un seul paramètre dynamique " α " doit être identifié à partir des mesures sinusoïdales. L'autre paramètre γ dynamique est extrait de la résistivité et des dimensions de noyau. Les expériences confirment la précision de la prédiction des pertes obtenues à partir de modèle avec une erreur maximale de 3% (MSE).

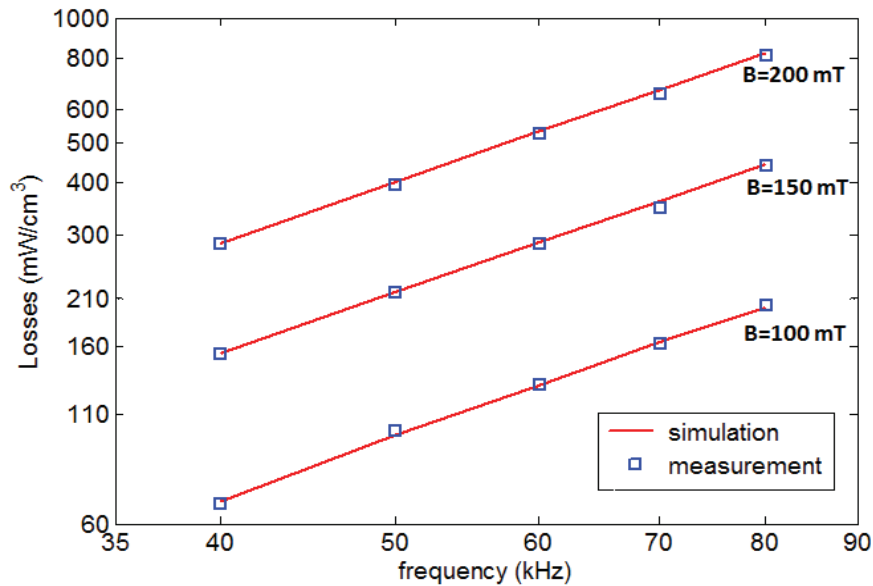


Figure 4-10: Pertes fer mesurées et simulées dans le noyau de poudre HKBH

En outre, la tension et le courant d'inductance dans les deux modes de conduction sont disponibles dans la simulation circuit et sont tracées. Figure 4-11 et Figure 4-12 montrent les résultats de mesure et de simulation des tensions et courants respectivement à 50 kHz. Simulations et mesures sont en bon accord.

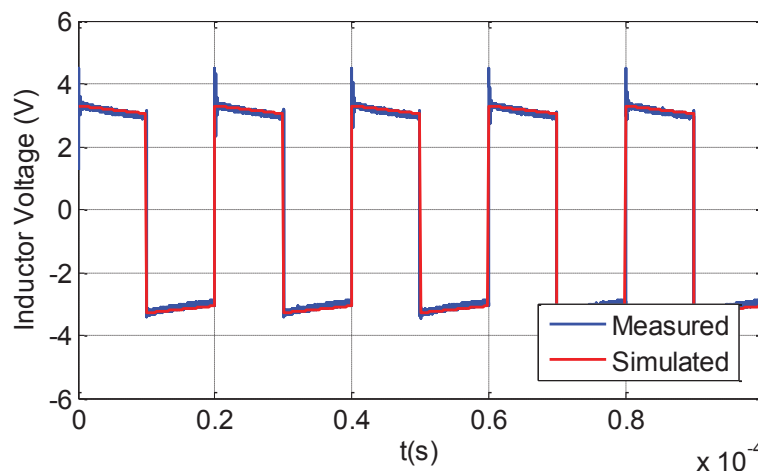
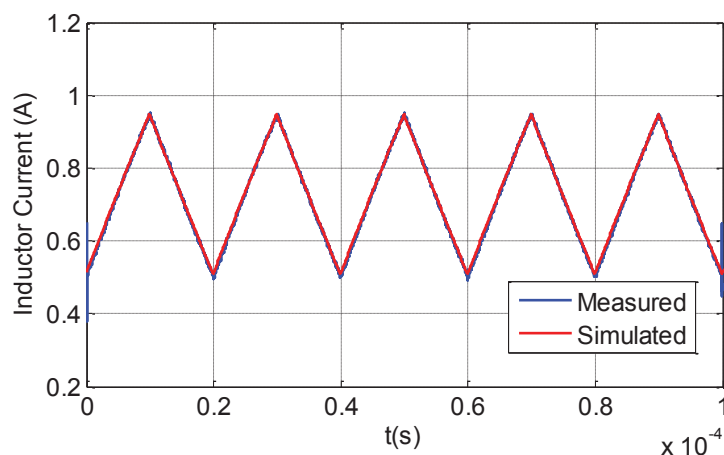


Figure 4-11: Tension de l'inductance mesurée et simulée à $f=50$ kHz

Figure 4-12: Courant de l'inductance mesuré et simulé a $f=50$ kHz

Pour tester le modèle dans le mode de conduction discontinue et sous composant continue variable, les simulations sont effectuées à différentes charges identiques à ceux utilisés dans les mesures. Dans les mêmes conditions, les pertes fer simulées et mesurées par unité de volume sont comparées et présentées dans la Figure 4-13. Les résultats montrent l'accord entre les simulations et les mesures pour les cinq charges (2, 3, 4, 5, et 6 ohms). Cela indique l'efficacité du modèle pour les deux modes de conduction continues et discontinues du convertisseur abaisseur.

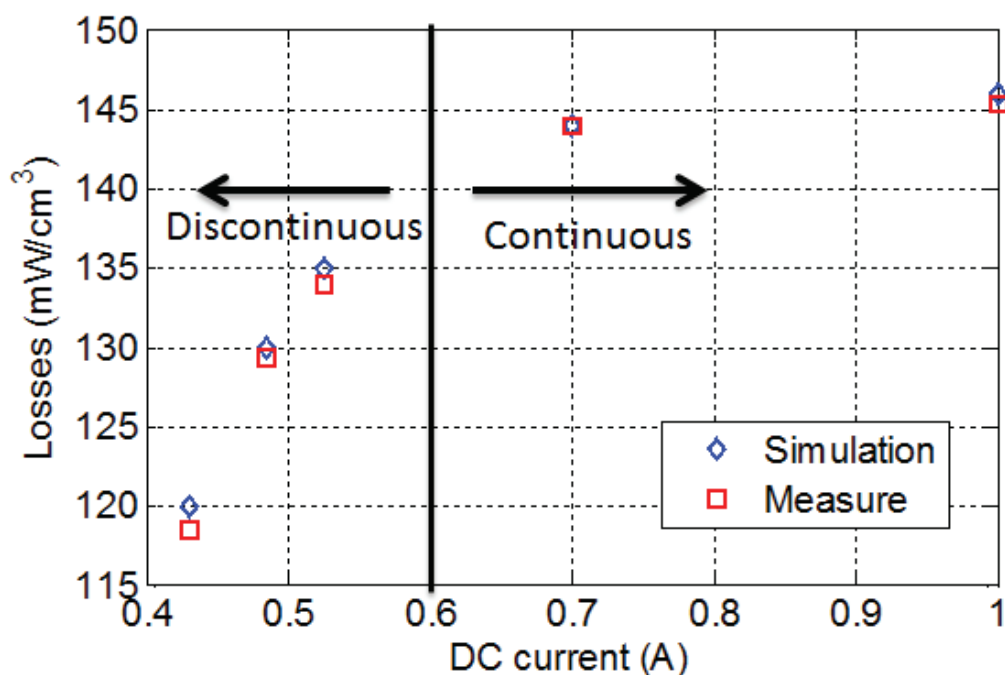


Figure 4-13: Pertes fer simulées et mesurées sous des courants de charge variables.

Conclusion

Dans cette thèse, nous introduisons les matériaux magnétiques, leurs classes et leurs applications en se concentrant sur les matériaux magnétiques doux utilisés dans l'électronique de puissance. Les deux principales catégories de matériaux étudiées dans notre travail sont les

matériaux poudres de fer et nanocristallins. Chacun de ces matériaux étudiés a des comportements hystérésis, dynamiques et thermiques spécifique. Ces comportements ont été étudiés par la caractérisation des matériaux pour différentes fréquences et températures.

Les lois de modélisation magnétiques statiques et dynamiques bien connus et largement utilisés en génie électrique sont présentées en se concentrant sur les modèles actuellement utilisés dans la simulation de circuit. En outre, les principes de la modélisation thermique, des modèles thermiques et le couplage magnétothermique sont expliqués

Le modèle de composant magnétique développé dans cette thèse est un modèle dynamique non linéaire pour une utilisation dans les simulateurs de circuit. Il comprend les comportements d'hystérésis et dynamiques de matériau avec une modélisation précise de pertes dans le noyau et l'enroulement en plus des effets thermiques. Le modèle est basé sur le principe de la séparation des contributions statiques et dynamiques. Afin de s'adapter à différents types de matériaux magnétiques, le modèle de composant magnétique se compose de trois grands blocs: un bloc de bobinage permettant le couplage entre les domaines électriques et magnétiques en utilisant les lois de Ampère et de Faraday, un second bloc (modèle statique) pour décrire la comportement d'hystérésis statique du matériau magnétique et un troisième bloc (modèle dynamique) pour inclure les effets dynamiques du noyau.

Pour décrire le comportement statique des matériaux utilisés dans notre travail, un modèle mathématique polynomiale est utilisé. En ce qui concerne le comportement dynamique du matériau, le modèle de Bertotti est utilisé. Les paramètres de deux modèles et leurs évolutions en fonction de la température sont également étudié.

Dans le but de tester l'adaptabilité, la fiabilité et la précision du modèle développé pour une utilisation dans des applications d'électronique de puissance, il a été mis en œuvre dans une application de convertisseur abaisseur. Le modèle de composant magnétique développé est testé pour deux matériaux candidats, un noyau de poudre Sendust et un noyau nanocristallin à faible perméabilité. Les formes d'onde et les pertes des deux inducteurs poudre de fer et nanocristallins sont simulées et comparées à celles mesurées (erreur maximum de 3%). Le modèle est validé pour différentes ondulations de courant, différentes charges résistives et une large plage de fréquences (10 à 100 kHz). La polarisation continue est prise en compte. Les deux modes de conduction continue et discontinue sont étudiés. Les effets de la température sur les pertes fer pour l'inducteur nanocristallin sont également discutés.

Enfin, le modèle développé est limité à des effets de peau négligeables, puisque le modèle ne prend pas en compte la diffusion magnétique. Les pertes de relaxation sont partiellement prises en compte (seulement dynamique) par le modèle de composant proposé. Les deux effets de la diffusion magnétique et les pertes de relaxation seront étudiées dans les travaux futurs de la mise en œuvre statique plus complexe (relaxation) et les lois dynamiques (diffusion). Aussi un futur travail sera consacré à développer le modèle de transformateur et la validation expérimentale des simulations. Un transformateur triphasé serait aussi l'un de nos perspectives d'avenir.